

# **Graphene–Based Electrocatalysts for Oxygen Reduction Reaction in High Temperature Proton Exchange Membrane Fuel Cells**

---

**Graphen–basierte Elektrokatalysatoren für die Sauerstoffreduktionsreaktion  
in Hochtemperatur–Protonenaustauschmembran–Brennstoffzellen**

Von der Fakultät für Mathematik und Naturwissenschaften der Carl von Ossietzky  
Universität Oldenburg zur Erlangung des Grades und Titels

Doktor der Naturwissenschaften  
– Dr. rer. nat. –

angenommene Dissertation

von Frau Dana Schonvogel  
geboren am 13.05.1987 in Varel

angefertigt am  
DLR–Institut für Vernetzte Energiesysteme e.V. in Oldenburg

### **Erstgutachter**

Prof. Dr. Michael Wark

(Institut für Chemie, Carl von Ossietzky Universität Oldenburg)

### **Zweitgutachter**

Prof. Dr. K. Andreas Friedrich

(Institut für Gebäudeenergetik, Thermotechnik und Energiespeicherung,  
Universität Stuttgart)

**Tag der Disputation:** 20.12.2018

# Abstract

Proton exchange membrane fuel cells (PEMFCs) play an essential role in a sustainable energy supply and have a wide application range from stationary to mobile power generation. However, higher lifetimes are mandatory to enhance their competitiveness with conventional systems. A great challenge is the catalyst degradation regarding instability of Pt nanoparticles and corrosion of carbon support. This necessitates a catalyst development towards enhanced durability. Strategy of this study is the deposition of Pt on alternative supports. Nanocomposites combine the carbon support with corrosion-resistant metal oxides. In this study, reduced graphene oxide (rGO) presents the basis for precipitation of two different metal oxide particles: tin-doped indium (III) oxide (ITO) and fluorine-doped tin (IV) oxide (FTO). Beyond these two composites, various carbons are tested for comparison: Multi-walled carbon nanotubes (MWCNTs), common carbon black (C), a newly developed carbon from hydrothermal carbonization of coconut shells (HTC-C) and rGO. Each catalyst is studied by several physical and electrochemical techniques. Stress testing ( $0.05\text{--}1.47\text{ V}_{\text{RHE}}$ ) induces degradation and provides the assessment of these materials towards their durability.

Reduced graphene oxide is synthesized from natural graphite via Hummer's method. Exfoliation of layers is achieved with specific surface area enlarged by factor of 36 and with increased defective structure by more than 250 %. Comparison to the other carbons reveals highly different morphologies. MWCNTs with rolled-up graphene layers possessing the lowest specific surface area of  $111\text{ m}^2\text{ g}^{-1}$  and HTC-C with highest amorphousness and greatest specific surface area of  $546\text{ m}^2\text{ g}^{-1}$  are the most contrary materials. Common Pt/C and especially Pt/HTC-C show much stronger carbon corrosion than Pt/MWCNTs and Pt/rGO caused by low degrees of graphitization. Pt stability is comparable on rGO, MWCNTs and C. Enforced Pt degradation on HTC-C showing the lowest carbon stability is shown in the form of loss of the electrochemical surface area and activity for oxygen the reduction reaction.

The nanocomposites are characterized by highly covered rGO with ITO and FTO particles, respectively. In case of FTO-rGO, Pt nanoparticles are preferentially deposited on FTO than rGO, whereas the contrary behavior is proven for ITO-rGO. Thus, a varying Pt distribution is revealed suggesting different Pt-support interaction. A positive effect of incorporated metal oxides is evidenced during CO stripping voltammetry in terms of enhanced CO tolerance. Regarding the durability, Pt aging on the composites is in

similar range to Pt/rGO. Comparable Pt degradation paths like agglomeration are proven by identical location transmission electron microscopy (IL-TEM). However, the support aging highly deviates. IL-TEM and electrochemical measurements demonstrate for Pt/ITO-rGO strongly changed and partially disappeared ITO particles as well as carbon corrosion. On one hand ITO dissolution uncovers the carbon surface without any protection against corrosion anymore, and on other hand preferred Pt deposition on rGO than on ITO can further enforce carbon corrosion. In contrast, support degradation of Pt/FTO-rGO is insignificant. FTO aggregates are unchanged in size, shape and position onto rGO. Formation of surface oxides on rGO is not electrochemically detected. The double layer capacitance is completely constant.

In conclusion, FTO is not only more stable but persistently protects rGO from corrosion, whereas ITO-rGO suffers from ITO degradation and carbon corrosion. Thus, the choice of metal oxide is crucial for catalyst's durability. Pt/FTO-rGO is a promising candidate for application in especially high temperature PEMFCs, which exposes the catalyst to harsher conditions than low temperature PEMFCs and hence requires a highly stable catalyst support. Substitution of ITO by FTO is furthermore very useful against the background of fuel cell catalyst costs.

# Zusammenfassung

Protonenaustauschmembran-Brennstoffzellen (PEMFCs) leisten in einer nachhaltigen Energieversorgung einen zentralen Beitrag und besitzen ein breites Anwendungsbereich von stationärer bis mobiler Stromerzeugung. Für die Wettbewerbsfähigkeit mit konventionellen Systemen sind jedoch höhere Lebensdauern notwendig. Insbesondere die Degradation des Katalysatormaterials hinsichtlich der Instabilität von Pt Nanopartikeln sowie der Korrosion des Kohlenstoffträgers erfordert eine Katalysatorentwicklung mit dem Ziel höherer Stabilität. Ansatz dieser Arbeit ist die Platinabscheidung auf alternativen Trägern in Form von Nanokompositen, welche den Kohlenstoffträger mit korrosionsbeständigeren Metalloxiden vereinen. Reduziertes Graphenoxid (rGO) stellt die Basis für die Abscheidung zweier verschiedener Metalloxidpartikel dar: Zinndotiertes Indium(III)-oxid (ITO) sowie fluordotiertes Zinn(IV)-oxid (FTO). Zusätzlich werden zum Vergleich unterschiedliche Kohlenstoffmaterialien untersucht: Mehrwandige Kohlenstoffnanoröhrchen (MWCNTs), konventionelles Carbon Black (C), ein neu entwickelter Kohlenstoff aus hydrothormaler Karbonisierung von Kokosnussschalen (HTC-C) sowie rGO. Neben physikalischen und elektrochemischen Analysetechniken werden die Katalysatoren mittels eines Stresstests ( $0.05\text{--}1.47\text{ V}_{\text{RHE}}$ ) untersucht, welcher Degradation induziert und die Bewertung elektrochemischer Stabilität ermöglicht.

Die Synthese des reduzierten Graphenoxids erfolgt ausgehend von natürlichem Graphit mithilfe der Hummer's Methode und führt zur Exfolierung der Graphenschichten. Die spezifische Oberfläche wird um den Faktor 36 sowie das Maß an Strukturdefekten um mehr als 250 % erhöht. Im Vergleich weisen die weiteren Kohlenstoffmaterialien deutlich unterschiedliche Morphologien auf. MWCNTs mit röhrenförmigen Graphenschichten und der niedrigsten spezifischen Oberfläche von  $111\text{ m}^2\text{ g}^{-1}$  sowie HTC-C mit der amorphesten Struktur und der größten spezifischen Oberfläche von  $546\text{ m}^2\text{ g}^{-1}$  stellen hier die gegensätzlichsten Materialien dar. Bedingt durch den niedrigen Grad an Graphitisierung weisen konventionelles Pt/C und insbesondere Pt/HTC-C in Gegenwart des Stresstests eine stärkere Kohlenstoffdegradation hinsichtlich der Bildung von elektrochemisch aktiven Oberflächenoxide und zunehmender Doppelschichtkapazität als Pt/MWCNTs und Pt/rGO auf. Neben einer vergleichbaren Platinstabilität auf den Trägern rGO, MWCNTs und C findet eine verstärkte Platindegradation in Form von Verlusten der elektrochemisch aktiven Fläche sowie der Aktivität für die Sauerstoffreduktionsreaktion auf HTC-C als instabilstes Kohlenstoffmaterial statt.

Zur Herstellung der Nanokomposite werden ITO beziehungsweise FTO Partikel auf rGO gefällt und anschließend Pt Nanopartikel abgeschieden. Im Falle des FTO-rGO kann eine bevorzugte Platinabscheidung auf FTO anstatt auf rGO gezeigt werden, wohingegen ein gegensätzliches Verhalten für ITO-rGO und somit eine abweichende Platinpartikelverteilung besteht. Für beide Katalysatoren mit Anwesenheit von Metalloxiden kann mittels der Stripping Voltammetrie eine verbesserte CO Toleranz nachgewiesen werden. Während des Stresstests findet eine zu Pt/rGO vergleichbare Platindegradation statt. Transmissionselektronenmikroskopie mit identischer Position (IL-TEM) vor und nach dem Stresstest zeigt zusätzlich vergleichbare Degradationspfade wie der Platinagglomeration. Die Alterung der Trägermaterialien hingegen weicht stark voneinander ab. Elektrochemische Messungen in Kombination mit IL-TEM offenbaren für Pt/ITO-rGO neben verändertem und teilweise nicht mehr vorhandenem ITO eine im Vergleich zu Pt/FTO-rGO erhöhte Kohlenstoffkorrosion. Zum einen führt eine Auflösung von ITO Partikeln zu verringertem Korrosionsschutz des rGO. Zum anderen kann die präferierte Pt Abscheidung auf rGO anstelle des ITO zu verstärkter katalysierter Kohlenstoffkorrosion führen. Die Trägerdegradation von Pt/FTO-rGO hingegen ist vernachlässigbar. FTO Partikel sind in Größe, Form und Position unverändert. Auch die Bildung von Oberflächenoxiden auf rGO sowie eine veränderte Doppelschichtkapazität sind elektrochemisch nicht detektiert.

Somit ist FTO nicht nur stabiler als ITO, sondern schützt außerdem rGO vor Korrosion. Im Gegensatz dazu leidet ITO-rGO während des Stresstests unter Degradation der ITO Partikel sowie des Kohlenstoffs, sodass die Wahl des Metalloxids für die Katalysatorstabilität entscheidend ist. Insgesamt ist Pt/FTO-rGO ein vielversprechender Kandidat für die Anwendung vor allem in Hochtemperatur-PEMFCs, wo der Katalysator korrosiveren Bedingungen als in der Niedrigtemperatur-PEMFC ausgesetzt und somit ein hochstabiler Katalysatorträger erforderlich ist. Die Substitution von ITO durch FTO ist weiterhin hinsichtlich der Brennstoffzellenherstellungskosten sinnvoll.



# Contents

<b>1</b>	<b>Motivation</b>	<b>1</b>
<b>2</b>	<b>Objective</b>	<b>2</b>
<b>3</b>	<b>Fundamentals</b>	<b>5</b>
<b>3.1</b>	<b>PEM Fuel Cells</b>	<b>6</b>
3.1.1	Assembly and Operating Principle of PEMFCs	6
3.1.2	High Temperature PEM Fuel Cells	8
<b>3.2</b>	<b>Pt Catalysts</b>	<b>9</b>
3.2.1	Thermodynamics and Kinetics	10
3.2.2	Oxygen Reduction Reaction	12
3.2.3	Catalyst Degradation	15
3.2.4	Support Materials	22
<b>4</b>	<b>Experimental Methods</b>	<b>35</b>
<b>4.1</b>	<b>Catalyst Synthesis</b>	<b>35</b>
4.1.1	Pt Nanoparticles	36
4.1.2	Support Materials	38
<b>4.2</b>	<b>Physical Characterization</b>	<b>40</b>
4.2.1	Microscopy	41
4.2.2	Spectroscopy	42
4.2.3	Further Methods	44
<b>4.3</b>	<b>Electrochemical Characterization</b>	<b>47</b>
4.3.1	Setup	47
4.3.2	Cyclic and CO Stripping Voltammetry	49
4.3.3	RDE Experiments	52
4.3.4	Accelerated Stress Testing	55
<b>5</b>	<b>Results and Discussion</b>	<b>57</b>
<b>5.1</b>	<b>Physical Characterization of Graphene-Based Supports</b>	<b>57</b>
5.1.1	Reduced Graphene Oxide	57
5.1.2	Comparison of Carbons	64

5.1.3	Nanocomposites of Reduced Graphene Oxide with Doped Metal Oxides	76
<b>5.2</b>	<b>Physical Characterization of Platinum on Supports</b>	<b>84</b>
5.2.1	Analysis of Pt Nanoparticles	85
5.2.2	Location of Platinum on the Nanocomposites	89
<b>5.3</b>	<b>Electrochemical Characterization of Pt Catalysts</b>	<b>93</b>
5.3.1	Carbon-Based Pt Catalysts	93
5.3.2	Pt Catalyst based on Activated Carbon from HTC	108
5.3.3	Pt Catalysts based on Nanocomposites	115
<b>6</b>	<b>Summary and Conclusions</b>	<b>130</b>
6.1	Comparison of Carbon Supports	130
6.2	Suitability of Nanocomposite Supports	132
<b>7</b>	<b>Outlook</b>	<b>135</b>

# 1 Motivation

Restructuring of the primary energy supply presents today's great challenge because of limited fossil resources on one and climate change on the other hand. Since the relation between emission of greenhouse gases and rise of global air temperature has already been started to be investigated in the 1,800s,<sup>[1-3]</sup> the anthropogenic impact on global warming is widely accepted nowadays. Thus, on annual UN Climate Change Conferences important milestones like the *Kyoto Protocol* including firm commitments to reduce gas emission have already been achieved. A newer convention from the 21<sup>st</sup> conference is the *Paris Agreement* which contains the two degree goal.<sup>[4]</sup> This describes that the increase of global air temperature compared to pre-industrial times may not exceed the limit of 2 °C. Figure 1a) shows the increased temperature and by regression analysis its exponential progression over time. Indeed, an increase of 1 °C is already exceeded, whereas in 2016 the highest global air temperature has been reached since 1850.<sup>[5]</sup> Furthermore, Figure 1b) depicts the increase of the worldwide carbon dioxide emission in the period from 1850 to 2014. Regression analysis reveals the exponential growth of annual CO<sub>2</sub> emission since 1850.

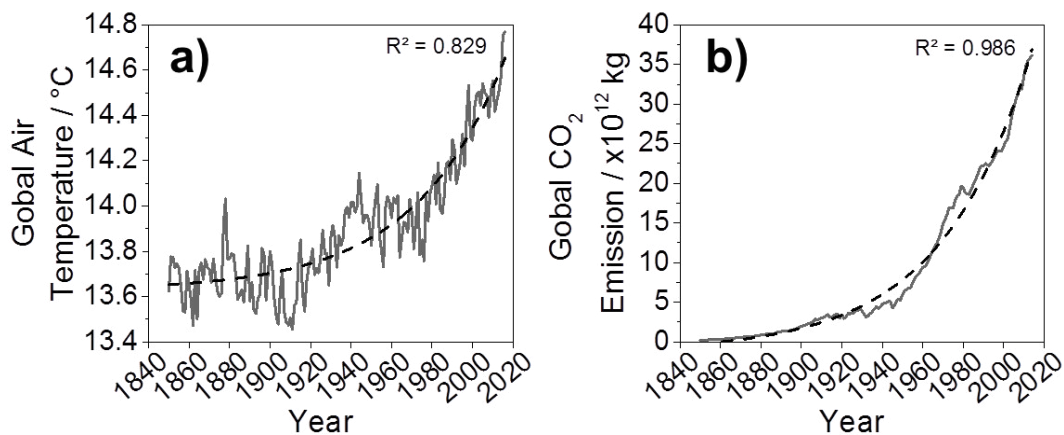


**Figure 1** Global air temperature against the year, adapted from<sup>[5]</sup> (a) and global emission of carbon dioxide against the year, adapted from<sup>[6]</sup> (b).

Against this background, Germany's goals are summarized in the *Climate Action Plan 2050* including greenhouse gas neutrality until 2050.<sup>[7]</sup> For achieving this goal, the use of renewable energies and thus a new way of providing energy is mandatory. Conventional centralized power plants are expected to be replaced by a decentralized power generation based on e.g. solar and wind energy.<sup>[8]</sup> This implies infrastructural challenges but also the issue of required energy storage through batteries, capacitors and especially hydrogen to ensure a continuous supply of energy through compensation of its irregularly availability and fluctuating consumption. Overall, using renewable sources complementarity to hydrogen and fuel cell technology, a sustainable energy supply is feasible.

## 2 Objective

Fuel cells can provide an important contribution in such a scenario of energy supply. Timed power production is enabled through direct conversion of chemical energy in the form of hydrogen into electrical energy. In view of sustainability, fuel cells in operation only release water and thermal energy and thus support the aim of greenhouse gas neutrality. Regarding the thermal energy further utilization in terms of heating is possible to obtain increased energy efficiencies. Especially, high temperature proton exchange membrane fuel cells (HT-PEMFCs) are characterized by a simplified cell design and possible utilization of reformat, being attractive for combined heat and power systems.<sup>[9-11]</sup> However, the difficulty in widespread implementation of fuel cell technologies is uncompetitive durability in comparison to the incumbent stationary and transport power systems.<sup>[12]</sup> Thus, enhancement of lifetime is important to achieve competitiveness of fuel cell systems and to relativize the costs in production. The *U.S. Department of Energy* (DOE) specifies targets for this purpose. Fuel cells ought to demonstrate 5,000 h until 2020 or ultimately 8,000 h in mobile as well as 60,000 h until 2020 in stationary applications with less than 10 % performance loss.<sup>[12, 13]</sup> At European level, the *Fuel Cells and Hydrogen Joint Undertaking* (FCH JU) drafted lifetime targets of 6,000 h for passenger cars and 13 years for combined heat and power systems (CHP) up to 5 kW until 2020.<sup>[14]</sup>

Up to now, cell components still show degradation leading to limited fuel cell lifetimes, although meanwhile the literature provides comprehensive studies on fuel cell aging mechanisms.<sup>[15-17]</sup> Particularly the commonly used platinum based catalyst causes performance losses through corrosion of the carbon support<sup>[18, 19]</sup> as well as instability of the platinum nanoparticles.<sup>[15, 20, 21]</sup> The exposure to automotive conditions in terms of load-cycled conditions with temporarily high cell potentials presents an enforced stressor for catalysts.<sup>[22, 23]</sup> Consequently, the modification of catalysts towards enhanced durability may contribute to longer fuel cell lifetimes. One possible strategy to increase catalyst stabilities is the application of platinum on alternative support materials. On one hand graphitic carbons with altered nanostructures and on the other hand metal oxides are candidates and could substitute the commonly used carbon black. Graphene-based catalysts have shown enhanced electrochemical stability due to their two-dimensional character,<sup>[24]</sup> whereas stability under cathodic potentials of fuel cells is also expected for several metal oxides due to their corrosion resistance.<sup>[25, 26]</sup> To obtain sufficient electrical conductivity, especially doped metal oxides like tin-doped indium (III) oxide (ITO) and fluorine-doped tin (IV) oxide (FTO) might be useful as fuel cell catalyst supports.<sup>[27]</sup>

In this work, the advantages of graphene-based carbons and doped metal oxides are combined in nanocomposites to investigate their suitability as durable Pt support for the reduction of oxygen. Two composites are in focus comprising reduced graphene oxide (rGO) as well as ITO nanoparticles on one side and FTO nanoparticles on the other. Besides these ITO-rGO and FTO-rGO nanocomposites, further supports are considered — common carbon black (C), multi-walled carbon nanotubes (MWCNTs) and a new sustainable carbon derived from hydrothermal carbonization of coconut shells (HTC-C) — enabling a comparative assessment of support durabilities. Platinum nanoparticles are deposited on each support to obtain the final electrocatalysts and to study their electrochemical stability.

Firstly, support materials and final Pt catalysts are synthesized, studied and compared by physical and electrochemical characterization techniques. Pt catalysts are analyzed in an electrochemical cell towards electrochemical surface areas (ECSA) and activity for oxygen reduction using the rotating disk electrode (RDE) technique. Experiments are performed in aqueous perchloric acid at room temperature ensuring the necessary conditions to get access to ORR kinetics.<sup>[28-32]</sup> Support characteristics are analyzed in terms of double layer capacitances and redox activity of functional groups. Secondly, accelerated stress testing (0.05–1.47 V<sub>RHE</sub>) is used to induce harsh electrochemically cycled conditions and hence to study platinum and support degradation. Outline of this work is provided in the following:

### **1. Synthesis and Physical Analysis**

- i. Synthesis of Reduced Graphene Oxide in Two Steps (4.1.2, 5.1)
- ii. Physical Comparison of the Carbon Supports (5.1.2)
- iii. Precipitation of Doped Metal Oxide Nanoparticles — ITO and FTO — on Reduced Graphene Oxide (4.1.2, 5.1.3)
- iv. Pt Nanoparticle Synthesis and Deposition on Supports (4.1.1, 5.2)

### **2. Evaluation of Electrochemical Durability**

- i. Accelerated Stress Testing of Carbon-based Pt Catalysts and Comparison to a Commercial Catalyst (5.3.1)
- ii. Investigation of a Pt Catalyst with Sustainable Support from HTC (5.3.2)
- iii. Accelerated stress testing of Pt Catalysts based on the Nanocomposites of Reduced Graphene Oxide with Doped Metal Oxides (5.3.3)

## 3 Fundamentals

Redox reactions in galvanic cells are spatially separated into reduction and oxidation. Fuel cells are classified as special galvanic cells due to continuous feed of reactants and thus continuous conversion of chemical into electrical energy. Based on this principle, types of fuel cells are differentiated by their operation temperature, the ion conductor, pH value or by the utilized fuel. Some fuel cell types are already commercially available and satisfy different application fields, while other types are in state of research and development.

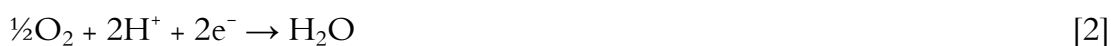
Starting with distinction by pH value, anion exchange membrane fuel cells (AEMFCs) facilitate the use of cheaper non-precious metal catalysts like cobalt or iron owing to their stability in alkaline environment.<sup>[33, 34]</sup> The operating temperature of AEMFCs is usually below 100 °C.<sup>[35, 36]</sup> In the similar temperature range but at lower pH values, low temperature PEMFCs (LT-PEMFCs) consist of a proton exchange membrane and platinum-containing catalysts. They exhibit commercial applications from stationary power generation in CHPs to application in the transport sector for transit buses and passenger cars.<sup>[37, 38]</sup> Further applications are portable power units and backup power systems.<sup>[37]</sup> The high temperature PEMFC uses polybenzimidazol as proton exchange membrane with phosphoric acid as electrolyte and operates at enhanced temperature between 120–180 °C<sup>[39]</sup> being attractive in CHP systems.<sup>[9-11]</sup> These two PEMFC types are highlighted in the following section. At higher operation temperature between 600–1,000 °C molten carbonate (MCFCs) and solid oxide fuel cells (SOFCs) supply the market for stationary application with utilization of natural gas.<sup>[38]</sup> Other fuel cell types operate with e.g. methanol as fuel<sup>[40]</sup> or use microorganisms as part of the electrode to produce energy from organic compounds.<sup>[41]</sup>

## 3.1 PEM Fuel Cells

PEM fuel cells are described towards their assembly and the principle of operation. Section 3.1.1 introduces the membrane electrode assembly with single components and layers by example of high temperature PEM fuel cells and elucidates in detail the catalyst layer. Section 3.1.2 then introduces and compares the HT-PEM with the LT-PEM fuel cell system.

### 3.1.1 Assembly and Operating Principle of PEMFCs

Figure 2 illustrates a schematic PEM fuel cell assembly exemplified by a HT-PEMFC and allows an enlarged view into the catalyst layer. The left side shows the membrane electrode assembly (MEA) consisting of the centered proton conducting membrane and the gas diffusion electrodes (GDE) on both sides of the membrane. The MEA is framed by mostly graphitic bipolar plates with gas in- and outlets. Bipolar plates serve for mass and heat transport as well as electron conduction. Incoming reaction gases are distributed through channels among the MEA. The GDE includes usually the gas diffusion layer (GDL) being in contact with the bipolar plates, the micro porous layer (MPL) and the catalyst layer which is in contact with the membrane. The GDL ensures further distribution of the reactants coming from the bipolar plates by means of woven or randomly pressed carbon fibers, whereas the MPL consists of porous carbon particles for further reactant distribution. Finally, the oxidation of hydrogen in Equation [1] and the reduction of oxygen in Equation [2] occur inside the anodic and the cathodic catalyst layers, respectively.<sup>[40]</sup>



Furthermore, right part of Figure 2 shows a schematic representation of the cathodic catalyst layer on the basis of common platinum on carbon black (Pt/C) from macroscopic to microscopic scale. The catalyst layer has a thickness of around 25  $\mu\text{m}$  and consists of carbon aggregates loaded with Pt nanoparticles. These aggregates result from van der Waals interaction of single spherical carbon black particles with a diameter of about 30 nm. An ionomer surrounds the aggregates to ensure proton transfer inside the catalyst layer. Coming to smaller scales, platinum particles

with a size of around 2 nm are deposited on the support surface. Morphology and particle size of platinum and of the carbon determine the Pt distribution and its electronic structure being significant for catalytic activity and stability.<sup>[42-49]</sup>

Finally, Figure 2 illustrates a triple phase boundary area leading to a catalytic active site and the reduction of oxygen at the PEMFC cathode. The pores enable diffusion of reactants and products, the ionomer provides proton transport and the catalyst particle itself catalyzes the reaction and ensures electron transfer. In the image, the oxygen reduction is separated into single steps and labeled with numbers. First,  $O_2$  diffuses through the gas phase into the porous catalyst layer and further through the ionomer reaching the catalyst.<sup>[50, 51]</sup> Electrons migrate through the carbon aggregates, whereas protons migrate through the membrane and ionomer (1). Second, oxygen adsorbs onto platinum, is dissociated and can migrate on the surface. Charge transfer with molecular recombination results in the formation of water (2). Desorption of the water molecule followed by its diffusion through the pores presents the last step (3).

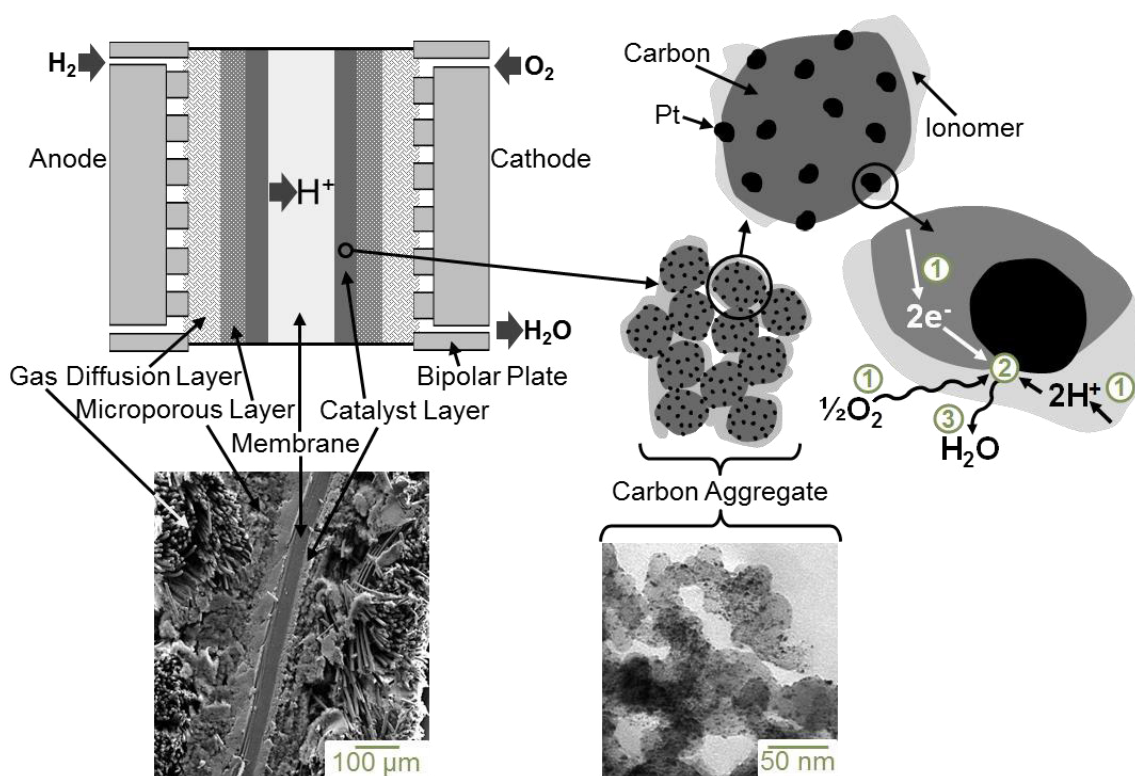


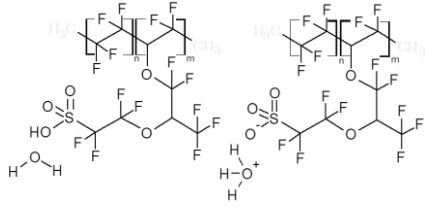
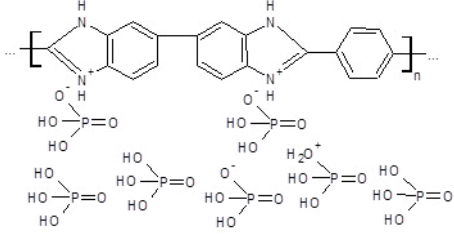
**Figure 2** Schematic depiction of a PEM fuel cell with microscopic image of a membrane electrode assembly (left) and schematic enlarged view into the catalyst layer with microscopic image of Pt on carbon black (right), adapted from<sup>[52]</sup>.

### 3.1.2 High Temperature PEM Fuel Cells

Both PEMFC types are contrasted in Table 1. The deviation of temperature has various consequences for the fuel cell components and management of operation. Basically, the idea of increasing the temperature from around 25–90 °C in LT-PEMFCs to usually 120–180 °C in HT-PEMFCs is the simplification of cell design and operation. In terms of the MEA the biggest difference presents the electrolyte. LT-PEMFCs usually comprise Nafion<sup>®</sup> which is a sulfonic tetrafluoroethylene-based membrane incorporating liquid water as proton conducting medium. At temperatures above 100 °C, Nafion<sup>®</sup> becomes unsuitable due to insufficient stability.<sup>[40]</sup> Therefore, in HT-PEM fuel cells polybenzimidazole (PBI) has been established and guarantees the proton transport with the aid of phosphoric acid. On one side absence of liquid water eliminates a system unit for water management and allows the operation with dry gases, and on the other side the heat rejection is easier at enhanced temperatures. Thereby, HT-PEMFCs enable a more simplified cell design against the background of saving system space and weight.<sup>[10, 11, 53]</sup>

Although both PEMFC types typically use platinum or platinum-alloy catalysts based on carbon black, an increased temperature generally has a positive impact on the reaction kinetics being described in Section 3.2.1 and has the effect of lowered carbon monoxide sorption on the catalyst.<sup>[40]</sup> Regarding simplified operation, greater catalyst tolerances towards fuel impurities like CO cease cost-intensive fuel purification in terms of HT-PEMFC application.<sup>[10, 11, 53]</sup> Despite these advantages, loss of phosphoric acid and catalyst degradation in HT-PEMFCs are frequently reported in literature.<sup>[9, 10, 16]</sup> Stronger carbon corrosion as well as strengthened Pt nanoparticle agglomeration are consequences of catalyst exposure to enhanced temperatures.<sup>[53]</sup>

**Table 1** Comparison of PEMFC types.<sup>[53]</sup>

Aspect	LT-PEMFC	HT-PEMFC
Operation Temperature	25 – 90 °C	120 – 180 °C
Electrolyte	Sulfonic tetrafluoroethylene-based polymer / H <sub>2</sub> O: 	Polybenzimidazole-based polymer / H <sub>3</sub> PO <sub>4</sub> : 
Catalyst	Pt or Pt-alloys on carbon black	Pt or Pt-alloys on carbon black
CO Tolerance	<50 ppm	<30,000 ppm

### 3.2 Pt Catalysts

Catalysis in PEM fuel cells is affected by several steps of diffusion, sorption, dissociative and recombinant processes as already outlined in Figure 2. Pt catalysts are used to increase the kinetics of hydrogen oxidation reaction (HOR) and oxygen reduction reaction (ORR), while the rate of ORR is much slower than the rate of HOR.<sup>[40]</sup> This section begins with the PEMFC thermodynamics and kinetics and further describes the mechanism and requirements of ORR. Degradation of Pt catalysts on common carbon is then focused and against this background alternative support materials for Pt are introduced and discussed.

### 3.2.1 Thermodynamics and Kinetics

In thermodynamic perspective the overall PEMFC reaction is equal to hydrogen combustion with a reaction enthalpy  $\Delta H$  of  $-286 \text{ kJ mol}^{-1}$  and thus equal to the standard enthalpy of  $\text{H}_2\text{O}$ .<sup>[54]</sup> Disregarding the released thermal energy through exothermic reaction, the Gibbs free energy  $\Delta G^\circ$  at standard conditions amounts to  $-237 \text{ kJ mol}^{-1}$ . Dependency of the Gibbs free energy  $\Delta G$  on temperature  $T$  and partial pressures  $p_i$  of educts and products is described by the Nernst Equation [3] including the gas constant  $R$ . Assuming  $\Delta G$  is completely released in form of electrical energy leads to Equation [4] containing the number of transferred electrons  $n$ , the Faraday constant  $F$  and the reversible potential  $E$ . Hence, insertion of the Gibbs free energy under standard conditions  $\Delta G^\circ$  would result into the standard potential  $E^\circ$  of  $1.23 \text{ V}$ .<sup>[54]</sup> The Nernst Equation [5] then describes the dependence of  $E$  on temperature and partial pressures, so that the open circuit voltage (OCV) under real PEMFC conditions is usually lower than  $1.23 \text{ V}$ .

$$\Delta G = \Delta G^\circ - RT \cdot \ln \left( \frac{p_{\text{H}_2} p_{\text{O}_2}^{1/2}}{p_{\text{H}_2\text{O}}} \right) \quad [3]$$

$$\Delta G = -n F E \quad [4]$$

$$E = E^\circ + \frac{RT}{nF} \cdot \ln \left( \frac{p_{\text{H}_2} p_{\text{O}_2}^{1/2}}{p_{\text{H}_2\text{O}}} \right) \quad [5]$$

Further electrochemical processes inside the cell occurring in parallel to HOR and ORR are short circuit currents or the formation of a mixed cathodic potentials resulting from reactions like Pt oxidation above  $0.6 \text{ V}$ <sup>[20]</sup> or oxidation of crossed  $\text{H}_2$  through the membrane<sup>[55, 56]</sup> and can result in lowered OCV. Besides the OCV conditions, polarization of PEM fuel cells leads to further voltage losses outlined in Figure 3. Operation at low current (below  $0.1 \text{ A cm}^{-2}$ ) leads to losses due to HOR and mainly ORR kinetics. On the contrary, the operation at much higher current requires higher amount of reactants at catalytic active sites and can consequently result in mass transport limitation.

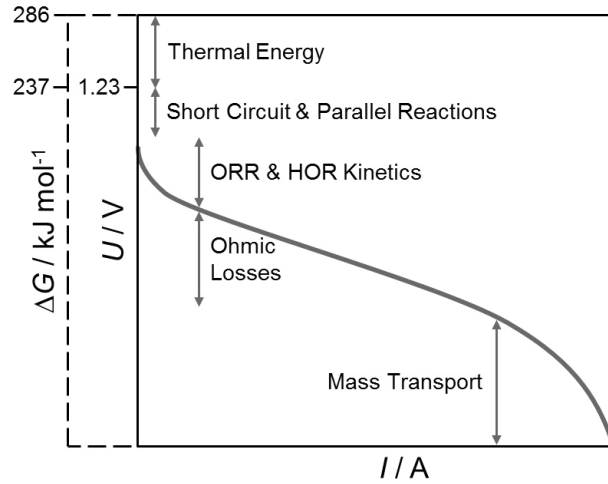


**Figure 3** Schematic PEMFC polarization curve; indication of  $\Delta G$  and subscription of voltage  $U$  losses as a function of the current  $I$ , adapted from<sup>[57]</sup>.

In electrochemical reactions, the current density  $j$  is according to Equation [6] reliant on the transferred charge  $nF$  and the reaction rate  $r$ , meaning the speed of electron consumption or release. Since the reaction at electrodes includes forward and backward reaction,  $r$  consists of the forward and backward rate constants  $k_i$  as well as product and educt concentrations  $c_i$ . The rate constant  $k_i$  in turn is calculated by the Arrhenius Equation [7] and is a function of the standard rate constant  $k_0$ , the activation energy  $E_a$  and  $T$ . This relation demonstrates the possibility of higher reaction rates through decreasing  $E_a$  or increasing the temperature for instance by use of HT-PEMFCs. If the activation energy is adapted to electrochemical reactions,  $E_a$  becomes a function of the transfer coefficient  $\alpha$ , the number of transferred electrons  $n$  during the determining step and overpotential  $\eta$ , according to Equation [7].

$$j = n F r = n F (k_f c_p - k_b c_e) \quad [6]$$

$$k_i = k_0 e^{-\frac{E_a}{RT}} = k_0 e^{-\frac{\alpha n F \eta}{RT}} \quad [7]$$

For the evaluation of kinetics, the Butler-Volmer Equation [8] is used. The exchange current density  $j_0$  describes the equilibrium of forward and backward reaction with a current density  $j$  of zero. The first exponential term is attributed to the forward and the second term to the backward reaction. ORR in PEMFCs with neglecting the backward reaction leads to the Tafel Equation [9], which presents the linear relation between overpotential  $\eta$  and  $\ln(j)$ .

$$j = j_0 \left( e^{\frac{-\alpha n F \eta}{RT}} - e^{\frac{(1-\alpha) n F \eta}{RT}} \right) \quad [8]$$

$$\eta = \frac{RT}{\alpha n F} \ln(j_0) - \frac{RT}{\alpha n F} \ln(j) \quad [9]$$

### 3.2.2 Oxygen Reduction Reaction

In the following, the mechanism of Pt catalyzed electrochemical oxygen reduction is deliberated. Basically, catalysts lower the activation energy through adsorption of reactants and thereby enable energetically favorable transition states during reaction. Adsorbed intermediates in the form of  $O_2$ ,  $O$ ,  $OH$ ,  $O_2H$  and  $H_2O_2$  are discussed to appear during ORR.<sup>[58]</sup> The mechanism of oxygen reduction strongly depends on the degree of catalyst interaction with oxygen, which in turn depends on catalyst's nature and further external influences as discussed below. Critical steps during ORR are diffusion, adsorption and dissociation of  $O_2$ , proton and electron transfers and binding of intermediates, whereas each step of catalysis exhibits varying energy states. Currently, Pt is the most active metal for ORR as expressed by the Volcano plot in Figure 4, considering the ORR activity of metals as function of the oxygen binding energy. If oxygen binding is too weak, no catalysis or catalysis of only two-electron-reduction forming  $H_2O_2$  instead of  $H_2O$  occurs. If oxygen binding is too strong the catalyst surface is blocked with oxygen resulting in suppression of the reaction.<sup>[58]</sup> Studies on Pt alloys like  $Pt_3Ni$  nanoparticles showed a further positive impact on ORR activity through affecting the binding of oxygen intermediates.<sup>[59]</sup>

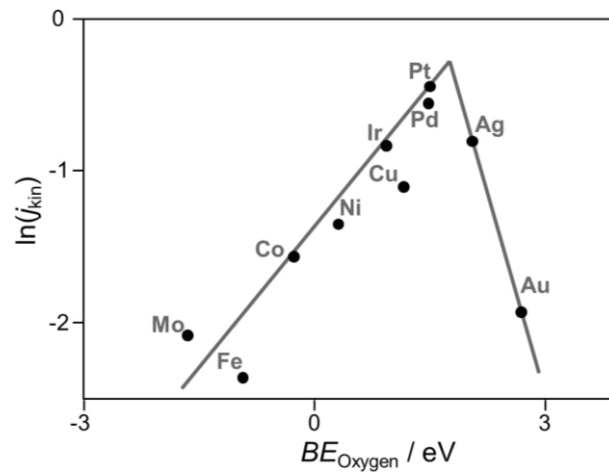
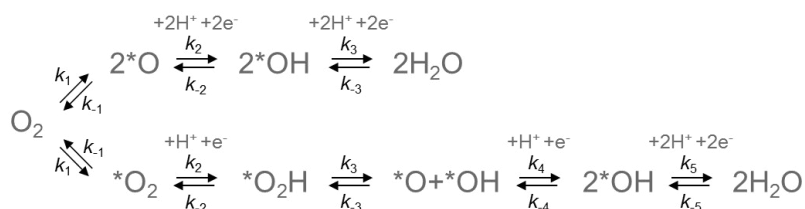


**Figure 4** Volcano plot showing ORR activity in the form of kinetic current density  $j_{kin}$  plotted against oxygen binding energy  $BE_{Oxygen}$ , adapted from<sup>[58]</sup>.

Concentrating on catalysis through platinum, two simplified mechanisms are proposed in literature, the dissociative and the associative mechanism in Scheme 1. The difference between both mechanisms arises from the way of  $O_2$  adsorption and therefore the probability of immediate  $O_2$  dissociation. The dissociative path starts with strong platinum–oxygen–interaction in terms of bridge bonding on two Pt atoms. The O–O bond is stretched and weakened so that  $O_2$  dissociates in energetically preferred atomic oxygen. Then, further reaction of O and OH intermediates via proton and electron transfers to final  $H_2O$  takes place. The bottom path in Scheme 1 illustrates the associative mechanism. Due to lower Pt– $O_2$ –interaction end-on adsorption and formation of the hydrogenperoxo intermediate occurs. In presence of platinum, OOH and  $H_2O_2$  species are unstable. Therefore, the following steps are OOH dissociation and charge transfers leading to  $H_2O$ .<sup>[40, 58, 60]</sup>



**Scheme 1** Dissociative (upper path) and associative (bottom path) ORR mechanism, adapted from<sup>[58]</sup>. The symbol \* stands for an active surface site of platinum.

The mechanism of Pt catalyzed ORR depends on the electrode potential evidenced in theoretical and experimental studies, which is obviously caused by Pt surface oxidation above 0.6 V.<sup>[20]</sup> Considering the Tafel relation in Equation [9], experimental studies reported a slope of  $60 \text{ mV dec}^{-1}$  above around  $0.8 V_{SHE}$  and  $120 \text{ mV dec}^{-1}$  below around  $0.8 V_{SHE}$ .<sup>[61, 62]</sup> Furthermore, intermediate stabilities in dependence on the electrode potential using density functional theory (DFT) were calculated and resulted in dissociative mechanism occurring at high electrode potentials and associative mechanism occurring at lower electrode potentials.<sup>[58]</sup>

Although the mechanism of oxygen reduction in real FC environment is still not completely decoded,<sup>[60]</sup> several impact factors on platinum's activity for ORR have frequently been reported. Next to conditions of cell operation like electrode potential and temperature, the electrolyte can influence the catalytic activity of Pt. On one hand, the electrolyte must provide the proton transfer during ORR. However on the other hand, competing adsorbates originating from the electrolyte can reduce the ORR activity.<sup>[63]</sup> In HT-PEM fuel cells, phosphate anions are known to adsorb on Pt.<sup>[64]</sup> Furthermore, the possible presence of contaminants also leads to blocked Pt sites and a reduced activity.<sup>[65]</sup>

Beside external impacts, the ORR activity strongly depends on the nature of platinum. Hammer and Nørskov<sup>[66]</sup> introduced the  $d$ -band model to describe the relation between the electronic band structure of Pt and its catalytic activity. Figure 5 illustrates electronic structures during the chemisorption of oxygen onto platinum. After interaction of oxygen with platinum  $sp$  states, covalent bonding and antibonding are formed due to interaction with the  $d$ -band of platinum. Thus, affecting the electronic band structure of platinum can downshift the  $d$ -band state, which enhances the antibonding state. Thereby the binding strength of oxygen is lowered and in consequence the activity for ORR is enhanced.<sup>[67-69]</sup>

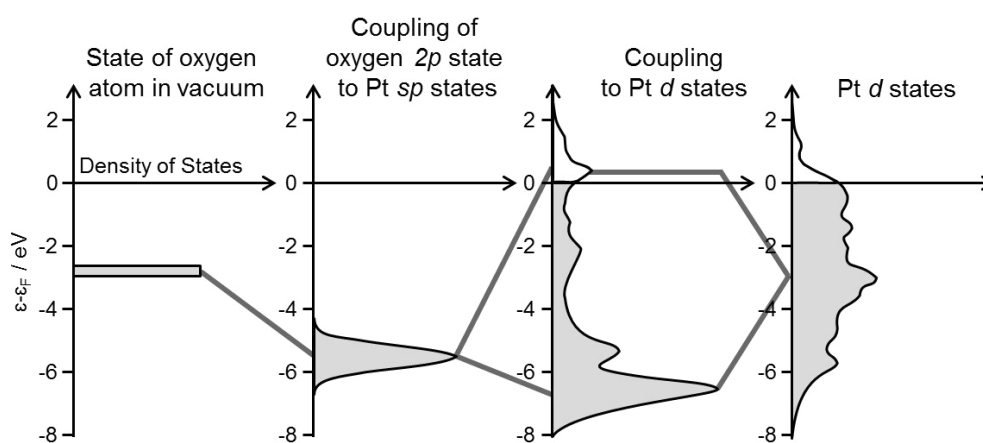


**Figure 5** Change in electronic structure by O atom adsorption on Pt (111) surface with energy states  $\epsilon$  and the Fermi energy  $\epsilon_F$  and the formation of covalent bonding and antibonding states, adapted from<sup>[66]</sup>.

The electronic structure of Pt is dictated by several impact factors. First, the electronic structure depends on the morphology of Pt providing different surface facets for oxygen reduction. For example, Pt (111) surface was shown to be more active than (100) surface in the presence of HClO<sub>4</sub> electrolyte.<sup>[70]</sup> Second, the size of platinum particles can influence the atomic lattice through geometric effects.<sup>[43]</sup> Third, interaction of platinum and support particles can additionally impact the electronic structure of Pt.<sup>[47, 49]</sup> Electrical contact between platinum and support particles with electrical conductance is furthermore necessary for ORR steps including transfer of electrons. Strongly anchored and distributed Pt particles onto a support surface enable a high ECSA being important to achieve a high ORR activity. Therefore, the support requires a high surface area with defect sites explained in Section 3.2.4 in more detail.

### 3.2.3 Catalyst Degradation

After discussing the catalyst activity for ORR, here stability issues are focused. In PEM fuel cell cathodes, Pt/C catalysts are exposed to a corrosive environment due to high and changing potentials depending on cell operation, low pH values, presence of water and O<sub>2</sub> and enhanced temperatures in view of HT-PEMFCs. The ECSA loss of catalysts decreases fuel cell performances and makes the degradation of Pt/C a great challenge in research. Here, the degradation mechanisms of Pt nanoparticles are introduced first, followed by the view on carbon corrosion.

#### 3.2.3.1 Pt Degradation

Figure 6 schematically presents paths of Pt aging occurring in a PEM fuel cell. Each picture includes the carbon support (grey), parts of ionomer (light grey) and the Pt particles (black), which underlie different changes. Firstly, dissolution due to Pt oxidation is depicted (1) with three possibilities of further degradation inside the PEMFC. Dissolved Pt ions can diffuse into the ionomer and membrane with reprecipitation due to chemical reduction by H<sub>2</sub> (1a). Furthermore, Pt ions can be discharged through the product water (1b) or Ostwald-Ripening leads to Pt agglomeration (1c). Secondly, detachment of Pt particles is shown (2) Thirdly, Pt migration on the support surface is illustrated (3), which can lead to particle coalescence (3a). These degradation processes shown in Figure 6 can occur in parallel and

are influenced by effects of operation conditions, by particle size and morphology of platinum.<sup>[15]</sup> Furthermore, especially the detachment of Pt particles is induced by support corrosion. But dissolution and migration can also be strengthened due to insufficient anchoring and hence insufficient stabilization of platinum through the substrate. Support instabilities are concretized in Section 3.2.3.2.

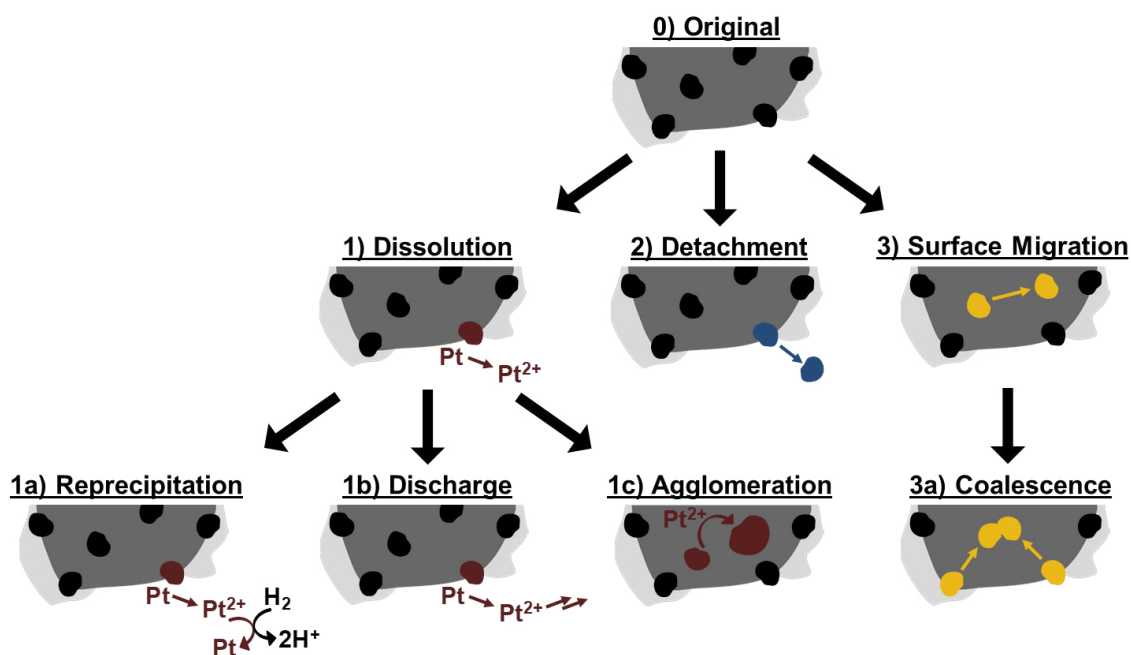


**Figure 6** Schematically presented paths of Pt degradation occurring in a PEM fuel cell, adapted from<sup>[15, 17, 71]</sup>.

The Pt dissolution is depicted in Equation [10] and thermodynamically reliant on the electrode potential and temperature following the Nernst principle [5]. Exposing platinum to high potential and enhanced temperature exponentially enforces the dissolution, which is evidenced by several experimental studies and shown in Figure 7.<sup>[72-75]</sup>

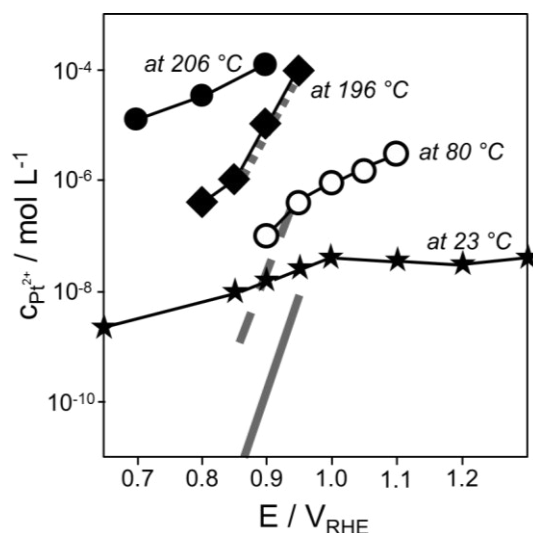


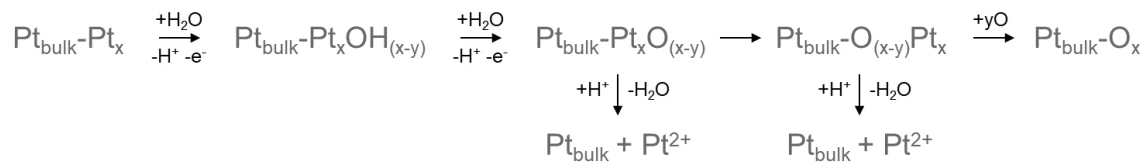
**Figure 7**  $\text{Pt}^{2+}$  concentration in dependence of electrode potential and temperature. Theoretical data from Pourbaix<sup>[76]</sup> in grey lines (solid 25 °C, dashed 80 °C and dotted 196 °C) and experimental data in black lines (filled dots Honji<sup>[77]</sup>, squares Bindra<sup>[78]</sup>, unfilled dots Ferreira<sup>[79]</sup> and stars Wang<sup>[74]</sup>), adapted from<sup>[15]</sup>.

Pourbaix further specified the thermodynamic behavior of Pt dissolution and calculated the solubility of Pt in water under consideration of pH. Equation [11] presents the electrooxidation to PtO, which can chemically dissolve through reaction with protons as depicted in Equation [12]. At increased potential PtO is oxidized to PtO<sub>2</sub> as shown in Equation [13]. Overall, Pourbaix suggested that platinum exposed to an environment with pH 0 starts to dissolve around a potential of 0.85 V<sub>RHE</sub>.<sup>[76, 80]</sup>



The principle of Pt surface oxidation presents the key to understanding the Pt dissolution mechanism. Angerstein-Kozłowska et al.<sup>[81]</sup> performed cyclic voltammetry (CV) on bulk Pt in 0.5 mol L<sup>-1</sup> H<sub>2</sub>SO<sub>4</sub> at 25 °C and proposed the basics of the mechanism in Scheme 2 for the first time. This Pt dissolution mechanism has been refined over time by several studies. The formation of hydroxy species starts at around 0.6 V due to water adsorption and is followed by oxide formation.<sup>[20]</sup> Meanwhile, platinum is chemically dissolved with enforced solubility at lower pH as experimentally shown.<sup>[82]</sup> At further increased potentials a place exchange of Pt

surface atoms and oxygen occurs. Finally, the surface passivation via formation of a complete oxide layer takes place. Wang et al.<sup>[74]</sup> reported an increase in Pt solubility between 0.85 and 1.00  $V_{\text{RHE}}$  and the achievement of a plateau above 1.00  $V_{\text{RHE}}$ , which goes well with numerical modelling of Darling and Meyers.<sup>[20]</sup> Their kinetic model showed Pt solubility in similar potential range and reaching of a plateau at 1.10  $V_{\text{SHE}}$ . Furthermore, the place exchange of Pt atoms with O atoms in atomic lattice was evidenced to occur at around 1.2  $V_{\text{RHE}}$ , when the platinum surface is partially passivated through an oxide layer.<sup>[83, 84]</sup> The passivating oxide layer is expected to be completed at around 1.8  $V_{\text{RHE}}$ .<sup>[73]</sup> A recent study of Lopes et al.<sup>[85]</sup> confirmed this dissolution route via Pt oxide using a combination of electrochemical experiments and mass spectrometry with inductive coupled plasma (ICP-MS).



**Scheme 2** Mechanism of Pt dissolution at PEMFC cathodes. Increasing electrode potential from left to right.<sup>[81]</sup>

Exceeding the dependency of Pt dissolution on the electrode potential, dynamic load profiles with respective voltage changes during PEMFC operation present special circumstances for platinum degradation. For the first time studied by Kinoshita et al.,<sup>[86]</sup> strong dissolution and particle growth of platinum in an electrochemical cell was observed during potential cycling between 0.05 and 1.25  $V_{\text{RHE}}$ . This is according to enforced Pt dissolution and theoretically explained by repeating Pt oxidation and reduction events during potential cycling.<sup>[20, 87]</sup> Enhanced cycle frequency<sup>[73]</sup> as well as an increased upper potential limit<sup>[88]</sup> further intensify the solubility of Pt. Recently, Søndergaard et al.<sup>[89]</sup> applied square-wave cycled potentials between 0.6 and 1.0  $V_{\text{RHE}}$  to HT-PEMFC cathodes — on one hand with dry and on the other hand with humidified nitrogen flow. Pt degradation was strongly enforced in case of humidification. The authors concluded that dynamic potentials lead to strong Pt dissolution and re-precipitation events only in presence of water.

Moreover, Pt dissolution is impacted by the surface structure and surface energy of the particles, because this degradation path of dissolution arises from oxidizing and dissolving of surface atoms. First, morphology effects describe instable surface sites like step edges or grain boundaries which dissolve with higher probability than more stable facets.<sup>[15]</sup> Komanicky et al.<sup>[90]</sup> reported the stability of Pt surface facets at 0.95 V<sub>RHE</sub> in the decreasing order of (111), (100) and (110). To emphasize again, potential cycling is critical for Pt's stability caused by generating new and high energy Pt surface sites.<sup>[15]</sup> Second, particle size effects are theoretically described by the Gibbs-Thomson principle. The chemical energy state of particles depends on the ratio of surface and volume so that in consequence Pt nanoparticles e.g. exhibit higher instability than bulk Pt.

As depicted in Figure 6, three degradation paths are possible after platinum dissolution (1). The first path shows the discharge from the cell verified by detection of Pt ions inside the product water (1b).<sup>[91, 92]</sup> The second path illustrates diffusion of dissolved Pt<sup>2+</sup> into the ionomer of the catalyst layer and further into the membrane and the reaction with H<sub>2</sub> (1a). By use of scanning electron microscopy a metallic Pt band inside the membrane was observed in LT-<sup>[88, 93, 94]</sup> and HT-PEM fuel cells<sup>[89, 95, 96]</sup>. The third path includes ion diffusion and electron transfer followed by deposition on another platinum particle leading to Pt agglomeration (1c). The driving force is Ostwald-Ripening, which tends to lower the surface energy.<sup>[77, 97, 98]</sup> Smaller particles with higher surface energy and thus higher instability shrink and finally disappear, whereas larger particles grow due to precipitation of Pt<sup>2+</sup>.<sup>[99]</sup> Basically, Pt agglomeration depends on similar factors like the Pt dissolution because it presents the prerequisite. During constant FC operation, agglomeration was shown to be strong within the first hours and strives to a more stabilized system with less agglomeration during further operating hours.<sup>[100]</sup> High and cyclic FC voltages would dramatize the Pt agglomeration as discussed before.

Figure 6 further images Pt detachment (2) due to support corrosion. Pt particles exhibiting complete electronically isolation take no catalytic active part in ORR anymore. In previous steps before the final detachment, a destabilization of platinum anchoring can intensify dissolution and the further downstream degradation paths. Moreover, surface migration of incompletely anchored Pt particles (3) can be strengthened resulting in the coalescence of particles.<sup>[15]</sup> The last Pt aging possibility is the surface migration of particles already mentioned as possible subsequent

degradation of support corrosion. The principle of two-dimensional Pt particle motion on the support surface was firstly suggested by Bett et al.<sup>[101]</sup>. The evidence of moved and coalesced Pt particles on carbon was then provided using transmission electron microscopy.<sup>[102-104]</sup>

In sum, platinum degradation becomes problematic at enhanced temperature like in HT-PEM fuel cells and at enhanced electrode potentials occurring at the cathode and under special operation conditions like cycled current requests,<sup>[105, 106]</sup> OCV,<sup>[107]</sup> start-stop operation and fuel starvation<sup>[108-111]</sup>. Although Pt alloys may exhibit improved catalytic activity towards ORR, they suffer from further strengthened instability due to thermodynamic leaching in acidic environments.<sup>[112, 113]</sup>

### 3.2.3.2 Carbon Corrosion

The previous section discussed Pt degradation and indicated consequences of support instability for the Pt nanoparticles. This section discusses support degradation concerning the corrosion of graphitic carbon, since carbon blacks are the frequently used support candidates in fuel cells. Carbon corrosion can lead to the loss of platinum ECSA caused by enforced Pt degradation as described in Section 3.2.3.1. Beyond affecting platinum, corroded carbon can show an increased porosity first<sup>[79]</sup> and then lead to a collapse of the catalyst layer<sup>[114, 115]</sup> with the consequence of inhibited mass transport.<sup>[114, 116]</sup> Electrical resistance as well as hydrophilicity of the catalyst layer increase after carbon corrosion, which can further negatively impact the FC performance.<sup>[40, 116, 117]</sup>

The electrooxidation mechanism of graphitic carbon is elucidated in Scheme 3 and starts with partial oxidation of carbon surface atoms. Intermediates in the form of carbonyl, carboxyl or hydroxyl types and moreover hydroquinone and quinone (HQ/Q) similar species showing redox activity at around 0.6 V<sub>SHE</sub> are generated.<sup>[118-121]</sup> These carbon sites are further oxidized to finally form carbon dioxide.



**Scheme 3** Electrooxidation mechanism of carbon.<sup>[19, 122, 123]</sup>

Carbon corrosion is thermodynamically possible at a potential of 0.207 V<sub>SHE</sub> but exhibits slow kinetics.<sup>[17]</sup> However, the oxidation of carbon is present at PEMFC cathodes, especially during critical operation conditions in terms of start-stop dynamics and occurrence of fuel starvation. Such conditions with cell voltages of around 1.4 V<sup>[108, 124]</sup> cause significant carbon corrosion and catalyst layer damaging, which was highlighted in several theoretical and experimental works.<sup>[108, 110, 111, 124-126]</sup> Next to electrode potential, further operation conditions affecting the carbon stability are cell temperature and cell humidity. Stevens et al.<sup>[127]</sup> demonstrated strengthened carbon corrosion through increased cell humidification, while Scheme 3 already emphasizes the necessary role of water during the progress of carbon oxidation. Oh et al.<sup>[128]</sup> compared a typical LT-PEMFC operation under humidified conditions to a HT-PEMFC operation without humidification. CO<sub>2</sub> generation was lower in case of LT-PEMFC operation so that the authors concluded more critical carbon degradation in HT-PEMFCs.

Besides the impact of operation conditions, the catalytic effect of attached Pt on the carbon surface was proven in diverse studies.<sup>[18, 19, 127, 129]</sup> The presence of platinum can enhance the reaction kinetics and thus deteriorate carbon corrosion starting at around 0.6 V<sub>RHE</sub>.<sup>[20]</sup> In addition, the degree of carbon corrosion seems to be related to the Pt loading.<sup>[19, 127]</sup> However, Ball et al.<sup>[122]</sup> suggested that the type of carbon is more crucial rather than the presence of platinum. Different stabilities of different carbon types have frequently been reported identifying two main reasons for carbon instability, a high specific surface area<sup>[127]</sup> and a low degree of graphitization<sup>[22, 130, 131]</sup>. Types of carbon supports are introduced in Section 3.2.4.1.

### 3.2.4 Support Materials

Table 2 lists the criteria for Pt support materials in PEM fuel cells and the challenge of corrosion. This section reviews on the one hand frequently used substrates in form of graphitic carbons and metal oxide particles and on the other hand nano-composites of carbon and metal oxides against the background of durability.

**Table 2** Requirements on Pt supports in PEMFCs. [24, 46, 132, 133]

Properties	Task in PEMFC
1) Surface area	Providing pores for reactant mass transport and area for Pt distribution
2) Electrical conductivity	Electron transfer inside catalyst layer to active Pt sites
3) Defect sites	Pt anchoring for distribution, stabilization and electrical contact
Corrosion resistance	Assurance of stable FC performance through stable properties 1–3

#### 3.2.4.1 Carbons

Figure 8 summarizes the consequences of carbon properties for durability and activity regarding ORR. Pt particles can catalyze and hence exacerbate the carbon corrosion, whereas the extent of corrosion has been suggested to stronger depend on the type of carbon.<sup>[122]</sup> In turn carbon corrosion consequences platinum detachment and aging. To leave this degradation circle, efforts to modify carbon towards stability during PEMFC application were taken in the past years.<sup>[22, 134-136]</sup> Balancing between improvement of ORR activity through high surface area carbon containing many defect sites on one hand (i) and the assurance of carbon stability through a low surface area and less defect sites on the other hand is mandatory (ii). But in contradiction, a maximized surface area with many defect sites of carbon promotes the interaction with Pt and thus anchors and stabilizes the platinum nanoparticles (iii).<sup>[48, 49]</sup>

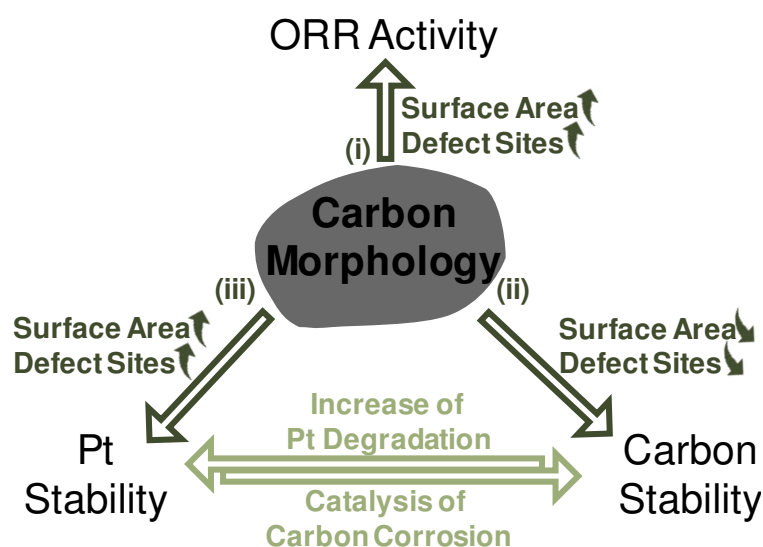


**Figure 8** Illustration of the carbon impact on stability and activity for ORR, summarized from Sections 3.2.2 and 3.2.3. Arrows up means higher and arrows down means lower number of appropriate carbon property required.<sup>[137]</sup>

Elemental carbon exists in various modifications, whereas two base allotropes are differentiated. Diamond consists of  $sp^3$ -hybridized atoms coordinated to electrical insulating cubic crystals, whereas graphite consists of  $sp^2$ -hybridized atoms leading to a two-dimensional hexagonal atomic lattice via strong  $\sigma$ -bonds. These layers contain delocalized electrons originated from  $\pi$ -binding, which cause electrical conductivity and a three-dimensional stacking of layers due to van der Waals force. Based on this graphite allotrope, different modifications arise from layer coordination. Hexagonal or rhombohedral interlayer coordination, schematically depicted in Figure 9a, means an enhanced density and electrical conductivity, whereas rotationally faulted layers show enhanced porosity along with electronic decoupling.<sup>[138]</sup> According to the requirements on catalyst supports described in Table 2, hexagonal or rhombohedral coordinated graphite is electrically conductive but has a lack of surface area and defect sites. Natural graphite for instance has a specific surface area of around  $9 \text{ m}^2 \text{ g}^{-1}$ .<sup>[139]</sup> This causes insufficient electrode porosity and Pt particle distribution and in consequence a hindered transport of reactants and a reduced number of active centers inside the catalyst layer.<sup>[133, 137]</sup>

Rotationally faulted modifications are much more suitable for fuel cell application and are distinguished by the 2D layer width, extent of defects in form of edges, vacancies and functional groups, the 3D layer arrangement and the degree of graphitization.<sup>[138]</sup> Some of the rotationally faulted modifications became relevant as Pt supports for FCs in recent years.<sup>[24, 46, 132, 133]</sup> The most commonly used catalyst support in fuel cells is carbon black like Vulcan<sup>®</sup>, which is schematically drawn in Figure 9d. The layers are rotationally faulted to form spherical particles with less graphitization and more defect sites compared to hexagonal or rhombohedral coordinated graphite.<sup>[140]</sup> Vulcan<sup>®</sup> particles have diameters of around 30 nm and are arranged to aggregates with sizes in  $\mu\text{m}$ -range due to van der Waals interaction. Pores from particle interspaces and inside the particle itself result into specific surface areas around  $240 \text{ m}^2 \text{ g}^{-1}$ .<sup>[22, 141]</sup> Other carbon blacks can have larger particles with less aggregation, so that their contact surface for electron transport decreases and the size of pores increases. In the large-scale production, natural gas is combusted first to generate the required atmosphere and temperature within the furnace. Then, liquid hydrocarbons from fossil sources are injected, partially combusted and pyrolyzed at temperatures of 1,400–1,700 °C to form carbon black. Further reaction of carbon black is stopped through water injection.<sup>[142]</sup>

#### 3.2.4.1.1 Carbons from HTC of Biomass

Next to fossil resources, graphitic carbon can further be obtained from renewable resources via two processes. The first process describes the carbonization of dry biomasses via pyrolysis at temperatures above 300 °C.<sup>[143, 144]</sup> The second process of hydrothermal carbonization allows the usage of lower temperatures of 180–260 °C and wet biomasses.<sup>[144–146]</sup> Both processes lead to the carbonization of biomass, whereas the pyrolysis produces a black coal with higher coalification and HTC produces a black–brownish coal with lower coalification. Reaction temperature and time, type of biomass and presence of salts during HTC impact the final coal.<sup>[147]</sup> Aim is to maximize the degree of aromatic structures with simultaneous increase of the surface area making the material suitable for instance as adsorption agent<sup>[147]</sup> or supercapacitors<sup>[148]</sup>. Conversion of lignin and cellulose are known to be catalyzed especially by zinc chloride.<sup>[147, 149, 150]</sup>

For the application in catalysis like as catalyst support in fuel cells, a subsequent activation of coal further enhances its surface area and enforces the graphitization. Such activation can physically be achieved by water steam treatment at around 500 °C or chemically achieved by similar treatment with additional use of acids or bases like potassium hydroxide.<sup>[151, 152]</sup> Moreover, thermal annealing at 800 °C or higher is known for graphitization.<sup>[137, 144, 146]</sup>

To date, only few studies apply graphitic carbon obtained from HTC with the aim of oxygen reduction reaction.<sup>[146, 153]</sup> Taleb et al.<sup>[146]</sup> used D-glucose for hydrothermal carbonization instead of biomass, which has a more complex chemical composition. D-glucose was hydrothermally carbonized at 260 °C for 24 h and further thermal treated between 800–900 °C in different atmospheres. They finally obtained an activated carbon in the form of spherical particles with diameters of about 1.1 μm and a specific surface area of 1,190 m<sup>2</sup> g<sup>-1</sup>. This carbon was used as support for Pt nanoparticles in acidic environment. An electrochemical surface area of 23 m<sup>2</sup> g<sub>Pt</sub><sup>-1</sup> and an ORR current density of 0.2 mA cm<sup>-2</sup> at 0.9 V<sub>SHE</sub> were achieved, which are in order of common fuel cell catalysts.<sup>[62, 136]</sup>

#### 3.2.4.1.2 Graphene-based Carbons

Another large part of FC catalyst supports comes from graphene-based carbons. Basically, graphene is defined as single layer of hexagonally arranged sp<sup>2</sup>-hybridized carbon atoms and, with respect to FC application, the graphene layer is defined as structural unit of 3D porous materials.<sup>[138]</sup> The morphology of graphene-based carbons strongly depends on the synthesis. Geim and Novoselov et al.<sup>[154]</sup> experimentally discovered graphene in 2004 and mechanically exfoliated graphene from graphite through adhesive tape. Since then, bottom-up and top-down methods are entrenched to synthesize graphene. During chemical vapor deposition (CVD), hydrocarbons like methane are pyrolyzed at around 900 °C followed by deposition of graphene on Cu or Ni foil.<sup>[155]</sup> The achieved graphene can have a width of several cm without significant defects.<sup>[156]</sup> During exfoliation of graphite, organic molecules like *N*-methyl-pyrrolidone intercalate between graphene layers and weaken their interaction. By use of sonication single graphene sheets are obtained.<sup>[155, 157, 158]</sup> These fabrication methods generate graphene with negligible defects, so that high electron mobility for electronic applications regarding sensors or transistors is ensured.<sup>[155]</sup>

With the aim of FC application, chemical oxidation of graphite followed by simultaneous reduction and layer exfoliation is established.<sup>[135, 136, 159, 160]</sup> First, graphite reacts in an oxidative aqueous solution — containing  $\text{H}_2\text{SO}_4$ ,  $\text{NaNO}_3$  and  $\text{KMnO}_4$  — to graphene oxide, which has several different oxygen groups and thus exhibits layer exfoliation via interaction with water.<sup>[160-162]</sup> This synthesis is widely-known as Hummers method<sup>[163]</sup> and allows large-scale production.<sup>[164, 165]</sup> If graphene oxide suspended in water is dried, layers are arranged to graphite oxide, which has widened layer distances due to the functional groups and is drawn in Figure 9b.<sup>[166, 167]</sup> Next to solvothermal<sup>[168, 169]</sup> and wet-chemical reduction using e.g. hydrazine<sup>[170]</sup>, the thermal reduction to reduced graphene oxide stands for a simple and fast synthesis.<sup>[161, 162]</sup> Sudden exposure to temperatures of around 1,000 °C in inert atmosphere enables sudden  $\text{CO}_2$  release and simultaneous layer exfoliation.<sup>[161, 166, 171]</sup> Obtained rGO is shown in Figure 9c and has a shrunken layer width of around 500 nm,<sup>[166]</sup> residual oxygen groups<sup>[162]</sup> and a partially destroyed aromatic structure<sup>[161]</sup>. Regarding FC application, the wrinkled and rotationally faulted rGO layers with dangling defect sites for Pt anchoring and distribution account for a randomly arranged porous structure.<sup>[24, 159, 170]</sup> Specific surface areas are in range of common Vulcan<sup>®</sup> or higher and vary from around 207  $\text{m}^2 \text{g}^{-1}$  to 456  $\text{m}^2 \text{g}^{-1}$ .<sup>[159, 172]</sup> The synthesis details will be experimentally described in Section 4.1.

Another graphene-based carbon comprises rolled-up graphene in form of a closed cylinder called carbon nanotube and is depicted in Figure 9e. These tubes differ in diameter (10–50 nm) and length (10–50  $\mu\text{m}$ ) and in number of graphene layers.<sup>[133]</sup> Single-walled carbon nanotubes (SWCNTs) consist of a single graphene layer and have a higher specific surface area and less defect sites<sup>[170]</sup> compared to multi-walled carbon nanotubes consisting of several concentric graphene layers as cylinder. MWCNTs can have edge-plane defect sites to anchor Pt nanoparticles<sup>[133]</sup> and show specific surface areas of 192–510  $\text{m}^2 \text{g}^{-1}$ .<sup>[22, 104, 173]</sup> During CVD as established but cost-intensive synthesis,<sup>[24]</sup> hydrocarbons like methane or ethylene are pyrolyzed at 500–1,200 °C in inert atmosphere.<sup>[174, 175]</sup> Gaseous carbon is then passed over metal clusters (e.g. Ni or Co) and catalyzed to form cylindrical aromatic structures growing to tubes.<sup>[133]</sup>

## 3.2.4.1.3 Carbon Supports in PEMFCs

Figure 9 summarizes the carbon materials discussed above. Each presented carbon material can be tuned towards the requirements for PEM fuel cell application listed in Table 2 and illustrated in Figure 8. Thermal treatment under inert gas can remove functional groups, amorphous carbon and impurities, which reduce defects and surface area and enforces graphitization.<sup>[133, 137]</sup> On the contrary, oxidative treatment through e.g. boiling in HNO<sub>3</sub> attacks the carbon surface and forms oxygen groups, which can create defects and an enhanced surface area and leads to a lower degree of graphitization.<sup>[133]</sup> An increase of defects and surface area can further be achieved, if heteroatoms like nitrogen are already incorporated into the graphitic network during synthesis.<sup>[136, 159]</sup> Pt anchoring to heteroatom-containing sites was shown to enhance the ORR activity because of greater electron density.<sup>[176, 177]</sup>

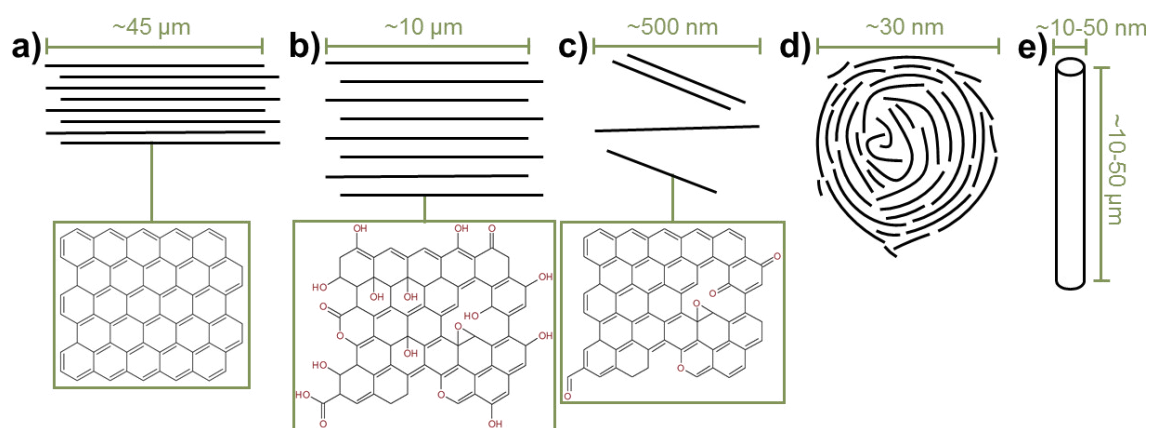


Figure 9 Scheme of layer arrangement in graphitic carbons with exemplary part of the chemical structure: Hexagonal coordinated graphite (a), graphite oxide (b), reduced graphene oxide (c), carbon black particle (d) and single-walled carbon nanotube (e).<sup>[133, 162, 166]</sup>

Speder et al.<sup>[119]</sup> compared the durability of Pt on two common carbon blacks, Vulcan<sup>®</sup> XC72R with 235 m<sup>2</sup> g<sup>-1</sup> and Ketjenblack<sup>®</sup> EC-300 with 795 m<sup>2</sup> g<sup>-1</sup>, by use of potential cycling (1.0–1.5 V<sub>RHE</sub>, 500 mV s<sup>-1</sup>, 27,000 cycles). Double layer capacitance and HQ/Q redox activities significantly increased in the same extent, so that oxidation of both carbons seemed comparable. However, Pt particles were more instable on Vulcan than on Ketjenblack. Difference in Pt stabilization might be caused by the difference in carbon surface areas according to Figure 8. A larger carbon black surface implies the higher number of defect sites and higher energetic

surface states, so that in consequence stronger van der Waals interaction with Pt nanoparticles occur. Other studies demonstrated the influence of graphitization on Pt/C catalyst stability.<sup>[178]</sup> Ye et al.<sup>[131]</sup> showed during potential holding (1.25 V followed by 1.40 V) in LT-PEMFCs lower carbon as well as lower Pt degradation in case of graphitized carbon. Cleemann et al.<sup>[22]</sup> observed similar trends in case of HT-PEMFCs using potential steps (0.9 and 1.2 V for 500 h). Thermal treatment of Vulcan<sup>®</sup> XC72R at 2,800 °C decreased the specific surface area from 208 to 66 m<sup>2</sup> g<sup>-1</sup> but resulted in a more stable FC performance and Pt particle size. A reason for enhanced stability might be the reduced carbon instability and subsequently less Pt degradation.

With respect to Pt/CNT catalysts, Asgari et al.<sup>[179]</sup> compared SWCNTs against MWCNTs with regard to durability under cycled potentials (0.0–1.0 V<sub>RHE</sub>, 600 cycles). SWCNTs showed a higher corrosion resistance. The ECSA of platinum supported on SWCNTs was significantly lower than on MWCNTs already at the beginning followed by a stronger loss after potential cycling. Additionally, the amount of dissolved Pt was higher, so that platinum is obviously less anchored and stabilized on SWCNTs. Other studies compared Pt/MWCNTs with common Pt/C and found higher stability of MWCNTs in combination with more stable Pt particles caused by the departing modification from carbon black.<sup>[104, 173, 180–182]</sup> Various other graphene-based carbons were tested towards cathodic PEMFC application. Partially exfoliated graphite with higher graphitic degree than carbon black and MWCNTs resulted in stabilized Pt.<sup>[134, 183]</sup> Kou et al.<sup>[135]</sup> compared Pt/rGO with common Pt/C after aging through cycled potentials (0.6–1.1 V<sub>RHE</sub>, 50 mV s<sup>-1</sup>, 5,000 cycles) and showed more durable ECSA and ORR in case of Pt/rGO. Further studies reported at least equal performance of Pt/rGO compared to Pt/C during other stress tests or LT-PEMFC operation.<sup>[184, 185]</sup>

In conclusion, high efforts in FC research have been made for obtaining stable carbon materials to this day. This demonstrates the difficulty to modify carbon in a proper way due to complex behavior according to Figure 8. To sum up the literature, the carbon support requires a maximized surface area with defect sites to achieve a high number of catalytic active centers by distributing the Pt nanoparticles and ensuring mass transport of reactants. Furthermore, the carbon support needs electrochemical stability, dictated by the quality of aromatic structure and the layer arrangement.

### 3.2.4.2 Metal Oxides

With respect to stability under cathodic PEMFC conditions some metal oxides are attractive as Pt support. Potential–pH diagrams from Pourbaix<sup>[76]</sup> show thermodynamic equilibria of metals in presence of water with regions of immunity, passivation or corrosion. If regions of passivation and cathodic PEMFC operation overlap, metal oxides are expected to be stable due to a corrosion-resistant state. Figure 10 illustrates the suitability of tin (IV) oxide for the cathode in PEMFCs, whereas in case of cobalt oxide solubility would prevail.<sup>[186, 187]</sup>

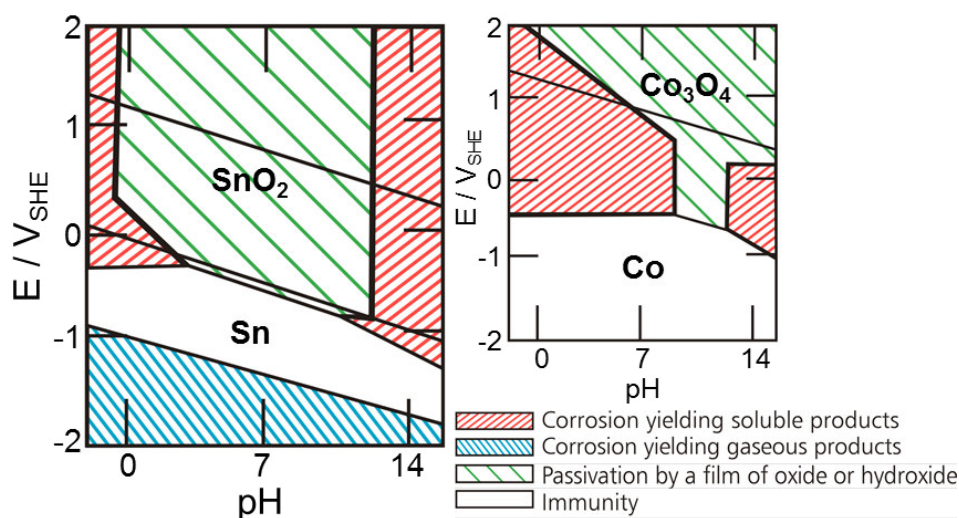


**Figure 10** Potential–pH diagram of tin (cobalt as example to show the opposite).<sup>[186]</sup>

Next to corrosion resistance of the substrate, the stability of platinum on the substrate is crucial. Tin (IV) oxide has ability to anchor and distribute Pt particles on its surface.<sup>[141, 188–190]</sup> Basically, the degree of van der Waals interaction between substrate and Pt particles depends on their electronic band structures and furthermore on functional groups and defect sites onto the surface. *d*-electronic interaction between SnO<sub>2</sub> and Pt<sup>[25]</sup> and the presence of hydroxyl surface groups from dissociative H<sub>2</sub>O adsorption on SnO<sub>2</sub><sup>[47]</sup> causes stronger Pt nanoparticle adsorption compared to Pt/C.<sup>[191]</sup> This strengthened interaction was further suggested to stabilize the Pt particles by affecting the electronic structure of platinum.<sup>[47]</sup> Daio et al.<sup>[191]</sup> revealed a higher lattice strain of 2 nm Pt particles on SnO<sub>2</sub> than Pt particles on graphitic carbon. Lattices were directly visualized by scanning transmission electron microscopy and further simulated using DFT. Furthermore, SnO<sub>2</sub> ability to dissociate water and adsorb OH can impact the Pt characteristics.<sup>[192]</sup> During

ORR, repulsion of OH groups on tin (IV) oxide and oxygen on Pt seems to weaken oxygen binding and enhance ORR activity.<sup>[47, 193]</sup> Both — electronic and repulsion impact of tin (IV) oxide — are described as synergistic effects on the ORR activity in literature.<sup>[46]</sup> These effects are further suggested to weaken CO binding on platinum, which increase the CO tolerance of the catalyst.<sup>[194]</sup> Furthermore, in direct alcohol fuel cells enhanced catalytic activity of Pt for the methanol oxidation was observed.<sup>[141]</sup>

In several studies, SnO<sub>2</sub>, TiO<sub>2</sub> and WO<sub>3</sub> are described to meet the criteria for PEMFC catalyst support best and have been prepared in various nanostructures and compositions.<sup>[25, 195]</sup> However, in view of Table 2, metal oxides need an optimization for the application in FC electrodes in terms of surface area and electrical conductivity.<sup>[133, 190]</sup> An increase of the surface area might be achieved by use of mesoporous metal oxides or metal oxide nanoparticles. Specific surface areas of mesoporous structures are 250 m<sup>2</sup> g<sup>-1</sup> with pore sizes of roughly around 4 nm for TiO<sub>2</sub><sup>[196]</sup> or 205 m<sup>2</sup> g<sup>-1</sup> with pore size distribution centered at 13 nm for SnO<sub>2</sub><sup>[193]</sup>. Nanoparticles showed specific surface areas of 50 m<sup>2</sup> g<sup>-1</sup> in case of SnO<sub>2</sub> particles with 3 nm diameters<sup>[197]</sup> or 100 m<sup>2</sup> g<sup>-1</sup> in case of Sb-doped SnO<sub>2</sub> particles with sizes of around 5 nm<sup>[141]</sup>.

Furthermore, most metal oxides are insulators and hence needs further modification.<sup>[133]</sup> Sub-stoichiometric metal oxides like Ti<sub>4</sub>O<sub>7</sub> have oxygen vacancies and show thus electrical conductivity.<sup>[198]</sup> But these materials are not suitable for FC application, because on the one hand oxidation during cell operation could eliminate the sub-stoichiometry and on the other hand their high temperature synthesis leads to limited surface areas.<sup>[199]</sup> Metal oxide doping is a more suitable way of enhancing the electrical conductivity. Atoms with similar radii but deviating number of valence electrons are incorporated into the metal oxide lattice, generate charge carriers and promote electrical conductivity. Transparent conductive oxides (TCOs) are well-known from solar cells and optoelectronics.<sup>[200, 201]</sup> For example ITO consists of In<sub>2</sub>O<sub>3</sub> incorporating Sn. Each tin atom provides an additional fourth valence electron, which is free and able to move from the valence into the conduction band. Other TCOs are ATO (SnO<sub>2</sub> with Sn<sup>4+</sup> replacement through Sb<sup>3+</sup>) or FTO (SnO<sub>2</sub> with O<sup>2-</sup> replacement through F<sup>-</sup>). Electrical resistances depend on the doping level. Ba et al.<sup>[202]</sup> investigated ITO nanoparticles with doping levels of 3–38 at% Sn in relation to In<sub>2</sub>O<sub>3</sub> and found electrical conductance of each

material with a maximum in case of 20 at% Sn-In<sub>2</sub>O<sub>3</sub>. Wu et al.<sup>[203]</sup> investigated FTO nanoparticles with doping levels of 3–8 at% F in relation to SnO<sub>2</sub> and found comparable electrical conductivities of the materials.

In addition, metal oxide doping has frequently been reported to influence ORR activity positively in comparison to non-doped oxides.<sup>[27, 197, 204, 205]</sup> In the following, research on stability of metal oxides used as Pt support for ORR is reviewed. Takabatake et al.<sup>[195]</sup> compared the durability of MoO<sub>3</sub>, SnO<sub>2</sub>, Nb<sub>2</sub>O<sub>5</sub>, Ta<sub>2</sub>O<sub>5</sub>, TiO<sub>2</sub> and WO<sub>3</sub> under harsh cathodic conditions (cycled potentials between 1.0–1.5 V<sub>RHE</sub>) and reported the most stable performance in case of Pt on SnO<sub>2</sub>. The Pt/SnO<sub>2</sub> catalyst<sup>[187, 195]</sup> and doping variants using for example 2 at% Nb or 4 at% Sb<sup>[188, 206]</sup> exceeded the limited stability of standard Pt/C. ITO nanoparticles have also been frequently tested on durability towards Pt supporting. Liu et al.<sup>[205, 207]</sup> demonstrated significantly higher Pt stability on 5 at% doped ITO than on carbon black. After 1,000 potential cycles between 0.0–1.4 V<sub>RHE</sub> the ECSA of Pt/ITO was still constant, whereas ECSA of Pt/C decreased by 35 %. The ORR investigation showed an insignificant curve shift in case of Pt/ITO. Despite the stable Pt characteristics, microscopic images revealed disappeared parts of ITO after AST. The same authors compared Pt on 5 at% Sn-doped In<sub>2</sub>O<sub>3</sub> and Pt on 5 at% In-doped SnO<sub>2</sub> in a further study using the same stress test and found higher stability of Pt/ITO.<sup>[208]</sup> Schmies et al.<sup>[209]</sup> recently investigated Pt/ITO stability via cycling in two different potential ranges: 0.60–0.95 V<sub>RHE</sub> and 1.0–1.5 V<sub>RHE</sub>. The catalyst performed more stable within the high potential window due to the ITO stability. In the lower potential window, ITO partially dissolved and re-precipitated forming larger particles. TEM images in Figure 11a show some larger ITO particles after their test. HAADF-STEM in Figure 11b demonstrates the merging of two ITO particles forming one particle and furthermore the recovery of indium within the Pt particle.

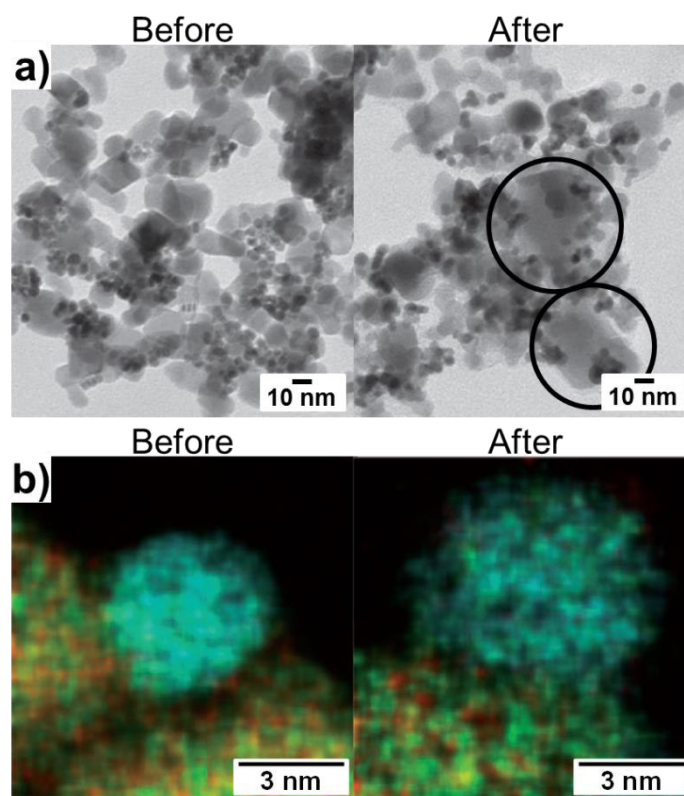


**Figure 11** TEM images (a) and HAADF-STEM images with Pt depicted in blue, In in green and Sn in red (b) before and after stressing Pt/ITO by potential cycling between 0.60–0.95  $V_{\text{RHE}}$ .<sup>[210]</sup>

Very recently, Geiger et al.<sup>[211]</sup> evaluated comprehensively TCOs in terms of their suitability as catalyst supports in FC and electrolyzer application. For this, dissolution rates of ATO, ITO and FTO during cyclic voltammetry between  $-0.60$ – $3.2 V_{\text{RHE}}$  in  $\text{H}_2\text{SO}_4$  electrolyte have been determined via ICP-MS. ATO is obviously unsuitable for fuel cells, because enhanced electrochemical Sb dissolution was measured at around  $0.3 V_{\text{RHE}}$ , which is indeed confirmed by thermodynamic Sb solubility<sup>[76]</sup> and the findings of other studies on ATO.<sup>[187, 212–214]</sup> Furthermore, ITO seems to suffer from continuous chemical dissolution in the whole tested potential range, which confirms the studies of Schmies et al.<sup>[209]</sup> and Liu et al.<sup>[205]</sup>. Lastly, FTO exhibited much lower dissolution rates than the others.  $\text{In}_2\text{O}_3$  and  $\text{Sb}_2\text{O}_3$  dissolved stronger than  $\text{SnO}_2$ . With respect to tin in each material, Sn in ATO and ITO was more instable than Sn in FTO, which might be triggered by Sb and In unsteadiness. In sum, they suggested the consideration of FTO as candidate for catalyst supporting in fuel cells, whereby current FC research on FTO is very limited up to now.<sup>[215, 216]</sup>

### 3.2.4.3 Nanocomposites of Carbon and Metal Oxide

The concept of nanocomposites containing carbon and metal oxides as Pt catalyst support for PEMFCs combines the carbon with metal oxide properties. With respect to metal oxide challenges of surface area and electrical conductivity, graphitic carbons can provide sufficient surface areas and support the electron transfer through a network of aromatic structures as discussed above. Regarding the graphitic carbon challenges, corrosion-resistant metal oxide nanoparticles may protect carbon from corrosion and hinder the restacking of two-dimensional graphene-types like rGO.<sup>[217, 218]</sup> Figure 12 depicts the carbon support with fixed metal oxide particles and anchored Pt nanoparticles at the interfaces. Studies on such nanocomposites as Pt support for ORR are reviewed below.

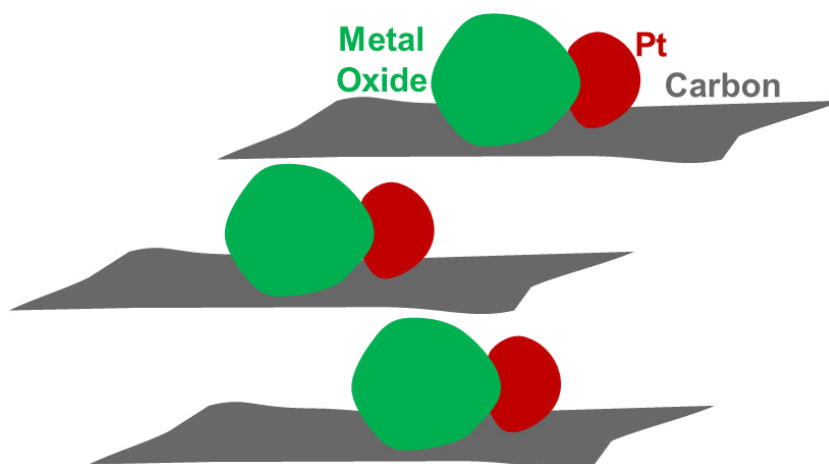


**Figure 12** Schematic view on a carbon section (grey) with a fixed metal oxide particle (green) and a Pt nanoparticle anchored at the carbon–metal oxide interface (red), adapted from<sup>[47]</sup>.

Ruiz–Camacho et al.<sup>[194]</sup> contrasted Pt on carbon black nanocomposites containing  $\text{TiO}_2$ ,  $\text{SnO}_2$  and  $\text{ZnO}$ , respectively. Stress testing (3,500 cycles, 0.05–1.2  $V_{\text{RHE}}$ ) resulted in ECSA loss of about 20 %, 40 % and 80 %, whereas Pt/C in comparison also lost 80 % of ECSA. Lv et al.<sup>[219]</sup> deposited a protecting  $\text{ZrO}_2$  shell on Pt/C causing an increased stability during potential cycling between 0.6–1.2  $V_{\text{RHE}}$ . With regard to tin oxide, Kinumoto et al.<sup>[220]</sup> analyzed Pt/ $\text{SnO}_2$ –C in varying oxide concentrations and investigated the relation between increase of the oxide content and improved ECSA stability (potential steps between 0.6–1.0  $V_{\text{RHE}}$ , 10,000 cycles). Zhang et al.<sup>[47]</sup> compared Pt/ $\text{SnO}_2$ –C with standard Pt/C using 8,000 cycles between 0.6–1.1  $V_{\text{RHE}}$ . The presence of tin oxide led to higher remaining ECSA and

ORR activity. Physical characterization revealed OH on SnO<sub>2</sub> and higher electron density in Pt, which was discussed to cause this performance difference of Pt/C with and without tin oxide. Furthermore, Pt/SnO<sub>2</sub>-C was tested in a HT-PEM fuel cell (H<sub>2</sub>/O<sub>2</sub>, 200 h, 180 °C) and showed a higher voltage than common Pt/C at 0.2 A cm<sup>-2</sup>.<sup>[221]</sup>

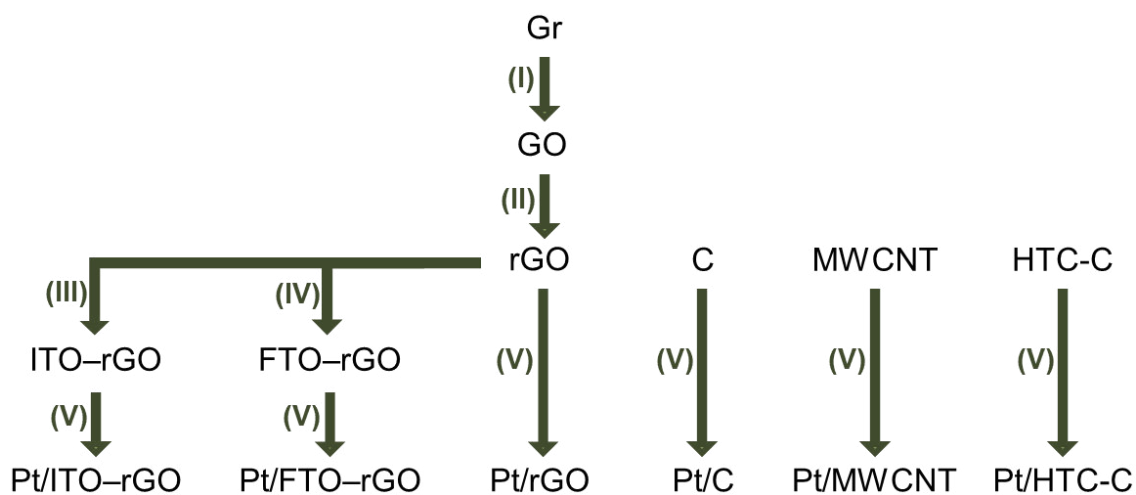
Leaving the studies on carbon black, Kou et al.<sup>[217]</sup> investigated ITO particles on reduced graphene oxide as Pt support for ORR. The presence of ITO resulted in a more stable ECSA and ORR activity than only Pt/rGO after 22 h potential switching between 0.85–1.40 V<sub>RHE</sub>. Considering only the substrates, corrosion currents at potentials greater than 1.2 V<sub>RHE</sub> were four times higher in case of unprotected rGO than in case of ITO-rGO. Finally, DFT calculations showed thermodynamic Pt stabilization at the interface between ITO and rGO through van der Waals interaction, which supports their experimental findings and opens new aspects of research on nanocomposites as Pt support in PEMFCs.

## 4 Experimental Methods

First, catalyst syntheses were elucidated starting with Pt nanoparticles followed by the substrates meaning reduced graphene oxide and its nanocomposites containing Sn-doped indium (III) oxide and F-doped tin (IV) oxide, respectively. Afterwards, the synthesized catalysts were characterized via series of physical and electrochemical methods.

### 4.1 Catalyst Synthesis

Scheme 4 provides an overview of investigated catalysts and their synthesis routes and introduces the abbreviations for each catalyst. Gr is used to produce first GO and finally rGO. Originating from rGO, two types of doped metal oxide nanoparticles are utilized to achieve the nanocomposites ITO-rGO and FTO-rGO. Further materials are C, MWCNTs as well as HTC-C. Each material is used as support for Pt nanoparticles to achieve the final catalysts. Syntheses are described in the following paragraphs using the numbers (I–V) from Scheme 4.

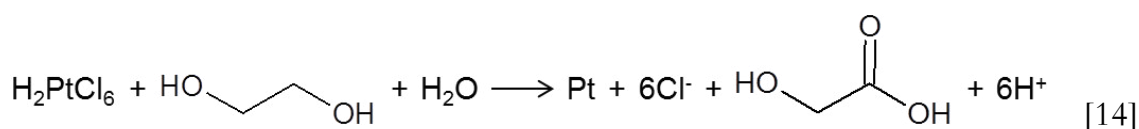


**Scheme 4** Overview of the tested catalysts and their synthesis routes.

Basically, nanomaterials of all sorts can be obtained through top-down or bottom-up methods.<sup>[222]</sup> Ball milling as example for top-down mechanically produces nanoparticles with large variation in size and shape and the risk of introducing impurities caused by abrasion. Bottom-up methods are used more frequently, because physicochemical self-organization of atoms and molecules leads to nanomaterials controllable in size and shape. This includes on one hand gas phase reactions like CVD, which was already named in the context of graphene and carbon nanotubes,<sup>[174, 175]</sup> and on other hand liquid phase reactions including the precipitation of nanoparticles. Reduction of metal salts is commonly used to obtain metallic nanoparticles, whereas sol-gel processes with possible assistance of solvothermal or hydrothermal treatment are commonly used to produce ceramic nanoparticles.<sup>[222, 223]</sup>

### 4.1.1 Pt Nanoparticles

Platinum presents the standard catalyst in fuel cells. In literature, the nanoparticles are mainly synthesized through precipitation, whereas the polyol method has been established in recent years.<sup>[136, 217, 224-226]</sup> Salts like hexachloroplatinic acid are chemically reduced through polyols, which are polyvalent alcohols like the often used ethylene glycol. First, ethylene glycol serves for dissolving the salt followed by reducing the platinum ions to metallic Pt at enhanced temperatures between 120–170 °C.<sup>[226, 227]</sup> During this redox reaction in Equation [14], ethylene glycol is chemically oxidized to glycolic acid, which gets deprotonated in alkaline solution. Glycolate anions then stabilize the formed platinum nanoparticles. Incidentally, the reaction of ethylene glycol to carbon monoxide becomes possible in the presence of Pt.<sup>[228]</sup>



Nucleation and growth of nanoparticles during precipitation reaction is illustrated using the model by LaMer et al.<sup>[229]</sup> in Figure 13, which divides the monomer concentration as function of time into four parts. Begin of reaction is an increase in monomer concentration due to formation of metallic Pt atoms exceeding the saturation threshold and reaching supersaturation (i). The starting nucleation changes the homogeneous liquid into a heterogeneous dispersion. The concentration of

monomers reaches a maximum and then decreases due to simultaneous nucleation and growth (ii). The monomer concentration then falls below the nucleation threshold, so that no nucleation but still particle growth occurs with continuing monomer consumption (iii). Finally, further growth until reaching the saturation threshold takes place (iv).<sup>[223, 229]</sup>

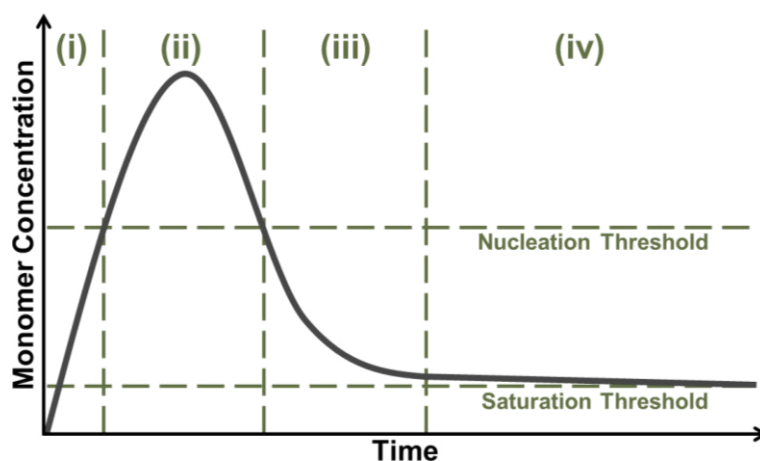


**Figure 13** LaMer model, adapted from<sup>[223]</sup>.

Scheme 4 outlines the synthesis routes including platinum deposition on supports as final step (V). Pt nanoparticles in this work were received using the polyol method described before. 725 mg of chloroplatinic acid hexahydrate was dissolved in 88 mL ethylene glycol. 12 mL of 2 mol L<sup>-1</sup> NaOH in ethylene glycol was added adjusting the pH to 12. The reduction to metallic platinum was carried out under stirring at 140 °C for 4 h. The obtained platinum suspension was stored being ready for deposition on supports. To prepare Pt catalysts, 1.6 mL of previously synthesized Pt suspension was centrifuged with 1 mol L<sup>-1</sup> hydrochloric acid three times followed by washing with deionized water. The platinum nanoparticles and 16 mg of support were given in acetone followed by sonication, until the solvent was evaporated. The catalyst was washed with deionized water and dried at 60 °C under vacuum for 48 h. During an analogous approach, the support was added into the reaction mixture and sonicated for 5 min before stirring at 140 °C for 4 h.<sup>[217, 230, 231]</sup> Obtained Pt nanoparticles are checked on their size, shape and distribution on supports later. Platinum particle sizes are listed in Table 9 of Section 5.2 and are highly comparable, which is expected if nanoparticles are well-stored as stable suspension in ethylene glycol.<sup>[232]</sup> For verification of customized catalysts, commercial platinum on Vulcan<sup>®</sup> XC72 (Sigma Aldrich Corporation, USA) was used as delivered and is listed in Table 9 as well.<sup>[217, 224, 233]</sup>

## 4.1.2 Support Materials

Scheme 4 includes the synthesis of reduced graphene oxide in two steps (I and II). The first step was a modified Hummers method in terms of chemical oxidation of natural graphite (Graphit Kropfmühl GmbH, Germany) to graphite oxide.<sup>[160]</sup> 1.0 g of graphite was sonicated for 1 h in 25 mL concentrated sulfuric acid (Carl Roth GmbH und Co. KG, Germany). 3.0 g of potassium permanganate (Carl Roth GmbH und Co. KG, Germany) and 1.0 g of sodium nitrate (Carl Roth GmbH und Co. KG, Germany) were slowly added in small portions under stirring at 0 °C. The mixture was stirred for 18 h at 35 °C oxidizing the graphite and then quenched through putting the flask into an ice bath and filling in 80 mL of deionized water. For decomposition of residual  $\text{KMnO}_4$ , 10 mL of hydrogen peroxide (30 wt%, VWR International GmbH, Germany) was added. The obtained brown suspension was washed and centrifuged a few times with 10 % hydrochloric acid and deionized water followed by rest water removal using a rotary evaporator. Finally, the brown solid was dried at 60 °C under vacuum for 48 h. In the second step, graphite oxide was thermally reduced to get reduced graphene oxide. The brown solid was put into a capped crucible filled with argon, which was placed into an oven with air atmosphere at 1,050 °C for 30 s.<sup>[160, 171]</sup> The crucible was removed from the oven and stored until reaching room temperature to finally gather rGO in the form of black powder.

Next to rGO, further carbon materials were tested. The carbon black Vulcan<sup>®</sup> XC72R was purchased from Cabot Corporation (Malaysia). MWCNTs were obtained from Ionic Liquids Technologies GmbH (Germany). Both commercial materials were used as delivered. Furthermore, a dark brown coal obtained by hydrothermal carbonization was provided by collaboration with the working group of Chemical Technology 1 from the Carl von Ossietzky University Oldenburg. There, HTC of coconut shell powder was carried out in 60 wt% aqueous zinc chloride solution at 180 °C for 12 h. The obtained coal was ground and stirred in 1 L of water overnight. Afterwards, the coal was washed with water, vacuum filtrated and dried overnight at 105 °C. Finally, the powder was ground again and sieved through a 0.63 mm mesh.<sup>[147]</sup> To modify the coal pyrolysis at 1,100 °C for 2 h in an argon atmosphere with 5 vol% of hydrogen (split tube furnace HZS from Carbolite Gero GmbH & Co. KG, Germany) was carried out followed by ball

milling for 1 min at 250 rpm (PM100 from Retsch GmbH, Germany) to finally obtain HTC-C.

Analogous to Scheme 4, two types of doped metal oxide particles were precipitated with mass fractions of 75 wt% onto the surface of rGO, respectively. The first nanocomposite contains ITO particles. During solvothermal induced sol-gel process (III), the metal alkoxides undergo thermal polycondensation to inorganic-organic intermediates first and crystallization to ITO particles second. By sonication for 1 h, 50 mg of rGO was dispersed in 10 mL benzyl alcohol (Carl Roth GmbH und Co. KG, Germany) to provide 25 wt% rGO for ITO deposition. At the same time, 40.9 mg of tin tert-butoxide (Sigma-Aldrich Chemie GmbH, Germany) and 4 mg of indium acetylacetonate (Sigma-Aldrich Chemie GmbH, Germany) were dissolved in 20 mL benzyl alcohol. Both solutions were united and stirred for 24 h under nitrogen. After that, the mixture was stored in an autoclave at 200 °C for 24 h to precipitate and crystallize ITO particles. Finally, the product was washed with ethanol first followed by chloroform, vacuum filtered and dried at 60 °C under vacuum for 48 h.<sup>[217, 230, 234]</sup>

The second nanocomposite consists of FTO particles. During sol-gel process (IV), a metal halide is hydroxylated in alkaline environment followed by polycondensation and crystallization to FTO particles during hydrothermal treatment. 50 mg of rGO and 348 mg of tin (IV) chloride hydrate (Alfa Aesar GmbH & Co KG, Germany) were dispersed in 60 mL deionized water to provide 25 wt% rGO for FTO deposition. Ammonium hydroxide (28 % NH<sub>3</sub> in H<sub>2</sub>O, Alfa Aesar GmbH & Co KG, Germany) was slowly added until the mixture reached a pH of 8. The suspension was washed with deionized water using vacuum filtration and re-dispersed in 40 mL water. 73.6 mg of ammonium fluoride (Alfa Aesar GmbH & Co KG, Germany) was added to dope with fluorine. The mixture was hydrothermally treated for 72 h in an autoclave at 180 °C to precipitate and crystallize FTO particles on rGO. Finally, the product was washed with deionized water, vacuum filtered and dried at 60 °C under vacuum for 48 h.<sup>[216, 231, 235]</sup>

## 4.2 Physical Characterization

Morphology and composition of the catalysts are characterized by use of physical techniques. Next to the Pt nanoparticles, especially the support materials are physically analyzed to assess their suitability for application as catalyst supports in fuel cells. Table 3 lists the applied methods — which are explained in the following paragraphs — and introduces their abbreviations.

**Table 3** Applied methods to physically analyze Pt nanoparticle and support properties.

Method	Abbreviation	Information
Scanning and transmission electron microscopy	SEM, TEM	Morphology; Particle size and shape
Energy-dispersive X-ray spectroscopy	EDS	Elemental composition; Distribution of elements
Raman spectroscopy	Raman	Structural graphitic defects
Infrared spectroscopy	IR	Identification of functional groups
X-ray photoelectron spectroscopy	XPS	Identification of functional groups; Elemental composition; Chemical states
X-ray diffraction	XRD	Crystallinity; Graphitic degree
Thermogravimetric analysis	TGA	Quantification of functional groups; Thermal stability
N <sub>2</sub> adsorption with Brunauer-Emmett-Teller (BET) evaluation	BET	Specific surface area
Mass spectrometry with inductively coupled plasma	ICP-MS	Pt mass fraction on supports
Four-point probe method	4-point	Electrical conductivity

### 4.2.1 Microscopy

Electron microscopy is widely used to image nanomaterials. During SEM, the electron beam scans solid surfaces in high vacuum with simultaneous detection of backscattered and secondary electrons. Image contrasting arises from surface topography and elemental composition. During TEM, electrons transmitted through nanoparticles or thin films are detected. Contrasts result from elemental composition and thickness of samples and additionally from diffraction in crystals. Other triggered processes during electron beam interaction with solid states are emission of X-ray photons or Auger electrons. Therefore, the opportunity of further analyses like EDS is provided in the course of SEM and TEM.<sup>[236, 237]</sup>

For SEM investigation, samples were fixed on holders (Plano GmbH, Germany) with carbonaceous adhesive. NEON 40 EsB CrossBeam (Carl Zeiss AG, Germany) device was used, which consists of a field emission electron gun applying an acceleration voltage of 30 kV and secondary and backscattered electron detector combined with photomultiplier and CCD camera for imaging and is operated by *Smart SEM* software. The range of magnification is 12–900,000x.

Sample preparation for TEM was done by suspending samples in ethanol and placing a drop on a polyvinyl formal coated copper grid with 200 meshes (Plano GmbH, Germany). After evaporation of ethanol, the coated grids were ready for microscopy. EM 902A (Carl Zeiss AG, Germany) system was used, which consists of an electron gun with tungsten wire and an acceleration voltage of 80 kV as well as a CCD sensor. The device is operated by the *iTEM Five* software. Imaging with magnification between 140–240,000x is possible. JEM2100F (JEOL USA Inc, USA) device served for high resolution microscopy with the range of magnification between 50–1,500,000x. The system is equipped with a field emission electron source at 200 kV, a CCD camera and the *Gatan Digital Micrograph* software. TEM images were evaluated towards nanoparticle sizes and atomic lattices. Diameters of 300 particles were determined and averaged by distance measuring tools in the software *ImageJ*, whereas distances in atomic lattices were measured with *Gwyddion* software.

The transmission electron microscopy was additionally used to image Pt degradation after accelerated stress testing explained in Section 4.3.4. For performance of

this identical location TEM (IL-TEM), a carbon film coated Au grid with 400 meshes (H7, Plano GmbH, Germany) was prepared by putting a drop of catalyst–water–suspension on a glass plate and placing the grid on the droplet. After drying in air, the grid was fixed onto the working electrode of glassy carbon using a Teflon<sup>®</sup> cap. The working electrode with catalyst coated TEM grid was then transferred into the electrochemical setup described in Section 4.3.1 and exposed to electrochemical stress. Finally, identical Pt particles can be imaged before and after testing under the microscope.

## 4.2.2 Spectroscopy

EDS was used in combination with SEM or TEM. The interaction of incident electrons with surfaces leads to emission of secondary electrons. Thereby, an unfavorable state occurs inside the solid followed by filling energetically lower vacancies with energetically higher electrons. As a result, X-ray photons are emitted and allow qualitative element-specific analysis.<sup>[238]</sup> Here, the sample preparation was done in the context of microscopy described in previous Section 4.2.1. The SEM device is expanded by X-Max silicon drift detector (Oxford Instruments plc, UK), whereas the high resolution TEM contains a X-Max80 silicon drift detector (Oxford Instruments plc, UK). In both cases, spectra evaluation was done using the *INCA* software.

Raman spectroscopy exploits inelastic reflected scattering of light at solid states. For example, phonon excitation leads to emitted light with lower energy  $E_{\text{emitted}}$  in contrast to the incident light energy  $E_{\text{incident}}$  according to Equation [15]. Difference in emitted and incident light energy is equal to difference in the product of Planck constant  $h$  and the frequency  $\nu$ . Bands in Raman spectra provide qualitative information about the material in terms of the frequency shift  $\Delta\nu$ .<sup>[239]</sup> With respect to graphitic carbon, intact aromatic structures are excited differently compared to defect sites, which enables quantitative analysis of the defect density. For Raman investigation, the sample was mixed with 2-propanol and sonicated until achieving a highly viscous suspension. The mixture was dropped onto a glass substrate and dried in air. The used SENTARRA (Bruker Corporation, USA) device is equipped with three different excitation sources (785, 633 and 488 nm), a light microscope BX51 (Olympus K.K., Japan) with magnification between 4–100x, the

spectrometer itself and a CCD sensor. The system is operated by the *OPUS* software. Measurements were carried out using a He-Ne laser with a wavelength of 633 nm, a power of 2 mW, an integration time of 60 s and averaging of two scans.

$$\Delta E = E_{\text{emitted}} - E_{\text{incident}} = -h \left( \nu - \nu_0 \right) = -h \Delta \nu \quad [15]$$

IR spectroscopy can be used for excitation of covalent bond vibration in solids through absorption of infrared radiation. The detected radiation exhibits absorption bands at defined frequencies. This allows qualitative analysis of chemical structures by identification of functional groups.<sup>[240]</sup> The FT-IR system Spectrum 100 Optica (Perkin Elmer Corporation, USA) with a ZnSe crystal for ATR was used operated by *Spectrum* software. After determining the background for spectrum correction, the sample was fixed onto the crystal and measured with averaging ten scans in a resolution of 4 cm<sup>-1</sup>.

XPS relies on irradiation of solid states with a beam of X-rays. Photoelectrons with a defined kinetic energy  $E_{\text{kin}}$  are emitted from the solid. Under consideration of incident beam energy  $E_{\text{incident}}$  and the spectrometer work function  $W$ , element specific binding energies  $BE$  are calculated from Equation [16]. Energy and number of emitted photoelectrons allow the quantitative determination of elemental surface composition of solids and moreover qualitative conclusions on chemical and electronic states.<sup>[241]</sup> Samples for XPS were prepared in terms of putting a drop of highly viscous suspension with 2-propanol onto a silicon wafer and drying in air. Spectra were recorded using a ESCALAB 250Xi (Thermo Fisher, UK) system with Al K $_{\alpha}$  X-ray source, hemispherical 180° analyzer and channeltron detector. Survey scans were done with a pass energy of 100 eV, 20 ms dwell time, 1 eV energy step sizes and averaging of 5 scans. High resolution scans were measured by applying a pass energy of 10 eV, 0.02 eV energy step sizes at 50 ms dwell time and averaging of 5 scans. Ten scans were recorded in case of doping atoms in metal oxides to collect spectra with better signal to noise ratios. Spectrum evaluation was carried out using the software *Avantage* with Smart background correction and peak fitting with Gauss-Lorentz line shapes.

$$BE = E_{\text{incident}} - E_{\text{kin}} - W \quad [16]$$

### 4.2.3 Further Methods

Next to microscopic and spectroscopic analyses, further methods were applied. The principle of XRD is based on reflection of X-rays at solid states, which exhibit crystallinity and thus act as diffraction grating. The Bragg law in Equation [17] defines the constructive interference of X-rays scattered at atomic lattices. The positive integer  $n$  of the radiation wavelength  $\lambda$  depends on interplanar atomic distance  $d$  and angle of reflection  $\theta$ . XRD patterns show the intensity of radiation in dependence on the reflection angle and enable crystallinity analysis of solid states.<sup>[242]</sup>

$$n\lambda = 2d \cdot \sin \theta \quad [17]$$

Samples for XRD were prepared similarly to the preparation for Raman spectroscopy. X'Pert Pro MPD (PANalytical B.V., The Netherlands) or EMPYREAN Series 2 (PANalytical B.V., The Netherlands) with Cu K $\alpha$  radiation and *DataCollector* software in each case were utilized. Gonio scans were recorded using 2 $\theta$  steps of 0.01°. Pattern evaluation was carried out by *HighScorePlus* software and comparison with the inorganic crystal structure database ICSD (FIZ Karlsruhe GmbH, Germany). Next to calculation of interplanar atomic distances  $d$  using Bragg's law in Equation [17], the crystallite size  $L$  is estimated using Scherrer's law in Equation [18] containing a form factor  $K$  of 0.89 and the fully peak width at half maximum  $FWHM$  corrected by  $FWHM$  of graphite showing high crystallinity. In case of the metal oxides, the three reflections with highest intensity were considered to get an averaged crystallite size.

$$L = \frac{K \cdot \lambda}{FWHM \cdot \cos \theta} \quad [18]$$

During thermogravimetric analysis, materials are weighed during a controlled heating at defined rates and in defined atmosphere. Mass losses are recorded and assigned to the temperature. Valuation of thermal stability and furthermore the quantitative analysis of material composition and decomposition is enabled.<sup>[243]</sup> TGA 4000 (Perkin Elmer Corporation, USA) consists of the furnace containing the balance with Al<sub>2</sub>O<sub>3</sub> crucible, a temperature sensor as well as heating and cooling elements. For data recording, the *Pyris* instrument software is used. Before starting TGA, the furnace was purged with N<sub>2</sub> with 40 mL min<sup>-1</sup> for 30 min and the crucible was baked out. Here, TGA was performed in N<sub>2</sub> atmosphere using the

following temperature program: Holding 3 min at 30 °C, heating from 30 °C to 100 °C at 10 °C min<sup>-1</sup>, holding 10 min at 100 °C, heating from 100 °C to 900 °C at 10 °C min<sup>-1</sup> and finally holding 1 min at 900 °C.

The next method is used to analyze surface area and porosity of solids by adsorption isotherms, which describes the sorption equilibrium of an adsorbate onto an adsorbent at constant temperature. The formalism of Langmuir describes the adsorbent coverage by an adsorbate in terms of a monolayer. The model neglects differences in the adsorbent surface and furthermore interactions between the adsorbates itself and is only applicable for e.g. the chemisorption of CO on platinum. The BET (Brunauer–Emmett–Teller) formalism is used for more complex processes and considers multilayer coverage during physisorption. During this method, nitrogen is delivered to solids at a constant temperature but variable pressures. During systematically pressure enhancement to below the saturation vapor pressure of nitrogen, N<sub>2</sub> physisorption onto the solid surface occurs and fills the porous network. Adsorption as well as desorption isotherms can be detected. In these dependencies of adsorbed amount of N<sub>2</sub> on its partial pressure, the porosity becomes visible and the specific surface area can be determined.<sup>[244]</sup> Samples for BET analysis were weighed into a glass tube, which was baked out to get ready for measurement using TriStar II 3020 (Micromeritics GmbH, Germany) with *MicroActive* software. Isotherms were evaluated towards the specific surface area using the relative pressure of 0.3.

ICP-MS is a method for quantification of elements in aqueous solution, which is injected into argon plasma leading to desolvation, evaporation, atomization and finally ionization. The single positively charged ions are focused by ion optics and enter a quadrupole. During the mass spectrometric measurement, ions are separated sequentially by their ratio of mass to charge.<sup>[245]</sup> 2.0 mg of each platinum sample was digested in 1.2 mL HNO<sub>3</sub> with 1.6 mL hydrochloric acid overnight. The solutions were filtered, diluted to 250 mL and further diluted by factor of 5. Calibration solutions for platinum were prepared in concentrations of 100, 200, 400, 600 and 800 µg L<sup>-1</sup> by use of an ICP standard solution with a concentration of 1,000 mg L<sup>-1</sup> (Carl Roth GmbH & Co. KG, Germany). Each solution contained Lutetium as internal standard in a concentration of 1 mg L<sup>-1</sup>. XSeries2 (Thermo Fisher Scientific GmbH, Germany) system served for analysis of Pt contents. During the measurement, the three platinum isotopes <sup>194</sup>Pt, <sup>195</sup>Pt and <sup>196</sup>Pt were detected to average the final Pt concentration. All calibrations showed a correlation coefficient of at least 0.999 and a recovery of Pt sample for validation of at least 95 %.

Electrical resistances were determined by the four-point probe method. Figure 14 illustrates its principle and shows the four probes with equal distances in contact with a thin film of solid. A current flows through the outer probes, whereas the voltage is recorded using the inner probes. Thereby, the electrical resistance of sheets is determined.<sup>[246]</sup> Before the measurement, a sample suspension analogous to electrode coating in Section 4.3 was prepared. Spray coating onto a glass substrate using a *devilbiss* spray gun (Carlisle Fluid Technologies Germany GmbH, Germany) operated with a nitrogen gas flow gave a thin film of sample. Finally, five sample positions on each thin film were measured and averaged by used of RM3-AR (Jandel Engineering Ltd, UK).

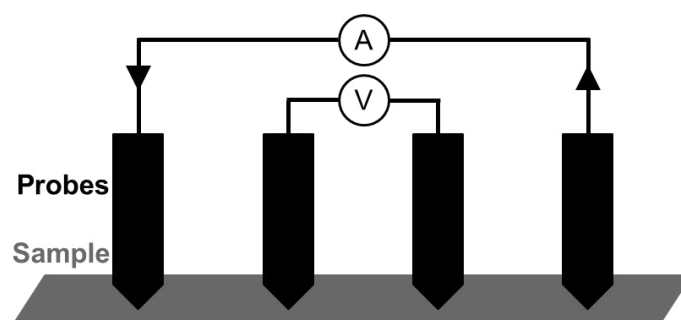
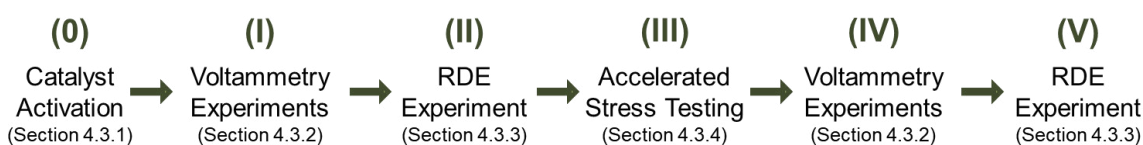


**Figure 14** Functional principle of the four-point probe method.

### 4.3 Electrochemical Characterization

Methods applied to investigate the electrochemical durability of the catalysts are introduced. Scheme 5 shows the progress in characterization, which starts with catalyst activation by potential sweeping (0). Voltammetry experiments were conducted in terms of cyclic and CO stripping voltammetry (I) to determine electrochemical surface areas and support characteristics. RDE experiment was then performed getting access to ORR kinetics (II). After that, catalysts were exposed to accelerated stress testing (AST) to trigger degradation. Finally, aged catalysts were characterized again (IV and V).



**Scheme 5** Sequence of electrochemical characterization.

#### 4.3.1 Setup

The setup for electrochemical measurements is depicted in Figure 15. The rotating disk electrode (RDE) coated with a thin film of catalyst was used as working electrode and is fixed into the rotator (1). The RDE consists of glassy carbon jacketed with PTFE and has a geometric area of 0.196 cm<sup>2</sup> (Pine Research Instrumentation Inc, USA) or 0.2 cm<sup>2</sup> (in-house production, University of Tartu, Estonia). The reference electrode was a saturated calomel electrode (SCE, KCl-saturation) inside a glass element separated with salt bridge and Luggin capillary (2). A wound Pt wire served as counter electrode (3). The three electrodes were introduced into the glass cell (4) with gas supply (5) and were connected to a bipotentiostat (Autolab PGSTAT128N or PGSTAT132N, Metrohm Autolab, The Netherlands) operated by the software *Nova*. Measurements were carried out at room temperature. Recorded potentials were converted from SCE to reversible hydrogen electrode (RHE) by use of Equation [19].

$$E_{\text{RHE}} = E_{\text{SCE}} + 0.059 \cdot \text{pH} + E_{\text{SCE}}^0 = E_{\text{SCE}} + 0.059 \cdot 1 + 0.244 \text{ V} = E_{\text{SCE}} + 0.303 \text{ V} \quad [19]$$

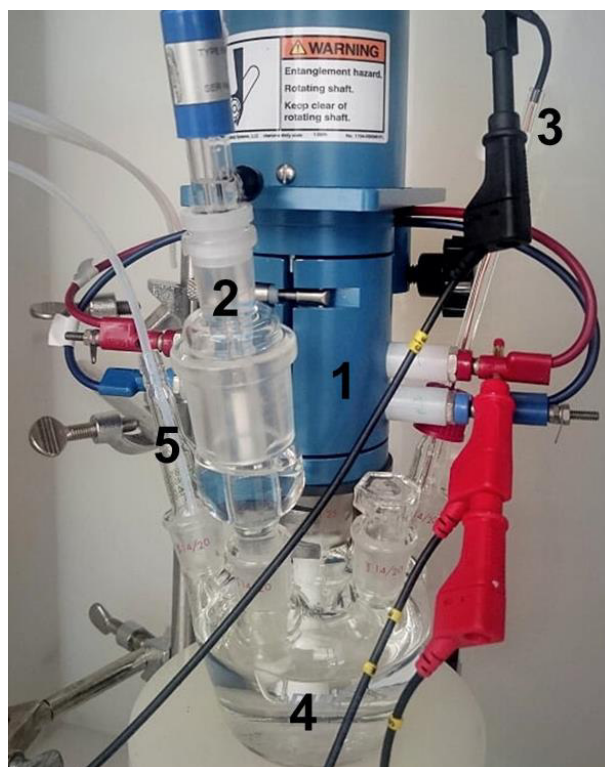


**Figure 15** Setup consisting of rotator with rotating disk electrode (RDE) as working electrode (1), reference electrode with salt bridge and Luggin capillary (2), counter electrode (3), glass cell filled with electrolyte (4) and gas inlet (5).

Before measurement, the cell was filled with aqueous  $0.1 \text{ mol L}^{-1}$  perchloric acid (70 wt%, Sigma–Aldrich Corporation, USA) as common electrolyte for RDE experiments.<sup>[28–30, 217]</sup> The preparation of RDEs started with electrode polishing for 5 min each using 1.0 and  $0.25\text{--}0.30 \text{ }\mu\text{m}$  alumina paste (Buehler, USA). Electrodes were then cleaned via sonication in 2-propanol for 5 min followed by deionized water for 5 min and were then ready for catalyst coating. Parameters for preparation of RDEs are listed in Table 4. First, the catalyst inks were prepared. Ink compositions were adapted to the catalyst material to achieve later a unique catalyst film onto the electrode. They are defined by the catalyst  $c_{\text{Catalyst}}$  and the Nafion<sup>®</sup> concentration  $c_{\text{Nafion}^{\text{®}}}$  and by the 2-propanol/ $\text{H}_2\text{O}$  ratio. After sonication for 1 h, the inks were dropped onto a polished and cleaned RDE and dried under rotation. The drop casting is defined by the ink volume  $V_{\text{Ink}}$ , depending on the geometric area of the used RDE, and the rotation speed  $\omega$  during drop casting. The proceeding of RDE preparation for supports was analogous to the related Pt catalyst.

**Table 4** RDE preparation in dependence on the catalyst being used.

Catalysts		Pt/C, Pt/C-commercial, Pt/MWCNT	Pt/rGO, Pt/ITO-rGO	Pt/FTO-rGO	Pt/HTC-C
<b>Catalyst Ink</b>	$c_{\text{Catalyst}} / \text{g L}^{-1}$	1	1	2	2
	$c_{\text{Nafion}^{\circledR}} / \mu\text{g L}^{-1}$	0.6	0.6	1.2	1.2
	2-propanol/ $\text{H}_2\text{O}$	1/3	1/2	1/2	1/3
<b>Catalyst Film</b>	$V_{\text{Ink}} / \mu\text{L}$	30 or 29.5	30 or 29.5	14.7	14.7
	$\omega / \text{rpm}$	700	300	300	700

After assembling the setup, filling the glass cell with electrolyte and connecting a freshly prepared RDE as well as counter and reference electrode to the bipotentiostat, measurements were started. Before actual characterization and stress testing of the catalyst, 100 potential cycles between 0.05–1.47  $V_{\text{RHE}}$  at a scan rate of 500  $\text{mV s}^{-1}$  were performed to activate the catalyst in terms of Pt surface cleaning and Pt particle arrangement on the carbon surface (see Appendix, Figure 64). Impurities like residual organic compounds from synthesis are oxidized and removed during activation.<sup>[247–249]</sup> Pt features of the cycles grow and finally reach a maximum after 100 cycles so that a maximized electrochemical surface area is arisen being determined in subsequent catalyst characterization.

### 4.3.2 Cyclic and CO Stripping Voltammetry

Cyclic and CO stripping voltammetry experiments (see Scheme 5, I and IV) are on one hand used for getting access to the electrochemical surface area of platinum and on the other hand for analysis of the support. To distinguish between analysis of platinum and analysis of the support within the figures, Pt features are marked green whereas support features are marked red.

First, both established methods — hydrogen underpotential deposition (HUPD) via cyclic voltammetry and CO stripping voltammetry (CO) — are applied in this work to obtain the ECSA of platinum. Therefore, a chemisorbed monolayer of redox active species on Pt and the released charge during their desorption was used. The electrochemical surface area depends directly on Pt particle conditions like particle size, anchoring and distribution on the substrate and the possible presence of competing adsorbates. ECSA depends indirectly on electrical conductivity, surface area and functional surface groups of the support as well as on Pt-support-interaction.

For the first method HUPD, a typical CV curve for Pt/C is shown in Figure 16a. Data were recorded from 0.05 to 1.00  $V_{\text{RHE}}$  with  $50 \text{ mV s}^{-1}$  in  $\text{N}_2$ -saturated electrolyte. Next to support characteristics discussed later (marked red), typical Pt features are visible (marked green). In the potential region of approximately 0.0–0.4  $V_{\text{RHE}}$  reductive hydrogen adsorption (i) and oxidative desorption (ii) takes place, whereas above approximately 0.6  $V_{\text{RHE}}$  water adsorption and an oxidation reaction to form oxygen species (iii) occurs. After that, desorption of oxygen species during a reduction reaction (iv) takes place. For ECSA determination via HUPD, previously adsorbed hydrogen desorbs from the Pt surface through electrochemical oxidation during anodic sweep of CV. The hydrogen oxidation signal is green crosshatched and used for evaluation as explained below.

For the second method CO, a typical CO stripping curve for Pt/C is depicted in Figure 16b. The stripping experiment started with CO bubbling through the electrolyte for 1 min at 0.15  $V_{\text{RHE}}$  to adsorb carbon monoxide on platinum. Second,  $\text{N}_2$  was bubbled for another 20 min through the electrolyte to remove residual CO. Third, CV curve between 0.05–0.30  $V_{\text{RHE}}$  with  $50 \text{ mV s}^{-1}$  was recorded for assurance of complete CO coverage on platinum. This curve is marked in Figure 16b by a red arrow and used for analysis of support characteristics later (see Figure 17a). Last, the actual CO stripping was performed by starting the anodic scan from 0.15  $V_{\text{RHE}}$  (V) and scanning up to 1.10  $V_{\text{RHE}}$  with  $50 \text{ mV s}^{-1}$ . For ECSA determination via CO, this curve contains the signal of electrochemical CO oxidation (vi) being crosshatched and used for evaluation as explained below.

The released charge amount  $Q_{Pt}$  during oxidation of hydrogen or CO is cross-hatched in Figure 16, respectively, and serves for ECSA calculation using Equation [20].  $Q_{Pt}$  is divided by the scan rate  $\nu$ , the Pt loading  $m_{Pt}$  onto the electrode and the charge density  $\rho$  being  $2.1 \text{ C m}_{Pt}^{-2}$  in case of hydrogen and  $4.2 \text{ C m}_{Pt}^{-2}$  in case of CO. The hydrogen atom adsorbs on one Pt atom, whereas CO oxidation mechanism supposes two involved Pt atoms. The linear bonded CO atom on one Pt atom is oxidized by means of an oxygen species on another Pt atom.<sup>[250, 251]</sup>

$$ECSA = \frac{Q_{Pt}}{\nu \cdot \rho \cdot m_{Pt}} \quad [20]$$

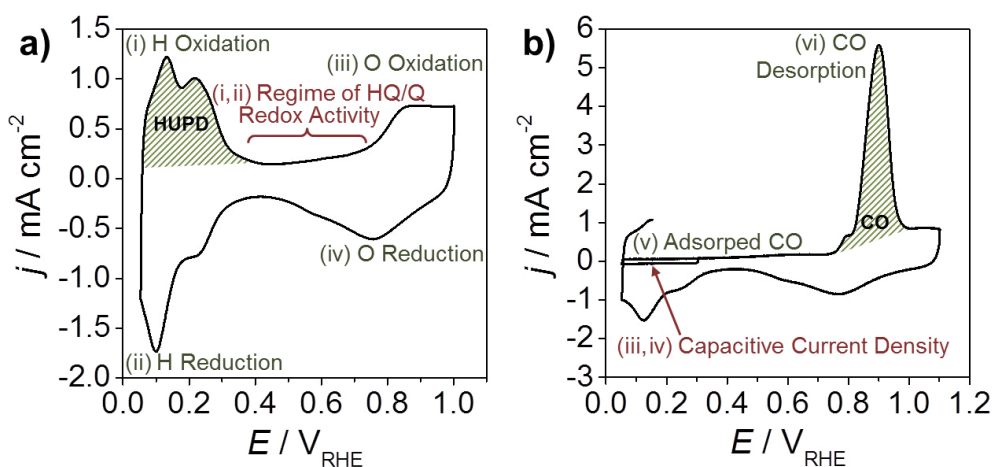


**Figure 16** Exemplary CV curve (a) and CO stripping curve (b) of commercial Pt/C in  $0.1 \text{ mol L}^{-1} \text{ HClO}_4$ . Illustration of typical electrochemical Pt signals with crosshatched signals for ECSA determination via HUPD and CO (green marks). Illustration of support characteristics (red marks).

Second, cyclic and CO stripping voltammetry were used for support analysis in terms of two parameters. The first parameter is obtained from redox reaction of HQ/Q similar groups during CV experiment in Figure 16a. Regime of HQ/Q redox activity is marked red (i, ii). Hydroquinone oxidation is detected at around  $0.6 \text{ V}_{RHE}$  and is more or less visible, depending on the amount of functional support surface groups. Figure 17a depicts an enlarged CV curve in the range of  $0.4\text{--}0.8 \text{ V}_{RHE}$  with visible hydroquinone oxidation (i) and quinone reduction (ii). The released charge amount  $Q_{HQ}$  during oxidation of hydroquinone to quinone is obtained by integration of this signal.<sup>[252]</sup>

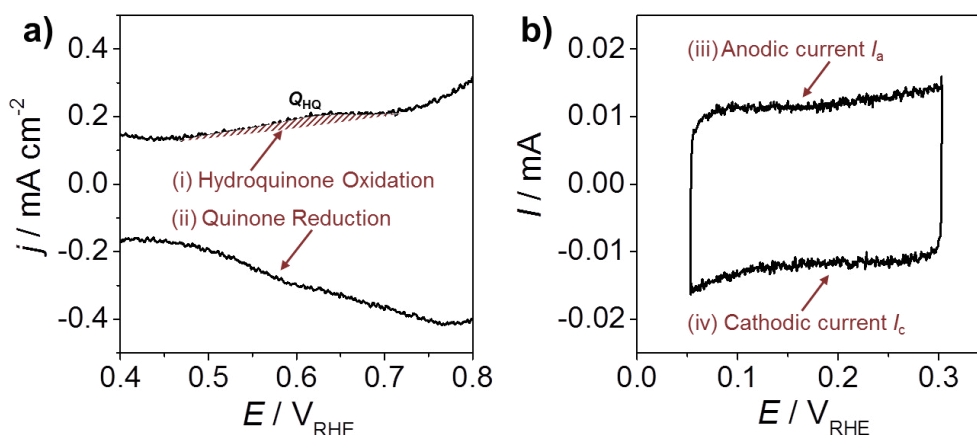


**Figure 17** Exemplary CV curve with suppressed faradaic currents (a) and CV curve with enlarged HQ/Q region (b) of commercial Pt/C in  $0.1 \text{ mol L}^{-1} \text{ HClO}_4$ .

The second parameter is the double layer capacitance  $C_{\text{DL}}$ , which relies on surface area and functional surface groups of the material. During CO stripping experiment in Figure 16b, Pt reactions were suppressed via adsorbed CO to record the capacitive current density. Cyclic voltammetry in presence of adsorbed CO is marked red (iii, iv). Figure 17a depicts the enlarged CV curve between  $0.05$ – $0.30 \text{ V}_{\text{RHE}}$ .<sup>[62, 136]</sup> To calculate the double layer capacitance, the anodic current  $I_a$  (iii) and the cathodic current  $I_c$  (iv) at potentials of  $0.16$ ,  $0.21$  and  $0.26 \text{ V}_{\text{RHE}}$  were used in Equation [21]. An averaged double layer capacitance was obtained from the currents at these potentials.

$$C_{\text{DL}} = \frac{(I_c - I_a)}{2 \cdot \nu} \quad [21]$$

### 4.3.3 RDE Experiments

Another electrochemical analysis is the ORR investigation (see Scheme 5, II and V) by RDE technique. Rotation of the electrode was used to achieve a controllable and defined mass transport of  $\text{O}_2$  molecules during ORR. The rotation speeds were  $400$ ,  $900$ ,  $1,200$ ,  $1,600$ ,  $2,000$  and  $2,500 \text{ rpm}$  each for recording ORR curves from  $0.16$  to  $1.05 \text{ V}_{\text{RHE}}$  with  $5 \text{ mV s}^{-1}$  in  $\text{O}_2$ -saturated electrolyte.

Figure 18a depicts a typical curve of Pt/C during electrode rotation at 1,600 rpm. In the high potential window of 1.0–1.1 V<sub>RHE</sub> the current density  $j$  of oxygen reduction counts zero because of kinetic inhibition. Then, the current density arises due to the onset of ORR (i) at around 1.0 V<sub>RHE</sub>. To determine the onset potential  $E_{\text{onset}}$  of O<sub>2</sub> reduction reaction, the first deviation of this curve was used to see the potential value with strong change in current density different to zero.

At a potential of around 0.9 V<sub>RHE</sub>  $j$  depends on limitation through ORR kinetics on one side and oxygen diffusion on other side. In this mixed limited regime (ii)  $j$  is the sum of current density limited by kinetics  $j_{\text{kin}}$  and the diffusion-limited current density  $j_{\text{lim}}$  as shown in Equation [22].

$$\frac{1}{j} = \frac{1}{j_{\text{kin}}} + \frac{1}{j_{\text{lim}}} \quad [22]$$

In the low potential range below approximately 0.7 V<sub>RHE</sub> ORR is mainly limited by reactant diffusion (iii), so that the current density  $j$  depends on speed of electrode rotation. This dependency is described by Koutecky–Levich (K–L). Equation [19] contains electrode rotation speed  $\omega$ , the Faraday constant  $F$  (96,485 C mol<sup>-1</sup>), the kinematic viscosity  $\mathcal{G}$  of electrolyte (0.01 cm<sup>2</sup> s<sup>-1</sup>)<sup>[181]</sup>, the diffusion coefficient of oxygen  $D_{\text{O}_2}$  (1.93×10<sup>-5</sup> cm<sup>2</sup> s<sup>-1</sup>)<sup>[181]</sup>, O<sub>2</sub> concentration in solution  $c^*_{\text{O}_2}$  (1.26×10<sup>-3</sup> mol L<sup>-1</sup>)<sup>[181]</sup>. The last parameter is the number of transferred electrons  $n$  during the reduction of one O<sub>2</sub> molecule and was determined from the slope in linear K–L relation according to Equation [23].

$$\frac{1}{j} = \frac{1}{0.62 \cdot n \cdot F \cdot \mathcal{G}^{-\frac{1}{6}} \cdot D_{\text{O}_2}^{2/3} \cdot c^*_{\text{O}_2}} \cdot \omega^{-1/2} \quad [23]$$

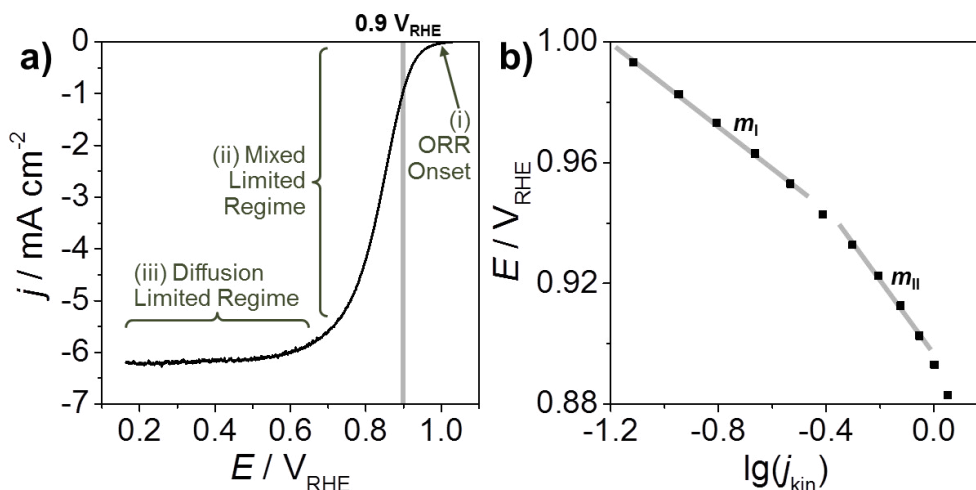


**Figure 18** Exemplary ORR curve of commercial Pt/C in  $0.1 \text{ mol L}^{-1} \text{ HClO}_4$  at 1,600 rpm (a) and the associated Tafel Plot (b).

From Figure 18a furthermore the activity for oxygen reduction was accessible. Therefore the current density  $j$  at the potential value of  $0.9 V_{\text{RHE}}$  was considered, and the diffusion-limited current density  $j_{\text{lim}}$  below approximately  $0.7 V_{\text{RHE}}$  was averaged and considered as well.  $j_{\text{kin}}$  was then accessible through Equation [22]. The specific activity  $SA$  correlates the kinetic current density with the ECSA, while the mass activity  $MA$  normalizes the kinetic current density by the mass of platinum.

Further investigation of ORR kinetics was done via the Tafel relation [9] using a rotation speed of 1,600 rpm. Figure 18b illustrates that plotting the potential against natural logarithm of  $j_{\text{kin}}$  results in two distinguishable Tafel slopes of  $m_I = 60 \text{ mV dec}^{-1}$  and  $m_{II} = 120 \text{ mV dec}^{-1}$ , which are characteristic for Pt catalysts.<sup>[61, 62]</sup>

### 4.3.4 Accelerated Stress Testing

Last, accelerated stress testing (see Scheme 5, III) served for inducing degradation of catalysts and to study their durability. Section 3.2.3 pointed out the impact factors on catalyst degradation from literature. Criteria to induce great stress on platinum catalysts are the fast change of potential, a high potential limit up to 1.40–1.50  $V_{\text{RHE}}$  as well as the presence of oxygen.<sup>[72–75, 88]</sup> Figure 19 shows the potential cycling applied to catalysts in this work to induce significant degradation. Figure 19a depicts the total number of 1,000 cycles between 0.05–1.47  $V_{\text{RHE}}$  performed in oxygen-saturated electrolyte. To see single triangle-waved cycles with a scan rate of  $500 \text{ mV s}^{-1}$ , Figure 19b shows the first seconds of stress test. This test allows on one hand catalyst degradation — especially in the upper potential range — and on the other hand *in-situ* detection of Pt features due to the chosen lower potential limit of 0.05  $V_{\text{RHE}}$ .

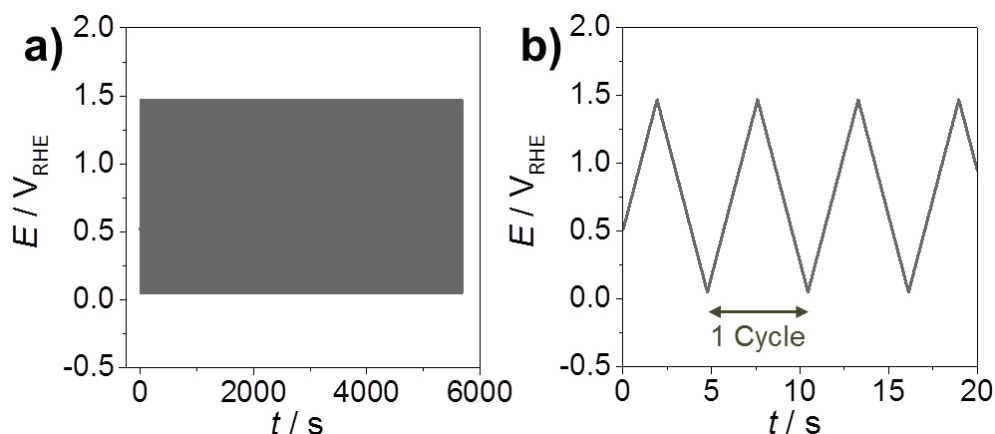


**Figure 19** Accelerated stress test in oxygen-saturated  $0.1 \text{ mol L}^{-1} \text{ HClO}_4$ . Potential against the time for the whole AST (a) and for a part of AST with one labeled cycle (b).

Table 5 specifies all technical parameters used during electrochemical characterization and lists the parameters that have been determined. To sum up, CV and CO stripping experiments (see Scheme 5, I and IV) result into  $ECSA_{\text{HUPD}}$  and  $Q_{\text{HQ}}$  as well as  $ECSA_{\text{CO}}$  and  $C_{\text{DL}}$ . The RDE experiment (see Scheme 5, II and V) gives access to the ORR parameters  $E_{\text{onset}}$ ,  $MA$ ,  $SA$ ,  $n$ ,  $m_{\text{I}}$ ,  $m_{\text{II}}$ . The accelerated stress test directly shows *in-situ* potential cycles and indirectly gives information about nature and extent of catalyst aging through all other parameters from catalyst characterization before and after AST.

**Table 5** Summary of technical parameters for electrochemical investigation.

Parameter	Activation	CV	CO Stripping	RDE	AST
Start potential / $V_{\text{RHE}}$	0.05	0.05	0.05	0.16	0.05
End potential / $V_{\text{RHE}}$	1.47	1.00	1.10	1.05	1.47
Scan rate / $\text{mV s}^{-1}$	500	50	50	5	500
No. of potential cycles	100	3	3	3	1,000
Electrolyte saturation	$\text{N}_2$	$\text{N}_2$	$\text{N}_2$	$\text{O}_2$	$\text{O}_2$
Parameters determined	–	$ECSA_{\text{HUPD}}$ , $Q_{\text{HQ}}$	$ECSA_{\text{CO}}$ , $C_{\text{DL}}$	$E_{\text{onset}}$ , $MA$ , $SA$ , $n$ , $m_{\text{I}}$ , $m_{\text{II}}$	<i>in-situ</i> potential cycles

## 5 Results and Discussion

Sections 5.1 and 5.2 present and discuss physical analyses using the methods in Table 3 of (i) each support material and (ii) each Pt catalyst. The physical characterization within the first two sections is then basis to discuss the electrochemical characterization of each catalyst in Section 5.3, which focusses on assessment of stability after accelerated stress testing.

### 5.1 Physical Characterization of Graphene-Based Supports

Reduced graphene oxide and progress in its synthesis is first physically evaluated in Section 5.1.1 and second physically compared to further carbon materials in Section 5.1.2. The carbon black Vulcan<sup>®</sup> XC72R — commonly used as catalyst support in fuel cells — and multi-walled carbon nanotubes — next to rGO a further alternative support — are considered. The fourth material is a new sustainable carbon originated from hydrothermal carbonization of coconut shells, which was modified for fuel cell application and is a result of collaboration with the Chemical Technology 1 of the Carl von Ossietzky University Oldenburg. Finally, Section 5.1.3 is about structure and morphology of the two nanocomposites based on rGO with first Sn-doped indium (III) oxide and second F-doped tin (IV) oxide nanoparticles.

#### 5.1.1 Reduced Graphene Oxide

Reduced graphene oxide has been obtained in two steps, chemical oxidation of graphite and subsequent thermal reduction of graphite oxide. To monitor the progress in preparation, the materials have been characterized and compared to each other. First, microscopic investigation is depicted in Figure 20 in terms of SEM. Graphite flakes as starting material and rGO as final product are compared in Figure 20a–b using the same magnification. In contrast to graphite rGO consists of smaller flakes with lower brightness under the microscope, which indicates the enhanced porous morphology. SEM images with higher magnification of rGO in Figure 20c–d show highly wrinkled and aggregated sheets with 3D arrangement,

which is based on their van der Waals interaction. In other parts, unfolded sheets are visible illustrating the 2D character of rGO (marked area in Figure 20d). In addition to the imaged morphology under SEM, physisorption of nitrogen was used to determine specific surface areas via BET formalism (see Appendix, Figure 63). Reduced graphene oxide has a specific surface area of  $286 \text{ m}^2 \text{ g}^{-1}$ ,<sup>[230]</sup> whereas graphite has a by factor of 36 lower specific surface area of  $8 \text{ m}^2 \text{ g}^{-1}$ . This demonstrates the porous structure of wrinkled and rotationally faulted rGO in contrast to graphite.

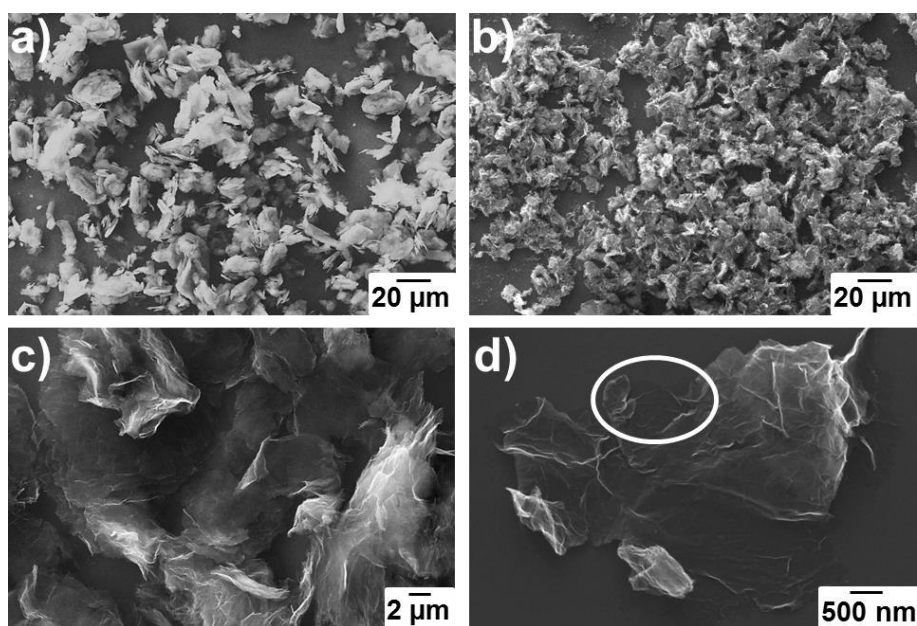


**Figure 20** SEM images of Gr (a) in contrast to rGO (b) with images of rGO in higher magnification (c, d).

TEM in Figure 21 shows further differences in the materials. The lateral size of flakes seems to decrease in each step of synthesis. McAllister et al.<sup>[166]</sup> found the same trend in flake diameters taking the similar synthesis route. They reported GO diameters of approximately  $10 \mu\text{m}$  and rGO diameters of approximately  $500 \text{ nm}$  independent of the graphite diameter. Moreover, the transparency of the materials seems to increase in each step of synthesis indicating the exfoliation of layers. However, TEM only gives small microscopic insight into the bulk so that further analysis by XRD, Raman, TGA and IR was performed.

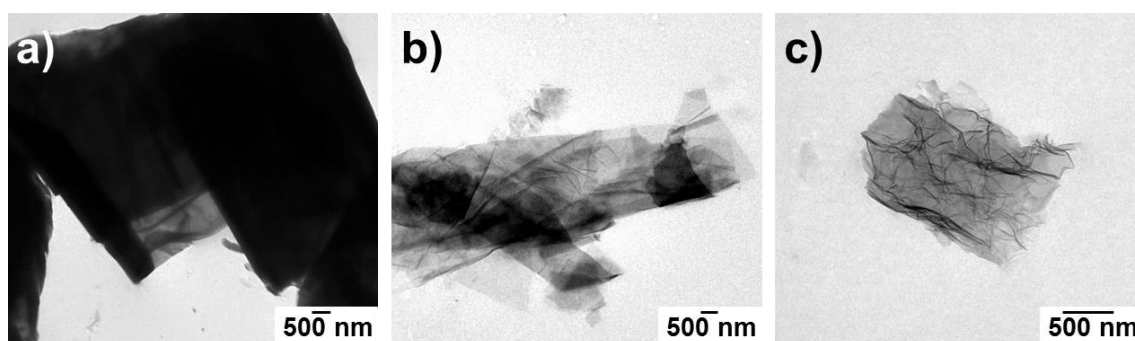


**Figure 21** TEM images of graphite (a), graphite oxide (b) and reduced graphene oxide (c).

XRD analysis is shown in Figure 22 and serves for comparison of crystallinity. Graphite exhibits by far the highest crystallinity, followed by graphite oxide and last reduced graphene oxide. Because rGO shows much lower crystallinity than graphite, no re-organization of graphene layers to an ordered graphitic structure has taken place during the reduction of GO. Hence, the success of layer exfoliation is verified.<sup>[166]</sup> If Gr as precursor in Figure 22a is compared to rGO as final product in Figure 22c, the (002) reflections appear at similar diffraction angles  $2\theta$  of about 26–27°. In contrast, graphite oxide as intermediate product in Figure 22b has a much lower (002) reflection angle of around 12°. This demonstrates a higher interlayer space in GO caused by the functional surface groups and intercalation of water molecules.<sup>[166, 253]</sup> Table 6 lists the parameters obtained from XRD analysis. Interlayer distances  $d$  of Gr, GO and rGO are calculated from the diffraction angle  $2\theta$  of (002) reflection and differ among each other. GO has a (002) distance of 0.740 nm, much higher than the layer distances of the other two materials. The functionalization of graphene layers through oxygen groups during GO synthesis leads to an expansion of GO layer distances. On the contrary, graphite and rGO obviously possess no higher amount of functional groups so that interlayer distances are much lower. However, rGO has a slightly larger value of 0.341 nm compared to 0.335 nm in case of graphite. Possible reason is a rotationally faulted morphology with widened layer distance for rGO in contrast to highly arranged layers in graphite. Moreover, residual oxygen content of rGO layers originated from the GO precursor is another reason.<sup>[159, 166]</sup>

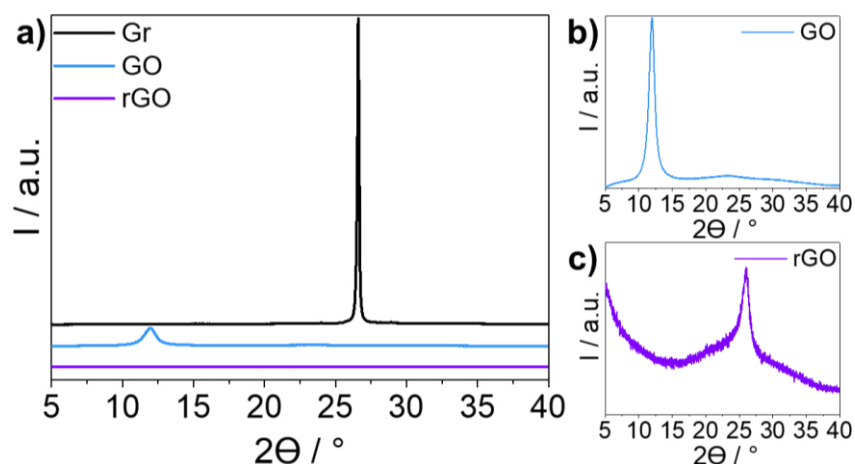


**Figure 22** XRD of graphite, graphite oxide and reduced graphene oxide (a) with zoomed XRD of GO (b) and of rGO sample (c).

Furthermore, the crystallite sizes  $L$  are calculated by Equation [18] on basis of the  $FWHM$  and are in the descending order of  $Gr > GO > rGO$ . Hence, XRD is in accordance with SEM and TEM images and confirms the highest crystallinity for graphite with a size of 52.1 nm. GO has a crystallite size of 9.5 nm. Last, rGO exhibits a size of 5.0 nm — a factor of 10 lower than the graphite starting component. Overall, XRD shows rGO in rotationally faulted modification with rarely graphitization. This is according to the previously supposed layer arrangement in rGO illustrated in Figure 9 of Section 3.2.4.1.2.

**Table 6** Parameters from XRD and Raman analyses for graphite, GO and rGO.<sup>[230]</sup>

Method	Parameter	Gr	GO	rGO
XRD	$2\theta / ^\circ$	26.6	12.0	26.1
	$d / \text{nm}$	0.335	0.740	0.341
	$FWHM / ^\circ$	0.2	0.8	1.6
	$L / \text{nm}$	52.1	9.5	5.0
Raman	G Position / $\text{cm}^{-1}$	1578	1599	1598
	$I_D/I_G$	0.37	1.28	0.96

Figure 23 presents the Raman spectra, whereas the Table 6 lists the associated Raman data. Each material shows the typical bands resulting from light scattering at graphitic carbons. Regarding shape and width of bands, Gr bands are more defined than GO and rGO,<sup>[254]</sup> which indicates a highly ordered structure of graphite in accordance with high crystallinity observed by XRD. Basically, the G band corresponds to  $E_{2g}$  vibrational mode of  $sp^2$ -hybridized carbon bonds in aromatic structures and is located at around  $1590\text{ cm}^{-1}$ . The D band is due to the  $A_{1g}$  vibrational breathing mode of  $sp^2$ -hybridized carbon bonds — only possible in aromatic rings adjacent to  $sp^3$ -hybridized defect sites — and is located at around  $1300\text{ cm}^{-1}$ . Therefore, the degree of structural defects is estimated by the ratio of D band intensity to G band intensity  $I_D/I_G$  and is in ascending order of  $Gr < rGO < GO$ .

Oxidation of Gr to GO introduces many functional oxygen groups and possibly some destroyed aromatic structures due to  $CO_2$  evolution. Therefore, GO possesses the highest  $I_D/I_G$  ratio of 1.28, which is 3.5 times higher than 0.37 in case of graphite, and thus the highest number of structural defects. The ratio above one shows that  $sp^3$ -hybridized carbon predominates. Further reaction of GO to rGO leads to lower structural defects, which is caused by the removal of functional groups and thus removal of interfering impact on the vibrational mode of aromatic rings.  $I_G/I_D$  of final rGO is 0.96. Literature values are 0.87,<sup>[159]</sup> 0.90<sup>[172]</sup> or even above 1.00<sup>[254]</sup> depending on the synthesis parameters.

Furthermore, G band position indicates exfoliation of graphene layers through a positive shifting. The Raman shift in case of rGO is  $1598\text{ cm}^{-1}$  and thus  $20\text{ cm}^{-1}$  higher than in case of graphite. If the number of graphene layers would be higher than 10, the G band position would get similar to that of graphite.<sup>[154]</sup>

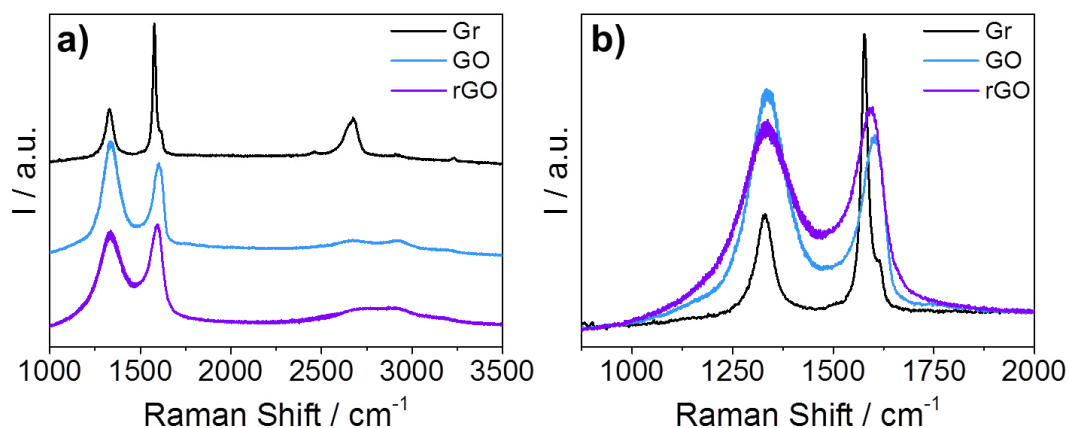


**Figure 23** Raman spectra of graphite, graphite oxide and reduced graphene oxide (a) with zoomed and lapped range of D- and G-band (b).

TGA and IR spectroscopy are used to quantify the oxygen content and to qualify the functional oxygen groups in GO, respectively. The results for rGO are depicted as well and clarify the change in material during the synthesis step of thermal reduction. In Figure 24a, thermogravimetric curves of GO and rGO and their first derivation are shown. The first derivative allows better recognition of steps in mass loss. GO exhibits a significant total loss of mass of 69.9 wt% during heating from 30 °C to 900 °C. The first step in mass loss of 7.2 wt% is at 100 °C and caused by water removal. Water was present in the hydrophilic GO sample due to interaction with functional oxygen groups. Second, the large mass loss of 41.3 wt% at around 200 °C is assigned to the removal of oxygen groups. If the mass fraction of water is subtracted from the total mass of sample, only graphite oxide is then considered. The oxygen content in graphite oxide then counts 45 wt%, which results into a C/O ratio of 2.2. Schniepp et al.<sup>[255]</sup> reported a ratio of 2.0 after similar synthesis, whereas basically GO is assumed to have a ratio between two and four.<sup>[161]</sup> The thermogravimetric curve of GO in this regime of around 200 °C consists of two inflection points at 220.0 °C and 269.8 °C as pointed out by the first derivation. This mass loss at slightly shifted temperatures around 200 °C suggests the removal of different functional groups. The further mass loss during heating up to 900 °C is 21.4 wt%. This loss does not exhibit a step but a continuous progression without inflection point and can result from amorphous thermally unstable parts inside the aromatic structure being left after the removal of oxygen groups.<sup>[162]</sup>

rGO in Figure 24a is thermally stable below 600 °C. Steps of mass loss at 100 °C and 200 °C are absent. This proves eliminated water and eliminated oxygen groups

in the rGO sample. Further heating to 900 °C results into a loss of 29.5 wt% but does not give a visible step or inflection point. This also indicates thermally unstable amorphous carbon being left after the thermal reduction of GO to rGO described in Section 4.1.2.

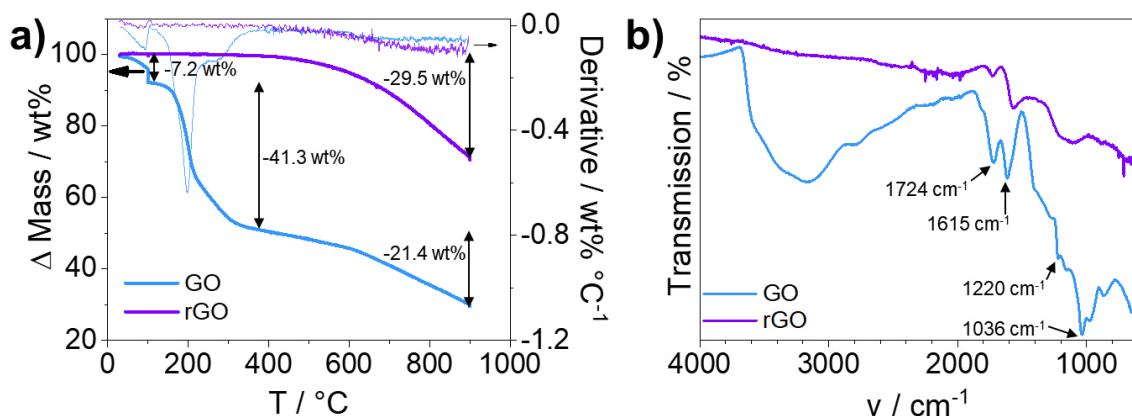


**Figure 24** TGA of GO and rGO from 30–900 °C using N<sub>2</sub> atmosphere and 10 min holding at 100 °C (a) and IR spectra of GO and rGO (b).

By means of the IR spectra in Figure 24b, functional oxygen groups within the two materials are identified. Beside the broad IR absorption band resulting from O–H stretching mode between 2600–3600 cm<sup>-1</sup>, carbonyl groups in terms of C=O stretching are detected at 1724 cm<sup>-1</sup>. The C=C stretching mode in aromatic structures occurs at 1615 cm<sup>-1</sup>. IR absorption bands of C–O stretching are visible in the range of 1220–1036 cm<sup>-1</sup>. In contrast to graphite oxide, rGO apparently possesses lower surface functionalities. TGA already revealed the absent mass loss at around 200 °C due to eliminated oxygen groups. IR spectroscopy shows that thermal reduction of GO removes next to intercalated water also any further hydroxyl groups, which would be visible between 2600–3600 cm<sup>-1</sup>. But C=O stretching at 1724 cm<sup>-1</sup> and C–O stretching at 1220 cm<sup>-1</sup> is still present in rGO.

Basically, thermal annealing of GO at temperatures between 700–1200 °C is known to completely remove hydroxyl and carboxyl groups.<sup>[161]</sup> However, epoxy, ether, ester and carbonyl groups need a thermal treatment of at least 1,200 °C to be removed.<sup>[161]</sup> Especially carbonyl groups are known to require higher temperatures of 1,730 °C for elimination from rGO.<sup>[256]</sup> In this work, thermal annealing was conducted using an oven temperature of 1,050 °C. In conclusion, the C=O stretching at 1724 cm<sup>-1</sup> is suggested to originate from carbonyl groups, whereas C–O stretching at 1220 cm<sup>-1</sup> can result from epoxy, ether and ester groups. Moreo-

ver, the thermal stability of functional oxygen groups depends not only on the group itself, but also on the binding site to the carbon surface in terms of basal planes or edges.<sup>[161]</sup>

## 5.1.2 Comparison of Carbons

Focus of this study is to use reduced graphene oxide as basic material for nanocomposite formation later. The previous section detailed the progress in synthesis of rGO. In this section, its structure and composition are compared to other types of graphitic carbons. Therefore, two materials — carbon black and multi-walled carbon nanotubes — were chosen as they are investigated more frequently in literature.<sup>[119, 134, 173]</sup> Beyond these common materials, a newly synthesized graphitic carbon from biomass was employed considering the issue of sustainability. Hydrothermal carbonization of coconut shells with further pyrolysis is described in Section 4.1.2 and provides the material HTC-C.

Figure 25 shows TEM images of rGO, C, MWCNTs and HTC-C. Coherent units of each material based on van der Waals interaction are illustrated. Due to different sizes of units TEM images are in different magnifications. rGO in Figure 25a has wrinkled sheets with diameters of around 1.5  $\mu\text{m}$ . Carbon black in Figure 25b consists of spherical particles of around 30 nm in diameter. These particles are aggregated to longish and ramified chains with a length of around 700 nm. MWCNTs in Figure 25c have highly differing diameters and lengths and are randomly intertwined to form a bundle in the order of approximately 1  $\mu\text{m}$ . According to manufacturer specification diameters are in range of 10–30 nm and lengths in the range of 5–15  $\mu\text{m}$ . The large and round aggregate of HTC-C in Figure 25d has a diameter of about 850 nm and an undefined carbonized network with visible porous structure.

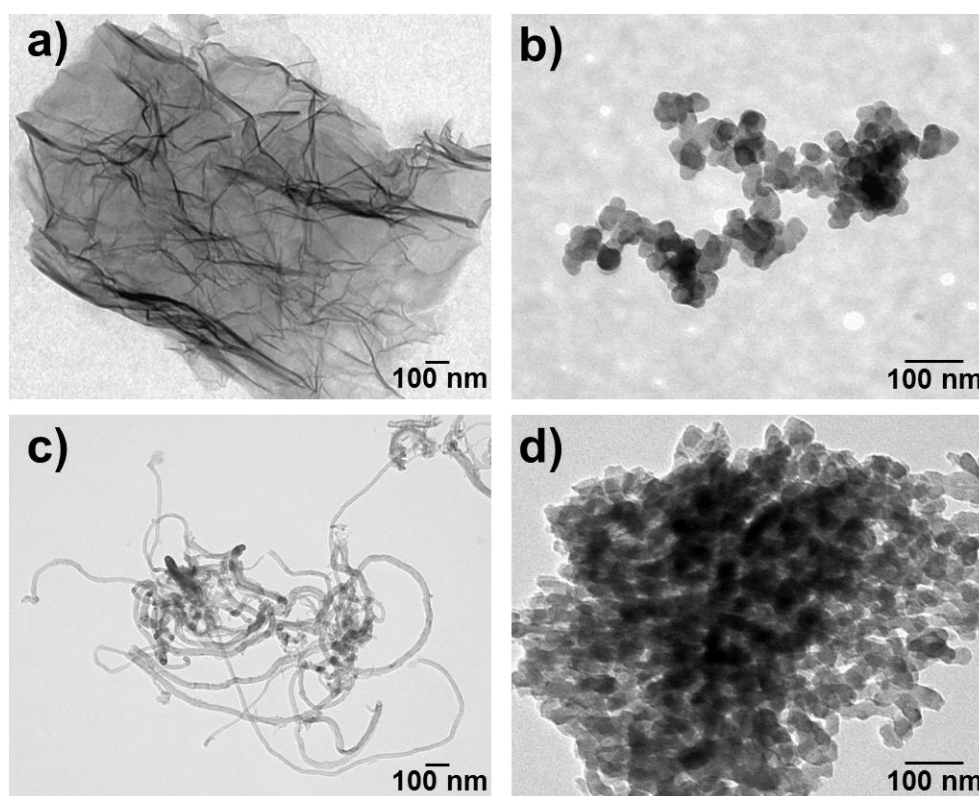


**Figure 25** TEM images of rGO (a), carbon black (b) MWCNTs (c) and HTC-C (d).

To further distinguish the porosities of each carbon, Figure 26 compares the  $N_2$  adsorption and desorption isotherms. The adsorption isotherms result in comparable curve shapes and correspond to type II of IUPAC classification.<sup>[244]</sup> This means that, first, a strong increase at relative pressures below  $p/p_0=0.05$  takes place due to first  $N_2$  physisorption and the filling of micropores. Second, a linear regime is present in the relative pressure range of approximately 0.05–0.75, which shows further  $N_2$  sorption and the coverage of larger pores. The slope in this pressure range depends on the extent of  $N_2$  multilayer formation.<sup>[244]</sup> Here, rGO has by far the highest slope of  $116 \text{ cm}^3 \text{ g}^{-1}$ , whereas the other three carbons have slopes between  $36\text{--}56 \text{ cm}^3 \text{ g}^{-1}$ . Last, the curves have a sharp increase again because of filling the macropores at high relative pressures above  $p/p_0=0.75$ . Overall, the curves reveal the predominance of micropores for C, MWCNTs and HTC-C given by porosity of the primary particles of carbon black, the carbon nanotubes and the carbon particles of HTC-C. A higher number of larger pores is proven for rGO due to the much higher slope of isotherm.

Desorption isotherms mostly overlap with the adsorption isotherms for the curves in Figure 26. However, for rGO adsorption and desorption exhibit a very pronounced hysteresis caused by capillary condensation of  $N_2$  inside the pores.<sup>[244]</sup> This hysteresis demonstrates the additional presence of mesopores with diameters between 2–50 nm.<sup>[244]</sup> HTC-C also suggests hysteresis, however, in much lower extent compared to rGO. If TEM images in Figure 25 are considered, they allow conjecturing of mesopores within the bulks of rGO and HTC-C. That means a wrinkled sheet of rGO depicted in Figure 25a could possess mesopores inside bulk aggregates of sheets. In literature, mesopores are found to be characteristic for rGO and arise from sheet kinks and wrinkles.<sup>[172]</sup> HTC-C in Figure 25d allows the presumption of mesopores in the form of voids between primary particles if scaling of the TEM image is considered. However, the microscopy in Figure 25 can only suggest pore sizes within the carbon frameworks, whereas the isotherms from nitrogen sorption in Figure 26 reveal micro-, meso- or macropores more significantly.

The specific surface areas from BET formalism are contrasted in Table 7. HTC-C has by far the highest specific surface area of  $546 \text{ m}^2 \text{ g}^{-1}$ . rGO has a lower specific surface area of  $286 \text{ m}^2 \text{ g}^{-1}$  followed by common carbon black with  $218 \text{ m}^2 \text{ g}^{-1}$ . Last, MWCNTs possess a specific surface area of  $111 \text{ m}^2 \text{ g}^{-1}$ , which is almost half of commonly used carbon black. Thus, the calculated values are in descending order of  $\text{HTC-C} > \text{rGO} > \text{C} > \text{MWCNTs}$ .

In general, porosity of the catalyst support dominates the porous network inside the catalyst layer of PEM fuel cells. The support surface area defines the Pt particle distribution generating catalytic active centers for HOR and ORR, whereas the pores of support define the reactant mass transport to these centers. Figure 2 already clarified the scale of transport and reaction processes within the PEMFC catalyst layer. This is explained on basis of common and well-studied carbon black, which was introduced in Section 3.2.4.1. Vulcan<sup>®</sup> shows particles with a size around 30 nm and with micropores (<2 nm). Van der Waals interaction between particles leads to aggregates with a size of 100–250 nm<sup>[40]</sup> and with mesopores (2–20 nm).<sup>[257]</sup> Pt nanoparticles of ~2 nm in diameter are incorporated here. Reactants diffuse inside these pores and reach platinum. The aggregates are further arranged and form meso- and macropores (>20 nm).<sup>[257]</sup> The ionomer is mainly incorporated here.

If these scales of catalytic transport and reaction processes in Figure 2 are compared to results of Figure 26, micropores and macropores much larger than 20 nm do not contribute to an increased number of catalytic active sites. Although HTC-C possesses the largest specific surface area, it contains micropores to much larger extent than the other carbons. On the contrary, rGO with the second largest specific surface area shows strongest occurrence of meso- and macropores.

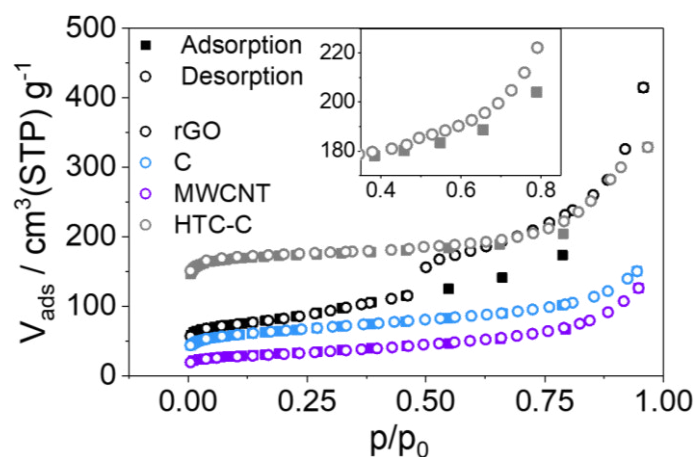


**Figure 26** BET isotherms of rGO, carbon black, MWCNTs and HTC-C.

Figure 27 contrasts the four carbon materials towards degree of graphitization by XRD as well as the degree of defects in the aromatic structures by Raman spectroscopy. X-ray diffraction at the interlayer (002) plane is depicted in Figure 27a occurring at varying angles dependent on the material. Reflections of rGO and MWCNTs appear at highly comparable angles of  $26.1^\circ$  and  $26.2^\circ$ , whereby the comparison of both signals indicates a small shoulder at lower angles in case of rGO. Because XRD is mainly dominated by the crystalline parts in materials, this small shoulder suggests more crystalline and more amorphous arrays in rGO. C shows a wide reflection centered at  $24.6^\circ$ , while in case of HTC-C also a wide reflection is detected at  $23.6^\circ$ . This indicates more amorphous parts in C and HTC-C than in rGO and MWCNTs.

Table 7 contains the interlayer distances  $d$  as well as the crystallite sizes  $L$  using the (002) reflections of Figure 27a. In accordance with the diffraction angles  $2\theta$ , the interlayer distances  $d$  of rGO and of MWCNTs are 0.341 nm and 0.340 nm and thus highly comparable. A greater layer distance of 0.362 nm is present in carbon black followed by HTC-C counting 0.377 nm. In consequence, the interlayer distances rise in the ascending order of rGO and MWCNTs with comparable distances followed by C and last HTC-C. Regarding the crystallinity, rGO and MWCNTs have crystallite sizes of 5.0 nm and 5.5 nm, whereas carbon black has a size of 1.4 nm and HTC-C of 1.0 nm. Both parameters  $d$  and  $L$  evince the significant lower degree of graphitization in case of carbon black and carbon derived from HTC compared to rGO and MWCNTs, which is according to more amorphous structures.<sup>[230]</sup> Carbon black is known for its problematic corrosion in FC application due to the amorphousness.<sup>[119, 131]</sup> MWCNTs for example with larger crystallinity were shown to have higher electrochemical stability,<sup>[104, 173]</sup> which is consistent to XRD findings here.

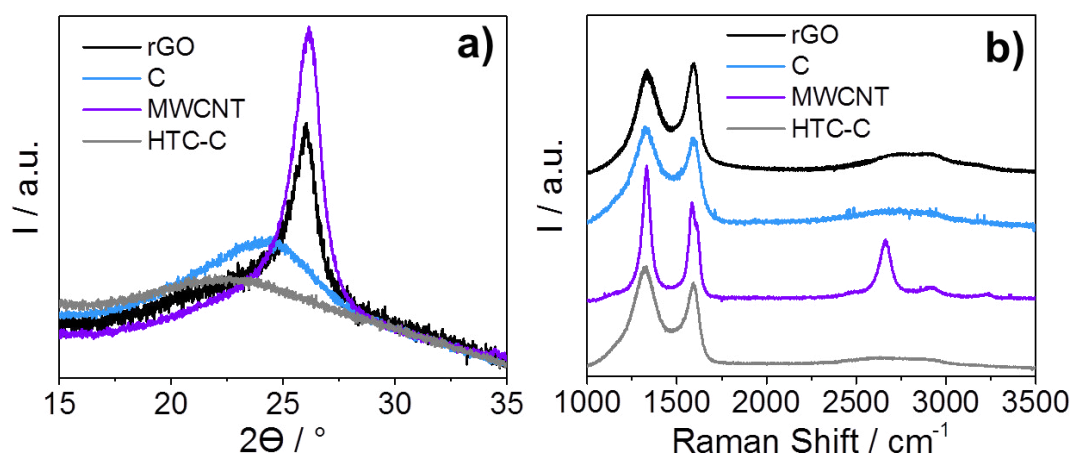


**Figure 27** XRD (a) and Raman (b) of rGO, C, MWCNTs and HTC-C.

Raman spectra are depicted in Figure 27b, whereby Table 7 refers to G band positions as well as  $I_D/I_G$ . The Raman bands for MWCNTs are the narrowest and most defined compared to the other materials. This spectrum is most similar to the results of graphite in Figure 23, which could be ascribed to highly concentric ordered cylindrical graphene layers in MWCNTs. Furthermore, the D band intensity of MWCNTs is much higher than the G band intensity, so that carbon nanotubes show the highest  $I_D/I_G$  ratio of 1.40 compared to the other carbons. Further  $I_D/I_G$  are in descending order of 1.21 for HTC-C, followed by 1.15 for C and last 0.96 in case of rGO. It should be noted that  $I_D/I_G$  for MWCNTs is one third higher

than that for rGO, although both materials have similar interlayer distances and crystallite size as revealed by XRD. Hence, interlayer arrangement of rGO and MWCNTs is comparable, whereas the basal layers have different defect densities of aromatic structures. Regarding the other carbons C and HTC-C, high comparability of graphitization from XRD and of structural defects from Raman is evinced. So, C and HTC-C have the most comparable interlayer and intralayer properties.

The G band position of rGO counts  $1598\text{ cm}^{-1}$  and thus occurs at the highest Raman shift in comparison with the other materials. G band positions are  $1593\text{ cm}^{-1}$  for HTC-C,  $1584\text{ cm}^{-1}$  for C and  $1583\text{ cm}^{-1}$  in case of MWCNTs. These differences illustrate the most exfoliated graphene layers for rGO in contrast to C and MWCNTs leading to its two-dimensional sheets. HTC-C shows a G band position very close to rGO, so that graphene layers in HTC-C are apparently more uncoupled than layers in C and MWCNTs. Uncoupling of layers might hinder the interlayer transfer of electrons and thus the electrical conductivity of materials. But it might strengthen the support interaction with Pt nanoparticles, since electron-rich carbon sites onto basal planes can cause electronic interaction with platinum.

**Table 7** Summarized physical parameters for rGO, C, MWCNTs and HTC-C.<sup>[230]</sup>

Method	Parameter	rGO	C	MWCNTs	HTC-C
BET	Spec. Surface Area / $\text{m}^2\text{ g}^{-1}$	286	218	111	546
XRD	$2\theta / ^\circ$	26.1	24.6	26.2	23.6
	$d / \text{nm}$	0.341	0.362	0.340	0.377
	$FWHM / ^\circ$	1.6	5.8	1.5	8.3
	$L / \text{nm}$	5.0	1.4	5.5	1.0
Raman	G Position / $\text{cm}^{-1}$	1598	1584	1583	1593
	$I_D/I_G$	0.96	1.15	1.40	1.21
4-point	Sheet Resistance / $\text{m}\Omega/\square$	$16\pm 2$	$10\pm 2$	$2\pm 1$	$22\pm 2$
XPS	C/O Ratio	10	24	24	49

Moreover, the electrical conductivity is an important issue for Pt supports in fuel cell application. Table 7 shows the sheet resistances measured by four-point probe method and reveals that electrical conductivities of the carbons are in the reversed order of their specific surface areas from BET. This highlights the contrary effect of electron conductance and surface area as described in literature.<sup>[133, 137]</sup> Basically, the transfer of electrons in carbon supports is affected by intraparticle transfer between graphene layers as well as by interparticle transfer through the agglomerates. In this work, XRD and Raman served for investigation of intraparticle properties, whereas interparticle properties are evaluated by TEM images and BET.

The lowest sheet resistance of  $2 \pm 1 \text{ m}\Omega/\square$  was measured for MWCNTs, which is consistent with the highest graphitic degree and the lowest surface area allowing electron transfer through densely arranged graphene layers and tubes. Carbon black possesses the second lowest resistance of  $10 \pm 2 \text{ m}\Omega/\square$ , although XRD and Raman revealed its amorphous structure with low graphitization of particles. However, their high aggregation seen by TEM leads to a high contact surface and small pores revealed by BET, which promotes the electron transfer. The resistance of rGO counts  $16 \pm 2 \text{ m}\Omega/\square$  and is a result of large sheets decoupled from the others proven by Raman and TEM with the largest pores in comparison revealed by BET, so that intersheet barriers for electron transfer might play a role. HTC-C possesses the highest resistance of  $22 \pm 2 \text{ m}\Omega/\square$ . XRD and Raman revealed its amorphous structure with low graphitization and higher decoupling of layers than MWCNTs and C. Furthermore, the interparticle properties are given by an undefined carbonized network under TEM with largest surface area and larger pores than MWCNTs and C as shown by BET. Thus, combination of intra- and interparticle properties is the reason for the lowest electrical conductance in case of HTC-C.

Characteristics of defect sites in terms of functional surface groups are investigated by TGA and XPS. Thermogravimetric curves are displayed in Figure 28. rGO and MWCNTs present very similar thermal properties and are stable to a temperature of at least 400 °C. After that, mass losses of around 30 wt% are detected during the temperature increase to 900 °C in both cases. C and HTC-C show the onsets of mass loss at around 600 °C. Carbon black lost 3.2 wt% and HTC-C lost 9.9 wt%, so that higher thermal stabilities are obtained for C and HTC-C compared to rGO and MWCNTs. The difference in thermal stability can be explained by synthesis conditions. HTC-C and rGO are self-synthesized as described in Section 4.1.2, whereby detailed manufacturing of purchased MWCNTs and C are unknown. Carbon black exhibits the lowest mass loss in Figure 28 and is usually produced at temperatures of 1,400–1,700 °C.<sup>[142]</sup> HTC-C was synthesized and annealed at lower temperature of 1,100 °C for 2 h and shows the second lowest mass loss. Higher losses are observed for rGO and MWCNTs, whereas rGO was synthesized at 1,050 °C for only 30 s. MWCNTs are usually produced at a temperature between 500–1,200 °C.<sup>[174, 175]</sup> Furthermore, mass losses at around 200 °C are absent for the four carbons, so that any larger hydroxy and carboxylic groups like for graphite oxide in Figure 24a are excluded.

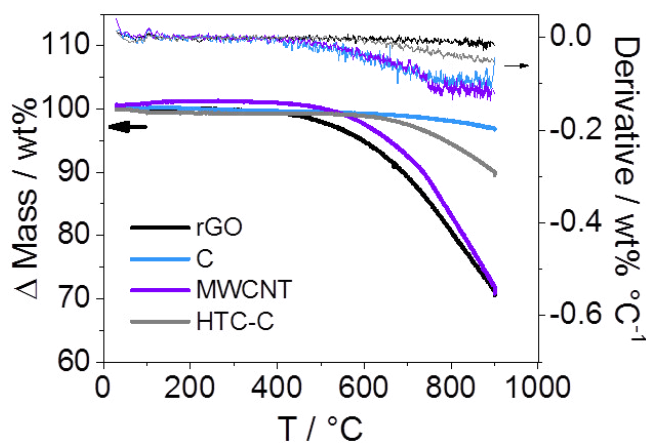


**Figure 28** TGA of rGO, C, MWCNTs and HTC-C from 30–900 °C using N<sub>2</sub> atmosphere and 10 min holding at 100 °C.

X-ray photoelectron survey spectra are depicted in Figure 29 showing the main elemental composition of the different carbon materials, which is carbon and oxygen. XPS reveals small sodium traces in case of rGO as well as small molybdenum traces in case of MWCNTs, suggested to originate from the syntheses. To clarify differences in the carbon materials, C1s and O1s signals from survey scans are integrated and divided. Table 7 lists the C/O ratios for each material. rGO has a C/O ratio of 10 and hence exhibits an oxygen content of 10 at%, which is comparable to 9.3 at% obtained by Schniepp et al.<sup>[255]</sup> Thermal reduction of GO in other literature gave a C/O ratio of 11 after treatment at 1,000 °C in argon<sup>[258]</sup> and a C/O ratio of 12 after treatment at 1,000 °C in vacuum.<sup>[259]</sup> Carbon black and MWCNTs have a ratio of 24, respectively. By far the lowest oxygen content was measured for HTC-C with a highest C/O ratio of 49. This is supposed to be a result of pyrolyzing the HTC coal in an Ar/H<sub>2</sub>-atmosphere.

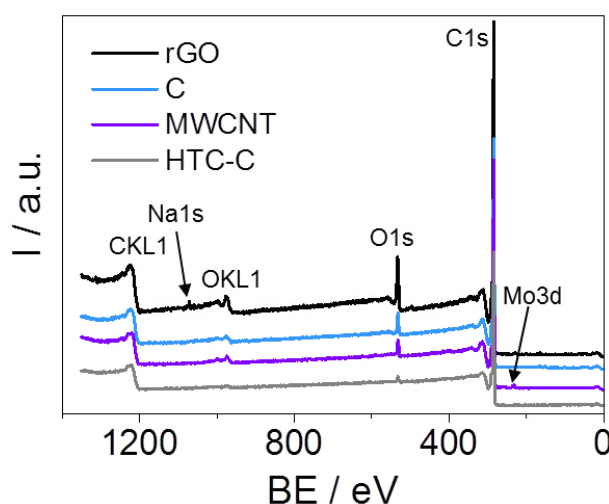


**Figure 29** XP survey spectra of rGO, C, MWCNTs and HTC-C.

Figure 30a displays the analysis of C1s spectra. The materials contain  $\pi$ -bonded carbon atoms embedded in the aromatic structures at a binding energy of  $284.4 \pm 0.2$  eV and  $\sigma$ -bonded carbon in terms of C-C or C-H at a binding energy of  $284.8 \pm 0.1$  eV. Carbon which is  $sp^3$ -hybridized usually occurs at 284.8 eV, whereas  $sp^2$ -carbon is expected at slight lower binding energies: 284.4 eV for N-doped rGO and 284.3 eV for rGO and CNTs, respectively.<sup>[160, 260]</sup> So, literature values are comparable to binding energies in Figure 30a. The  $sp^2$ -signals show much higher intensity than the  $sp^3$ -signals in all cases, so that electrical conductivity of each material was measured as discussed before. XPS qualitatively evinces the presence of defective aromatic structures in each of these graphitic carbons, which

is compliant with Raman spectra in Figure 27b. D bands in Raman spectra arise on one hand from  $sp^3$ -carbon and on other hand from further distortion of aromatic  $sp^2$ -rings due to defective rings or functional groups, so that  $I_D/I_G$ -ratios are not directly related to amounts of  $sp^2$ - and  $sp^3$ -carbon.<sup>[239]</sup> At much higher binding energies of  $290.3\pm 0.1$  eV a broad and low intensity signal occurs in Figure 30a.  $\pi$ -electron shake-up relaxation after emission of photoelectrons leads to detection of this satellite peak for graphitic and graphene-based carbons.<sup>[160, 261]</sup>

Moreover, carbon-oxygen bonds are detected in Figure 30a. First, C-O with  $\sigma$ -bonding is located at  $285.9\pm 0.1$  eV including epoxy, ether, ester or hydroxyl groups.<sup>[45]</sup> Second, C=O with  $\pi$ -bonding leads to a peak at  $287.9\pm 0.2$  eV originated from carbonyl groups.<sup>[45]</sup> Because TGA curves did not contain a mass loss at  $200$  °C in Figure 28, the presence of hydroxy and carboxyl groups is not expected inside the carbons. Hence, C-O and C=O signals in XPS must come from epoxy, ether, ester or carbonyl groups.<sup>[161]</sup> C1s of C, MWCNTs and HTC-C shows significantly lower carbon-oxygen intensities than the spectrum of rGO, whose C1s signal exhibits a more distinct shoulder at lower binding energies. C-O and C=O functionalities in rGO have already been visible in IR spectroscopy in Figure 24b. Jung et al.<sup>[262]</sup> compared rGO and C in XPS and also reported lower C-O and C=O contributions to C1s for carbon black compared to rGO. C=O groups bonded to aromatic carbons can have a quinone-similar structure, which would show HQ/Q redox activity during voltammetry experiments in Section 5.3. With respect to stability issues, these oxygen groups present intermediates in progress of carbon corrosion and can further be electrochemically oxidized to form  $CO_2$ , elucidated in Section 3.2.3.2.

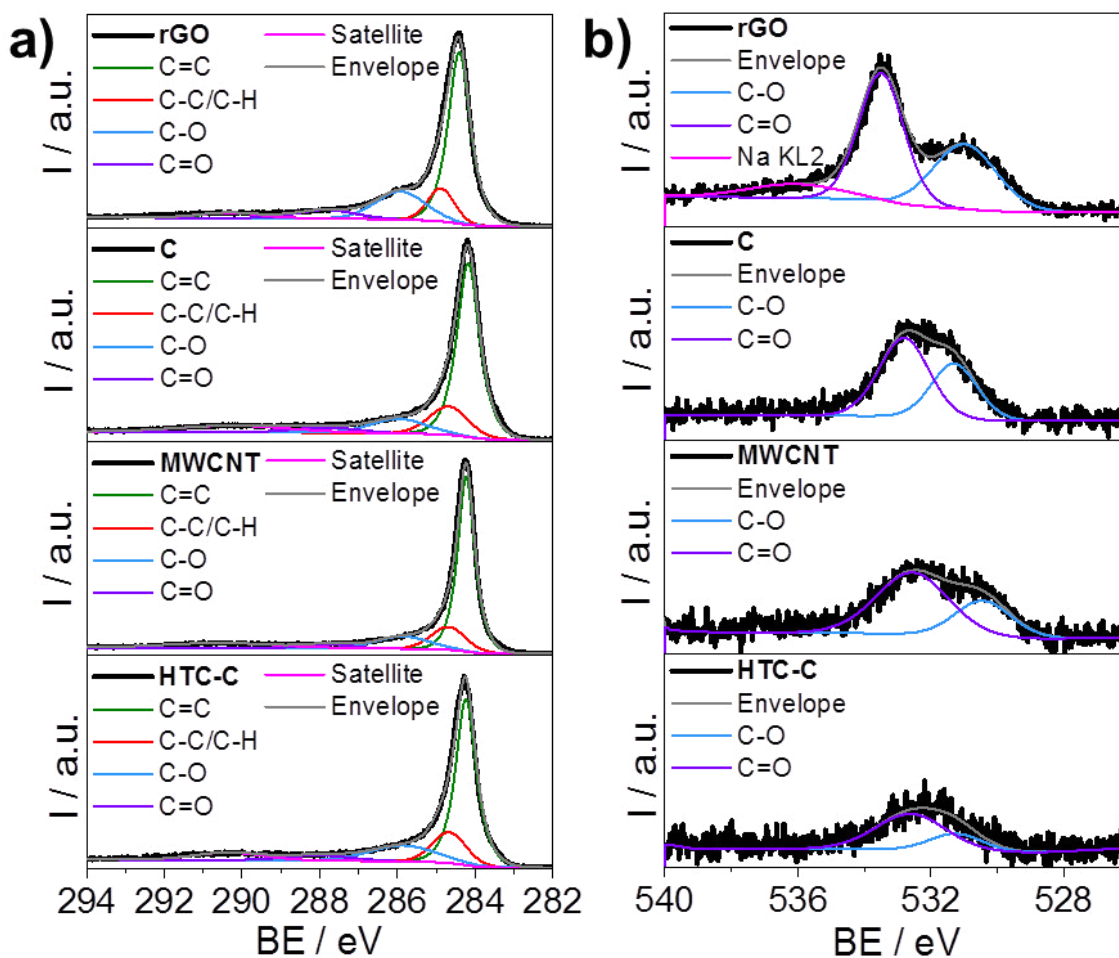


**Figure 30** XP spectra of rGO, C, MWCNTs and HTC-C. C1s high resolution spectra (a) and O1s high resolution spectra (b).

O1s spectra are shown in Figure 30b. C-O bonds are detected at  $531.0 \pm 0.4$  eV with lower intensity than C=O bonds detected at  $532.9 \pm 0.5$  eV. This demonstrates that carbonylic C=O groups are more present on the carbon surfaces than C-O groups in the form of epoxy, ether or ester. With respect to rGO, a further broad signal appears at 536.1 eV due to Auger electrons from sodium traces.<sup>[263]</sup> Moreover, the carbon-oxygen signals are more defined and separated in rGO than the signals with lower intensities in C, MWCNTs and HTC-C.

Overall, carbonyl and C-O functionalities in terms of epoxy, ether or ester groups are expected to be retained in rGO with a C/O ratio of 10,<sup>[161]</sup> whereas C, MWCNTs and HTC-C contain much lower surface functionalities.

To summarize the physical characterization of carbon supports, their morphologies are different as proven by TEM and consist of 2D sheets, spherical nanoparticles, tubes or a porous aggregate with an undefined carbon network in case of rGO, C, MWCNTs and HTC-C, respectively. The surface area was the highest for HTC-C and the lowest for MWCNTs. On the contrary, the degree of graphitization and electrical conductivity was the lowest for HTC-C and the highest for MWCNTs. With respect to defect sites, Raman showed the highest degree of defects in case of MWCNTs and the lowest degree for rGO. XPS evidenced the largest surface oxygen content in case of rGO with a C/O ratio of 10. These functional oxygen groups of rGO benefit to the metal oxide and Pt nanoparticle anchoring later. In conclusion, the most contrary materials in structure and composition are MWCNTs with highly ordered and rolled-up graphene layers on one hand and HTC-C with the most amorphous structure on other hand. Carbon structures are finally summarized by drawing:

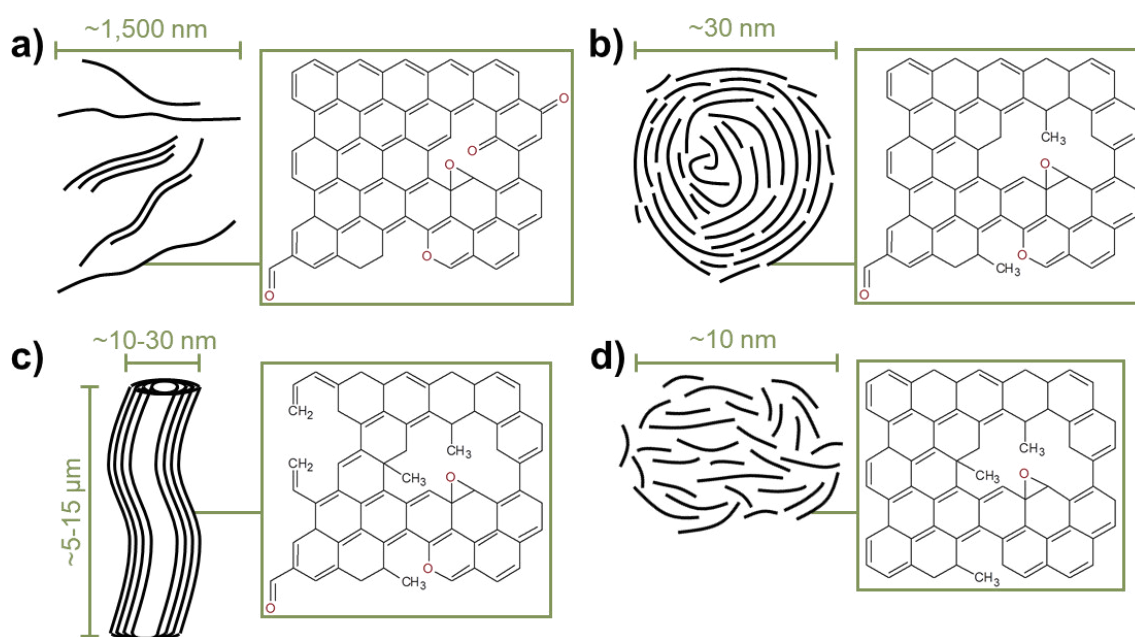


**Figure 31** Scheme of the proposed carbon structures:  
Reduced graphene oxide (a), carbon black (b), MWCNT (c) and HTC-C (d).

### 5.1.3 Nanocomposites of Reduced Graphene Oxide with Doped Metal Oxides

Section 5.1.2 showed structure and composition of the carbon materials, whereas this section concentrates on investigation of the composite materials. Two types of doped metal oxides, Sn-doped indium (III) oxide (ITO) nanoparticles and F-doped tin (IV) oxide (FTO) nanoparticles were precipitated on rGO.

First, SEM and TEM are used to analyze their morphology and microstructure. SEM in Figure 32a reveals that the porous microstructure of ITO-rGO is still given by the aggregated rGO sheets, if the image of rGO in Figure 20b is compared. Additionally, SEM illustrates particles incorporated into the porous structure of rGO. These particles being visible under SEM are further investigated by TEM in Figure 32b. In some parts of ITO-rGO larger crystals are located at the edges of rGO sheets and must arise from the solvothermal crystallization. These crystals are identified as ITO, since high resolution TEM evidences an atomic lattice distance of 0.28 nm. This distance correlates to the (222) plane of indium (III) oxide with bixbyite crystal structure (ICSD, 00-001-0929).

Beside the larger ITO crystals, Figure 32c–d show the distribution of smaller ITO nanoparticles onto the rGO surface in two different magnifications. In some areas the ITO nanoparticles exist as separate single particles anchored on the surface (circle in Figure 32c marked with 1), and in other parts the nanoparticles are present in the form of aggregates (circle in Figure 32c marked with 2). The ITO particle size distribution is depicted in Figure 32e. A Gaussian size distribution shows an average ITO size of  $7.1 \pm 1.9$  nm.<sup>[230]</sup> By use of HR-TEM in Figure 32f, atomic lattices of these nanoparticles become visible. A measured distance of 0.29 nm corresponds to the distance measured for the larger crystals and illustrates the (222) plane of indium (III) oxide. Further analysis of crystallinity is done below by means of XRD.<sup>[230]</sup>

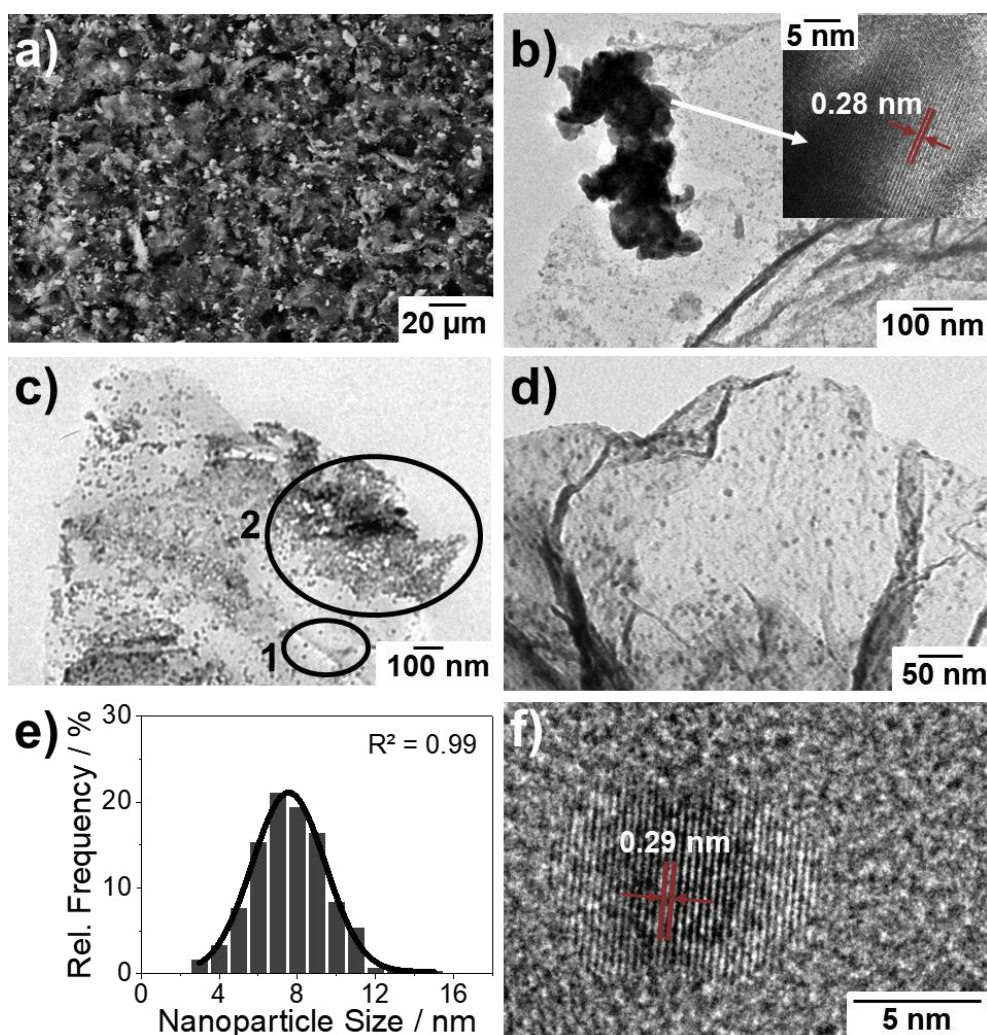


**Figure 32** Electron microscopy of ITO-rGO: SEM image (a), TEM and HR-TEM of larger ITO crystals at rGO edges (b), TEM images of distributed ITO nanoparticles on rGO (c, d), ITO nanoparticle size distribution (e) and atomic lattice distances of ITO at rGO surface (f).

Electron microscopic analysis of the other nanocomposite FTO-rGO is depicted in Figure 33. First, the SEM image in Figure 33a shows FTO particles incorporated into porous structure given by rGO. TEM images in Figure 33b-c evince the absence of larger crystals and instead distribution of FTO nanoparticles on reduced graphene oxide in two different TEM magnifications. Similar to ITO-rGO this composite also contains metal oxide particles appearing as aggregates in some parts of the rGO surface. Size analysis in Figure 33d shows smaller particles in case of FTO compared to ITO, while the Gaussian curve gives a FTO size of  $2.8 \pm 0.9$  nm.<sup>[231]</sup> The FTO particles are seen to form aggregates onto the carbon surface, which was observed for FTO after similar synthesis in other works as

well.<sup>[216, 235]</sup> Additionally, atomic lattices are observed via HR-TEM in Figure 33e. The marked distances are determined to be 0.35 nm, which is associated with the (110) plane in tin (IV) oxide (ICSD, 98-000-9163). Further analysis of crystallinity is carried out below using XRD.<sup>[231]</sup>

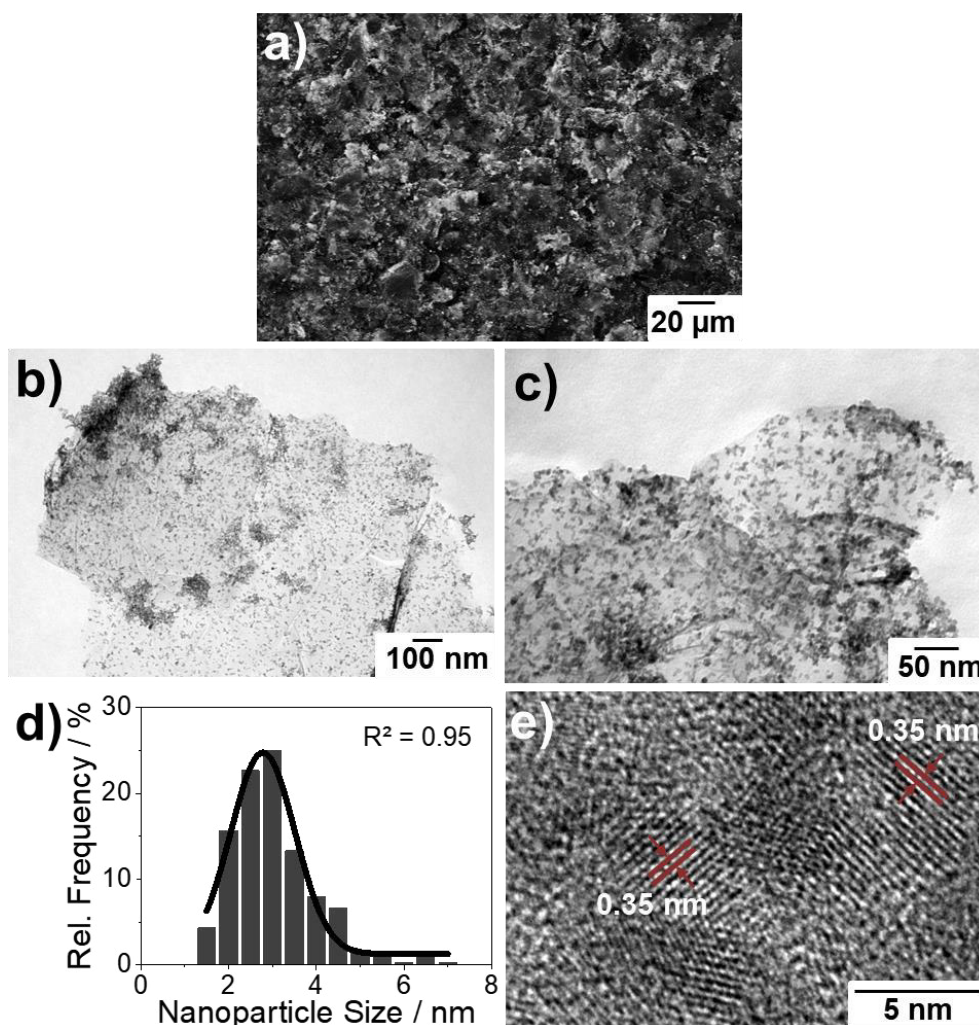


**Figure 33** Electron microscopy of FTO-rGO: SEM image (a), TEM images of distributed FTO nanoparticles on rGO (b, c), FTO nanoparticle size distribution (d) and atomic lattice distances of FTO (e).

Specific surface areas from  $N_2$  adsorption (BET formalism) are determined to further investigate the nanocomposite morphologies. Table 8 reports  $69 \text{ m}^2 \text{ g}^{-1}$  for ITO-rGO and  $110 \text{ m}^2 \text{ g}^{-1}$  for FTO-rGO. Because the initial area of rGO was  $286 \text{ m}^2 \text{ g}^{-1}$ , the deposition of metal oxides leads to reduction of the surface area for both composites. Nanoparticles of metal oxides often show lower specific surface areas in contrast to carbon blacks or graphene-based materials due to larger density.<sup>[197, 264]</sup> Furthermore, since nanoparticles are known to precipitate at defect sites

of carbons,<sup>[49]</sup> pores of rGO might be blocked by metal oxides. Kou et al.<sup>[217]</sup> prepared ITO particles with a size of approximately 10 nm and deposited them in different amounts on reduced graphene oxide. They observed a shrinking specific surface area by increasing the ITO content.

Figure 34 shows the XRD pattern of the composites. ITO-rGO in Figure 34a shows high agreement with the typical pattern of indium (III) oxide having the structure of the bixbyite mineral (ICSD, 00-001-0929). The (222) plane at  $30.9^\circ$  gives the reflection with highest intensity and was also visible under HR-TEM before. The FTO-rGO pattern in Figure 34b is referred to tin (IV) oxide showing the crystal structure of cassiterite mineral (ICSD, 98-000-9163). The (110) plane with strongest reflection at  $26.2^\circ$  was observed using HR-TEM before. A closer view on the position of reflections in both graphs indicates slight shifts to lower  $2\theta$  values compared to the references. This negative shift was also reported in other studies for ITO<sup>[202, 265, 266]</sup> and FTO nanoparticles<sup>[203]</sup> and is attributed to slight lattice expansion caused by the metal oxide doping. Although the ionic radii of the doping atoms are smaller than the substituted atoms ( $\text{Sn}^{4+}$  replaces  $\text{In}^{3+}$  inside  $\text{In}_2\text{O}_3$ ;  $\text{F}^-$  replaces  $\text{O}^{2-}$  inside  $\text{SnO}_2$ ), the lattice is distorted to form slightly enlarged atomic distances. This is ascribed to repulsive forces between the atoms due to their different charges.<sup>[202, 266]</sup>

Reflections of ITO-rGO are more intense than reflections of FTO-rGO, so that larger ITO than FTO crystallites are expected from XRD. Table 8 lists the FWHM and the crystallite sizes. The high incidence of reflections for both metal oxides allows the calculation of values through considering the three reflections with highest intensity — (222), (400) and (440) for ITO-rGO and (110), (011) and (121) for FTO-rGO. The ITO particles show a size of  $22.5 \pm 1.5$  nm<sup>[230]</sup>, whereas FTO particles have a size of  $5.1 \pm 0.4$  nm.<sup>[231]</sup> XRD analysis gives for both metal oxides larger sizes than the values obtained by TEM as seen in Table 8. The Scherrer Equation [18] includes assumptions e.g. the form factor, while TEM is limited to the degree of contrast and to the two-dimensional depiction of materials. In consequence, both methods of particle size determination are considered in this study because of these uncertainties.

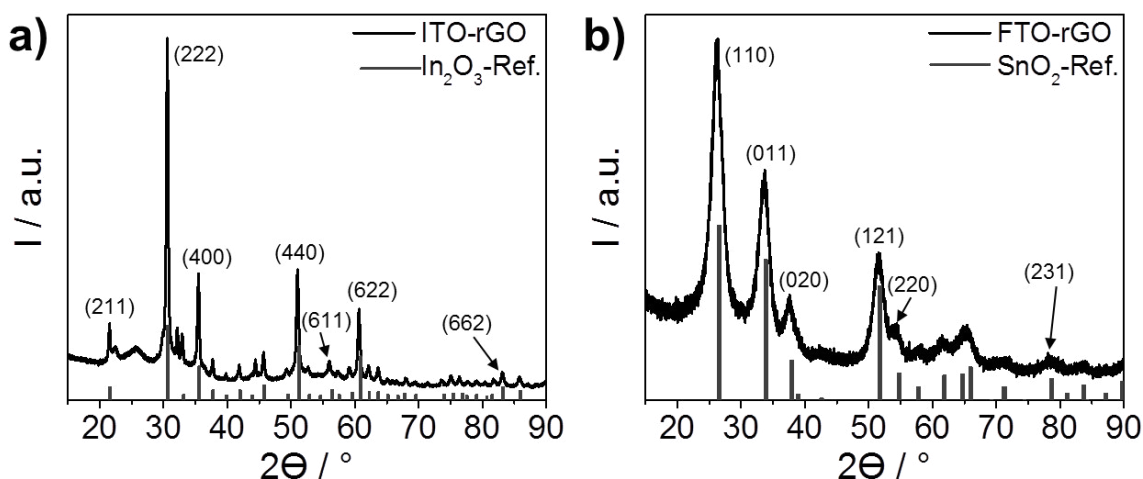


**Figure 34** XRD of ITO-rGO with ICSD reference pattern 00-001-0929 (a) and FTO-rGO with ICSD reference pattern 98-000-9163 (b).<sup>[230, 231]</sup>

Table 8 further includes the electrical conductivities. Before metal oxide precipitation, rGO had a sheet resistance of  $16 \pm 2 \text{ m}\Omega/\square$ . The resistance of ITO-rGO is  $23 \pm 2 \text{ m}\Omega/\square$  and of FTO-rGO  $18 \pm 3 \text{ m}\Omega/\square$ , so that electrical resistances are increased due to incorporation of metal oxide nanoparticles into the rGO structure. While the electrical conductance of graphitic carbons is given by delocalized  $\pi$ -electrons, conductivity of metal oxides is restricted to delocalized electrons from doping with foreign atoms as previously discussed in Section 3.2.4.2. Therefore nanostructured metal oxides often show lower conductivity than graphitic carbons.<sup>[267]</sup> Moreover, the mobility of electrons depends on the particle size. Smaller particles can have more charge transfer barriers so that metal oxides in the form of nanoparticles in this work can affect the electrical conductivity.<sup>[268]</sup>

**Table 8** Summarized physical parameters for ITO-rGO and FTO-rGO.<sup>[230, 231]</sup>

Method	Parameter	ITO-rGO	FTO-rGO
TEM	Nanoparticle Size / nm	$7.1 \pm 1.9$	$2.8 \pm 0.9$
BET	Spec. Surface Area / $\text{m}^2 \text{g}^{-1}$	69	110
XRD	$FWHM / ^\circ$	$0.4 \pm 0.04$	$1.6 \pm 0.10$
	$L / \text{nm}$	$22.5 \pm 1.5$	$5.1 \pm 0.4$
4-point	Sheet Resistance / $\text{m}\Omega/\square$	$23 \pm 2$	$18 \pm 3$
XPS	Doping Level / at%	32	8

Last, XPS is carried out to measure the elemental composition of the two materials and to determine the doping levels of metal oxides. Figure 35a–c show the spectroscopic scans for ITO–rGO. The survey scan in Figure 35a verifies the presence of C, O, In and Sn atoms. In3d and Sn3d scans in Figure 35b–c assess the chemical states of indium and tin, respectively. Because the In3d doublet is located at 445.2 eV for In3d<sub>5/2</sub> and at 452.8 eV for In3d<sub>3/2</sub>, the presence of indium in a trivalent oxidation state is proven. The Sn3d doublet occurs at 487.1 eV for Sn3d<sub>5/2</sub> and at 495.6 eV for Sn3d<sub>3/2</sub>, so that tin is shown to be in a tetravalent oxidation state. These values for ITO nanoparticles are in good agreement with literature data.<sup>[205, 209, 264]</sup> The doping level of ITO is calculated by the substance amount fraction of Sn in relation to In<sub>2</sub>O<sub>3</sub> and counts 32 at%. The XRD in Figure 34 proved the In<sub>2</sub>O<sub>3</sub> crystallinity, so that Sn is completely incorporated as a dopant into the In<sub>2</sub>O<sub>3</sub> lattice.

Figure 35d–f depicts the X-ray photoelectron spectra of FTO–rGO in the same way. The survey scan evinces the presence of C, O, Sn and F atoms. The doping level is determined by the substance amount fraction of F related to SnO<sub>2</sub> and counts 8 at%. XRD in Figure 34 shows SnO<sub>2</sub> crystallinity, so that F atoms are incorporated into the SnO<sub>2</sub> nanoparticles. In Figure 35e the Sn3d doublet appears at a binding energy of 487.4 eV for Sn3d<sub>5/2</sub> and at 495.8 eV for Sn3d<sub>3/2</sub>, which is assigned to the oxidation state IV and is in accordance with literature values for FTO.<sup>[203, 269]</sup> The comparison of Sn3d scans in Figure 35c for ITO–rGO and in Figure 35e for FTO–rGO reveals a slight shift to higher binding energies for FTO — 0.3 eV for Sn3d<sub>5/2</sub> and 0.2 eV for Sn3d<sub>3/2</sub>. This can be related to the partial bonding of Sn to the most electronegative fluorine, which is incorporated into the SnO<sub>2</sub> crystals. Wang et al.<sup>[269]</sup> also reported a shift to higher binding energies in FTO compared to the undoped material. The positive shift in case of 30 at% and 50 at% doped FTO was much higher than the shift of 8 at% FTO here, respectively. However, the shift for 10 at% doped FTO nanoparticles was of around 0.3 eV and thus most similar to the FTO here due to the most comparable doping level. Figure 35f shows the F1s scan with the centered peak at 684.9 eV. The peak position at this binding energy verifies the F bonding to metals, which means the bonding to tin atoms in this case. FTO nanoparticles in literature showed F1s at a comparable binding energy of 684.8 eV.<sup>[235]</sup>

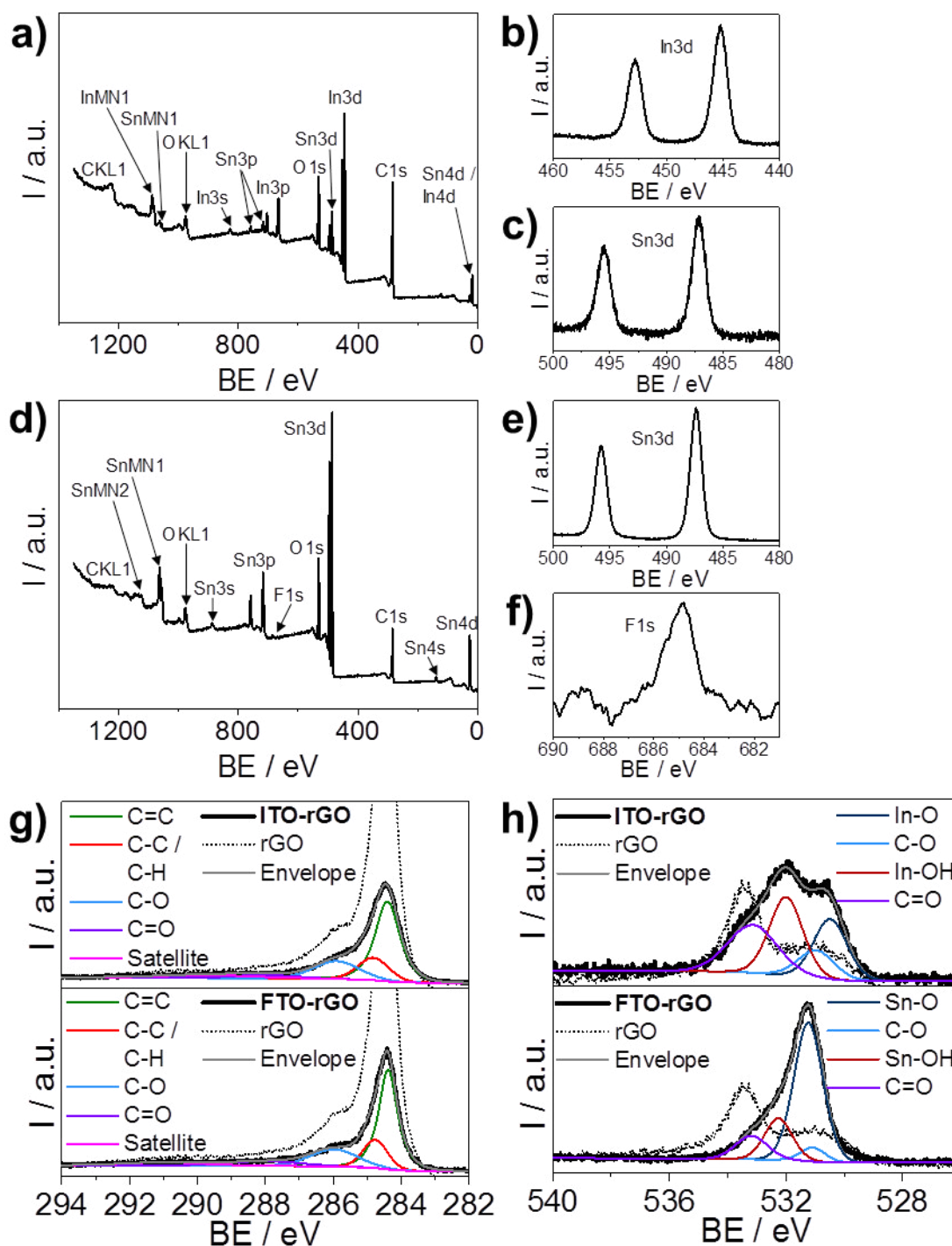


**Figure 35** XPS of ITO-rGO and FTO-rGO nanocomposites. Survey scan (a), In3d (b) and Sn3d (c) scans of ITO-rGO; Survey scan (d), Sn3d (e) and F1s (f) scans of FTO-rGO; C1s (g) and O1s (h) spectra of both nanocomposites (solid lines) and of pristine rGO (dashed lines).<sup>[231]</sup>

C1s as well as O1s scans are analyzed in Figure 35 as well and are compared to pristine rGO in dashed lines. C1s spectra of ITO-rGO and FTO-rGO in Figure 35g evidence the high comparability to the spectrum of pristine rGO in peak shape and position. This shows that the carbon in the nanocomposites is originated from rGO. The C1s peak contributions of C=C, C-C/C-H, C-O, C=O and also  $\pi$ -electron satellite are closely related to rGO in Figure 30 before. By set of same parameters for XPS measurement, the C1s of ITO-rGO and FTO-rGO have much lower intensity than that of rGO. This shows that the metal oxide particles are deposited onto the surface of rGO, so that the detected surface fraction of carbon in case of the nanocomposites is lower compared to pure rGO.

O1s analysis is contrasted in Figure 35h. Differences towards the peak shape of pristine rGO and the shapes of the composite materials are visible. This is due to strong overlap of C-O and C=O contributions with the metal-oxygen contributions for the composites, which consequences a complex O1s evaluation. C-O is located at  $531.1 \pm 0.1$  eV with lower intensity than C=O located at  $533.1 \pm 0.1$  eV in the spectra for ITO and FTO composite. These peak locations are highly comparable to O1s of the carbons in Figure 30. However, main O1s contribution in ITO-rGO originates from In-O at 530.5 eV and In-OH at 532.0 eV as related to literature.<sup>[270]</sup> Also deficient oxygen as part of ITO and caused by doping with foreign Sn atoms might shift towards higher binding energies due to electron donation to the vacancies.<sup>[264]</sup>

The main contributions to O1s in FTO-rGO are positioned at 531.2 eV for Sn-O and 532.3 eV for Sn-OH. Although binding energies of Sn-O and In-O should be comparable,<sup>[270]</sup> the Sn-O is shifted by 0.7 eV to higher values. This is due to SnO<sub>2</sub> doping with electronegative fluorine as studied by Wang et al.<sup>[269]</sup> for various FTO doping levels. For FTO nanoparticles in literature, Sn-O is reported at 530.8 eV and Sn-OH at 532.0 eV.<sup>[203]</sup>

If the C–O and C=O contributions in Figure 35h are related to the metal–oxygen contributions within both materials, C–O and C=O in FTO–rGO are negligible compared to Sn–O and Sn–OH. This demonstrates that the larger part of the composite surface is given by FTO, which is in accordance with a highly covered carbon surface by FTO particles being visible via TEM in Figure 33. However, the O1s peak of ITO–rGO has a much more pronounced left shoulder, which is due to the C=O bonding originated from rGO. In consequence, ITO–rGO has a more vacant carbon surface. A direct explanation is given by ITO microcrystals located at edges of rGO sheets, which were illustrated in Figure 32b. Presence of these larger ITO particles next to the nanoparticles causes a lower ITO surface and in consequence a less covered carbon surface.

To sum up the physical analysis, ITO exists as nano- and microparticles on the surface of rGO and shows bixbyite crystallinity of  $\text{In}_2\text{O}_3$  with Sn as dopant. Furthermore, FTO exists as nanoparticles smaller than the ITO particles and consist of  $\text{SnO}_2$  with cassiterite crystallinity and F atoms as dopant. Both metal oxides contain surface oxides and hydroxides. Last, FTO leads to a higher coverage of the rGO surface than ITO.

## 5.2 Physical Characterization of Platinum on Supports

After investigation of the support materials on their morphology and composition, Pt nanoparticles were deposited on each material. Size, structure and content of Pt on the supports are analyzed via TEM, XRD and ICP–MS and presented in Section 5.2.1. Next to six self-prepared catalysts, a commercial Pt/C is investigated in the same way. With respect to ITO–rGO and FTO–rGO, the location of Pt particles on the composites is further thoroughly examined in Section 5.2.2. Sub-nanometer interfaces between Pt, metal oxide and rGO are discussed with HR–TEM. Elemental distribution of Pt on the composites is studied using EDS.

### 5.2.1 Analysis of Pt Nanoparticles

First, TEM serves for the visualization of Pt nanoparticle size and distribution on supports. Figure 36 compares the TEM images of platinum on carbon materials. The images show well-distributed platinum in the form of spherical particles for each case. Pt/rGO in Figure 36a contains distributed Pt particles anchored on basal plane and edges of rGO. Especially at the wrinkles of rGO (marked with arrow) platinum is deposited in higher concentrations. Pt/C in Figure 36b also contains Pt particles uniformly distributed on the support surface. In small areas some particles are coalescent (marked with arrow). Same observation is done for Pt/MWCNT in Figure 36c. Platinum is distributed onto the whole tubes, though less uniformly distributed in some parts due to the forming of small aggregates (marked with square and arrow). Pt/HTC-C and Pt/C-commercial also show the distribution of Pt particles on support surfaces.

In addition, Figure 36 compares the Pt size distribution on each carbon support after evaluation of 300 nanoparticle sizes and highlights a Gaussian distribution in all cases. Pt/rGO, Pt/C, Pt/MWCNT and Pt/HTC-C have Pt particle diameters of  $1.6\pm 0.4$  nm,  $1.7\pm 0.6$  nm,  $1.7\pm 0.5$  nm and  $1.8\pm 0.5$  nm, respectively. Pt/C-commercial has a Pt particle diameter of  $1.5\pm 0.4$  nm. The averaging of Pt sizes on all carbon supports gives  $1.7\pm 0.1$  nm. Thus, self-prepared Pt on carbons are highly comparable with each other and with the commercial catalyst in view of Pt particle size and distribution onto the supports.

TEM images of the nanocomposite catalysts Pt/ITO-rGO and Pt/FTO-rGO are shown in Figure 37. The rGO is highly covered by Pt particles and metal oxide particles. In some areas platinum is solely present on rGO (marked with arrows), while in other areas Pt and metal oxides are overlaid in the TEM images. Both images in Figure 37 show that Pt particles are well-distributed on the basal planes and edges of rGO. Hence, Pt-rGO interaction is suggested to occur equivalent to Pt/rGO in Figure 36a. Because of overlaying Pt and metal oxide particles on rGO, TEM study of Pt particle distribution on the composite supports is later supplemented by HR-TEM with EDS. Then, imaging of interfaces between single Pt and metal oxide particles as well as EDS mapping of Pt distribution on the composites is carried out.

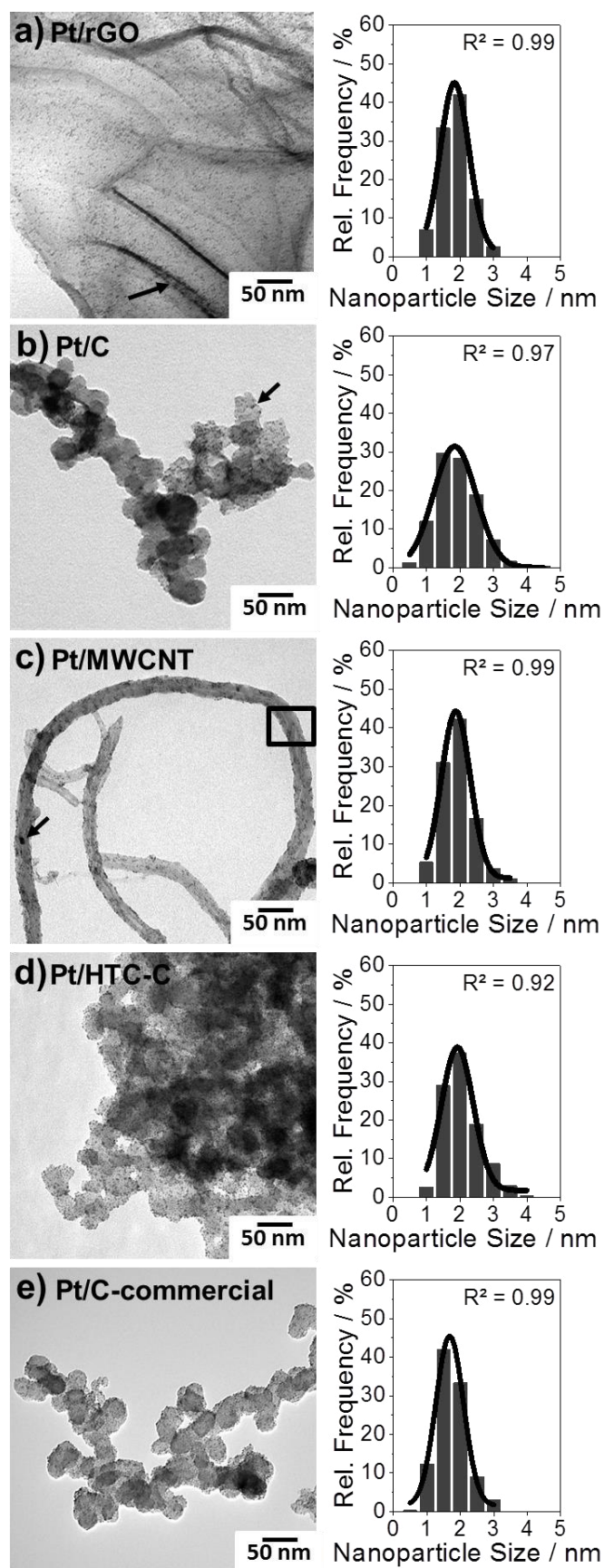


**Figure 36** TEM images with Pt particle size distribution of Pt/rGO (a), Pt/C (b), Pt/MWCNT (c), Pt/HTC-C (d) and Pt/C-commercial (e).

The evaluation of Pt particle sizes in Figure 37 leads to  $1.4 \pm 0.4$  nm platinum particles on ITO-rGO and  $1.6 \pm 0.4$  nm platinum particles on FTO-rGO. The size distributions are received from 300 nanoparticle sizes in both cases and highlights a Gaussian curve shape. In sum, sizes of Pt nanoparticles on seven different substrates are highly equivalent and show an averaged size of  $1.6 \pm 0.1$  nm. This provides a catalyst degradation study later allowing neglecting Pt particle size effects discussed in Section 3.2.3.1.

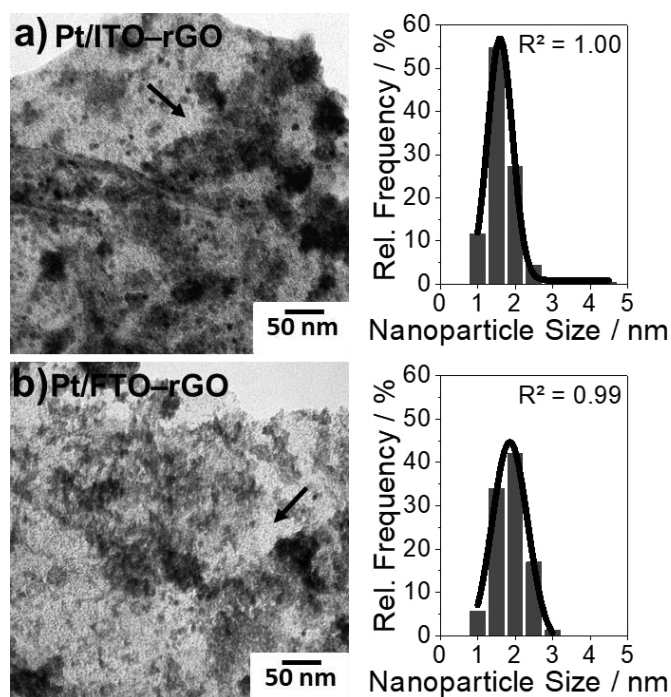


**Figure 37** TEM images with Pt particle size distribution of platinum on ITO-rGO (a) and FTO-rGO supports (b).

Figure 38 contrasts the Pt catalysts by use of X-ray diffraction. Pt reflections appear at  $40.0^\circ$  and  $46.5^\circ$  and are originated from (111) and (200) planes of platinum (ICSD, 00-001-1194). First, for the carbon-based catalysts Pt/rGO, Pt/C, Pt/MWCNT, Pt/HTC-C and Pt/C-commercial broad and low intensity Pt reflections are seen, so that both reflections overlap. This is due to the nanosized spherical particles observed under TEM in Figure 36. XRD further characterizes these particles to consist of (111) and (200) atomic lattices.<sup>[230]</sup> Second, the same Pt reflections appear for Pt/ITO-rGO and Pt/FTO-rGO, but the interference with reflections coming from ITO and FTO impede their observation, respectively. For instance, the FTO reflections at  $38.0^\circ$  and  $39.0^\circ$  overlap with the Pt reflection at  $40.0^\circ$ .

In total, XRD shows the same platinum crystallinity with (111) and (200) planes for the different catalysts, which is caused by identical Pt particle synthesis described in Section 4.1.1. Pt/C-commercial also shows the same Pt crystallinity. However, the platinum reflections for the composites overlap with reflections originated from metal oxides due to the use of nanoparticles in this work. For this reason, Pt particle sizes are not calculated from XRD, although the very broad and low-intensity reflections indicate the low size of platinum measured by TEM.<sup>[231]</sup>

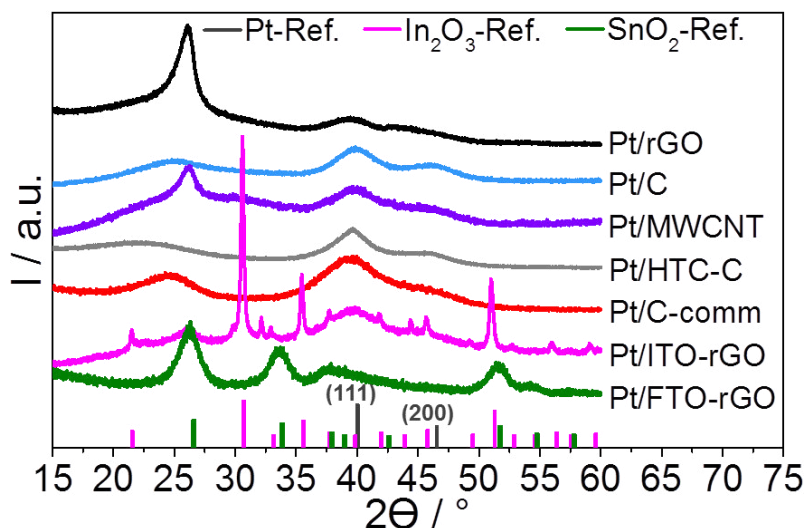


**Figure 38** XRD of Pt catalysts in comparison with ICSD reference patterns: 00-001-1194 for Pt, 00-001-0929 for  $\text{In}_2\text{O}_3$  and 98-000-9163 for  $\text{SnO}_2$ .<sup>[230, 231]</sup>

Next to platinum size and crystallinity, the Pt contents on the seven substrates are determined. Catalysts were dissolved in aqua regia and then analyzed with ICP mass spectrometry. The Pt content values are listed in Table 9 and vary from 8.3 wt% to 23.1 wt%. On one hand the Pt synthesis itself was shown by TEM and XRD to give high comparable Pt size and crystallinity among the catalysts. On the other hand the degree of Pt interaction with different supports during sample preparation might influence the Pt deposition and in consequence the Pt content within the catalysts. During the later electrochemical analysis in Section 5.3 Pt mass fractions of Table 9 serve for the normalization of electrochemical data in terms of ECSA and activity for ORR and guarantee their comparability.

**Table 9** Overview of Pt particle diameters from TEM and Pt contents on the supports materials from ICP-MS.<sup>[230, 231]</sup>

Catalyst	TEM	ICP-MS
	Pt Particle Diameter / nm	Pt Content / wt%
Pt/rGO	1.6±0.4	16.9±0.03
Pt/C	1.7±0.6	14.4±0.04
Pt/MWCNT	1.7±0.5	15.0±0.18
Pt/HTC-C	1.8±0.5	8.3±0.02
Pt/C-commercial	1.5±0.4	19.1±0.11
Pt/ITO-rGO	1.4±0.4	23.1±0.07
Pt/FTO-rGO	1.6±0.4	21.8±0.04

### 5.2.2 Location of Platinum on the Nanocomposites

Pt/ITO-rGO and Pt/FTO-rGO are further investigated using HR-TEM with EDS. Figure 39 displays HR-TEM images of Pt/ITO-rGO with two different magnifications. In Figure 39a, a sheet of reduced graphene oxide with kinks and with Pt and ITO particles on it is depicted. The marked area is further enlarged in Figure 39b-c, while both images show the same part of Pt/ITO-rGO with same magnification but a different focus. A change of focus enables the visualization of atomic lattices in different heights under the microscope. In the mid image the atomic lattice of ITO is visible, whereas in the right image atomic lattices of Pt are visualized. The visible ITO lattice has an atomic distance of 0.29 nm correlating with the (222) plane (ICSD, 00-001-0929), whereas the visible Pt lattices have an atomic distance of 0.22 nm coming from the (111) plane (ICSD, 00-001-1194).

Pt particles are deposited on rGO (1) and on ITO (2) as imaged in Figure 39. The kinks of the rGO sheet are shown to anchor Pt particles in a row (4). This coincides with the observation for Pt/rGO in Figure 36a. Thus, the unevenness of rGO sheets in terms of kinks and wrinkles is evidenced to provide preferred anchoring sites for Pt particles, which has also been discussed in literature.<sup>[24]</sup> Moreover, the interfaces between rGO and ITO are revealed to embed Pt particles as well (3). Kou et al.<sup>[217]</sup> observed very similar Pt-ITO-rGO interfaces using TEM and reported stabilized Pt nanoparticles there by use of DFT calculations.

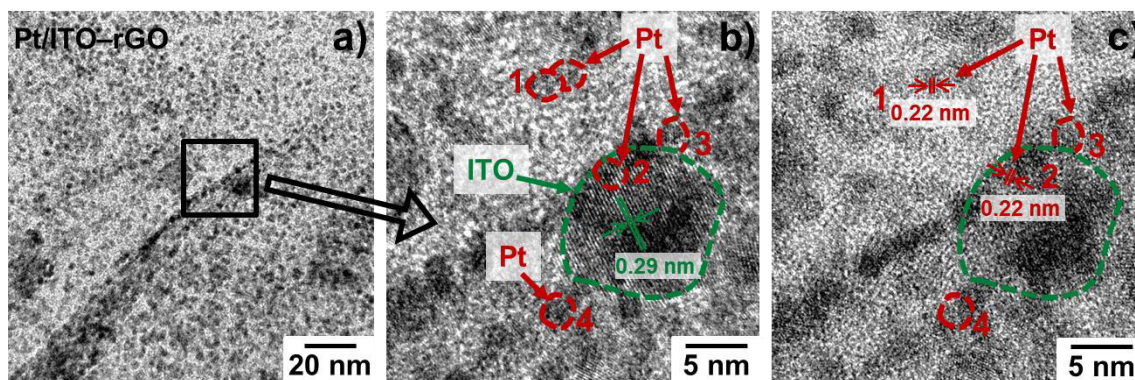


**Figure 39** HR-TEM images of Pt/ITO-rGO with visualized atomic lattice distances of ITO and Pt.

Figure 40 shows the HR-TEM images of Pt/FTO-rGO in the same way. Both particle types — platinum and FTO — are distributed on rGO. Because the FTO particles are smaller than the ITO particles, a further magnification is depicted in Figure 40c. Here, platinum and FTO are identified by use of visualized atomic lattice distances. Distances of 0.33 nm and 0.26 nm are caused by (110) and (011) planes of FTO (ICSD, 98-000-9163), whereas the measured distance of 0.22 nm verifies the (111) plane of platinum (ICSD, 00-001-1194). Also interfaces between Pt, FTO and rGO are seen in an analogous way to the other composite. Hence, the Pt particle deposition at FTO-rGO interfaces is demonstrated.<sup>[231]</sup>

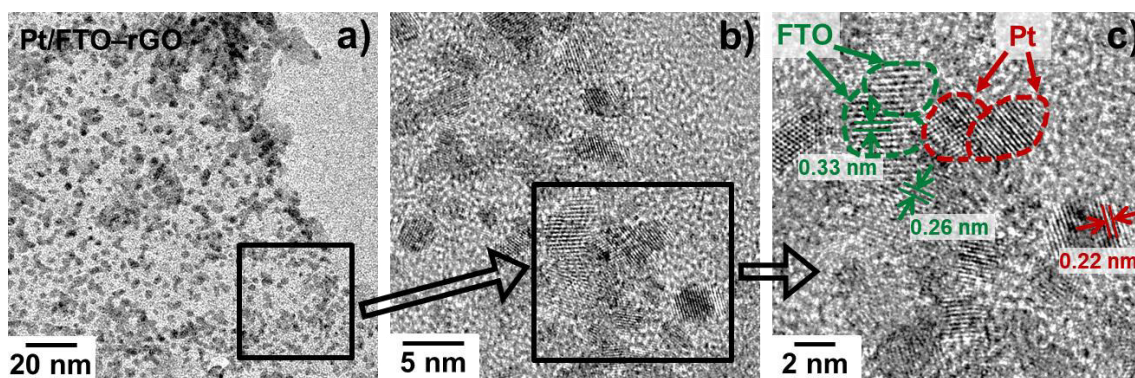


**Figure 40** HR-TEM images of Pt/FTO-rGO with visualized atomic lattice distances of FTO and Pt.<sup>[231]</sup>

High resolution TEM in Figure 39 and Figure 40 served for sub-nanometer analysis of atomic lattices and interfaces of single particles within the nanocomposites. However, the assessment of Pt particle distribution on the composites is limited by the contrasts of TEM images, because next to rGO metal oxide and Pt particles are present. EDS in Figure 41 is used to evaluate the location of Pt particles on the composite supports. Therefore, next to the microscopic image the related element distribution is shown. Figure 41a confronts the distribution of Pt, Sn and In in Pt/ITO-rGO. Inside the first circled area more Sn and In are detected (1). An increased detection of Pt particles compared to other imaged regions is not observed here. Inside the second circled area Pt is detected in larger extent (2). However, the detection of Sn und In decreased in the second area (2) compared to the first area (1).

In comparison, EDS mapping of Pt/FTO-rGO with elemental distribution of Pt, Sn and F is shown in Figure 41b. Both circles contain enhanced detection of Sn and F due to the presence of FTO aggregates (1, 2). The detection of fluorine is only possible in traces because of its low amount in the material. Inside these two circled areas platinum is also visible in higher extent compared to other imaged regions. In conclusion, EDS reveals a preferred deposition of Pt nanoparticles on FTO instead of rGO. The ability of SnO<sub>2</sub> to strongly interact with Pt nanoparticles was also reported by Daio et al.<sup>[191]</sup>, who investigated lattice strains of Pt particles on tin oxide via scanning transmission electron microscopy and DFT simulations. The good distribution of Pt particles on SnO<sub>2</sub> substrates is demonstrated in lots of literature.<sup>[141, 188-190]</sup> In case of the other nanocomposite with ITO, a preferred deposition of Pt particles on ITO is not seen. In literature, good Pt distribution is reported on ITO supports<sup>[205, 264]</sup> as well as on reduced graphene oxide<sup>[135, 227]</sup>. However, the investigation of Pt distribution on ITO-rGO is very limited. Kou et al.<sup>[217]</sup> compared HR-TEM of Pt nanoparticles on ITO-rGO to DFT calculations on the interaction of Pt<sub>6</sub> cluster with ITO, rGO and with ITO-rGO interfaces. Their results showed the preferred generation of Pt-ITO-rGO junctions, which were also observed in Figure 39 of this study. Moreover, they reported the preferred Pt deposition on rGO than on ITO in direct comparison. This is according to EDS in Figure 41a of this work. So, EDS mapping here points out the difference between ITO-rGO and FTO-rGO as platinum catalyst support.<sup>[231]</sup>

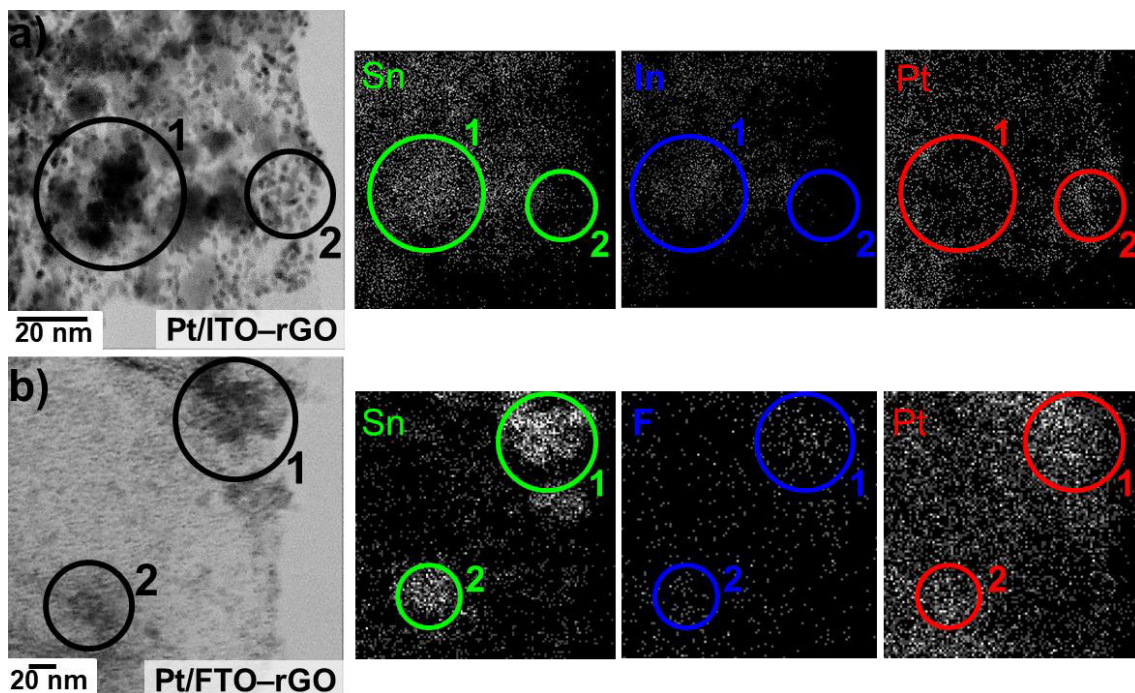


**Figure 41** EDS mapping of Pt/ITO-rGO with elemental distribution of Sn, In and Pt (a) and of Pt/FTO-rGO with elemental distribution of Sn, F and Pt (b).<sup>[231]</sup>

In summary, Pt nanoparticles on the seven different supports exhibit very comparable diameters and crystallinity, which are synthesized via the same method. Hence, possible impact of differences in Pt structure and size onto the catalyst degradation during electrochemical stress testing later is supposed to be negligible. The Pt mass fractions on the different supports deviate by about 5 wt% which has to be considered during electrochemical analysis. ECSA and ORR activities later are normalized towards the real content of platinum in the following section.

With respect to Pt particle distribution, particles on the carbon supports are well-distributed in each case. For platinum on ITO-rGO and FTO-rGO nanocomposites, particles are distributed on rGO as well as on the metal oxides. On FTO-rGO, preferred Pt deposition on FTO instead of rGO takes place, which is not observed for the other ITO-rGO composite. Pt particle anchoring at metal oxide-rGO interfaces occurs in both nanocomposites.

## 5.3 Electrochemical Characterization of Pt Catalysts

The materials are investigated on their suitability and durability for ORR. The carbon-based Pt catalysts are discussed in Section 5.3.1 and have further been presented in Publications II and IV. Section 5.3.2 focuses on carbon derived from hydrothermal carbonization being tested as Pt support for ORR the first time. This part of research was a collaboration with the working group of Chemical Technology 1 from the Carl von Ossietzky University Oldenburg and includes contents of Publication I. Finally, Section 5.3.3 compares the nanocomposite catalysts. Pt/ITO-rGO was presented within Publication IV, and Pt/FTO-rGO was focused in Publications II and III.

### 5.3.1 Carbon-Based Pt Catalysts

In this chapter, Pt/rGO and Pt/MWCNT are discussed as alternative catalysts for ORR and compared to Pt on common carbon black, which was self-synthesized on the one hand (Pt/C) and purchased on the other hand (Pt/C-commercial). Initial cyclic and CO stripping voltammetry as well as ORR analysis is presented in Section 5.3.1.1. Degradation of catalysts after electrochemical stress is studied in Section 5.3.1.2.

#### *5.3.1.1 Initial Characterization of Carbon-Based Pt Catalysts*

Cyclic and CO stripping voltammetry experiments are shown in Figure 42. CV in Figure 42a shows for each catalyst the Pt-related signals. They are located in the potential range between 0.0–0.4  $V_{\text{RHE}}$  for hydrogen and above 0.4  $V_{\text{RHE}}$  for oxygen. Highly similar curves for the catalysts Pt/C, Pt/MWCNT and Pt/C-commercial are seen. The intensity of Pt signals is slightly larger for Pt/C-commercial compared to Pt/C and Pt/MWCNT due to higher Pt loading.

Cyclic voltammetry of Pt/rGO is different and shows a stronger capacitive current density between approximately 0.3–0.5  $V_{\text{RHE}}$  than voltammetry of the others. The double layer capacitance is analyzed later in Figure 43. Also HQ/Q redox activity at around 0.6  $V_{\text{RHE}}$  is clearly visible for Pt/rGO, which is different to the other catalysts. Table 10 lists the released charges during oxidation of HQ species. The

charge for Pt/rGO counts  $217 \mu\text{C cm}^{-2}$ , while values for the others are at least one order of magnitude lower. Similar observation was done in other CV studies during the comparison of Pt/rGO and Pt/C.<sup>[262, 271, 272]</sup> The explanation of enhanced capacitive current density and HQ/Q redox activity is the higher specific surface area and the higher amount of oxygen surface groups for rGO compared to C and MWCNTs as illustrated in Table 7. A higher oxygen content of rGO compared to C was also reported in literature.<sup>[262]</sup>

Further differences between the catalysts become apparent by CO stripping voltammetry in Figure 42b. CO oxidation peaks for Pt/rGO and Pt/C are very comparable in position and shape. They center at  $0.88 V_{\text{RHE}}$  with an asymmetric shoulder at lower potential side. Taylor et al.<sup>[273]</sup> studied Pt loadings from 20 wt% to 80 wt% on same Vulcan<sup>®</sup> XC72 and found this shoulder with rising intensity through rising Pt loading. Particles started to aggregate onto the support by increasing the loading. CO oxidation on Pt aggregates was concluded to be facilitated compared to CO oxidation on isolated Pt particles on the support.<sup>[273]</sup> Here, Pt/rGO and Pt/C have Pt mass fractions of 16.9 wt% and 14.4 wt%, respectively. Their CO experiments are highly similar to CO oxidation on the 20 wt% catalyst tested by Taylor et al.<sup>[273]</sup>

Pt/C-commercial shows a similar CO stripping curve to Pt/rGO and Pt/C. Asymmetry due to the shoulder on lower potential side is also visible but less pronounced. However, CO stripping voltammetry of Pt/MWCNT is different to the other carbon-based catalysts. Oxidation of CO appears at lower potentials with two overlapped signals at  $0.77 V_{\text{RHE}}$  and  $0.83 V_{\text{RHE}}$ . A first reason could be the nanostructure of platinum, since the CO adsorption has different energies on different Pt surface facets.<sup>[250, 274, 275]</sup> But in this work Pt characteristics are excluded to impact CO stripping, since Pt particles are comparable in view of diameters, spherical shapes and crystallinity as described in Section 5.2. Another reason could be the impact of previously discussed Pt particle aggregates. TEM imaged in Figure 36c some uneven distributed Pt on MWCNTs, however with only nanometer scaling information. Also the Pt-support interaction might cause this different CO oxidation behavior. Recently, Novikova et al.<sup>[173]</sup> investigated various Pt/MWCNT catalysts and suggested the impact of carbon nanotube characteristics like the diameter on CO oxidation.

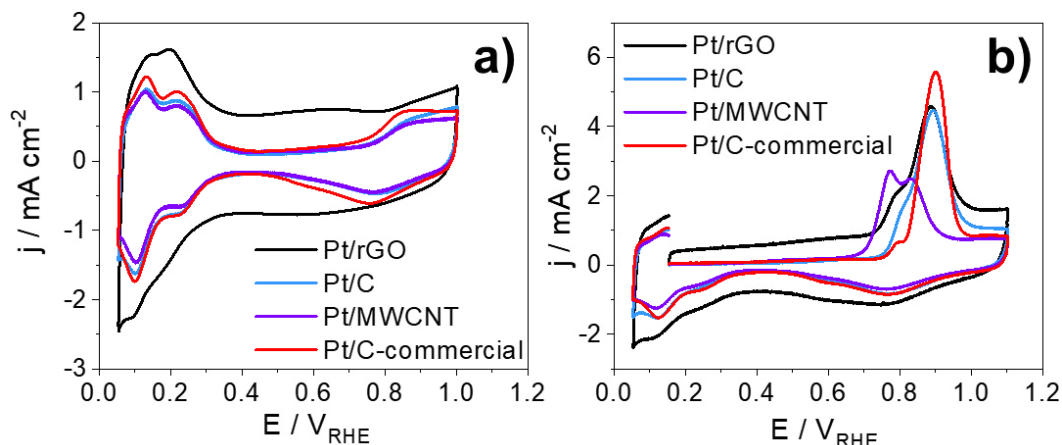


**Figure 42** Cyclic voltammetry (a) and CO stripping voltammetry (b) of carbon-based Pt catalysts in comparison.

ECSA values from absorbed hydrogen in Figure 42a and absorbed CO in Figure 42b are listed in Table 10. The values from both methods deviate from each other, because assumptions in ECSA calculation are done, respectively. HUPD assumes a monolayer of one H atom bonded to one Pt atom, whereas the CO adsorption is suggested to involve two Pt atoms. The mechanism includes one CO molecule on one Pt atom being oxidized by one oxygen species on one Pt atom.<sup>[250]</sup> Because spherical and polycrystalline Pt particles are used, Pt interaction with adsorbates is complex and differs between surface sites.<sup>[276]</sup> Therefore both methods are considered here.

Averaged ECSA values from both methods are  $87 \text{ m}^2 \text{ g}_{\text{Pt}}^{-1}$  for Pt/C,  $75 \text{ m}^2 \text{ g}_{\text{Pt}}^{-1}$  for Pt/rGO,  $69 \text{ m}^2 \text{ g}_{\text{Pt}}^{-1}$  for Pt/C-commercial and  $68 \text{ m}^2 \text{ g}_{\text{Pt}}^{-1}$  for Pt/MWCNT and deviate by only  $9 \text{ m}^2 \text{ g}_{\text{Pt}}^{-1}$  among each other. Hence, the electrochemical surface areas are very close to each other as a result of similar Pt particle morphology on the carbon supports. This was proven during the physical analysis in Section 5.2.1. But still, the slight ECSA differences might be due to the different supports. Carbon morphologies are contrasted in Figure 31. The morphology can impact the interaction with Pt particles, thus the electronic linking and finally the ECSA.<sup>[117]</sup> Comparing rGO, C and MWCNT the specific surface area of MWCNT was only half of the areas of the other two carbons in Table 7. Moreover, platinum on MWCNTs showed uneven distribution in Figure 36c for small arrays. This might lower the ECSA of Pt/MWCNT compared to Pt/C and Pt/rGO. However, the carbon morphologies do not affect the ECSAs to a greater extent.

Double layer capacitances are determined by CO adsorption on platinum to suppress faradaic currents and simultaneously record the capacitive currents. Figure 43 compares the CV curves of CO blocked Pt catalysts. The greatest double layer capacitance of  $8.9 \text{ mF cm}^{-2}$  is calculated for Pt/rGO followed by the other catalysts between  $0.7\text{--}1.2 \text{ mF cm}^{-2}$ . Impacts on  $C_{\text{DL}}$  are electrode porosity, surface hydrophilicities as well as electrolyte and scan rate during CV.<sup>[277]</sup> Because the two last parameters are constant during all measurements, the highest  $C_{\text{DL}}$  of Pt/rGO is a consequence of support surface area and functional groups. Comparing Pt/rGO, Pt/C and Pt/MWCNT the rGO support exhibited the largest specific surface area and the highest amount of functional oxygen groups in Table 7.

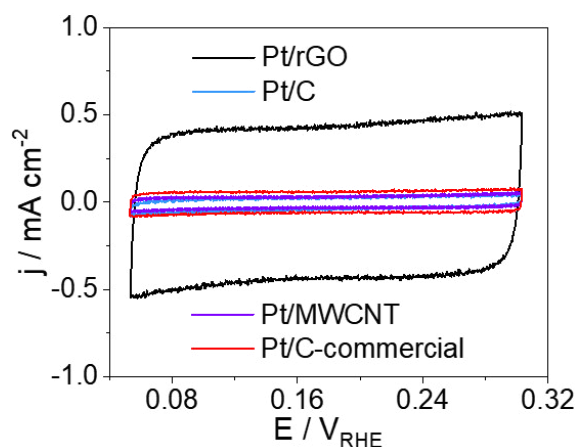


**Figure 43** Cyclic voltammetry of carbon-based Pt catalysts after CO sorption.

Figure 44 compares ORR for Pt on the alternative carbons rGO and MWCNT with Pt/C and Pt/C-commercial. Oxygen reduction is limited by diffusion in the potential range below  $0.8 \text{ V}_{\text{RHE}}$ , so that we see the dependency of current density on the rotation speed. Current densities at potentials of  $0.3$ ,  $0.4$  and  $0.5 \text{ V}_{\text{RHE}}$  are used for Koutecky–Levich analysis. K–L plots in Figure 44 show high linearity for each catalyst. The transferred electrons  $n$  per  $\text{O}_2$  molecule during ORR were calculated according to Equation [23]. Transferred electrons for the carbon-based Pt catalysts are contrasted in Table 10 and count  $3.8$ ,  $4.8$ ,  $4.3$  and  $4.4$  for Pt/rGO, Pt/C, Pt/MWCNT and Pt/C-commercial, respectively. The  $4e^-$  pathway of oxygen reduction is indicated, which is known for Pt catalysts.<sup>[278]</sup> Deviation of  $n$  values from the theoretical value of four is caused by the RDE experiment. On one side parameters  $F$ ,  $\mathcal{G}$ ,  $D$ ,  $c^*$  and  $\omega$  from Equation [23] are unchanged in each experiment. On the other side the current density  $j$  depends on the coverage of the electrode with catalyst material. Different support morphologies discussed before

can lead to a difference in coverage. In consequence, the real electrode area can deviate from the geometric area.<sup>[62]</sup> Furthermore, electrical conductivities are discussed to impact RDE experiments<sup>[267]</sup> and were shown in this study to be different. Indeed, rGO possesses a lower electrical conductivity in Table 7 compared to the others, while Pt/rGO results into lower diffusion-limited current densities in Figure 44 compared to the others.

ORR data are further analyzed towards Tafel relations, which are depicted in Figure 44. From literature, two linear regions are recognized for platinum at potentials of 0.95–1.00 V<sub>RHE</sub> which is region I and of 0.90–0.95 V<sub>RHE</sub> which is region II. In the first region, the Tafel slope is presumed to result from ORR catalyzed by Pt containing surface oxides<sup>[58]</sup> and is  $-60 \text{ mV dec}^{-1}$ .<sup>[61, 62]</sup> The slopes  $m_I$  for the catalysts Pt/rGO, Pt/C, Pt/MWCNT and Pt/C-commercial count  $-61 \pm 3 \text{ mV dec}^{-1}$  and thus are very close to the expected slope of  $-60 \text{ mV dec}^{-1}$ . In the second region, ORR on metallic Pt with a Tafel slope of  $-120 \text{ mV dec}^{-1}$  is reported in literature.<sup>[58]</sup> The slope  $m_{II}$  is  $119 \pm 4 \text{ mV dec}^{-1}$  for the catalysts here and thus very close to the expected slope of  $-120 \text{ mV dec}^{-1}$ .

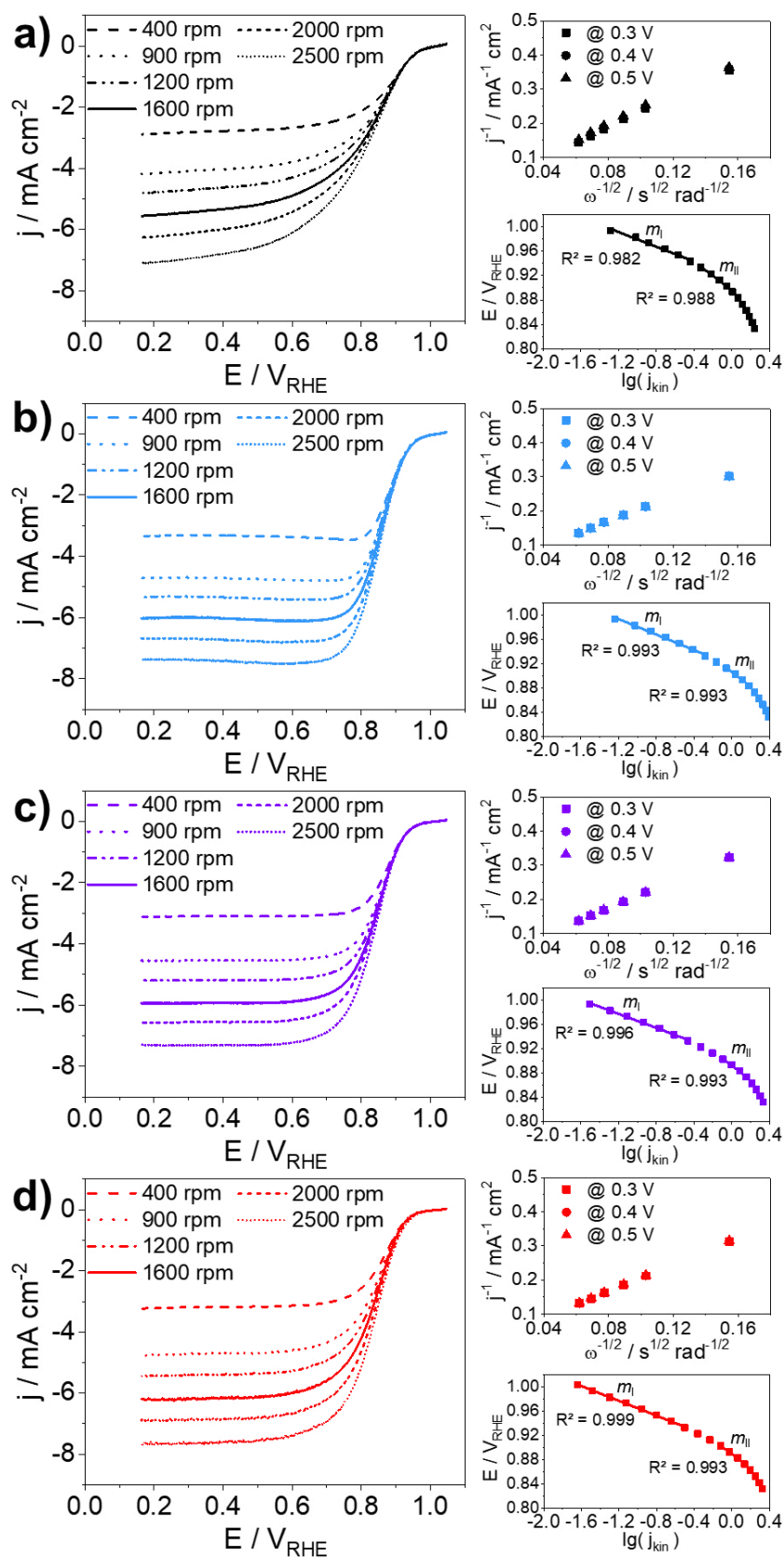


**Figure 44** ORR data of carbon-based Pt catalysts. Cathodic scans at different rotation speeds with K-L and Tafel plots for Pt/rGO (a), Pt/C (b), Pt/MWCNT (c) and Pt/C-commercial (d).

ORR activities are compared in view of the onset potential, the mass activity and the specific activity listed in Table 10. Onset potentials range 0.99–1.01 mV and are thus highly comparable, whereas mass and specific activities deviate among the catalysts. Both values demonstrate the largest ORR activity in case of self-prepared Pt/C with  $88.0 \text{ A g}_{\text{Pt}}^{-1}$  and  $0.103 \text{ mA cm}^{-2}$ . Second largest ORR activities are shown for the alternative catalysts Pt/rGO and Pt/MWCNT. Mass activities are  $56.4 \text{ A g}_{\text{Pt}}^{-1}$  and  $54.9 \text{ A g}_{\text{Pt}}^{-1}$  and specific activities exhibit the same value of  $0.076 \text{ mA cm}^{-2}$  for both materials. Last, Pt/C-commercial exhibits the lowest activity with  $38.3 \text{ A g}_{\text{Pt}}^{-1}$  and  $0.059 \text{ mA cm}^{-2}$ .

While physical characterization showed comparable Pt particle morphologies and sizes of the catalysts on one hand, electrochemical characterization gives different ORR activities in Table 10 on the other hand. Pt-support interaction plays a role in terms of electron transfer during ORR.<sup>[49]</sup> That means, the activity for ORR depends on a proper anchorage of Pt particles to the carbon, which guarantees electronic linking. In consequence, ORR activity of the catalysts here depends on their ECSAs and indeed shows similar trends to ECSA values. Self-prepared Pt/C gives the highest activity, whereas Pt/C-commercial gives the lowest activity according to their ECSAs. Comparison of self-prepared catalysts gives lower ORR activities for Pt/rGO and Pt/MWCNT than for Pt/C according to ECSA values.

In conclusion, the use of alternative carbon supports has no boosting effect on platinum's catalytic activity for ORR compared to Pt/C, although MWCNTs and rGO provide defect sites and larger specific surface areas than C. But considering their coherent units in the form of tubes, sheets and particles, C possesses by far the smallest units in nm-range compared to tubes and sheets with lengths and diameters in  $\mu\text{m}$ -range. These small C particles have significant higher amorphousness than MWCNTs and rGO. This can cause higher surface energies. Considering interaction of these units among each other, TEM demonstrated large aggregation of C particles to reduce surface energies but no comparable aggregation of tubes and sheets in MWCNTs and rGO. Further interaction of the most amorphous C nanoparticles with Pt nanoparticles can further reduce surface energies and might cause strong Pt anchoring with enhanced ECSA and ORR activity compared to MWCNTs and rGO with alternative carbon structures. However, amorphousness of carbon black can consequence corrosion in presence of cathodic potentials in fuel cells as discussed below in Section 5.3.1.2.

Comparison of ORR activity with other studies is limited due to varying Pt sizes and nanostructures or varying experimental details. Some examples of Pt/C tested in comparable RDE experiments are  $10.6 \text{ A g}_{\text{Pt}}^{-1}$  and  $0.020 \text{ mA cm}^{-2}$  using cathodic scans<sup>[279]</sup> or  $150.0 \text{ A g}_{\text{Pt}}^{-1}$  and  $0.291 \text{ mA cm}^{-2}$  using anodic scans.<sup>[104]</sup> Self-prepared and commercial Pt/C from this work show activities in the range of literature values.

**Table 10** Electrochemical parameters of carbon-based Pt catalysts.<sup>[230, 231]</sup>

Method	Parameter	Pt/rGO	Pt/C	Pt/MWCNT	Pt/C-commercial
CV	$ECSA_{\text{HUPD}} / \text{m}^2 \text{ g}_{\text{Pt}}^{-1}$	75	84	71	65
	$Q_{\text{HQ}} / \mu\text{C cm}^{-2}$	217	7	18	2
CO	$ECSA_{\text{CO}} / \text{m}^2 \text{ g}_{\text{Pt}}^{-1}$	74	90	64	73
	$C_{\text{DL}} / \text{mF cm}^{-2}$	8.9	0.7	0.7	1.2
ORR	$E_{\text{onset}} / \text{V}$	1.01	1.00	0.99	1.00
	$MA / \text{A g}_{\text{Pt}}^{-1}$	56.4	88.0	54.9	38.3
	$SA / \text{mA cm}_{\text{Pt}}^{-2}$	0.076	0.103	0.076	0.059
	$m_{\text{I}} / \text{mV dec}^{-1}$	-60	-64	-58	-60
	$m_{\text{II}} / \text{mV dec}^{-1}$	-117	-124	-120	-115
	$n$	3.8	4.8	4.3	4.4

### 5.3.1.2 Degradation of Carbon-Based Pt Catalysts

After analysis of initial electrochemical parameters, carbon-based Pt catalysts were exposed to accelerated stress testing. Figure 45 shows the change of current densities *in-situ* for selected numbers of potential cycles. Electrochemical reactions catalyzed by platinum are located at  $0.0\text{--}0.4 \text{ V}_{\text{RHE}}$  for hydrogen and above  $0.4 \text{ V}_{\text{RHE}}$  for oxygen. These signals decrease with the number of cycles and indicate degradation of the four catalysts.

The insets show the development of ECSA with progress in stress testing. ECSA losses seem to be stronger in the initial part than in the final part of potential cycling. Some degradation paths from Figure 6 in Section 3.2.3.1 are assumed to occur in higher extent during the first potential cycles. For example, smaller particles have higher surface energies than larger ones, so that Pt dissolution is enforced for

smaller particles. This consequences more pronounced Pt agglomeration due to Ostwald-Ripening during the first than during the final period of cycling.<sup>[97, 99]</sup> The loss of ECSA during the first cycles is less pronounced for the catalysts Pt/C and Pt/C-commercial with Vulcan<sup>®</sup> support compared to the other two alternative catalysts. A reason might be an enhanced Pt stabilization during the first potential cycles due to smaller and more amorphous C particles in contrast to MWCNTs and rGO as discussed before. Furthermore, a possible catalyst stability due to support corrosion should play a minor role at the beginning of stress test.

Next to Pt degradation, Figure 45 gives indication on support degradation due to the change in oxidation currents around  $0.6 V_{RHE}$ . Pt/rGO and Pt/C in Figure 45a–b are observed to have increasing current densities here, which is related to a change of support properties triggered by potential cycling.<sup>[119, 120]</sup> In the following paragraphs, Pt and support degradation are analyzed in detail.

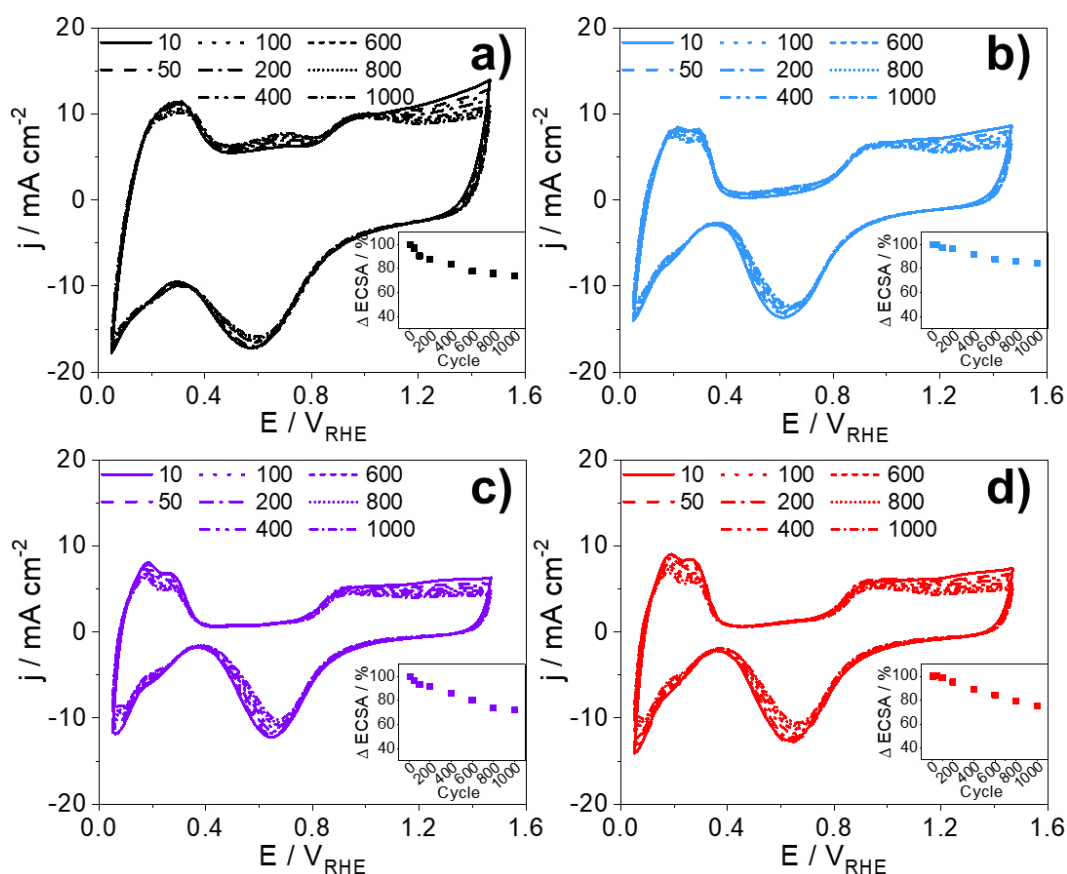


**Figure 45** Selected potential cycles during AST with inset of ECSA change for Pt/rGO (a), Pt/C (b), Pt/MWCNT (c) and Pt/C-commercial (d).

Figure 46 compares initial cyclic and CO stripping voltammetry curves with final curves after stress testing. Signal intensity of hydrogen reactions between 0.0–0.4  $V_{\text{RHE}}$  as well as oxygen reactions between 0.7–1.0  $V_{\text{RHE}}$  are lowered, which demonstrates Pt degradation within each catalyst. With respect to CO oxidation the signals are changed as well. For Pt/rGO and Pt/C the peak maxima are negatively shifted by 30 mV and 10 mV after AST. This indicates a reduced adsorption strength of CO on aged platinum particles. Maillard et al.<sup>[280]</sup> found that an increase of Pt particle sizes from 1.9 nm to 3.1 nm can result into negative potential shifting of CO oxidation. Next to potential shift, the stress testing on Pt/rGO and Pt/C leads to narrowed CO oxidation signals with a less pronounced shoulder, so that Pt is believed to appear in a higher ordered nanostructures after AST.

Furthermore, CO stripping on Pt/MWCNT is strongly changed after exposure to potential cycling. The signal at 0.77  $V_{\text{RHE}}$  remains, whereas the signal at 0.83  $V_{\text{RHE}}$  almost disappeared. Hence, the interaction of Pt/MWCNT with CO is significantly different after provoked degradation. In contrast to the self-synthesized catalysts, Pt/C-commercial shows no negative potential shift and no change in signal shape or width of CO desorption. Reduction of signal intensity only reports Pt degradation here.

ECSA losses due to accelerated stress testing are determined by HUPD and CO and are listed in Table 11. Averaging the losses gives -31 %, -29 %, -26 % and -19 % for Pt/C-commercial, Pt/MWCNT, Pt/rGO and Pt/C. Hence, the changes in ECSA are comparable for the carbon-based Pt catalysts. This is a consequence of comparable initial Pt particles regarding their size, shape and crystallinity as analyzed in Section 5.2.1.

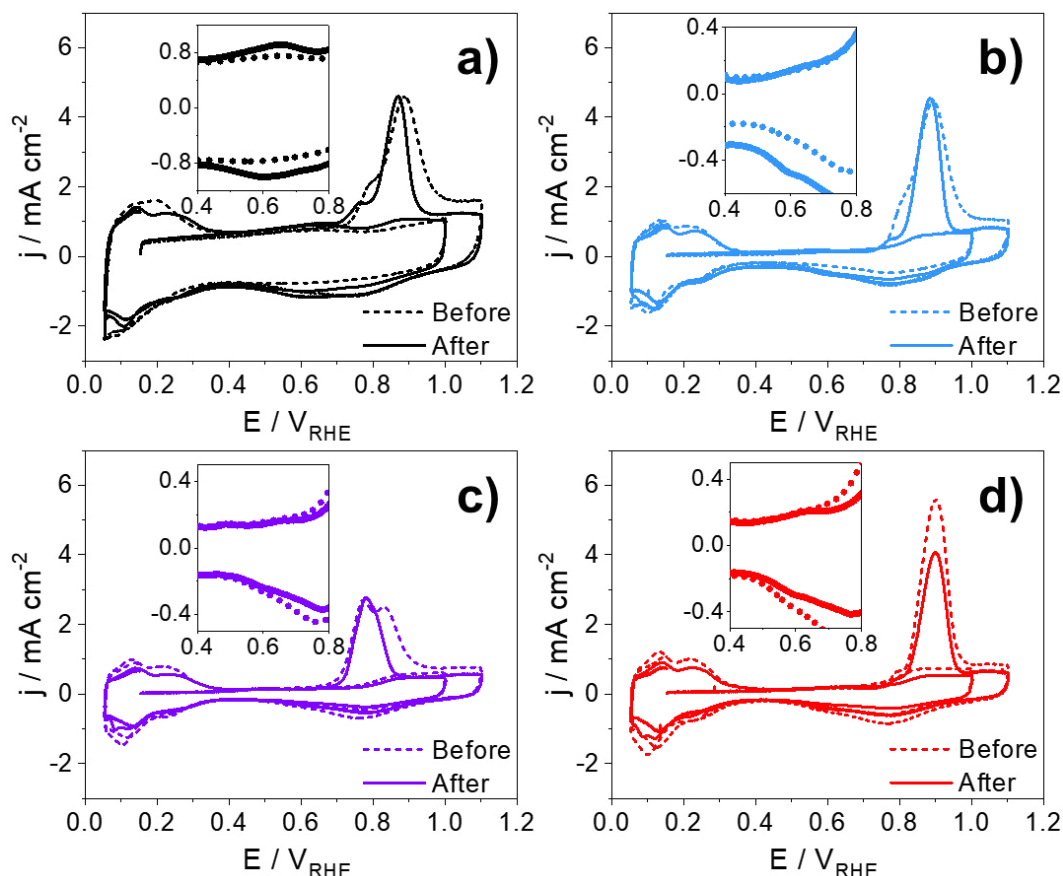


**Figure 46** Comparison of cyclic and CO stripping voltammetry curves before and after AST with insets of HQ/Q redox activities. Pt/rGO (a), Pt/C (b), Pt/MWCNT (c) and Pt/C-commercial (d).

Insets in Figure 46 enlarge the curve segment, where HQ/Q redox activity is located. In dependence on the catalyst the current densities in this range are changed after stress testing. Next to a change in the double layer capacitance determined later, the change of HQ/Q redox activity occurs after the test. Percentage changes are listed in Table 11 for each catalyst. The largest growth in charge amount of HQ oxidation is identified for Pt/C-commercial by factor of 25, followed by similar values for Pt/C and Pt/MWCNT of +137 % and +130 %. Pt/rGO already contained the most significant HQ/Q redox activity before stress testing compared to the other catalysts as illustrated in Table 10. The percentage change after AST is +36 % and is thus indeed the smallest change compared to the other catalysts. Basically, formation of HQ/Q similar species evinces the partial oxidation of carbon atoms as preliminary state to carbon corrosion generating  $\text{CO}_2$ .<sup>[119, 120]</sup> To sum up, the strongest carbon oxidation during potential cycling was observed for the commer-

cial catalyst Pt/C-commercial. Pt/rGO was shown to have highest HQ/Q amount in original state, however, the lowest carbon corrosion during potential cycling.

Figure 47 contrasts CV curves showing the capacitive current densities before and after stress testing. Relative changes in  $C_{DL}$  are compared in Table 11. Although Pt/C-commercial in Figure 46d had the strongest growth of HQ/Q species on its surface, the capacitive current density in Figure 47d is almost unchanged. It has to be mentioned that the detection of HQ/Q redox activity gives only partial information about carbon corrosion and cannot be directly related to change of catalyst surface area and amount of functional surface groups, which in turn impact the double layer capacitance.<sup>[281]</sup> The other three catalysts have increased double layer capacitances after potential cycling. While the absolute  $C_{DL}$  increase is stronger for Pt/rGO in Figure 47a than Pt/MWCNT in Figure 47c, their relative changes are comparable and count +12 % and +18 %, respectively.

Larger difference is recorded for Pt/C in Figure 47b. Its DL capacitance is enlarged to more than twice as the initial value. HQ/Q redox activity was shown to be enforced by potential cycling. However, electrochemically detected charge amounts of HQ oxidation cannot be directly linked to the amount of capacitive current. Rather a more complex impact of electrode porosity and hydrophilicity originated from a variety of functional groups on carbon surfaces contributes to the overall double layer capacitance.<sup>[277, 281]</sup> In conclusion, the durability test leads to the highest  $C_{DL}$  change in Pt/C as sign of the highest change in electrode porosity or functionalities.

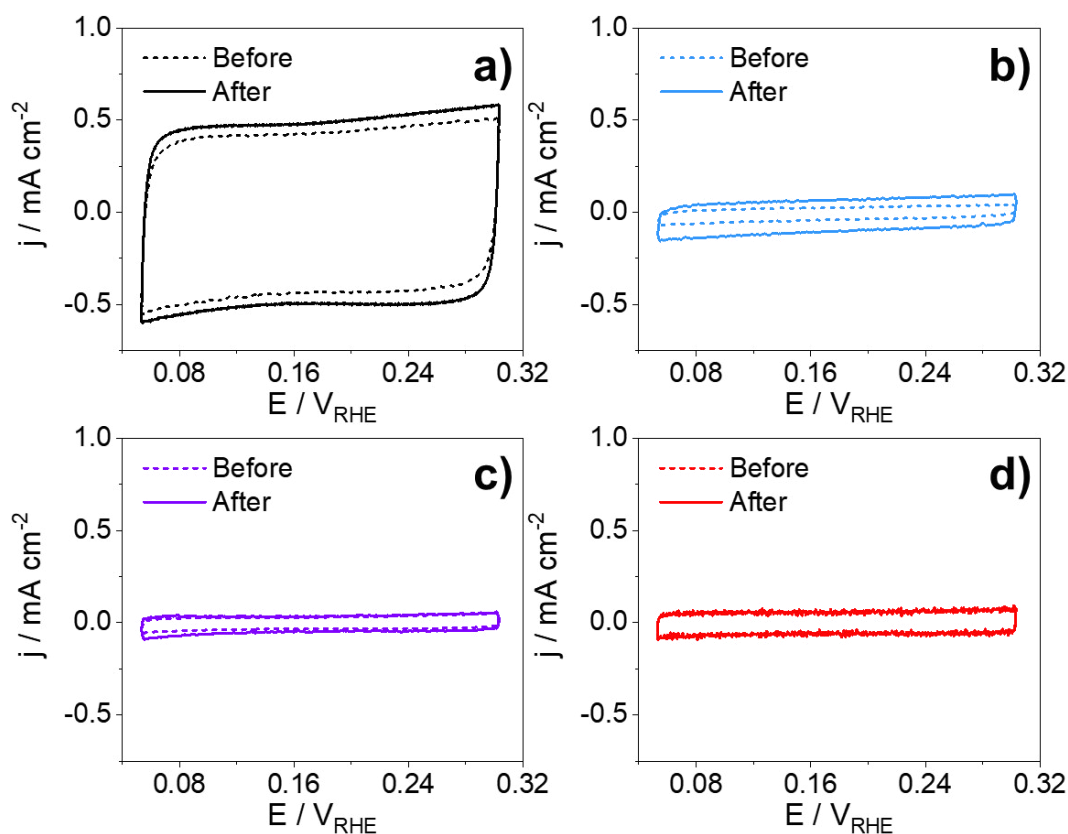


**Figure 47** Comparison of CV curves after CO sorption before and after AST. Pt/rGO (a), Pt/C (b), Pt/MWCNT (c) and Pt/C-commercial (d).

Figure 48 compares ORR curves before and after potential cycling. Oxygen reduction is negatively shifted to lower potentials after the stress test, which shows increased overpotentials for this reaction due to catalyst degradation. Table 11 shows that activity losses are in increasing order of Pt/MWCNT, Pt/C, Pt/rGO and Pt/C-commercial for mass as well as for specific activities. The mass activity losses of the three self-prepared materials are in similar range between 34–38 %, whereas the commercial catalyst lost 63 % of mass activity.

If changes in mass activity are compared to changes in specific activity, differences are visible. Specific activities already consider the change of ECSA due to degradation. Against this background, much lower specific activity losses than mass activity losses for Pt/rGO and Pt/MWCNT in Table 11 can be seen. This shows that the loss of catalytic activity is mainly caused by decreased ECSAs. On the contrary, losses in specific activity are higher for Pt/C and Pt/C-commercial, so that their activity loss is not dominated by the change in ECSA to that extent.

Insets of Tafel plots in Figure 48 show that slopes are the same after stress testing. The reaction mechanism of  $O_2$  reduction on each material is thus unaffected, although catalyst aging has taken place.

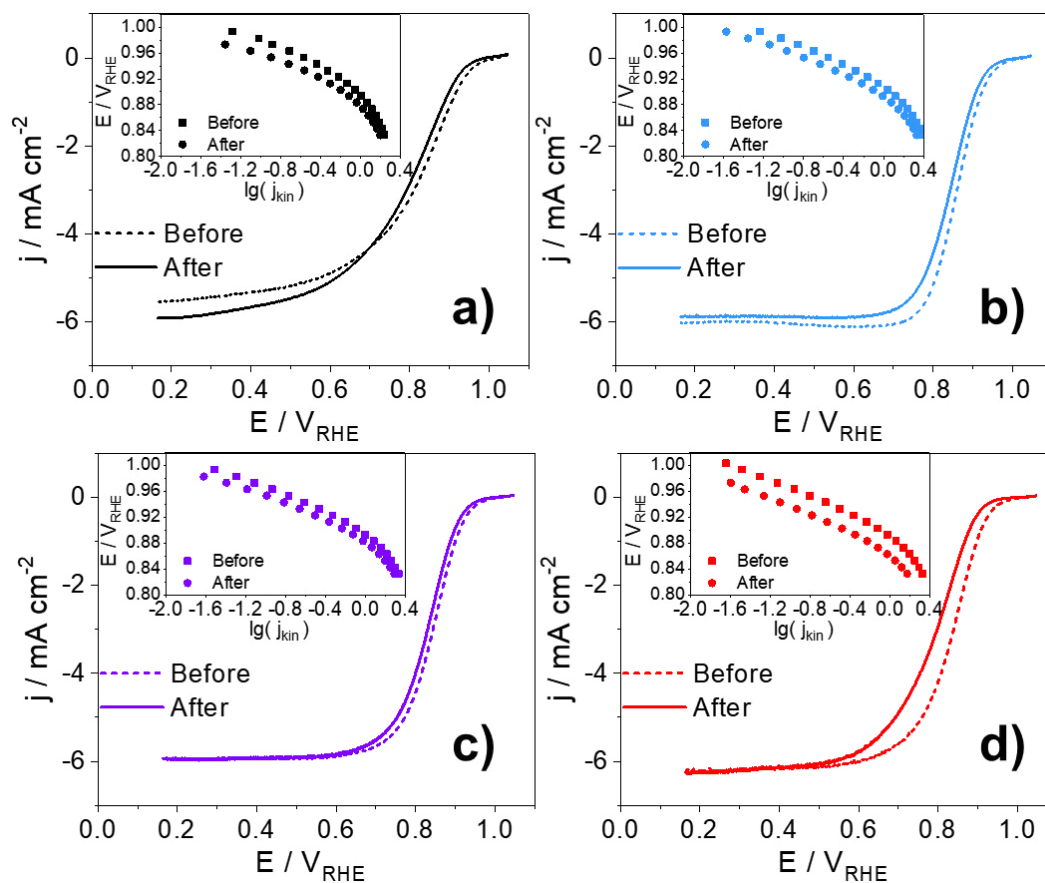


**Figure 48** Comparison of cathodic ORR scans at 1,600 rpm before and after AST with insets of Tafel plots. Pt/rGO (a), Pt/C (b), Pt/MWCNT (c) and Pt/C-commercial (d).

Figure 8 illustrated the carbon impact on catalyst activity and stability for ORR. Against this background the self-synthesized Pt catalysts are concluded towards their suitability. Initial electrochemical surface area and ORR activity were slightly higher for Pt/C compared to Pt/rGO and Pt/MWCNT. Carbon black was evaluated in Section 5.1.2 to combine the lowest graphitic degree with a defective aromatic structure shown by Raman and oxygen surface groups shown by XPS. These properties can enhance the interaction with Pt nanoparticles and can thereby enhance ECSA and activity for ORR. The alternative support materials rGO and MWCNTs have defect sites as well but strongly different morphologies with higher ordered graphene layers, which was pointed out in Figure 31. This can contribute to the lower ECSA and lower activity for ORR compared to Pt/C.

Regarding stability issues, results from changed HQ/Q amounts and changed DL capacitances reveal higher instability of carbon black than rGO and MWCNT as consequence of its most amorphous and rotationally faulted morphology. In view of Pt particle stabilities, ECSA and mass activity losses appeared to similar extents. Last, the Pt/C-commercial catalyst performed worst in comparison to self-prepared materials. On one hand initial ECSA and ORR activity were the lowest, and on other hand the loss of ECSA and ORR activity were the highest.

**Table 11** Change of electrochemical parameters during stress testing on carbon-based Pt catalysts.<sup>[230, 231]</sup>

Method	Parameter	Pt/rGO	Pt/C	Pt/MWCNT	Pt/C-commercial
CV	$\Delta ECSA_{HUPD} / \%$	-26	-15	-26	-27
	$\Delta Q_{HQ} / \%$	+36	+137	+130	+2426
CO	$\Delta ECSA_{CO} / \%$	-25	-23	-31	-34
Stripping	$\Delta C_{DL} / \%$	+12	+158	+18	-4
ORR	$\Delta E_{onset} / \%$	-2	-1	-1	-4
	$\Delta MA / \%$	-38	-37	-34	-63
	$\Delta SA / \%$	-16	-28	-11	-49

### 5.3.2 Pt Catalyst based on Activated Carbon from HTC

Coconut shells were used for hydrothermal carbonization to form a dark brown coal.<sup>[147]</sup> Pyrolysis resulted into an activated carbon, which was physically characterized in Section 5.1.2. This activated carbon is used the first time as support for Pt particles and tested on its electrochemical suitability and stability for ORR. Initial cyclic and CO stripping voltammetry and the ORR analysis are presented in Section 5.3.2.1. Degradation after exposure to electrochemical stress is discussed in Section 5.3.2.2.

#### *5.3.2.1 Initial Characterization of Pt Catalyst based on Activated Carbon from HTC*

To better understand the newly developed HTC-C, the Pt/HTC-C catalyst and the HTC-C support are electrochemically investigated in the same way. A similar electrochemical characterization for a carbon obtained from HTC of D-glucose was done by Taleb et al.<sup>[146]</sup> and serves for comparison to this work. Their synthesis and material properties is described in Section 3.2.4.1.1.

Cyclic and CO stripping experiments are depicted in Figure 49a. For Pt/HTC-C hydrogen reactions take place in the potential range of 0.0–0.4 V<sub>RHE</sub>, while above 0.4 V<sub>RHE</sub> the oxygen reactions take place. The CO oxidation is located at 0.86 V<sub>RHE</sub>, however, a shoulder at the lower potential side analogous to the others in Figure 42 does not appear. Rather one symmetric signal is detected. The Pt particle nanostructure onto the substrates was shown to be comparable in Section 5.2.1 and is excluded as impact on the CO stripping. Absence of a shoulder at lower potential due to the lower Pt loading of 8.3 wt% compared to 14.4–23.1 wt% is more reasonable. Literature reported a lowered onset potential of CO oxidation on Pt particle aggregates instead of isolated single particles.<sup>[173, 273, 282]</sup> At a lower Pt loading the possibility that Pt nanoparticles meet each other onto the support is more improbable.

ECSA values of Pt/HTC-C are determined by use of HUPD and CO counting  $54 \text{ m}^2 \text{ g}_{\text{Pt}}^{-1}$  and  $83 \text{ m}^2 \text{ g}_{\text{Pt}}^{-1}$ , respectively. The average of  $69 \text{ m}^2 \text{ g}_{\text{Pt}}^{-1}$  is in the same range of the other carbon-based catalysts of this work. Taleb et al.<sup>[146]</sup> used the HUPD method and found the electrochemical surface area of their HTC derived Pt catalyst to be only  $23 \text{ m}^2 \text{ g}_{\text{Pt}}^{-1}$ . This can be the consequence of the untypical high Pt loading of 74 wt% they used. High amounts of Pt nanoparticles on a substrate are known to decrease the ECSA due to high coalescence.<sup>[273]</sup> In comparison the Pt loading within Pt/HTC-C here is 8.3 wt%.

Analysis of the double layer capacitance was carried out using the curves with adsorbed CO in Figure 49b. Pt/HTC-C possesses a capacitance of  $1.7 \text{ mF cm}^{-2}$ , which is larger than the values between  $0.7\text{--}1.2 \text{ mF cm}^{-2}$  for previously tested Pt/MWCNT, Pt/C or Pt/C-commercial. However, the DL capacitance is by a factor of 5 smaller compared to Pt/rGO. Two characteristics from Table 7 can impact the double layer capacitance. HTC-C possesses the largest specific surface area of  $546 \text{ m}^2 \text{ g}_{\text{Pt}}^{-1}$ , which enhances the double layer capacitance.<sup>[281]</sup> On contrary, HTC-C possesses the lowest amount of oxygen groups onto its surface, which can reduce the double layer capacitance.<sup>[281]</sup> Reduced graphene oxide in comparison has only half of the specific HTC-C surface area, but has a five times higher amount of oxygen groups. Next to comparison of carbon characteristics in terms of the surface area and oxygen content, the deposition of Pt nanoparticles onto the carbons here can further impact  $C_{\text{DL}}$  of HTC-C and rGO, respectively. This is discussed in the next paragraph.

Furthermore, the support is investigated in Figure 49 as well. HTC-C exhibits no electrochemical adsorption/desorption of hydrogen and oxygen species or carbon monoxide in Figure 49a and thus no ECSA. This is expected here for carbon materials, because no chemisorption of hydrogen and oxygen species or CO molecules takes place. However, HQ/Q redox reaction is indicated at around  $0.6 \text{ V}_{\text{RHE}}$ . This is characteristic for carbons from a HTC process.<sup>[146]</sup> While Pt/HTC-C had a double layer capacitance of  $1.7 \text{ mF cm}^{-2}$  in Figure 49b, HTC-C gives a four times higher value of  $6.7 \text{ mF cm}^{-2}$ . This demonstrates that incorporation of Pt nanoparticles into the porous HTC-C network goes along with a reduced capacitance. The platinum particles possibly close pores, which would cause a reduced porosity and hence a reduced  $C_{\text{DL}}$ . A same trend was found in the study of Taleb et al.<sup>[273]</sup> The capacitance of their HTC derived carbon decreased by 30 % due to the platinum

deposition. They argued a lower carbon mass fraction in the Pt catalyst compared to the support only.

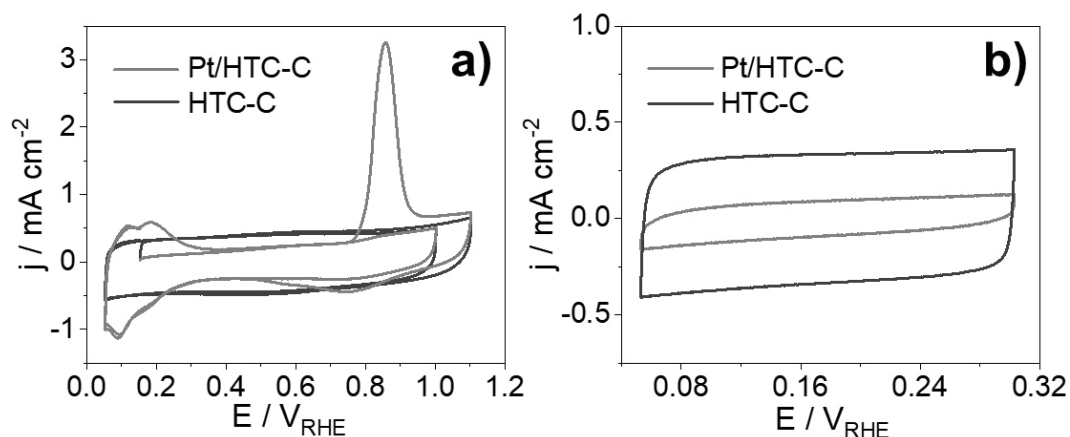


**Figure 49** Cyclic and CO stripping voltammetry of Pt/HTC-C catalyst and HTC-C support in comparison (a). CV of Pt/HTC-C catalyst and HTC-C support after CO sorption (b).

ORR analysis is done in Figure 50. In the potential range below approximately  $0.6 V_{\text{RHE}}$ , the diffusion-limited current density depends on the applied rotation speed of the RDE. The K-L plot shows linear dependency and gives access to the number of transferred electrons in ORR. The number of electrons counts 3.8 for Pt/HTC-C and is related to the ORR mechanism involving four electrons. This is typical for Pt catalysts and comparable to the previously tested catalysts of Section 5.3.1.1.

The catalytic activity for ORR is analyzed by use of the curves in Figure 50. HTC-C shows a negligible catalytic activity, whereas Pt/HTC-C shows an activity but with deviation to previous catalysts from Section 5.3.1.1. While the onset potentials for the others in Table 10 were between  $0.99\text{--}1.01 \text{ mV}$ , the onset potential for Pt/HTC-C is with  $0.94 V_{\text{RHE}}$  significantly lower. Other HTC based catalyst from literature exhibited the ORR onset in the same range between  $0.90\text{--}0.95 V_{\text{RHE}}$ .<sup>[146]</sup> Mass activity and specific activity of Pt/HTC-C have negligible values of  $2.0 \text{ A g}_{\text{Pt}}^{-1}$  and  $0.004 \text{ mA cm}^{-2}$ . Although the ECSA of Pt/HTC-C is in the same level as the others, the catalytic activity is much lower. Since the experimental details and the Pt particle characteristics are similar in this work, the effect should be related to the support material. Indeed, HTC-C possesses the lowest degree of graphitization as well as the lowest electrical conductivity in this study,

which is pointed out by the physical parameters of carbons in Table 7. This might hinder the charge transfers during ORR<sup>[58]</sup> and enlarge rate-determining steps.

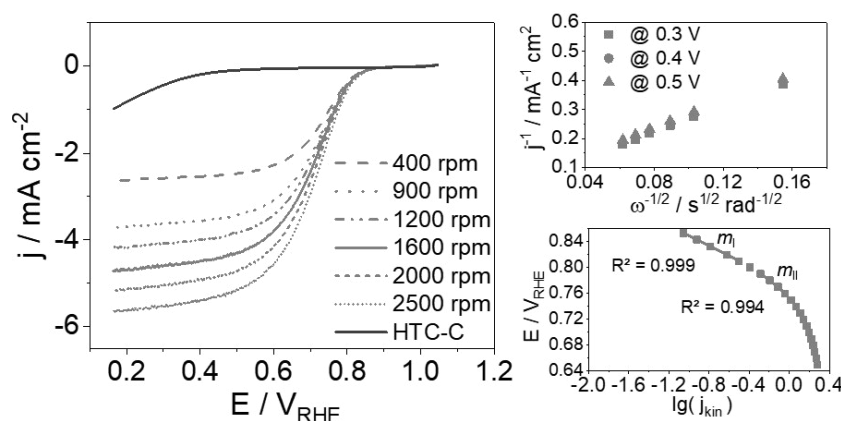


**Figure 50** ORR data of Pt/HTC-C catalyst and HTC-C support. Cathodic scans at different rotation speeds with K-L and Tafel plots for Pt/HTC-C and at 1,600 rpm for HTC-C.

Last, the Tafel plot is shown in Figure 50 and shows a curve progress similar to previous catalysts in Figure 44. Two slopes are identified. A slope  $m_{II}$  of  $-123 \text{ mV dec}^{-1}$  is calculated within the second region, which is very close to slopes in Table 10 of the other carbon-based catalysts before. However, the first slope  $m_I$  is  $-78 \text{ mV dec}^{-1}$  and differs from the others by approximately 30 %. Basically, the reduction reaction mechanism of  $\text{O}_2$  depends on the electrode potential as discussed in Section 3.2.2 and hence on the degree of Pt surface oxidation.<sup>[20, 61]</sup> Because ORR starts in this case at a lower potential of  $0.94 \text{ V}_{\text{RHE}}$ , Tafel analysis is carried out in a lower potential region of  $0.80\text{--}0.85 \text{ V}_{\text{RHE}}$  with less surface oxides on platinum, so that  $m_I$  increases.

The HTC based catalyst of Taleb et al.<sup>[146]</sup> had the onset potential for ORR in same range between  $0.90\text{--}0.95 \text{ V}_{\text{RHE}}$ . Their Tafel analysis was carried out within the potential range of  $0.90\text{--}1.00 \text{ V}_{\text{RHE}}$  and gave a higher slope  $m_I$  of  $-102 \text{ mV dec}^{-1}$  within this region. This larger slope indicates a lower reaction rate for  $\text{O}_2$  reduction of their HTC based catalyst compared to Pt/HTC-C from this study.

### 5.3.2.2 Degradation of Pt Catalyst based on Activated Carbon from HTC

After initial characterization, the focus is on the verification of the catalyst stability. Selected potential cycles during AST of Pt/HTC-C in Figure 51a are compared to analogous cycles of HTC-C in Figure 51b. Both materials underlie enormous changes of the carbon. First, capacitive current densities at approximately 0.3–0.4  $V_{\text{RHE}}$  increase during stress testing, and second, the amount of HQ/Q redox reaction at around 0.6  $V_{\text{RHE}}$  rises.

The *in-situ* ECSA change is depicted as inset in Figure 51a. Two particularities become apparent. First, the loss of electrochemical surface area here is twice as high as the loss for the other materials in Figure 45. Second, the catalyst degrades exponentially, starting with higher ECSA loss at beginning and lower ECSA loss at the end. This exponential behavior in ECSA is observed for all carbon-based catalysts in this work and explained by stronger instability of the small initial Pt particles compared to the larger aged particles.<sup>[97]</sup> In the following paragraphs initial and final Pt/HTC-C characterization before and after AST is contrasted to assess the degradation in detail.

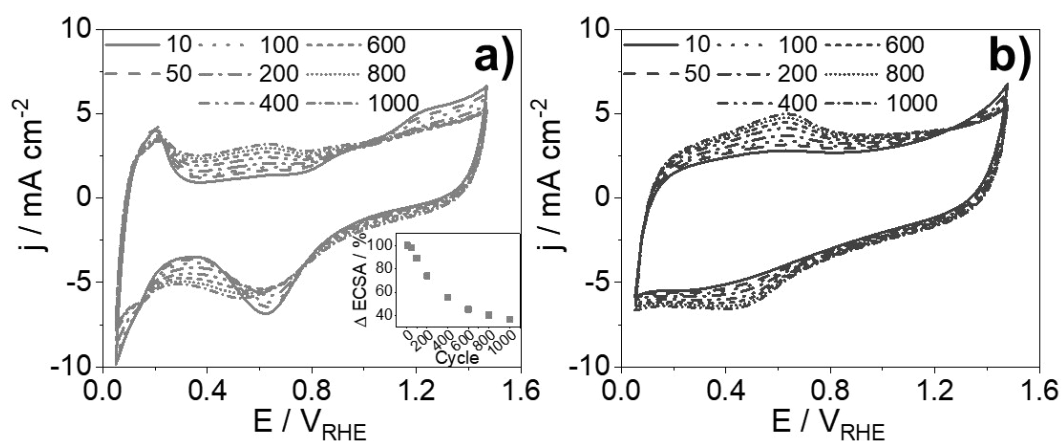


**Figure 51** Selected potential cycles during AST with inset of ECSA change for Pt/HTC-C catalyst (a) and HTC-C support (b).

Figure 52 shows double layer capacitances for the Pt/HTC-C catalyst and for HTC-C support before and after exposure to stress. The support exhibits an increase of +48 %, whereas Pt/HTC-C catalyst shows an increase of +208 %. Two effects of platinum might cause the enhanced raise in double layer capacitance for Pt/HTC-C. First, degradation of platinum in terms of dissolution, detachment or migration according to Figure 6 might re-open pores of the support and enhances the electrode porosity again. Or second, the Pt nanoparticles catalyze and enforce the degradation of HTC-C support as reported in literature<sup>[18, 19]</sup> and further illustrated in Figure 8. Overall, the capacitance change of +208 % for Pt/HTC-C presents the largest increase among all tested carbon-based Pt catalysts.

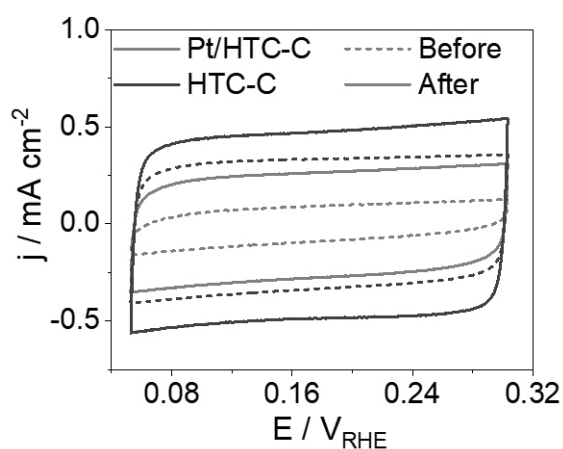


**Figure 52** Cyclic voltammetry of Pt/HTC-C catalyst and HTC-C support after CO sorption. Comparison of curves before and after AST.

Figure 53a illustrates cyclic and CO stripping voltammetry on Pt/HTC-C before and after stress testing and shows insets enlarging the HQ/Q redox activity. Redox activity of HQ/Q is more pronounced after the potential cycling. The signal integration of HQ oxidation before and after AST gives an increased charge by factor of 17. In comparison, the support without Pt nanoparticles on its surface shows an increase by a factor of 9, which is much lower. This corresponds to previous observations regarding the double layer capacitance and evidences the platinum influence on the HTC-C corrosion. In sum, two reinforcing factors for support degradation come together. Next to the mentioned catalyzed carbon corrosion through platinum,<sup>[18, 19]</sup> the type of carbon is crucial for the electrochemical stability. High surface area and rare graphitization impose carbon instability.<sup>[122, 127, 130]</sup> HTC-C was physically identified in Table 7 to be a high amorphous and defective carbon with the largest specific surface area in this study.

Figure 53a additionally shows the signal change of hydrogen, oxygen and carbon monoxide reactions on platinum due to the catalyst degradation. Lowered signals in the hydrogen range and a lowered oxidation signal of previously adsorbed CO are detected. One peak resulting from CO oxidation is centered at  $0.86 V_{\text{RHE}}$  before stress testing, however, peak position and peak shape changed after stress testing. That means that the signal is positively shifted to  $0.88 V_{\text{RHE}}$  and exhibits a distinct asymmetry due to an arisen shoulder at lower potential side. So, catalyst degradation is visible here as reduced signal intensity and an altered signal shape. 65 % of ECSA is lost calculated by HUPD, and 68 % of ECSA is lost determined by CO sorption. This is more than twice as high as the losses of the other catalysts between 19–31 %. This enforced Pt degradation is believed to be the result of significant electrochemical HTC-C support instability.

Figure 53b depicts the ORR curves with Tafel plots. The onset potential is negatively shifted by 10 % from  $0.94$  to  $0.85 V_{\text{RHE}}$ . The other onset potentials in Table 11 were negatively shifted by only 1–4 %, so that the oxygen reduction on Pt/HTC-C is more affected caused by its enforced degradation. The Tafel plot illustrates the increased overpotential for ORR due to a curve downshift to lower potential values. The slopes in region I and II are unchanged. This demonstrates the same ORR mechanism catalyzed by Pt/HTC-C before and after exposure to stress.

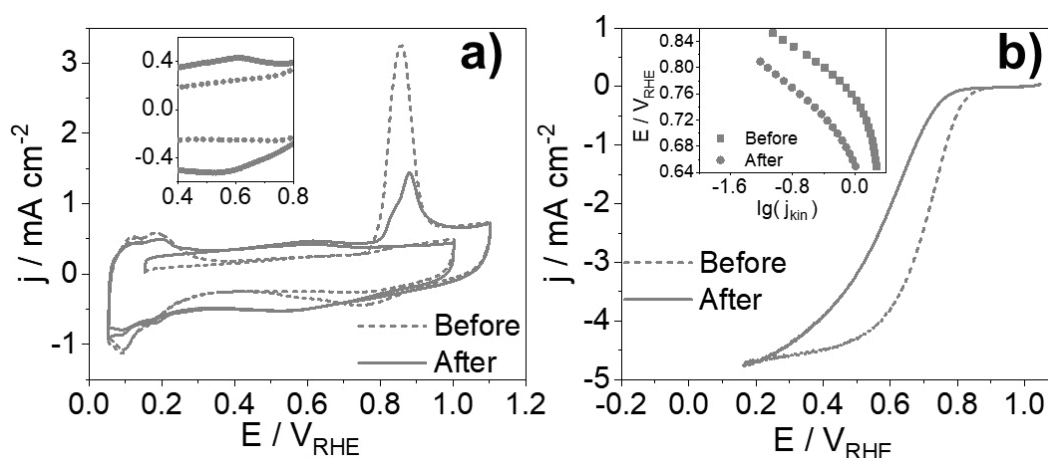


**Figure 53** Comparison of cyclic and CO stripping voltammetry curves before and after AST with insets of HQ/Q redox activities for Pt/HTC-C (a) and comparison of cathodic ORR scans at 1,600 rpm before and after AST with insets of Tafel plots for Pt/HTC-C (b).

In summary, two support characteristics of HTC-C are noticeably different to common carbon black and alternative rGO and MWCNTs. First, the lowest graphitic degree plays an important role for stability here. This was reported for Vulcan<sup>®</sup> XC72R, which was exposed to thermal annealing at 2,800 °C to reduce the carbon corrosion.<sup>[22]</sup> Furthermore, Pt particles on the thermally treated and thus more graphitized sample showed less Pt agglomeration than particles on the untreated sample. That means that less carbon corrosion leads to less Pt degradation.<sup>[22, 131]</sup> Second, HTC-C possesses by far the largest specific surface area, which causes a larger area for electrochemical attacks and in consequence larger support degradation followed by larger Pt degradation.<sup>[22, 131]</sup> In accordance to the scheme of Figure 8, which summarizes the recent state of degradation research, it has to be noticed that the mutual influences of Pt and carbon degradation are highly complex and need more research. Also, HTC-C might be optimized as Pt support in PEMFCs. Studies on thermal post-treatments to tune the electrochemical characteristics can be useful.

### 5.3.3 Pt Catalysts based on Nanocomposites

Physical characterization of the composite-based materials Pt/ITO-rGO and Pt/FTO-rGO was presented in Section 5.1.3 with focus on the support structure and in Section 5.2.2 with focus on Pt nanoparticle distribution onto the composites. This chapter discusses initial electrochemical characteristics of the composites in Section 5.3.3.1 and their degradation after electrochemical stress in Section 5.3.3.2. Finally, identical location TEM in Section 5.3.3.3 gives insight into the degradation of complex Pt-metal oxide-carbon structures.

#### *5.3.3.1 Initial Characterization of Pt Catalysts based on Nanocomposites*

Figure 54a demonstrates cyclic and CO stripping voltammetry for Pt/ITO-rGO catalyst and ITO-rGO support, whereas Figure 54b shows appropriate curves for Pt/FTO-rGO catalyst and FTO-rGO support. While CV curves of both composite catalysts are very similar, CO stripping deviates from each other. In Figure 54a, oxidation of previously adsorbed CO on Pt/ITO-rGO starts already at around 0.4 V<sub>RHE</sub> and results into an asymmetric peak with a maximum at 0.74 V<sub>RHE</sub>.

Thus, the peak is located at lower potentials compared to previous carbon-based materials in Figure 42. Especially the comparison to similar Pt/rGO without the metal oxide reveals a shifted peak maximum by 140 mV. The Pt particles of Pt/rGO and Pt/ITO-rGO showed their comparability in TEM and XRD analysis of Section 5.2.1. Hence, the presence of Sn-doped  $\text{In}_2\text{O}_3$  as only difference influences the CO stripping experiment. The negative potential shift demonstrates a weaker CO adsorption on Pt and thus an improved tolerance against carbon monoxide for Pt/ITO-rGO in contrast to Pt/rGO.

CO stripping on the other composite Pt/FTO-rGO is depicted in Figure 54b and leads to two individual signals with similar intensities at 0.76 and 0.86  $V_{\text{RHE}}$ . The peak at 0.86  $V_{\text{RHE}}$  is similarly located to the peak of Pt/rGO at 0.88  $V_{\text{RHE}}$  in Figure 42. CO oxidation on Pt being in contact with rGO is believed to occur here. The peak at 0.76  $V_{\text{RHE}}$  is suggested to arise from CO oxidation on Pt being in contact with FTO. Ruiz Camacho et al.<sup>[194]</sup> investigated Pt catalysts based on composites with carbon black and metal oxides by CO stripping voltammetry and *in-situ* IR absorption spectroscopy. They also observed lowered potentials for CO stripping, when metal oxides were incorporated into the catalysts. Increased stretching frequencies of CO on Pt/SnO<sub>2</sub>-C than on Pt/C are reported. They suggested the electronic influence of metal oxides like SnO<sub>2</sub> on platinum, which causes a reduced electron donation from Pt to CO and in turn a lowered adsorption energy for carbon monoxide on Pt. The weaker CO sorption causes a negative CO peak shift in voltammetry experiments. Next to electronic influences of SnO<sub>2</sub> on Pt, the presence of hydroxy groups is believed to impact the CO oxidation.<sup>[141]</sup> Basically, CO oxidation mechanism is described to involve Pt surface oxygen species,<sup>[250, 251]</sup> which appears at a potential higher 0.6  $V_{\text{RHE}}$ .<sup>[20]</sup> However, OH groups on metal oxides can promote CO oxidation already in a lower potential range.<sup>[25]</sup> XPS in Figure 35 revealed hydroxy surface species on ITO and FTO nanoparticles.

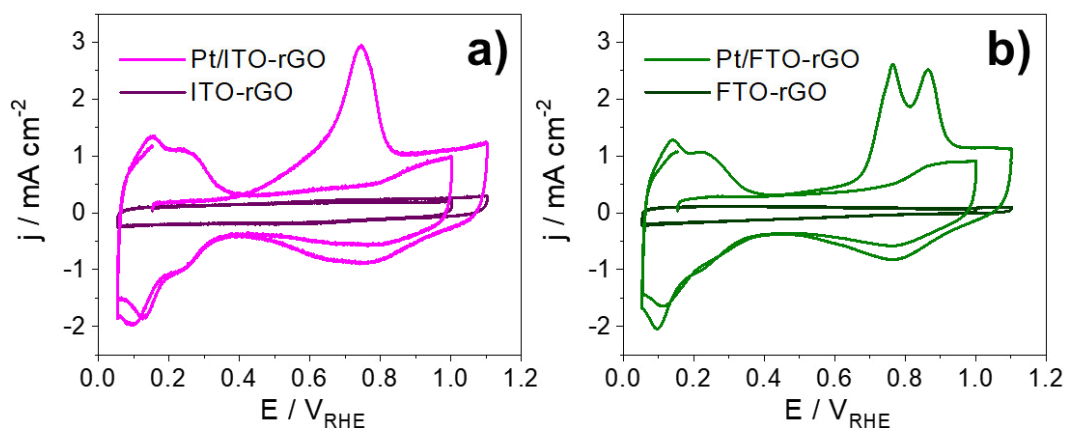


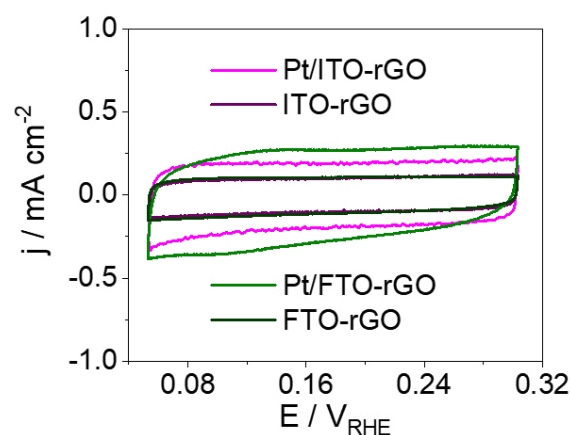
**Figure 54** Cyclic voltammetry and CO stripping voltammetry for Pt/ITO-rGO catalyst and ITO-rGO support (a) and for Pt/FTO-rGO catalyst and FTO-rGO support (b) in comparison.

ECSAs from Table 12 are averaged and count  $51 \text{ m}^2 \text{ g}_{\text{Pt}}^{-1}$  for Pt/ITO-rGO and  $46 \text{ m}^2 \text{ g}_{\text{Pt}}^{-1}$  for Pt/FTO-rGO. Thus, the surface areas of composite-based materials are lower than the areas of carbon-based materials. Direct comparison to Pt/rGO showing  $75 \text{ m}^2 \text{ g}_{\text{Pt}}^{-1}$  clarifies the ECSA decrease by 32 % and 39 %, so that the incorporated metal oxide particles affect the electrochemical surface area of Pt. Electrical conductivity and specific surface area are impact factors on the ECSA. Comparing Table 7 with Table 8, both parameters are lower for the composites than for rGO.

Furthermore, HUPD and CO stripping give a higher ECSA for Pt/ITO-rGO including Sn-doped  $\text{In}_2\text{O}_3$  particles than for Pt/FTO-rGO including F-doped  $\text{SnO}_2$  particles. During EDS mapping in Figure 41 Pt on ITO-rGO seemed to have the preferred interaction with rGO instead of ITO. In contrast, Pt on FTO-rGO had the preferred interaction with FTO. Based on the higher ECSA of Pt/rGO, it is suggested that the stronger Pt location onto the carbon in case of ITO-rGO benefits to the enhanced ECSA compared to Pt/FTO-rGO, which showed a preferred Pt location on FTO instead of the carbon. In comparison ITO-rGO and FTO-rGO without platinum were tested analogously and show no electrochemical surface during CV and CO stripping measurements in Figure 54.

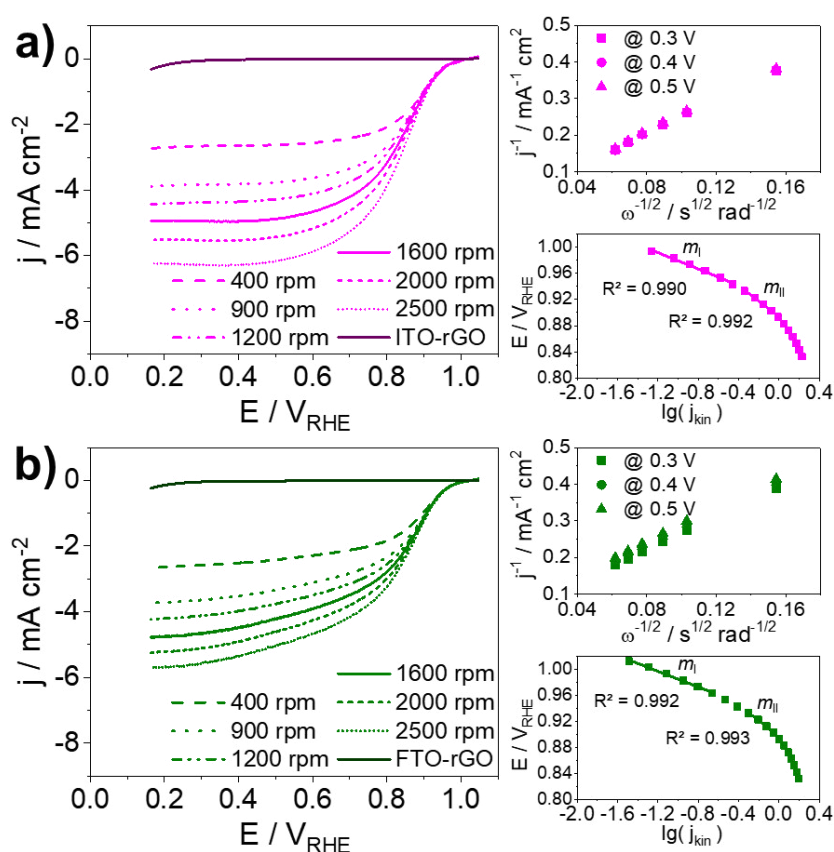
A further observation is that the known HQ/Q redox activity of rGO at around  $0.6 V_{\text{RHE}}$  is not visible to that extent in Figure 54 as the HQ/Q redox activity of Pt/rGO in Figure 42. This proves that metal oxide particles are anchored to the oxygen groups of rGO. Released charges during oxidation of HQ species are  $217 \mu\text{C cm}^{-2}$  for Pt/rGO and in comparison  $32 \mu\text{C cm}^{-2}$  for Pt/ITO-rGO. In case of Pt/FTO-rGO the HQ/Q redox reaction is absent. During the TEM and the XPS analysis of Section 5.1.3 the FTO particles were shown to highly cover rGO and to constitute the main part of the composite surface. ITO particles were shown to cover rGO as well, however, leaving behind a more vacant carbon surface.

Figure 55 highlights the curves recorded during CO sorption. The capacitive current densities are highly similar for the supports ITO-rGO and FTO-rGO. Current densities of the related Pt catalysts are larger, whereas a larger current is measured for Pt/FTO-rGO than for Pt/ITO-rGO. Double layer capacitances in Table 12 are  $5.1 \text{ mF cm}^{-2}$  for Pt/FTO-rGO and  $3.7 \text{ mF cm}^{-2}$  for Pt/ITO-rGO, which is by factors of 1.8 and 2.4 lower than  $8.9 \text{ mF cm}^{-2}$  in case of Pt/rGO without the metal oxides. This observation is well in line with reduced specific surface areas for the composites compared to rGO as discussed in Section 5.1.3. It is caused by the precipitation of metal oxides, which usually have less porosity than graphitic carbons.<sup>[197]</sup>



**Figure 55** Cyclic voltammetry of Pt/ITO-rGO catalyst and ITO-rGO support as well as Pt/FTO-rGO catalyst and FTO-rGO support after CO sorption.

The RDE experiments are contrasted in Figure 56. The current density of oxygen reduction below approximately  $0.8 V_{\text{RHE}}$  is seen to depend on the rotation speed of the electrode. On this basis, K-L plots at 0.3, 0.4 and 0.5  $V_{\text{RHE}}$  show linearity for both composites and result in transferred electrons per reduced  $\text{O}_2$  molecule of 3.7 and 3.8, respectively. Hence, these nanocomposite-based catalysts are proven to involve four electrons during ORR as stated for Pt.<sup>[278]</sup> This confirms to the  $4e^-$  pathway of ORR shown for all catalysts under study. Figure 56 further depicts the Tafel relations. Linear fitting in potential ranges of about 0.95–1.00  $V_{\text{RHE}}$  and 0.90–0.95  $V_{\text{RHE}}$  gives the slopes in Table 12, which are very close to slopes of the carbon-based catalysts in Table 10 and very close to reference slopes from literature.<sup>[58]</sup> Pt/ITO-rGO has slopes of  $-63 \text{ mV dec}^{-1}$  and  $-119 \text{ mV dec}^{-1}$ , while Pt/FTO-rGO has slopes of  $-60 \text{ mV dec}^{-1}$  and  $-121 \text{ mV dec}^{-1}$ . So, the same mechanism of ORR catalysis for composite-based and for carbon-based catalysts is evinced by Tafel evaluation.



**Figure 56** ORR data of Pt catalysts based on nanocomposites. Cathodic scans at different rotation speeds with K-L and Tafel plots for Pt/ITO-rGO and at 1,600 rpm for ITO-rGO (a) and scans for Pt/FTO-rGO and FTO-rGO (b).

In terms of the catalytic activity for O<sub>2</sub> reduction, Table 12 provides the values of onset potentials, mass activities and specific activities. While onsets for oxygen reduction are highly comparable between 1.00–1.01 V<sub>RHE</sub>, the kinetic current densities at 0.9 V<sub>RHE</sub> and thus the normalized mass and specific activity values are different between the composites. Both values are higher for the FTO-containing material showing 49.9 A g<sub>Pt</sub><sup>-1</sup> and 0.095 mA cm<sup>-2</sup> than for the ITO-containing material showing 34.6 A g<sub>Pt</sub><sup>-1</sup> and 0.059 mA cm<sup>-2</sup>.

If the preferred interaction of Pt particles with FTO particles from EDS is considered, influences of this interaction on ORR activity is supposed. Kinumoto et al.<sup>[283]</sup> tested SnO<sub>2</sub>/carbon supports in different ratios. The highest ORR activity is reported in case of the largest SnO<sub>2</sub> amount. Zhang et al.<sup>[47]</sup> observed a boosting effect of SnO<sub>2</sub> on the ORR catalysis as well. In this work higher mass and specific activity for Pt/FTO-rGO containing F-SnO<sub>2</sub> compared to Pt/ITO-rGO containing Sn-In<sub>2</sub>O<sub>3</sub> is found, so that the type of metal oxide plays a crucial role for catalytic activity. Although SnO<sub>2</sub> supports without any doping were already shown to positively impact the ORR activity as reviewed in Section 3.2.4.2, fluorine-doping was shown to be useful for enhancing the electrical conductivity of the support.<sup>[203]</sup> Overall, ORR activities of the nanocomposites here are in same range as carbon-based catalysts from Section 5.3.1, so that a large effect on ORR due to the utilization of metal oxides is not observed.

**Table 12** Electrochemical parameters of Pt catalysts based on nanocomposites.<sup>[230, 231]</sup>

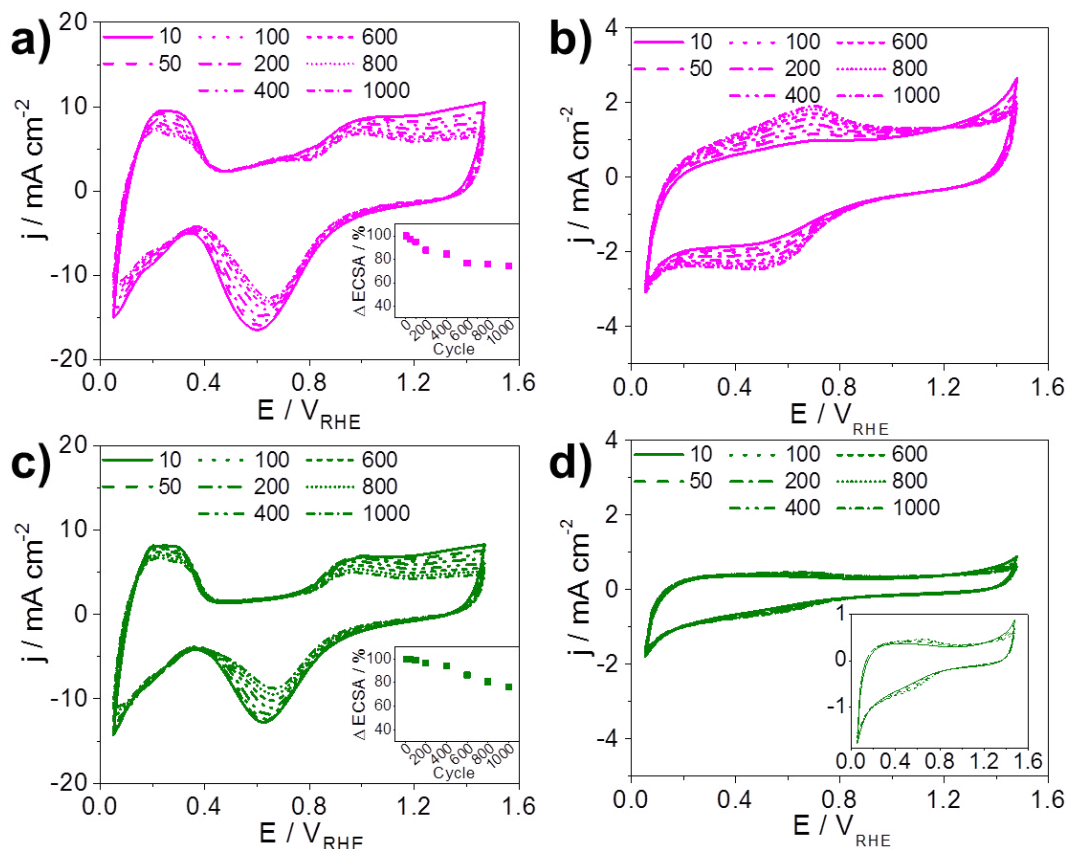
Method	Parameter	Pt/ITO-rGO	Pt/FTO-rGO
CV	$ECSA_{HUPD} / m^2 g_{Pt}^{-1}$	58	53
	$Q_{HQ} / \mu C cm^{-2}$	32	0
CO	$ECSA_{CO} / m^2 g_{Pt}^{-1}$	43	38
Stripping	$C_{DL} / mF cm^{-2}$	3.7	5.1
ORR	$E_{onset} / V$	1.00	1.01
	$MA / A g_{Pt}^{-1}$	34.6	49.9
	$SA / mA cm_{Pt}^{-2}$	0.059	0.095
	$m_I / mV dec^{-1}$	-63	-60
	$m_{II} / mV dec^{-1}$	-119	-121
	$n$	3.7	3.8

### 5.3.3.2 Degradation of Pt Catalysts based on Nanocomposites

After initial characterization, the catalysts were stressed by 1,000 potential cycles. Figure 57 shows selected cycles during the stress testing. To better understand the degradation of self-developed composites the stress test was carried out on composites with and without deposited platinum.

First, Pt/ITO-rGO in Figure 57a and Pt/FTO-rGO in Figure 57c show a pronounced decrease of Pt-related signals, which is observed for all catalysts of this work and indicates Pt aging. The insets depict the ECSA development during stress testing. For carbon-based catalysts in Figure 45 — including Pt/rGO as the same material without the incorporation of metal oxides — stronger losses were visualized during the first cycles than during the progressing cycles. The same trend is observed for Pt/ITO-rGO in Figure 57a. On the contrary, Pt/FTO-rGO in Figure 57c shows a more stable ECSA during the first potential cycles, so that enforced Pt degradation starts after approximately four hundred cycles.

Furthermore, HQ/Q redox activity around  $0.6 V_{\text{RHE}}$  is changed to different extents. Pt/ITO-rGO in Figure 57a and Pt/rGO in Figure 45a have a slight increasing HQ oxidation during increasing number of potential cycles, whereas Pt/FTO-rGO in Figure 57c is remarkably constant in this range. Capacitive current densities of the composites in Figure 57a and c at approximately  $0.4 V_{\text{RHE}}$  are indicated to slightly decrease, whereas capacitive current density of Pt/rGO in Figure 45a is indicated to slightly increase. The right graphs of Figure 57 compare the change of ITO-rGO and FTO-rGO without deposited Pt on them. Here, current density changes of FTO-rGO in Figure 57d are much smaller than the changes of ITO-rGO in Figure 57b. Analysis of Pt and support degradation is detailed in the next paragraphs.



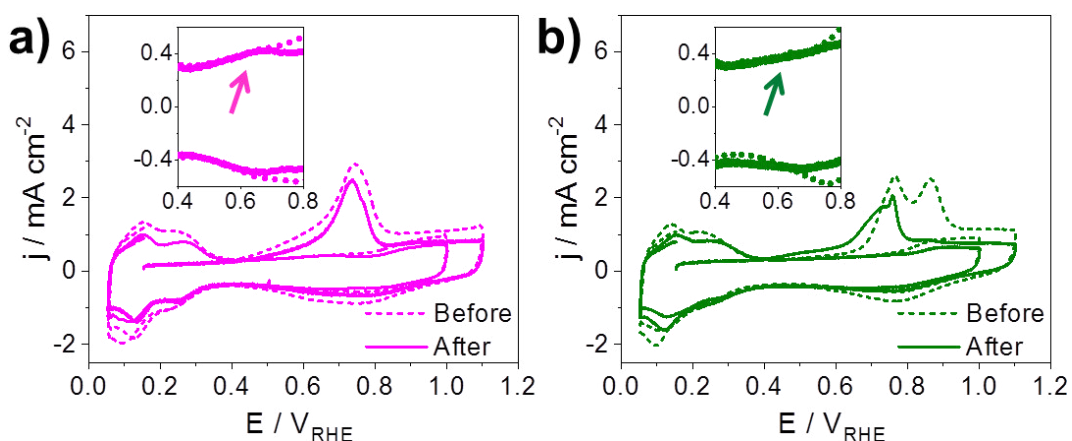
**Figure 57** Selected potential cycles during AST with inset of ECSA change for Pt/ITO-rGO (a) and ITO-rGO (b) and for Pt/FTO-rGO (c) and FTO-rGO (d).

Figure 58 contrasts cyclic and CO stripping voltammetry of Pt/ITO-rGO and Pt/FTO-rGO after potential cycling. CV curves show decreased Pt-related signals in both materials after stress testing. CO stripping experiments show decreased and altered signals of the carbon monoxide oxidation. While CO oxidation does not exhibit a notable change in shape and potential for Pt/ITO-rGO in Figure 58a, the CO oxidation on Pt/FTO-rGO in Figure 58b changed dramatically. The peak at  $0.86 V_{RHE}$  almost disappeared due to stress testing. The other peak at  $0.76 V_{RHE}$  is still present after testing, however, in narrower shape and with less intensity. Instead, CO oxidation now partially appears in a lower potential range. This means that a distinct asymmetry of the signal at  $0.76 V_{RHE}$  on the lower potential side has arisen and a further very broad low intensity peak starts already at  $0.4 V_{RHE}$ .

This illustrates that degradation of platinum on FTO-rGO strongly weakens the CO adsorption. Especially the signal at  $0.86 V_{RHE}$  was assigned to CO interaction with platinum on rGO and is not present anymore after stress testing. An explanation could be that CO adsorption/desorption is strongly influenced by the FTO

particles after AST. To remember, an enhanced CO tolerance was assigned to SnO<sub>2</sub> containing catalysts.<sup>[141]</sup> It is postulated that known Pt degradation like dissolution and re-precipitation events<sup>[15, 71]</sup> occur during the potential cycling and that FTO competes with rGO during these Pt degradation events. This might influence the Pt degradation and re-precipitation. Investigation by IL-TEM in Section 5.3.3.3 later gives microscopic insights into the catalyst degradation. But still we have to consider for interpretation of CO stripping experiments, that various impact factors play a role. Next to impact of the support, Pt surface sites are important as well for CO adsorption/desorption.<sup>[250, 274]</sup> Pt/ITO-rGO in Figure 58a was also subjected to degradation, because the intensity of CO oxidation signal decreased after exposing to 1,000 potential cycles. However, degradation obviously took place with less change of interactions between Pt and ITO-rGO due to comparable peak shape of CO oxidation in Figure 58a.

ECSA losses are listed in Table 13. Pt/ITO-rGO has a 20 % lowered ECSA using HUPD and a 34 % lowered ECSA using CO sorption. Pt/FTO-rGO has a 24 % reduced ECSA using HUPD and a 30 % reduced ECSA using CO stripping. Thus, an average loss of exactly 27 % is given for both composites and is highly comparable with Pt/rGO, which lost 26 % of ECSA. Although electrochemical surface areas of Pt/ITO-rGO and Pt/FTO-rGO during their initial characterization were approximately one third lower than the area of Pt/rGO, differences towards the ECSA stability between Pt/rGO, Pt/ITO-rGO and Pt/FTO-rGO are not distinguishable.



**Figure 58** Comparison of cyclic and CO stripping voltammetry curves with insets of HQ/Q redox activities before and after AST. Pt/ITO-rGO (a) and Pt/FTO-rGO (b).

Figure 58 further shows insets with a zoomed potential range in CV curves, where HQ/Q redox activity is visible. For both composites HQ/Q signals are negligible before exposure to electrochemical stress (dashed line). For Pt/ITO-rGO in Figure 58a HQ/Q redox activity is arisen after AST (solid line). This indicates partial oxidation of the carbon surface in Pt/ITO-rGO. On the contrary, Pt/FTO-rGO in Figure 58b still shows the absence of such a signal after AST (solid line), so that no redox active oxygen species is formed during potential cycling.

Basically, HQ/Q redox activity is known for rGO<sup>[272]</sup> and was shown for this study in Figure 46. And metal oxides were shown to suppress HQ/Q redox activity of rGO in Figure 54, where fresh Pt/ITO-rGO and fresh Pt/FTO-rGO were discussed. This behavior stays unchanged for Pt/FTO-rGO but changed for Pt/ITO-rGO during potential cycling caused by two possible reasons. First, EDS demonstrated that platinum does not prefer the deposition on ITO particles. In consequence, Pt must be deposited in higher extent on rGO and is known to catalyze carbon corrosion.<sup>[19, 127]</sup> Second, Liu et al.<sup>[205]</sup> reported disappeared parts of ITO after very similar potential cycling. Schmies et al.<sup>[209]</sup> furthermore localized ITO dissolution and re-precipitation at potentials below 1.0 V<sub>RHE</sub>. Thus, oxygen surface groups of rGO may anchor less ITO particles so that HQ/Q redox activity becomes visible again. IL-TEM gives insights into the catalyst aging later.

Furthermore, Geiger et al.<sup>[211]</sup> directly compared ITO and FTO dissolution in the fuel cell relevant potential window and reported higher stability of FTO. Indeed FTO reliably protects rGO from corrosion here, because HQ/Q redox reaction is still absent in Figure 58 even after harsh potential cycling. As a reminder, Pt/rGO without incorporated metal oxides had highly visible HQ/Q redox activity and an additional increase of Q<sub>HQ</sub> due to stress testing.

**Table 13** Change of electrochemical parameters due to stress testing on Pt catalysts based on nanocomposites.<sup>[230, 231]</sup>

Method	Parameter	Pt/ITO- rGO	Pt/FTO- rGO
CV	$\Delta ECSA_{HUPD} / \%$	-20	-24
	$\Delta Q_{HQ} / \%$	+568	$\pm 0$
CO	$\Delta ECSA_{CO} / \%$	-34	-30
Stripping	$\Delta C_{DL} / \%$	-10	-8
ORR	$\Delta E_{onset} / \%$	-1	-2
	$\Delta MA / \%$	-25	-57
	$\Delta SA / \%$	-7	-43

Figure 59 in combination with Table 13 shows the change in DL capacitances. They are slightly reduced by -10 % and -8 % for Pt/ITO-rGO and Pt/FTO-rGO, whereas the capacitance of Pt/rGO in Table 11 was increased by +12 %. These opposite trends must be traced back to the presence of ITO and FTO, respectively. Furthermore, if the higher capacitance of untested Pt/rGO with  $8.9 \text{ mF cm}^{-2}$  is compared to untested composites with  $3.7 \text{ mF cm}^{-2}$  and  $5.1 \text{ mF cm}^{-2}$ , the absolute  $C_{DL}$  change of Pt/rGO is more pronounced than changes of Pt/ITO-rGO and Pt/FTO-rGO. So, incorporation of metal oxides leads to a more constant double layer capacitance. For Pt/rGO, an increasing  $C_{DL}$  can be caused by carbon corrosion known for enhancing porosity and oxygen surface groups. For Pt/ITO-rGO and Pt/FTO-rGO, the very slight decreasing  $C_{DL}$  might be caused by platinum particle or metal oxide particle aging. Larger particles due to degradation have of course lower surface areas.

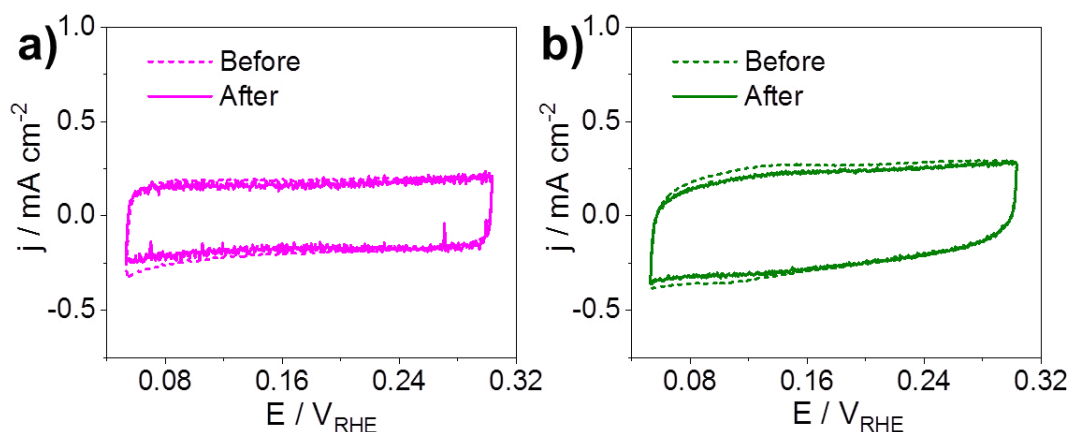


**Figure 59** Comparison of CV curves after CO sorption before and after AST. Pt/ITO-rGO (a) and Pt/FTO-rGO (b).

Last, Figure 60 compares the ORR data. Both materials contain increased overpotentials for  $\text{O}_2$  reduction due to the stress test, which is visible through the negative curve shift to lower potentials. The insets show Tafel plots containing this potential shift. Tafel slopes are unchanged so that ORR mechanisms for both catalysts are not affected by the stress test. Changes in onset potential, mass activity and specific activity are listed in Table 13. On the one hand, the fresh FTO-containing catalyst showed a more than 30 % higher specific activity for ORR than fresh ITO-containing catalyst in Table 12. On the other hand, activity losses in Table 13 caused by degradation are more pronounced for Pt/FTO-rGO despite comparable ECSA losses. Pt/ITO-rGO lost 25 % of mass activity and 7 % of specific activity, while Pt/FTO-rGO lost 57 % of mass activity and 43 % of specific activity.

The very low change of specific activity of 7 % for Pt/ITO-rGO demonstrates the decreased ECSA as main cause for the activity loss. However, this is not the case for activity loss of Pt/FTO-rGO, whose specific activity changed much stronger by 43 %. Next to a change in ECSA, additional degradation effects must be relevant. For instance, CO stripping experiments in Figure 58 showed remarkably changed CO sorption, which indicates changed electronic states in Pt-FTO-rGO interaction. Basically,  $d$ -electronical interaction appears between  $\text{SnO}_2$  and Pt nanoparticles,<sup>[25, 47]</sup> which can change the electronic band structure of platinum and influence the chemisorption of  $\text{O}_2$  or CO molecules. For ORR, downshifting the  $d$ -band state of platinum is reported to enhance the catalytic activity.<sup>[67-69]</sup> Here, degradation of platinum takes place during the stress test. The paths illustrated in Figure 6 could appear due to potential cycling and include Pt dissolution and re-

precipitation or the migration of Pt particles. Thereby, Pt anchoring to other sites of the support is assumed, so that especially  $d$ -electronical interaction between FTO substrate and Pt catalyst can be changed. This might affect the activity for ORR. Moreover, surface sites of FTO and Pt particles can alter provoked by potential cycling, which might cause a different catalyst–substrate interaction. Change of Pt and FTO particles regarding their location on rGO after the test is investigated by IL-TEM in the next section.

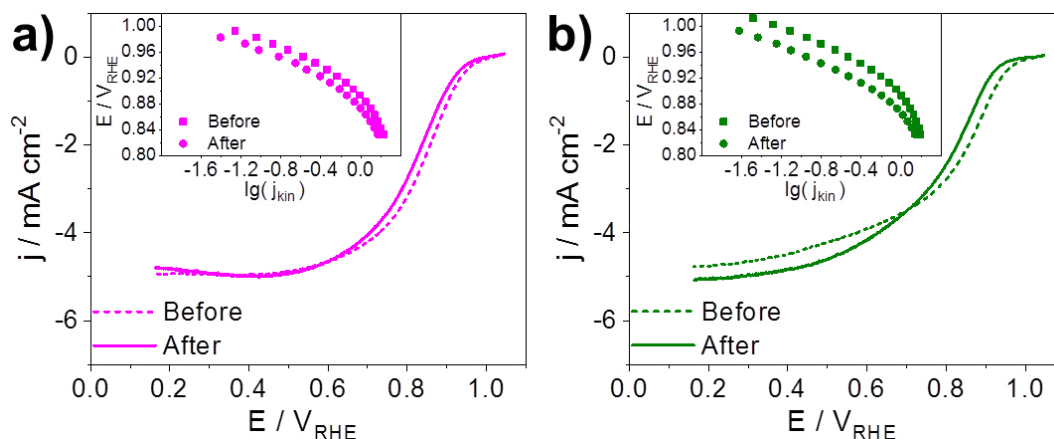


**Figure 60** Comparison of cathodic ORR scans at 1,600 rpm with insets of Tafel plots before and after AST. Pt/ITO-rGO (a) and Pt/FTO-rGO (b).

### 5.3.3.3 Identical Location TEM of Pt Catalysts based on Nanocomposites

IL-TEM was carried out to confirm electrochemical results. The same accelerated stress test of Figure 19 was performed using a TEM grid onto the working electrode instead of the RDE. Figure 61 contrasts the same part of catalyst before and after 1,000 potentials cycles for Pt/rGO, Pt/ITO-rGO and Pt/FTO-rGO. The images are going to be discussed on degradation phenomena but not on changes in Pt particle sizes. Gold originating from TEM grid may dissolve and precipitate elsewhere during the exposure to cycling up to  $1.47 V_{\text{RHE}}$ . This hampers the evaluation of Pt particle sizes.<sup>[284, 285]</sup>

Figure 61a depicts Pt/rGO before and after electrochemical stress. Before the test, Pt particles on rGO are highly distributed. After the test, platinum appears in large agglomerates. Inside the marked area (1) the Pt particles were well-dispersed before AST. After AST, the Pt nanoparticles merged together. These degradation pro-

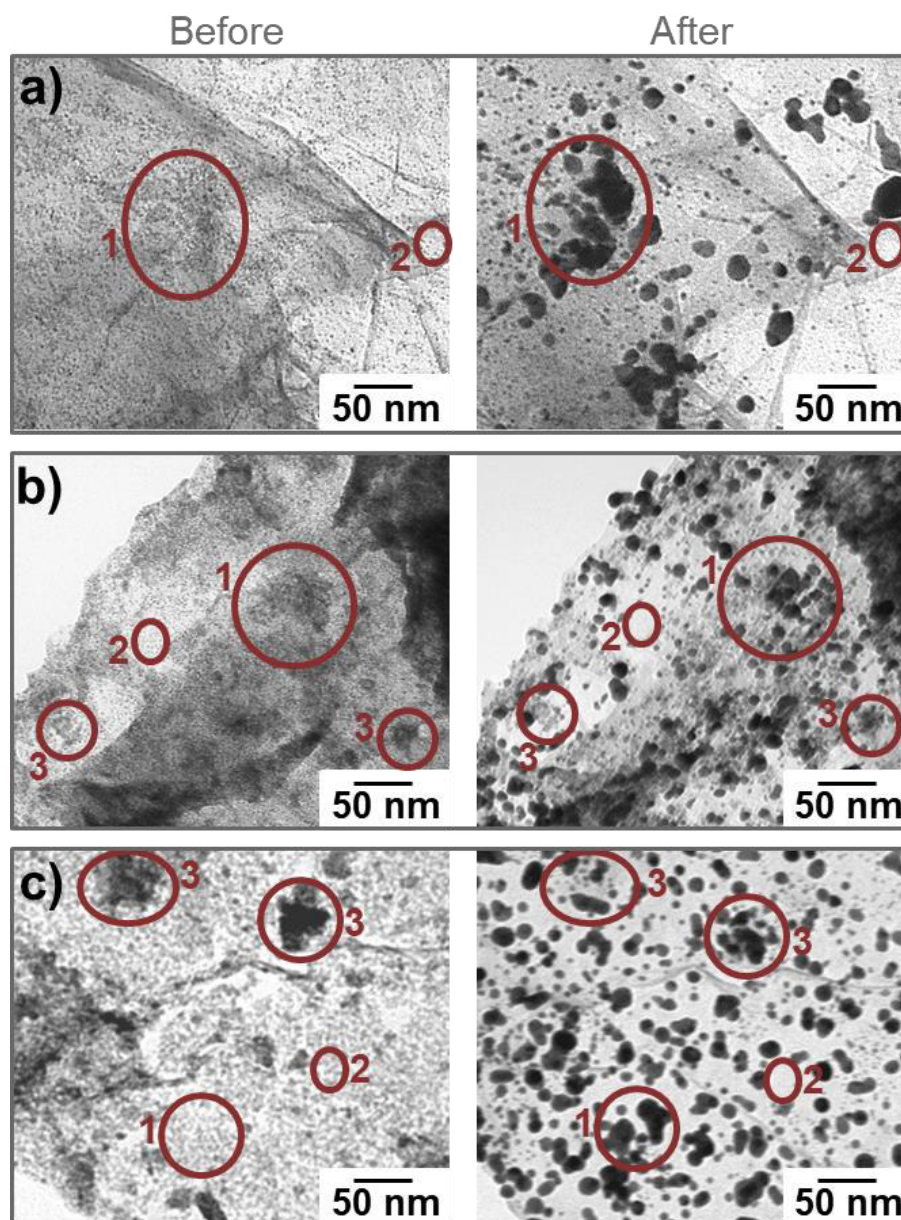
cesses are assigned to loss of ECSA during electrochemical analysis before. Furthermore, Pt disappearance due to particle dissolution, detachment or migration is evidenced within the marked area (2). Zana et al.<sup>[102]</sup> studied Pt aging on carbon black using IL-TEM and reported square-wave potential steps between 0.6–1.0  $V_{\text{RHE}}$  in frequency of 3 s to provoke Pt migration and Ostwald-Ripening and triangle-wave cycling in higher potential range between 1.0–1.5  $V_{\text{RHE}}$  to provoke Pt detachment. Based on their study, cycling in a larger potential range between 0.05–1.47  $V_{\text{RHE}}$  within this work is expected to include particle detachment as well as dissolution with Ostwald-Ripening.

Figure 61b depicts Pt/FTO-rGO before and after exposure to stress. Before the test, Pt particles are well-distributed on FTO-rGO. After the test, IL-TEM reveals large Pt agglomerates (1) and Pt disappearance due to dissolution, detachment or migration (2). These phenomena have also been visualized for Pt/rGO in Figure 61a without incorporated metal oxides before. Beyond the Pt degradation, Figure 61b further depicts the FTO particles (3). Especially the left circle illustrated the unchanged aggregate of metal oxide particles in size, shape and position on the carbon surface. The right circle shows darker contrast due to FTO and Pt presence. After the test, FTO stayed unchanged and Pt occurs in larger particles. This demonstrates the stability of F-doped  $\text{SnO}_2$  in presence of harsh potentials between 0.05–1.47  $V_{\text{RHE}}$ . IL-TEM verifies the stability, which was electrochemically observed through negligible changes of the double layer capacitance and the absent formation of HQ/Q-like species. Furthermore, the marked area (1) before the stress testing suggests the presence of FTO aggregates and Pt particles as well due to enhanced contrast in TEM. After electrochemical stress large Pt agglomerates are identified on FTO (1). This supports the assumption based on electrochemical results of Section 5.3.3.2 that the FTO particles have an enhanced interaction with platinum during the degradation.

Figure 61c shows Pt/ITO-rGO before and after electrochemical stress. Before the test, Pt particles are well-distributed on reduced graphene oxide. After the test, same aging paths of platinum in terms of agglomeration (1) and disappearance due to dissolution, detachment or migration (2) are visible and lead to loss of ECSA. Next to Pt particles the ITO particles, which are larger in size, are imaged before stress testing (3). After the test, ITO is strongly changed and obviously disappeared

to some extent. IL-TEM verifies the previous assumption of instable ITO during the discussion of electrochemical results in Section 5.3.3.2.

In summary, Pt degradation is very similar on these substrates and goes along with the similar ECSA losses. Activity losses of ORR were different and possibly depend on Pt-support interaction.



**Figure 61** IL-TEM images of Pt/rGO (a), Pt/FTO-rGO (b) and Pt/ ITO-rGO (c) before and after AST. Pt agglomeration marked with 1, Pt dissolution/ detachment/ migration marked with 2 and metal oxide particles marked with 3.

## 6 Summary and Conclusions

### 6.1 Comparison of Carbon Supports

This work uses the approach of combining graphene-based carbon in the form of reduced graphene oxide with metal oxide particles to nanocomposites and provides the assessment of their suitability as durable Pt support for ORR. rGO presenting the basis for nanocomposites is synthesized in two steps with verification of progress in synthesis. In contrast to natural graphite as starting material, rGO demonstrates exfoliated graphene layers with lateral sizes of around 1.5  $\mu\text{m}$  and an increased degree of structural defects by more than 250 %. Layer exfoliation serves for enlargement of the specific surface area by factor of 36 and makes the material suitable for application as FC catalyst support (Section 5.1.1).

Next to rGO other carbon supports with highly different morphologies are studied. Besides utilization of Vulcan<sup>®</sup> XC72R and MWCNTs as common materials, a new carbon is developed under the important aspect of sustainability. Hydrothermal carbonization of biomass provides a black-brownish coal<sup>[147]</sup> being activated by thermal annealing and called HTC-C. MWCNTs with highly ordered and rolled-up graphene layers and HTC-C with the greatest amorphous structure are the most contrary carbon materials in this work. Based on physical analysis, carbon structures are concluded by drawing in Figure 31. In the following the carbon characteristics (Section 5.1.2) are summarized:

- i. The *specific surface area* is the highest for HTC-C counting 546  $\text{m}^2 \text{g}^{-1}$  and the lowest for MWCNTs counting 111  $\text{m}^2 \text{g}^{-1}$ . Micropores predominate each carbon, though reduced graphene oxide also possesses larger pores.
- ii. *Electrical conductivity* and *degree of graphitization* is the lowest for HTC-C and the highest for MWCNTs pointing out the opposite trend to the surface area. Rarely graphitization of HTC-C can particularly be a drawback for electrochemical stability.
- iii. Raman shows the highest *degree of structural defects* in MWCNTs and the lowest degree in rGO. Reduced graphene oxide originates from graph-

ite with pronounced aromatic structure, whereas aromatic structures of the other carbons are at first formed during synthesis.

- iv. Largest amount of **oxygen surface groups** is revealed for rGO and by far the lowest for HTC-C. Reduced graphene oxide is obtained via graphite oxide so that some functional oxygen groups remain. On contrary, HTC-C is thermally annealed in Ar/H<sub>2</sub> atmosphere so that organic compounds but also functional oxygen groups are removed.

These carbon characteristics have consequences on the catalyst stability. The electrochemical analysis (Sections 5.3.1 and 5.3.2) is summed up below:

- i. With respect to **initial carbon characteristics**, double layer capacitance and redox active carbon oxides are most pronounced for rGO caused by its high surface area and surface oxygen content in combination.
- ii. **Electrochemical surface areas** are comparable between 68–87 m<sup>2</sup> g<sub>Pt</sub><sup>-1</sup>, so that a significant impact of the carbon support on ECSA is not seen.
- iii. **Catalytic activities for ORR** are comparable as well, however, much worse activity is detected for Pt/HTC-C with an onset potential of 0.94 V<sub>RHE</sub> instead of 0.99–1.01 V<sub>RHE</sub>.
- iv. With respect to **carbon stability**, Pt/HTC-C has a strongly increased double layer capacitance and redox active carbon oxides followed by Pt/C as consequence of most amorphous and rotationally faulted morphologies of HTC-C and carbon black.
- v. With respect to **platinum stability**, loss of ECSA and loss of activity for ORR occur in similar extents for platinum on rGO, C and MWCNTs. However, platinum on HTC-C not only shows highest ECSA loss but also largest loss of catalytic activity. Low carbon stability causes enforced Pt degradation.

To conclude, modification of carbon morphology in terms of 2D sheets in reduced graphene oxide or intertwined carbon nanotubes as opposite to spherical particles of carbon black affect the catalyst durability to an insignificant extent. Rather the expansion of aromatic arrays and proper graphitic arrangement determine the catalyst durability as proven for HTC-C.

## 6.2 Suitability of Nanocomposite Supports

Nanocomposites are obtained by precipitation of ITO and FTO nanoparticles on rGO and studied on their durability in application as Pt support for ORR. Summarized physical analysis (Sections 5.1.3 and 5.2.2) is given below:

- i. **Morphology** on microscale is still given by reduced graphene oxide. ITO is incorporated as 7.1 nm nanoparticles and microparticles — showing bixbyite crystallinity of  $\text{In}_2\text{O}_3$  containing  $\text{Sn}^{4+}$  as dopant. On the contrary, FTO is incorporated as 2.8 nm nanoparticles — having the cassiterite crystallinity of  $\text{SnO}_2$  containing  $\text{F}^-$  as dopant.
- ii. Both metal oxide types exhibit next to **surface oxides** also **hydroxides**.
- iii. Surface of rGO is **highly covered** with ITO or FTO, whereas the composite using ITO possesses a more uncovered carbon surface.
- iv. Incorporation of metal oxide particles not only increase the **electrical resistance** but also reduce the **specific surface area** by at least a factor of 2.
- v. Single Pt particles are located via HR-TEM at interfaces between rGO and metal oxide in both composites. However, using FTO-rGO **preferred deposition of Pt on FTO** than on the carbon is revealed. On contrary, ITO-rGO exhibits **no preference of ITO during Pt deposition**.

In conclusion, stronger interaction of platinum with FTO particles than with reduced graphene oxide is evidenced, which is not seen for ITO and reduced graphene oxide. Consequence of contrary Pt distributions for catalyst stability is proven by accelerated stress testing. The electrochemical analysis (Section 5.3.3) is summed up below:

- i. **Electrochemical surface areas** are reduced by approximately one third compared to Pt/rGO due to incorporation of metal oxides. Nanocomposites suffer from lowered specific surface area and electrical conductivity affecting the ECSA.
- ii. **Catalytic activities for ORR** are in range of carbon-based catalysts, with exception of Pt/HTC-C with lower activity. Activity using FTO is higher than using ITO as consequence of deviating Pt interaction between FTO and ITO.

- iii. During CO stripping experiments, the presence of metal oxides ensure CO desorption at significant lower potential compared to Pt/rGO and in consequence a higher CO tolerance. *Enhanced CO tolerance* is an important benefit for FC operation.
- iv. With respect to platinum stability, loss of electrochemical surface area is highly comparable for both composite catalysts and for Pt/rGO. *Similar ECSA loss* corresponds to *similar Pt degradation paths* proven by identical location TEM. Agglomeration and disappearance due to dissolution, detachment or migration appear during AST.
- v. *Activity losses for ORR* of composite-based catalysts are in range of carbon-based catalysts, with exception of Pt/HTC-C. Platinum on FTO-rGO suffers more from activity loss than platinum on ITO-rGO. This suggests a FTO impact on Pt degradation. CO sorption in combination with IL-TEM reveals significantly *stronger interaction of platinum and FTO* after AST — which is not seen for the ITO composite.
- vi. With respect to support stability, identical location TEM highlights *unchanged FTO aggregates* in size, shape and position onto rGO. Formation of redox active carbon oxides is completely absent and double layer capacitance is highly stable during AST.
- vii. In contrast, *ITO particles strongly change* in size, shape and position and partially disappear. HQ/Q similar species onto rGO remarkably increase by factor of 7. Two promoting factors are believed — enforced Pt deposition on reduced graphene oxide instead of ITO catalyzing carbon corrosion and ITO dissolution re-activating HQ/Q redox activity of rGO.

To conclude, FTO is not only more stable than ITO but additionally protects persistently rGO from carbon corrosion. However, Pt degradation occurs on both composites. The choice of metal oxide is crucial for the durability of electrocatalysts. Based on combining our findings with other recent studies,<sup>[209, 211]</sup> degradation mechanisms for the nanocomposite-based catalysts are proposed in following scheme:

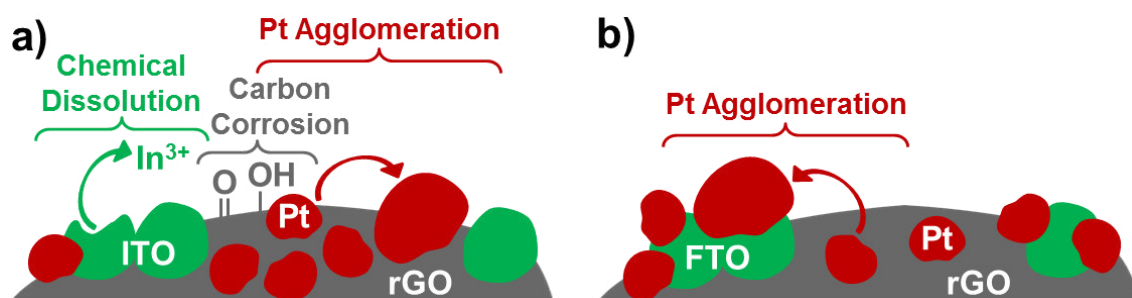


**Figure 62** Scheme of proposed degradation mechanisms for Pt/ITO–rGO (a) and Pt/FTO–rGO (b).

With respect to original catalyst states, this scheme illustrates the assumption that more Pt nanoparticles are on reduced graphene oxide for ITO–rGO, and more Pt nanoparticles are on F-doped tin oxide for FTO–rGO. With respect to catalyst aging, Pt/ITO–rGO in Figure 62a is assumed to suffer from various degradation paths. Support degradation occurs in two respects: Chemical dissolution of ITO at low pH<sup>[211]</sup> and corrosion of reduced graphene oxide. Pt degradation appears in the form of agglomeration, while dissolution, detachment or migration are also assumed but not clearly identified in this work. Support degradation of Pt/FTO–rGO in Figure 62b is insignificant. However, same Pt degradation paths with enforcing interaction between Pt and FTO are assumed.

Although some studies in the past showed stable ECSA and ORR performance for ITO-based platinum catalysts,<sup>[205, 208]</sup> suitability of Pt/ITO–rGO for long term FC operation is not confirmed. Based on the knowledge about Pt degradation,<sup>[15]</sup> instability of ITO–rGO support must impact the fuel cell performance during proceeded time of operation. Moreover, against the background of production costs and sustainability it is reasonable to substitute ITO containing the rare element indium by another material like FTO.

## 7 Outlook

The assessment of nanocomposites combining rGO and metal oxides in this work shows the importance of adequate modification to achieve stability under FC conditions. FTO on rGO not only addresses the challenge of production costs through substitution of ITO, but also addresses the challenge of catalyst durability through protecting carbon from corrosion in a stable and constant way. This provides the basis for future research. First, the tuning of fluorine-doping can reach enhanced electrical conductance. The use of carbon as basis is still useful to further reduce electrical resistances and to enlarge the surface area. Both parameters — maximized electrical conductivity and surface area — would positively affect the ECSA.

Second, due to the important aspect of sustainability carbons from renewable resources might be applied and tested on their protection against corrosion through the deposition of FTO particles. Such a carbon from biomass was already introduced in this work, however, necessitates further optimization of activity and stability for ORR. Thermal annealing with elevated temperature and duration can further graphitize the carbon, and using inert gas without hydrogen can remain more oxygen surface groups. Thereby, a balance between graphitization and electrical conductivity on one hand and surface area and functional groups on other hand is expedient.

Expensive ITO was already substituted by FTO in a successful way. Further development of composites could be the implementation of other metal oxides. Titanium dioxide for instance is more assessable than  $\text{In}_2\text{O}_3$  or  $\text{SnO}_2$  leading to reduced FC production costs. A drawback is the negligible electrical conductivity, so that the strategy must be an adapted doping of  $\text{TiO}_2$  first and distribution on a carbon substrate second. Thereby, the competing interaction of Pt with carbon on one hand and  $\text{TiO}_2$  on other hand must be carefully investigated similar to this study. Pt-support interaction is crucial for stability issues in fuel cells.

Last, the application of nanocomposite-based catalysts in HT-PEMFCs is proposed, which exposes the catalyst to harsher conditions than for instance the LT-PEM fuel cell and hence requires a more stable catalyst support than carbon black. Next to cathodic application, the nanocomposite-based catalysts might be tested for anodic HT-PEMFC operation, because their enhanced CO tolerance could be an important benefit and is relevant for operation with reformat.<sup>[286]</sup> Beyond the oxidation of CO, these catalysts might also promote the electrooxidation of alcohols like methanol or ethanol and could be useful in direct alcohol fuel cells.<sup>[141]</sup>

Since the ITO-rGO and FTO-rGO nanocomposites are porous materials showing electrical conductivity, further applications are conceivable. Anode materials in lithium ion batteries require electrical conductivity and the ability to reversibly incorporate  $\text{Li}^+$  inside porous structures. Regarding charging/discharging and  $\text{Li}^+$  insertion/extraction, the electrode further requires high capacity and structural stability. For this,  $\text{SnO}_2$  nanoparticles were shown to have a lithium storage capacity twice as high as common graphite.<sup>[287, 288]</sup> Suitability of FTO in combination with rGO as such anode material was already proven in literature,<sup>[235]</sup> where  $\text{SnO}_2$  stored lithium, the fluorine-doping increased the electrical conductivity and rGO provided a stable porous network. FTO-rGO from this study has dispersed FTO particles on rGO and thus good preconditions for the anodic Li ion battery application as well. Therefore, this nanocomposite could be further investigated on the effect of FTO particle sizes for an optimized  $\text{Li}^+$  insertion/extraction and on the fluorine-doping to maximize the electrical conductivity. Moreover, composites with FTO and porous carbons from renewable resources instead of rGO could be investigated on their suitability. This would consider sustainable aspects during manufacturing of anodes for Li ion batteries.

Another application field of such composites is given by optoelectronic devices and solar cells in terms of transparent conducting electrodes. The use of large-area graphene produced by CVD as a transparent conducting electrode provides mechanical flexibility and stability of devices.<sup>[156]</sup> To enhance light in-coupling these electrodes can be optimized.<sup>[289]</sup> Deposition of nanostructured transparent conducting ITO or FTO onto flexible graphene enables a large field of possible electrode surface textures and roughness for better light trapping.

# References

- [1] J. B. Fourier, *J. Mem. Acad. R. Sci. Inst. France* **1827**, 7, 569-604.
- [2] J. Tyndall, *Philos. Mag.* **1861**, 22, 169-194.
- [3] J. Tyndall, *Philos. Mag.* **1861**, 22, 273-285.
- [4] United nations, in *United Nations Climate Change Conference*, **2015**, pp. 1-27.
- [5] Quantifying uncertainties in global and regional temperature change using an ensemble of observational estimates: The HadCRUT4 dataset, 24.01.2018.
- [6] G. Marland, T. A. Boden, R. J. Andres, in *Global, Regional, and National Fossil-Fuel CO<sub>2</sub> Emissions*, Carbon Dioxide Information Analysis Center, Oak Ridge National Laboratory, U.S. Department of Energy, Oak Ridge, Tenn., U.S.A, **2017**.
- [7] Federal Ministry for the Environment, Nature Conservation, Building and Nuclear Safety, in *Climate Action Plan 2050 - Principles and goals of the German government's climate policy*, Berlin, Germany, **2016**.
- [8] T. Benz, J. Dickert, M. Erbert, N. Erdmann, C. Johae, B. Katzenbach, W. Glaunsinger, H. Müller, P. Schegner, J. Schwarz, R. Speh, H. Stagge, M. Zdrallek, in *Der zellulare Ansatz - Grundlage einer erfolgreichen, regionenübergreifenden Energiewende*, Energietechnische Gesellschaft im VDE, Frankfurt a. M., Germany, **2015**.
- [9] S. S. Araya, F. Zhou, V. Liso, S. L. Sahlin, J. R. Vang, S. Thomas, X. Gao, C. Jeppesen, S. K. Kær, *Int. J. Hydrogen Energy* **2016**, 41, 21310-21344.
- [10] A. Chandan, M. Hattenberger, A. El-Kharouf, S. Du, A. Dhir, V. Self, B. G. Pollet, A. Ingram, W. Bujalski, *J. Power Sources* **2013**, 231, 264-278.
- [11] R. E. Rosli, A. B. Sulong, W. R. W. Daud, M. A. Zulkifley, T. Husaini, M. I. Rosli, E. H. Majlan, M. A. Haque, *Int. J. Hydrogen Energy* **2017**, 42, 9293-9314.
- [12] Fuel Cell Technologies Office, in *Multi-Year Research, Development, and Demonstration Plan*, U.S. Department of Energy, Washington D. C., U.S.A, **2016**.
- [13] J. Wang, *Appl. Energ.* **2017**, 189, 460-479.
- [14] Fuel Cells and Hydrogen Joint Undertaking, in *Multi - Annual Work Plan 2014 - 2020*, **2014**.
- [15] Y. Shao-Horn, W. C. Sheng, S. Chen, P. J. Ferreira, E. F. Holby, D. Morgan, *Top. Catal.* **2007**, 46, 285-305.
- [16] D. Schonvogel, M. Rastedt, P. Wagner, M. Wark, A. Dyck, *Fuel Cells* **2016**, 16, 480-489.
- [17] R. Borup, J. Meyers, B. Pivovar, Y. S. Kim, R. Mukundan, N. Garland, D. Myers, M. Wilson, F. Garzon, D. Wood, P. Zelenay, K. More, K. Stroh, T. Zawodzinski, J. Boncella, J. E. McGrath, M. Inaba, K. Miyatake, M. Hori, K. Ota, Z. Ogumi, S. Miyata, A. Nishikata, Z. Siroma, Y. Uchimoto, K. Yasuda, K.-i. Kimijima, N. Iwashita, *Chem. Rev.* **2007**, 107, 3904-3951.
- [18] P. T. Yu, Z. Liu, R. Makharia, *J. Electrochem. Soc.* **2013**, 160, F645-F650.
- [19] L. M. Roen, C. H. Paik, T. D. Jarvi, *Electrochem. Solid State Lett.* **2004**, 7, A19-A22.
- [20] R. M. Darling, J. P. Meyers, *J. Electrochem. Soc.* **2003**, 150, A1523-A1527.
- [21] G. Liu, H. Zhang, J. Hu, Y. Zhai, D. Xu, Z.-G. Shao, *J. Power Sources* **2006**, 162, 547-552.
- [22] L. N. Cleemann, F. Buazar, Q. Li, J. O. Jensen, C. Pan, T. Steenberg, S. Dai, N. J. Bjerrum, *Fuel Cells* **2013**, 13, 822-831.

- [23] C. Wannek, B. Kohnen, H. F. Oetjen, H. Lippert, J. Mergel, *Fuel Cells* **2008**, *8*, 87-95.
- [24] X. Zhou, J. Qiao, L. Yang, J. Zhang, *Adv. Energy Mater.* **2014**, *4*, 1301523.
- [25] E. Antolini, E. R. Gonzalez, *Solid State Ionics* **2009**, *180*, 746-763.
- [26] O. Lori, L. Elbaz, *Catalysts* **2015**, *5*, 1445.
- [27] T. Tsukatsune, Y. Takabatake, Z. Noda, T. Daio, A. Zaitso, S. M. Lyth, A. Hayashi, K. Sasaki, *J. Electrochem. Soc.* **2014**, *161*, F1208-F1213.
- [28] Y. Hu, Y. Jiang, J. O. Jensen, L. N. Cleemann, Q. Li, *J. Power Sources* **2018**, *375*, 77-81.
- [29] M. J. Fleige, G. K. H. Wiberg, M. Arenz, *Rev. Sci. Instrum.* **2015**, *86*, 064101.
- [30] G. K. H. Wiberg, M. J. Fleige, M. Arenz, *Rev. Sci. Instrum.* **2014**, *85*, 085105.
- [31] M. Prokop, M. Carda, T. Bystron, M. Paidar, K. Bouzek, *Electrochim. Acta* **2017**, *245*, 597-606.
- [32] M. Prokop, R. Kodym, T. Bystron, M. Paidar, K. Bouzek, *Electrochim. Acta* **2017**, *245*, 634-642.
- [33] L. M. Uhlig, D. Stewart, G. Sievers, V. Brüser, A. Dyck, G. Wittstock, *Int. J. Hydrogen Energy* **2016**, *41*, 22554-22559.
- [34] I. Kruusenberg, L. Matisen, Q. Shah, A. M. Kannan, K. Tammeveski, *Int. J. Hydrogen Energy* **2012**, *37*, 4406-4412.
- [35] B. Britton, S. Holdcroft, *J. Electrochem. Soc.* **2016**, *163*, F353-F358.
- [36] M. Alesker, M. Page, M. Shviro, Y. Paska, G. Gershinsky, D. R. Dekel, D. Zitoun, *J. Power Sources* **2016**, *304*, 332-339.
- [37] J. Töpler, J. Lehmann, *Wasserstoff und Brennstoffzelle - Technologie und Marktperspektiven*, Springer Vieweg, Berlin/Heidelberg, Germany, **2014**.
- [38] S. Curtin, J. Gangi, in *Fuel Cell Technologies Market Report 2014*, Fuel Cell Technologies Office, U.S. Department of Energy, Washington D. C., U.S.A, **2014**.
- [39] M. A. Haque, A. B. Sulong, K. S. Loh, E. H. Majlan, T. Husaini, R. E. Rosli, *Int. J. Hydrogen Energy* **2017**, *42*, 9156-9179.
- [40] J. Zhang, *PEM Fuel Cell Electrocatalysts and Catalyst Layers*, Springer, London, **2008**.
- [41] B. E. Logan, B. Hamelers, R. Rozendal, U. Schroeder, J. Keller, S. Freguia, P. Aelterman, W. Verstraete, K. Rabaey, *Environ. Sci. Technol.* **2006**, *40*, 5181-5192.
- [42] C. Wang, H. Daimon, T. Onodera, T. Koda, S. Sun, *Angew. Chem.* **2008**, *120*, 3644-3647.
- [43] M. Peuckert, T. Yoneda, R. A. D. Betta, M. Boudart, *J. Electrochem. Soc.* **1986**, *133*, 944-947.
- [44] K. Kinoshita, *J. Electrochem. Soc.* **1990**, *137*, 845-848.
- [45] J. Ma, A. Habrioux, Y. Luo, G. Ramos-Sanchez, L. Calvillo, G. Granozzi, P. B. Balbuena, N. Alonso-Vante, *J. Mater. Chem. A* **2015**, *3*, 11891-11904.
- [46] E. Antolini, *Appl. Catal. B - Environ.* **2012**, *123-124*, 52-68.
- [47] N. Zhang, S. Zhang, C. Du, Z. Wang, Y. Shao, F. Kong, Y. Lin, G. Yin, *Electrochim. Acta* **2014**, *117*, 413-419.
- [48] S. C. Hall, V. Subramanian, G. Teeter, B. Rambabu, *Solid State Ionics* **2004**, *175*, 809-813.
- [49] X. Yu, S. Ye, *J. Power Sources* **2007**, *172*, 133-144.
- [50] T. Sousa, M. Mamlouk, K. Scott, *Chem. Eng. Sci.* **2010**, *65*, 2513-2530.
- [51] J.-R. Kim, J. S. Yi, T.-W. Song, *J. Power Sources* **2012**, *220*, 54-64.

- [52] T. Thampan, S. Malhotra, J. Zhang, R. Datta, *Catal. Today* **2001**, *67*, 15-32.
- [53] M. A. Haque, A. B. Sulong, K. S. Loh, E. H. Majlan, T. Husaini, R. E. Rosli, *Int. J. Hydrogen Energy*.
- [54] P. Kurzweil, in *Brennstoffzellentechnik*, Springer Fachmedien Wiesbaden, Wiesbaden, Germany, **2013**, pp. 17-52.
- [55] S. S. Kocha, J. D. Yang, J. S. Yi, *AIChE J.* **2006**, *52*, 1916-1925.
- [56] X. Cheng, J. Zhang, Y. Tang, C. Song, J. Shen, D. Song, J. Zhang, *J. Power Sources* **2007**, *167*, 25-31.
- [57] K. Lee, J. Zhang, H. Wang, D. P. Wilkinson, *J. Appl. Electrochem.* **2006**, *36*, 507-522.
- [58] J. K. Nørskov, J. Rossmeisl, A. Logadottir, L. Lindqvist, J. R. Kitchin, T. Bligaard, H. Jónsson, *J. Phys. Chem. B* **2004**, *108*, 17886-17892.
- [59] V. R. Stamenkovic, B. Fowler, B. S. Mun, G. Wang, P. N. Ross, C. A. Lucas, N. M. Markovic, *Science* **2007**, *315*, 493-497.
- [60] I. Katsounaros, S. Cherevko, A. R. Zeradjanin, K. J. J. Mayrhofer, *Angew. Chem. Int. Ed.* **2014**, *53*, 102-121.
- [61] U. A. Paulus, T. J. Schmidt, H. A. Gasteiger, R. J. Behm, *J. Electroanal. Chem.* **2001**, *495*, 134-145.
- [62] K. J. J. Mayrhofer, D. Strmcnik, B. B. Blizanac, V. Stamenkovic, M. Arenz, N. M. Markovic, *Electrochim. Acta* **2008**, *53*, 3181-3188.
- [63] M. Nesselberger, S. Ashton, J. C. Meier, I. Katsounaros, K. J. J. Mayrhofer, M. Arenz, *J. Am. Chem. Soc.* **2011**, *133*, 17428-17433.
- [64] Q. He, X. Yang, W. Chen, S. Mukerjee, B. Koel, S. Chen, *Phys. Chem. Chem. Phys.* **2010**, *12*, 12544-12555.
- [65] J. Biesdorf, N. Zamel, T. Kurz, *J. Power Sources* **2014**, *247*, 339-345.
- [66] B. Hammer, J. K. Nørskov, in *Advances in Catalysis, Vol. 45*, Academic Press, **2000**, pp. 71-129.
- [67] J. R. Kitchin, J. K. Nørskov, M. A. Barteau, J. Chen, *Phys. Rev. Lett.* **2004**, *93*, 156801.
- [68] J. Greeley, J. K. Nørskov, M. Mavrikakis, *Annu. Rev. Phys. Chem.* **2002**, *53*, 319-348.
- [69] A. Nilsson, L. Pettersson, B. Hammer, T. Bligaard, C. H. Christensen, J. K. Nørskov, *Catal. Lett.* **2005**, *100*, 111-114.
- [70] S. Guo, S. Zhang, S. Sun, *Angew. Chem.* **2013**, *125*, 8686-8705.
- [71] J. Monzo, D. F. van der Vliet, A. Yanson, P. Rodriguez, *Phys. Chem. Chem. Phys.* **2016**, *18*, 22407-22415.
- [72] J. Aragane, H. Urushibata, T. Murahashi, *J. Appl. Electrochem.* **1996**, *26*, 147-152.
- [73] S. Mitsushima, S. Kawahara, K.-I. Ota, N. Kamiya, *J. Electrochem. Soc.* **2007**, *154*, B153-B158.
- [74] X. Wang, R. Kumar, D. J. Myers, *Electrochem. Solid State Lett.* **2006**, *9*, A225-A227.
- [75] J. Aragane, T. Murahashi, T. Odaka, *J. Electrochem. Soc.* **1988**, *135*, 844-850.
- [76] M. J. N. Pourbaix, *Atlas of Electrochemical Equilibria in Aqueous Solutions*, Pergamon Press Oxford, New York, U.S.A., **1966**.
- [77] A. Honji, T. Mori, K. Tamura, Y. Hishinuma, *J. Electrochem. Soc.* **1988**, *135*, 355-359.
- [78] P. Bindra, S. J. Clouser, E. Yeager, *J. Electrochem. Soc.* **1979**, *126*, 1631-1632.
- [79] P. J. Ferreira, G. J. la O', Y. Shao-Horn, D. Morgan, R. Makharia, S. Kocha, H. A. Gasteiger, *J. Electrochem. Soc.* **2005**, *152*, A2256-A2271.

- [80] M. J. N. Pourbaix, J. Van Muylder, N. de Zoubov, *Platinum Met. Rev.* **1959**, *3*, 47-53.
- [81] H. Angerstein-Kozłowska, B. E. Conway, W. B. A. Sharp, *J. Electroanal. Chem. Interfacial Electrochem.* **1973**, *43*, 9-36.
- [82] K. Ota, Y. Koizumi, S. Mitsushima, N. Kamiya, *ECS Trans.* **2006**, *3*, 619-624.
- [83] G. Jerkiewicz, G. Vatankhah, J. Lessard, M. P. Soriaga, Y.-S. Park, *Electrochim. Acta* **2004**, *49*, 1451-1459.
- [84] Z. Nagy, H. You, *Electrochim. Acta* **2002**, *47*, 3037-3055.
- [85] P. P. Lopes, D. Tripkovic, P. F. Martins, D. Strmcnik, E. A. Ticianelli, V. R. Stamenkovic, N. M. Markovic, *J. Electroanal. Chem.* **2017**.
- [86] K. Kinoshita, J. T. Lundquist, P. Stonehart, *J. Electroanal. Chem. Interfacial Electrochem.* **1973**, *48*, 157-166.
- [87] R. M. Darling, J. P. Meyers, *J. Electrochem. Soc.* **2005**, *152*, A242-A247.
- [88] K. Yasuda, A. Taniguchi, T. Akita, T. Ioroi, Z. Siroma, *Phys. Chem. Chem. Phys.* **2006**, *8*, 746-752.
- [89] T. Søndergaard, L. N. Cleemann, L. Zhong, H. Becker, T. Steenberg, H. A. Hjuler, L. Seerup, Q. Li, J. O. Jensen, *Electrocatalysis* **2018**, *9*, 302-313.
- [90] V. Komanicky, K. C. Chang, A. Menzel, N. M. Markovic, H. You, X. Wang, D. Myers, *J. Electrochem. Soc.* **2006**, *153*, B446-B451.
- [91] D. Schonvogel, Bachelor thesis, Carl-von-Ossietzky Universität Oldenburg (Oldenburg, Germany), **2012**.
- [92] J. Xie, D. L. Wood, K. L. More, P. Atanassov, R. L. Borup, *J. Electrochem. Soc.* **2005**, *152*, A1011-A1020.
- [93] K. Yasuda, A. Taniguchi, T. Akita, T. Ioroi, Z. Siroma, *J. Electrochem. Soc.* **2006**, *153*, A1599-A1603.
- [94] G. de Moor, C. Bas, F. Lesage, A. S. Danerol, E. Claude, E. Rossinot, M. Paris, L. Flandin, N. D. Alberola, *J. Appl. Polym. Sci.* **2011**, *120*, 3501-3510.
- [95] M. Rau, A. Niedergesäß, C. Cremers, S. Alfaro, T. Steenberg, H. A. Hjuler, *Fuel Cells* **2016**, *16*, 577-583.
- [96] C. Hartnig, T. J. Schmidt, *J. Power Sources* **2011**, *196*, 5564-5572.
- [97] W. Ostwald, *Z. Phys. Chem.* **1900**, *34*, 495-503.
- [98] A. C. C. Tseung, P. R. Vassie, *Electrochim. Acta* **1976**, *21*, 315-318.
- [99] A. V. Virkar, Y. Zhou, *J. Electrochem. Soc.* **2007**, *154*, B540-B547.
- [100] G. A. Gruver, R. F. Pascoe, H. R. Kunz, *J. Electrochem. Soc.* **1980**, *127*, 1219-1224.
- [101] J. A. Bett, K. Kinoshita, P. Stonehart, *J. Catal.* **1974**, *35*, 307-316.
- [102] A. Zana, J. Speder, M. Roefzaad, L. Altmann, M. Bäumer, M. Arenz, *J. Electrochem. Soc.* **2013**, *160*, F608-F615.
- [103] L. Dubau, L. Castanheira, G. Berthomé, F. Maillard, *Electrochim. Acta* **2013**, *110*, 273-281.
- [104] F. Hasche, M. Oezaslan, P. Strasser, *Phys. Chem. Chem. Phys.* **2010**, *12*, 15251-15258.
- [105] C. A. Rice, P. Urchaga, A. O. Pistono, B. W. McFerrin, B. T. McComb, J. Hu, *J. Electrochem. Soc.* **2015**, *162*, F1175-F1180.

- [106] J. A. Gilbert, N. N. Kariuki, X. Wang, A. J. Kropf, K. Yu, D. J. Groom, P. J. Ferreira, D. Morgan, D. J. Myers, *Electrochim. Acta* **2015**, *173*, 223-234.
- [107] Z. Qi, S. Buelte, *J. Power Sources* **2006**, *161*, 1126-1132.
- [108] J. Kim, J. Lee, Y. Tak, *J. Power Sources* **2009**, *192*, 674-678.
- [109] H. Tang, Z. Qi, M. Ramani, J. F. Elter, *J. Power Sources* **2006**, *158*, 1306-1312.
- [110] Y. Yu, H. Li, H. Wang, X.-Z. Yuan, G. Wang, M. Pan, *J. Power Sources* **2012**, *205*, 10-23.
- [111] N. Yousfi-Steiner, P. Moçotéguy, D. Candusso, D. Hissel, *J. Power Sources* **2009**, *194*, 130-145.
- [112] H. A. Gasteiger, S. S. Kocha, B. Sompalli, F. T. Wagner, *Appl. Catal. B - Environ.* **2005**, *56*, 9-35.
- [113] K. J. J. Mayrhofer, K. Hartl, V. Juhart, M. Arenz, *J. Am. Chem. Soc.* **2009**, *131*, 16348-16349.
- [114] H. Schulenburg, B. Schwanitz, N. Linse, G. G. Scherer, A. Wokaun, J. Krbanjevic, R. Grothausmann, I. Manke, *J. Phys. Chem. C* **2011**, *115*, 14236-14243.
- [115] J. Li, P. He, K. Wang, M. Davis, S. Ye, *ECS Trans.* **2006**, *3*, 743-751.
- [116] M. F. Mathias, R. Makharia, H. A. Gasteiger, J. J. Conley, T. J. Fuller, C. I. Gittleman, S. S. Kocha, D. P. Miller, C. K. Mittelsteadt, T. Xie, S. G. Yan, P. T. Yu, *Electrochem. Soc. Interface* **2005**, *14*, 24-35.
- [117] C. He, S. Desai, G. Brown, S. Bollepalli, *Electrochem. Soc. Interface* **2005**, *14*, 41-44.
- [118] K. Kinoshita, J. Bett, *Carbon* **1973**, *11*, 237-247.
- [119] J. Speder, A. Zana, I. Spanos, J. J. K. Kirkensgaard, K. Mortensen, M. Arenz, *Electrochem. Commun.* **2013**, *34*, 153-156.
- [120] K. Kinoshita, J. A. S. Bett, *Carbon* **1973**, *11*, 403-411.
- [121] H. P. Boehm, *Carbon* **2002**, *40*, 145-149.
- [122] S. C. Ball, S. L. Hudson, D. Thompsett, B. Theobald, *J. Power Sources* **2007**, *171*, 18-25.
- [123] Y. Yang, Z. G. Lin, *J. Appl. Electrochem.* **1995**, *25*, 259-266.
- [124] C. A. Reiser, L. Bregoli, T. W. Patterson, J. S. Yi, J. D. Yang, M. L. Perry, T. D. Jarvi, *Electrochem. Solid State Lett.* **2005**, *8*, A273-A276.
- [125] F. Zhou, S. J. Andreasen, S. K. Kær, D. Yu, *Int. J. Hydrogen Energy* **2015**, *40*, 2833-2839.
- [126] J. P. Meyers, R. M. Darling, *J. Electrochem. Soc.* **2006**, *153*, A1432-A1442.
- [127] D. Stevens, M. Hicks, G. Haugen, J. Dahn, *J. Electrochem. Soc.* **2005**, *152*, A2309-A2315.
- [128] H.-S. Oh, J.-H. Lee, H. Kim, *Int. J. Hydrogen Energy* **2012**, *37*, 10844-10849.
- [129] E. Passalacqua, P. L. Antonucci, M. Vivaldi, A. Patti, V. Antonucci, N. Giordano, K. Kinoshita, *Electrochim. Acta* **1992**, *37*, 2725-2730.
- [130] C.-C. Hung, P.-Y. Lim, J.-R. Chen, H. C. Shih, *J. Power Sources* **2011**, *196*, 140-146.
- [131] S. Ye, M. Hall, H. Cao, P. He, *ECS Trans.* **2006**, *3*, 657-666.
- [132] M. Liu, R. Zhang, W. Chen, *Chem. Rev.* **2014**, *114*, 5117-5160.
- [133] S. Samad, K. S. Loh, W. Y. Wong, T. K. Lee, J. Sunarso, S. T. Chong, W. R. W. Daud, *Int. J. Hydrogen Energy* **2018**, *43*, 7823-7854.
- [134] Y. Shao, S. Zhang, C. Wang, Z. Nie, J. Liu, Y. Wang, Y. Lin, *J. Power Sources* **2010**, *195*, 4600-4605.

- [135] R. Kou, Y. Shao, D. Wang, M. H. Engelhard, J. H. Kwak, J. Wang, V. V. Viswanathan, C. Wang, Y. Lin, Y. Wang, I. A. Aksay, J. Liu, *Electrochem. Commun.* **2009**, *11*, 954-957.
- [136] K. Jukk, N. Kongi, P. Rauwel, L. Matisen, K. Tammeveski, *Electrocatalysis* **2016**, *7*, 428-440.
- [137] P. Stonehart, *Carbon* **1984**, *22*, 423-431.
- [138] A. Bianco, H.-M. Cheng, T. Enoki, Y. Gogotsi, R. H. Hurt, N. Koratkar, T. Kyotani, M. Monthieux, C. R. Park, J. M. D. Tascon, J. Zhang, *Carbon* **2013**, *65*, 1-6.
- [139] M. Wissler, *J. Power Sources* **2006**, *156*, 142-150.
- [140] Y.-Y. Li, C.-T. Li, M.-H. Yeh, K.-C. Huang, P.-W. Chen, R. Vittal, K.-C. Ho, *Electrochim. Acta* **2015**, *179*, 211-219.
- [141] K.-S. Lee, I.-S. Park, Y.-H. Cho, D.-S. Jung, N. Jung, H.-Y. Park, Y.-E. Sung, *J. Catal.* **2008**, *258*, 143-152.
- [142] H. Schmidt, PhD thesis, Universität Duisburg-Essen, Duisburg, Germany, **2003**.
- [143] M. Dhelipan, A. Arunchander, A. Sahu, D. Kalpana, *Journal of Saudi Chemical Society* **2017**, *21*, 487-494.
- [144] H. W. Lee, Y.-M. Kim, S. Kim, C. Ryu, S. H. Park, Y.-K. Park, *Carbon Lett.* **2018**, *26*, 1-10.
- [145] J. A. Libra, K. S. Ro, C. Kammann, A. Funke, N. D. Berge, Y. Neubauer, M.-M. Titirici, C. Fühner, O. Bens, J. Kern, K.-H. Emmerich, *Biofuels* **2011**, *2*, 71-106.
- [146] M. Taleb, J. Nerut, T. Tooming, T. Thomberg, A. Jänes, E. Lust, *J. Electrochem. Soc.* **2015**, *162*, F651-F660.
- [147] H. Mulhaupt, PhD thesis, Carl von Ossietzky Universität Oldenburg, Oldenburg, Germany, **2018**.
- [148] W. Lu, S. Marta, F. A. B., M. Robert, Y. Gleb, *Adv. Energy Mater.* **2011**, *1*, 356-361.
- [149] M. Sevilla, A. B. Fuertes, *Carbon* **2009**, *47*, 2281-2289.
- [150] T. Deng, X. Cui, Y. Qi, Y. Wang, X. Hou, Y. Zhu, *Chem. Commun.* **2012**, *48*, 5494-5496.
- [151] A. Jain, R. Balasubramanian, M. P. Srinivasan, *Chem. Eng. J.* **2016**, *283*, 789-805.
- [152] M. Sevilla, G. A. Ferrero, A. B. Fuertes, *Carbon* **2017**, *114*, 50-58.
- [153] S.-A. Wohlgemuth, R. J. White, M.-G. Willinger, M.-M. Titirici, M. Antonietti, *Green Chem.* **2012**, *14*, 1515-1523.
- [154] K. S. Novoselov, A. K. Geim, S. V. Morozov, D. Jiang, Y. Zhang, S. V. Dubonos, I. V. Grigorieva, A. A. Firsov, *Science* **2004**, *306*, 666-669.
- [155] K. Balasubramanian, M. Burghard, *Chem. unserer Zeit* **2011**, *45*, 240-249.
- [156] X. Li, W. Cai, J. An, S. Kim, J. Nah, D. Yang, R. Piner, A. Velamakanni, I. Jung, E. Tutuc, *Science* **2009**, *324*, 1312-1314.
- [157] V. Nicolosi, M. Chhowalla, M. G. Kanatzidis, M. S. Strano, J. N. Coleman, *Science* **2013**, *340*, 1226419.
- [158] M. Lotya, A. Rakovich, J. F. Donegan, J. N. Coleman, *Nanotechnology* **2013**, *24*, 265703.
- [159] D. Geng, S. Yang, Y. Zhang, J. Yang, J. Liu, R. Li, T.-K. Sham, X. Sun, S. Ye, S. Knights, *Appl. Surf. Sci.* **2011**, *257*, 9193-9198.
- [160] S. Ratso, I. Kruusenberg, M. Vikkisk, U. Joost, E. Shulga, I. Kink, T. Kallio, K. Tammeveski, *Carbon* **2014**, *73*, 361-370.

- [161] S. Pei, H.-M. Cheng, *Carbon* **2012**, *50*, 3210-3228.
- [162] S. Eigler, A. Hirsch, *Angew. Chem. Int. Ed.* **2014**, *53*, 7720-7738.
- [163] W. S. Hummers, R. E. Offeman, *J. Am. Chem. Soc.* **1958**, *80*, 1339-1339.
- [164] N. M. Julkapli, S. Bagheri, *Int. J. Hydrogen Energy* **2015**, *40*, 948-979.
- [165] L. Zhang, J. Liang, Y. Huang, Y. Ma, Y. Wang, Y. Chen, *Carbon* **2009**, *47*, 3365-3368.
- [166] M. J. McAllister, J.-L. Li, D. H. Adamson, H. C. Schniepp, A. A. Abdala, J. Liu, M. Herrera-Alonso, D. L. Milius, R. Car, R. K. Prud'homme, I. A. Aksay, *Chem. Mater.* **2007**, *19*, 4396-4404.
- [167] M. Acik, G. Lee, C. Mattevi, A. Pirkle, R. M. Wallace, M. Chhowalla, K. Cho, Y. Chabal, *J. Phys. Chem. C* **2011**, *115*, 19761-19781.
- [168] Y. Zhou, Q. Bao, L. A. L. Tang, Y. Zhong, K. P. Loh, *Chem. Mater.* **2009**, *21*, 2950-2956.
- [169] X. Xu, Y. Zhou, T. Yuan, Y. Li, *Electrochim. Acta* **2013**, *112*, 587-595.
- [170] S. Stankovich, D. A. Dikin, R. D. Piner, K. A. Kohlhaas, A. Kleinhammes, Y. Jia, Y. Wu, S. T. Nguyen, R. S. Ruoff, *Carbon* **2007**, *45*, 1558-1565.
- [171] R. I. Jafri, N. Rajalakshmi, S. Ramaprabhu, *J. Mater. Chem.* **2010**, *20*, 7114-7117.
- [172] S. K. Singh, V. M. Dhavale, R. Boukherroub, S. Kurungot, S. Szunerits, *Appl. Mater. Today* **2017**, *8*, 141-149.
- [173] K. Novikova, A. Kuriganova, I. Leontyev, E. Gerasimova, O. Maslova, A. Rakhmatullin, N. Smirnova, Y. Dobrovolsky, *Electrocatalysis* **2018**, *9*, 22-30.
- [174] B. C. Satishkumar, A. Govindaraj, C. N. R. Rao, *Chem. Phys. Lett.* **1999**, *307*, 158-162.
- [175] V. N. Popov, *Materials Science and Engineering: R: Reports* **2004**, *43*, 61-102.
- [176] D. R. Kauffman, A. Star, *Analyst* **2010**, *135*, 2790-2797.
- [177] M. N. Groves, A. S. W. Chan, C. Malardier-Jugroot, M. Jugroot, *Chem. Phys. Lett.* **2009**, *481*, 214-219.
- [178] M.-X. Wang, F. Xu, H.-F. Sun, Q. Liu, K. Artyushkova, E. A. Stach, J. Xie, *Electrochim. Acta* **2011**, *56*, 2566-2573.
- [179] M. Asgari, E. Lohrasbi, *ISRN Electrochemistry* **2013**, *vol. 2013*, 564784.
- [180] Y. Shao, G. Yin, Y. Gao, P. Shi, *J. Electrochem. Soc.* **2006**, *153*, A1093-A1097.
- [181] W. Sheng, S. W. Lee, E. J. Crumlin, S. Chen, Y. Shao-Horn, *J. Electrochem. Soc.* **2011**, *158*, B1398-B1404.
- [182] S. Park, Y. Shao, R. Kou, V. V. Viswanathan, S. A. Towne, P. C. Rieke, J. Liu, Y. Lin, Y. Wang, *J. Electrochem. Soc.* **2011**, *158*, B297-B302.
- [183] A. Marinkas, R. Hempelmann, A. Heinzl, V. Peinecke, I. Radev, H. Natter, *J. Power Sources* **2015**, *295*, 79-91.
- [184] A. Ghosh, S. Basu, A. Verma, *Fuel Cells* **2013**, *13*, 355-363.
- [185] Y. Devrim, A. Albostan, *J. Electron. Mater.* **2016**, *45*, 3900-3907.
- [186] O. T. Holton, J. W. Stevenson, *Platinum Met. Rev.* **2013**, *57*, 259-271.
- [187] K. Sasaki, F. Takasaki, Z. Noda, S. Hayashi, Y. Shiratori, K. Ito, *ECS Trans.* **2010**, *33*, 473-482.
- [188] K. Kakinuma, Y. Chino, Y. Senoo, M. Uchida, T. Kamino, H. Uchida, S. Deki, M. Watanabe, *Electrochim. Acta* **2013**, *110*, 316-324.

- [189] T. Binninger, R. Mohamed, A. Patru, K. Waltar, E. Gericke, X. Tuaeov, E. Fabbri, P. Levecque, A. Hoell, T. J. Schmidt, *Chem. Mater.* **2017**, *29*, 2831-2843.
- [190] L. Du, Y. Shao, J. Sun, G. Yin, J. Liu, Y. Wang, *Nano Energy* **2016**, *29*, 314-322.
- [191] T. Daio, A. Staykov, L. Guo, J. Liu, M. Tanaka, S. Matthew Lyth, K. Sasaki, *Sci. Rep.* **2015**, *5*, 13126.
- [192] M. Batzill, U. Diebold, *Prog. Surf. Sci.* **2005**, *79*, 47-154.
- [193] P. Zhang, S.-Y. Huang, B. N. Popov, *J. Electrochem. Soc.* **2010**, *157*, B1163-B1172.
- [194] B. Ruiz Camacho, C. Morais, M. A. Valenzuela, N. Alonso-Vante, *Catal. Today* **2013**, *202*, 36-43.
- [195] Y. Takabatake, Z. Noda, S. M. Lyth, A. Hayashi, K. Sasaki, *Int. J. Hydrogen Energy* **2014**, *39*, 5074-5082.
- [196] S.-Y. Huang, P. Ganesan, S. Park, B. N. Popov, *J. Am. Chem. Soc.* **2009**, *131*, 13898-13899.
- [197] F. Takasaki, S. Matsuie, Y. Takabatake, Z. Noda, A. Hayashi, Y. Shiratori, K. Ito, K. Sasaki, *J. Electrochem. Soc.* **2011**, *158*, B1270-B1275.
- [198] R. F. Bartholomew, D. R. Frankl, *Phys. Rev.* **1969**, *187*, 828-833.
- [199] G. Chen, S. R. Bare, T. E. Mallouk, *J. Electrochem. Soc.* **2002**, *149*, A1092-A1099.
- [200] H. Hosono, *Thin Solid Films* **2007**, *515*, 6000-6014.
- [201] H. Liu, V. Avrutin, N. Izyumskaya, Ü. Özgür, H. Morkoç, *Superlattices Microstruct.* **2010**, *48*, 458-484.
- [202] J. Ba, D. Fattakhova Rohlfing, A. Feldhoff, T. Brezesinski, I. Djerdj, M. Wark, M. Niederberger, *Chem. Mater.* **2006**, *18*, 2848-2854.
- [203] S. Wu, S. Yuan, L. Shi, Y. Zhao, J. Fang, *J. Colloid Interface Sci.* **2010**, *346*, 12-16.
- [204] E. Fabbri, A. Rabis, Y. Chino, M. Uchida, T. J. Schmidt, *Electrochem. Commun.* **2017**, *83*, 90-95.
- [205] Y. Liu, W. E. Mustain, *J. Am. Chem. Soc.* **2013**, *135*, 530-533.
- [206] T. Tsukatsune, Y. Takabatake, Z. Noda, A. Hayashi, K. Sasaki, *ECS Trans.* **2013**, *58*, 1251-1257.
- [207] Y. Liu, W. E. Mustain, *ECS Trans.* **2013**, *53*, 1-6.
- [208] Y. Liu, W. E. Mustain, *Electrochim. Acta* **2014**, *115*, 116-125.
- [209] H. Schmies, A. Bergmann, J. Drnec, G. Wang, D. Teschner, S. Köhl, D. J. S. Sandbeck, S. Cherevko, M. Gocyla, M. Shviro, M. Heggen, V. Ramani, R. E. Dunin-Borkowski, K. J. J. Mayrhofer, P. Strasser, *Adv. Energy Mater.* **2018**, 1701663-n/a.
- [210] H. Schmies, A. Bergmann, J. Drnec, G. Wang, D. Teschner, S. Köhl, D. J. S. Sandbeck, S. Cherevko, M. Gocyla, M. Shviro, M. Heggen, V. Ramani, R. E. Dunin-Borkowski, K. J. J. Mayrhofer, P. Strasser, *Adv. Energy Mater.* **2018**, *8*, 1701663.
- [211] S. Geiger, O. Kasian, A. M. Mingers, K. J. J. Mayrhofer, S. Cherevko, *Sci. Rep.* **2017**, *7*, 4595.
- [212] J.-P. Suchsland, B. Klose-Schubert, D. Herein, T. Martin, C. Eickes, M. Lennartz, *ECS Trans.* **2012**, *50*, 1659-1667.
- [213] E. Fabbri, A. Rabis, R. Kotz, T. J. Schmidt, *Phys. Chem. Chem. Phys.* **2014**, *16*, 13672-13681.
- [214] G. Ozouf, G. Cognard, F. Maillard, M. Chatenet, L. Guétaz, M. Heitzmann, P.-A. Jacques, C. Beauger, *J. Electrochem. Soc.* **2018**, *165*, F3036-F3044.
- [215] S. Yang, Y. Huang, W. Zhu, B. Deng, H. Wang, Z. Zhang, P. Bao, G. Wang, *Int. J. Hydrogen Energy* **2014**, *39*, 15063-15071.

- [216] D.-J. Guo, Z.-H. Jing, *J. Colloid Interface Sci.* **2011**, *359*, 257-260.
- [217] R. Kou, Y. Shao, D. Mei, Z. Nie, D. Wang, C. Wang, V. V. Viswanathan, S. Park, I. A. Aksay, Y. Lin, Y. Wang, J. Liu, *J. Am. Chem. Soc.* **2011**, *133*, 2541-2547.
- [218] S. Park, Y. Shao, H. Wan, P. C. Rieke, V. V. Viswanathan, S. A. Towne, L. V. Saraf, J. Liu, Y. Lin, Y. Wang, *Electrochem. Commun.* **2011**, *13*, 258-261.
- [219] H. Lv, N. Cheng, T. Peng, M. Pan, S. Mu, *J. Mater. Chem.* **2012**, *22*, 1135-1141.
- [220] T. Kinumoto, N. Eguchi, M. Matsuoka, T. Tsumura, M. Toyoda, *ECS Trans.* **2013**, *58*, 1259-1265.
- [221] J. Parrondo, F. Mijangos, B. Rambabu, *J. Power Sources* **2010**, *195*, 3977-3983.
- [222] C. Raab, M. Simkó, U. Fiedeler, M. Nentwich, A. Gzásó, *ITA NanoTrust Dossiers* **2008**, *6*, 1-4.
- [223] J. Park, J. Joo, S. G. Kwon, Y. Jang, T. Hyeon, *Angew. Chem.* **2007**, *119*, 4714-4745.
- [224] Y. Wang, J. Ren, K. Deng, L. Gui, Y. Tang, *Chem. Mater.* **2000**, *12*, 1622-1627.
- [225] C. Xu, X. Wang, J. Zhu, *J. Phys. Chem. C* **2008**, *112*, 19841-19845.
- [226] A. Marinkas, F. Arena, J. Mitzel, G. M. Prinz, A. Heinzl, V. Peinecke, H. Natter, *Carbon* **2013**, *58*, 139-150.
- [227] C.-C. Chou, C.-H. Liu, B.-H. Chen, *Energy* **2014**, *70*, 231-238.
- [228] C. Bock, C. Paquet, M. Couillard, G. A. Botton, B. R. MacDougall, *J. Am. Chem. Soc.* **2004**, *126*, 8028-8037.
- [229] V. K. LaMer, R. H. Dinegar, *J. Am. Chem. Soc.* **1950**, *72*, 4847-4854.
- [230] D. Schonvogel, J. Hülstede, P. Wagner, I. Kruusenberg, K. Tammeveski, A. Dyck, C. Agert, M. Wark, *J. Electrochem. Soc.* **2017**, *164*, F995-F1004.
- [231] D. Schonvogel, J. Hülstede, P. Wagner, A. Dyck, C. Agert, M. Wark, *J. Electrochem. Soc.* **2018**, *165*, F3373-F3382.
- [232] S. Neumann, S. Grotheer, J. Tielke, I. Schrader, J. Quinson, A. Zana, M. Oezaslan, M. Arenz, S. Kunz, *J. Mater. Chem. A* **2017**, *5*, 6140-6145.
- [233] J. Speder, L. Altmann, M. Roefzaad, M. Baumer, J. J. K. Kirkensgaard, K. Mortensen, M. Arenz, *Phys. Chem. Chem. Phys.* **2013**, *15*, 3602-3608.
- [234] J. Ba, A. Feldhoff, D. Fattakhova Rohlfing, M. Wark, M. Antonietti, M. Niederberger, *Small* **2007**, *3*, 310-317.
- [235] H. Xu, L. Shi, Z. Wang, J. Liu, J. Zhu, Y. Zhao, M. Zhang, S. Yuan, *ACS Appl. Mater. Interfaces* **2015**, *7*, 27486-27493.
- [236] W. Zhou, Z. L. Wang, *Scanning Microscopy for Nanotechnology: Techniques and Applications*, Springer New York, New York, U.S.A., **2007**.
- [237] K. C., *Transmission Electron Microscopy Characterization of Nanomaterials*, Springer Berlin/Heidelberg, Berlin/Heidelberg, Germany, **2014**.
- [238] D. C. Bell, A. J. Garratt-Reed, *Energy Dispersive X-ray Analysis in the Electron Microscope*, Garland Science, U.S.A., **2003**.
- [239] S.-L. Zhang, *Raman Spectroscopy and its Application in Nanostructures*, Wiley, Chichester, U.K., **2012**.
- [240] B. H. Stuart, *Infrared spectroscopy fundamentals and applications*, NJ Wiley-Interscience, Hoboken, U.S.A., **2005**.

- [241] P. van der Heide, *X-ray photoelectron spectroscopy : An introduction to principles and practices*, Wiley, Hoboken, U.S.A., **2012**.
- [242] H. Ibach, H. Lüth, *Festkörperphysik: Einführung in die Grundlagen*, Springer Berlin/Heidelberg, Berlin/Heidelberg, Germany, **2009**.
- [243] P. J. Haines, *Principles of Thermal Analysis and Calorimetry*, The Royal Society of Chemistry, London, U.K., **2002**.
- [244] M. Thommes, K. Kaneko, V. Neimark Alexander, P. Olivier James, F. Rodriguez-Reinoso, J. Rouquerol, S. W. Sing Kenneth, *Pure Appl. Chem.* **2015**, *87*, 1051.
- [245] K. Cammann, *Instrumentelle analytische Chemie: Verfahren, Anwendungen und Qualitätssicherung*, Spektrum, Heidelberg, Berlin, **2001**.
- [246] Y. Singh, *International Journal of Modern Physics: Conference Series* **2013**, *22*, 745-756.
- [247] P. S. Fernández, D. S. Ferreira, C. A. Martins, H. E. Troiani, G. A. Camara, M. E. Martins, *Electrochim. Acta* **2013**, *98*, 25-31.
- [248] R. B. de Lima, V. Paganin, T. Iwasita, W. Vielstich, *Electrochim. Acta* **2003**, *49*, 85-91.
- [249] Y. B. Vassiliev, S. A. Sarghisyan, *Electrochim. Acta* **1986**, *31*, 645-655.
- [250] P. Urchaga, S. Baranton, C. Coutanceau, G. Jerkiewicz, *Langmuir* **2012**, *28*, 3658-3663.
- [251] T. Vidakovic, M. Christov, K. Sundmacher, *Electrochim. Acta* **2007**, *52*, 5606-5613.
- [252] L. Li, Y. Xing, *J. Electrochem. Soc.* **2006**, *153*, A1823-A1828.
- [253] A. Buchsteiner, A. Lerf, J. Pieper, *J. Phys. Chem. B* **2006**, *110*, 22328-22338.
- [254] S. Eigler, M. Enzelberger-Heim, S. Grimm, P. Hofmann, W. Kroener, A. Geworski, C. Dotzer, M. Röckert, J. Xiao, C. Papp, O. Lytken, H.-P. Steinrück, P. Müller, A. Hirsch, *Adv. Mater.* **2013**, *25*, 3583-3587.
- [255] H. C. Schniepp, J.-L. Li, M. J. McAllister, H. Sai, M. Herrera-Alonso, D. H. Adamson, R. K. Prud'homme, R. Car, D. A. Saville, I. A. Aksay, *J. Phys. Chem. B* **2006**, *110*, 8535-8539.
- [256] X. Gao, J. Jang, S. Nagase, *J. Phys. Chem. C* **2010**, *114*, 832-842.
- [257] T. Sobolyeva, PhD thesis, Simon Fraser University, Burnaby, Canada, **2010**.
- [258] D. Yang, A. Velamakanni, G. Bozoklu, S. Park, M. Stoller, R. D. Piner, S. Stankovich, I. Jung, D. A. Field, C. A. Ventrice, R. S. Ruoff, *Carbon* **2009**, *47*, 145-152.
- [259] C. Mattevi, G. Eda, S. Agnoli, S. Miller, K. A. Mkhoyan, O. Celik, D. Mastrogiovanni, G. Granozzi, E. Garfunkel, M. Chhowalla, *Adv. Funct. Mater.* **2009**, *19*, 2577-2583.
- [260] Y. Shao, J. Wang, M. Engelhard, C. Wang, Y. Lin, *J. Mater. Chem.* **2010**, *20*, 743-748.
- [261] L. Zhao, Z.-B. Wang, J.-L. Li, J.-J. Zhang, X.-L. Sui, L.-M. Zhang, *Electrochim. Acta* **2016**, *189*, 175-183.
- [262] J. H. Jung, H. J. Park, J. Kim, S. H. Hur, *J. Power Sources* **2014**, *248*, 1156-1162.
- [263] R. L. Calabro, D.-S. Yang, D. Y. Kim, *J. Colloid Interface Sci.* **2018**, *527*, 132-140.
- [264] G. Wang, E. Niangar, K. Huang, D. Atienza, A. Kumar, N. Dale, K. Oshihara, V. K. Ramani, *ECS Trans.* **2015**, *69*, 1179-1205.
- [265] T. Seibel, PhD thesis, Johannes Gutenberg-Universität Mainz, Mainz, Germany, **2007**.
- [266] N. Nadaud, N. Lequeux, M. Nanot, J. Jové, T. Roisnel, *J. Solid State Chem.* **1998**, *135*, 140-148.

- [267] G. Cognard, G. Ozouf, C. Beauger, I. Jiménez-Morales, S. Cavaliere, D. Jones, J. Rozière, M. Chatenet, F. Maillard, *Electrocatalysis* **2017**, *8*, 51-58.
- [268] E. Yuliza, R. Murniati, A. Rajak, Khairurrijal, M. Abdullah, in *International Conference on Advances in Education Technology (ICAET 2014)*, **2014**.
- [269] X. Wang, X. Wang, Q. Di, H. Zhao, B. Liang, J. Yang, *Materials* **2017**, *10*, 1398.
- [270] S. Major, S. Kumar, M. Bhatnagar, K. L. Chopra, *Appl. Phys. Lett.* **1986**, *49*, 394-396.
- [271] Y. Li, Y. Li, E. Zhu, T. McLouth, C.-Y. Chiu, X. Huang, Y. Huang, *J. Am. Chem. Soc.* **2012**, *134*, 12326-12329.
- [272] Y. Devrim, E. D. Arıca, A. Albostan, *Int. J. Hydrogen Energy* **2018**, *43*, 11820-11829.
- [273] S. Taylor, E. Fabbri, P. Levecque, T. J. Schmidt, O. Conrad, *Electrocatalysis* **2016**, *7*, 287-296.
- [274] Q.-S. Chen, J. Solla-Gullón, S.-G. Sun, J. M. Feliu, *Electrochim. Acta* **2010**, *55*, 7982-7994.
- [275] R. A. Martínez-Rodríguez, F. J. Vidal-Iglesias, J. Solla-Gullón, C. R. Cabrera, J. M. Feliu, *ChemElectroChem* **2016**, *3*, 1601-1608.
- [276] H.-J. Krebs, H. Lüth, *Applied physics* **1977**, *14*, 337-342.
- [277] D. Lozano-Castelló, D. Cazorla-Amorós, A. Linares-Solano, S. Shiraishi, H. Kurihara, A. Oya, *Carbon* **2003**, *41*, 1765-1775.
- [278] N. M. Markovioc, H. A. Gasteiger, P. N. Ross, *J. Phys. Chem.* **1996**, *100*, 6715-6721.
- [279] K. Jukk, J. Kozlova, P. Ritslaid, V. Sammelselg, N. Alexeyeva, K. Tammeveski, *J. Electroanal. Chem.* **2013**, *708*, 31-38.
- [280] F. Maillard, M. Eikerling, O. V. Cherstiouk, S. Schreier, E. Savinova, U. Stimming, *Faraday Discuss.* **2004**, *125*, 357-377.
- [281] M. J. Bleda-Martínez, J. A. Maciá-Agulló, D. Lozano-Castelló, E. Morallón, D. Cazorla-Amorós, A. Linares-Solano, *Carbon* **2005**, *43*, 2677-2684.
- [282] A. López-Cudero, J. Solla-Gullón, E. Herrero, A. Aldaz, J. M. Feliu, *J. Electroanal. Chem.* **2010**, *644*, 117-126.
- [283] T. Kinumoto, N. Eguchi, M. Matsuoka, T. Tsumura, M. Toyoda, *ECS Trans.* **2013**, *50*, 1701-1706.
- [284] K. Schlögl, K. J. J. Mayrhofer, M. Hanzlik, M. Arenz, *J. Electroanal. Chem.* **2011**, *662*, 355-360.
- [285] A. J. Bard, R. Parsons, J. Jordan, *Standard Potentials in Aqueous Solution*, CRC Press, Boca Raton, U.S.A., **1985**.
- [286] F. J. Pinar, M. Rastedt, N. Pilinski, P. Wagner, A. Dyck, *Int. J. Hydrogen Energy* **2017**, *42*, 13860-13875.
- [287] H. Yang, T. Song, S. Lee, H. Han, F. Xia, A. Devadoss, W. Sigmund, U. Paik, *Electrochim. Acta* **2013**, *91*, 275-281.
- [288] J.-Y. Lin, M.-H. Chou, Y.-C. Kuo, *J. Alloys Compd.* **2014**, *589*, 472-478.
- [289] R. Nowak, S. Geißendörfer, K. Chakanga, M. Juilfs, N. Reininghaus, M. Vehse, K. v. Maydell, C. Agert, *IEEE Journal of Photovoltaics* **2015**, *5*, 479-486.

# Appendix

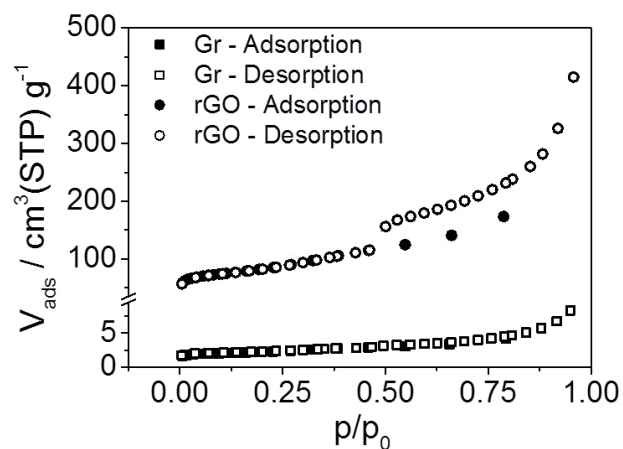


**Figure 63** BET isotherms of reduced graphene oxide in comparison to the precursor material graphite.

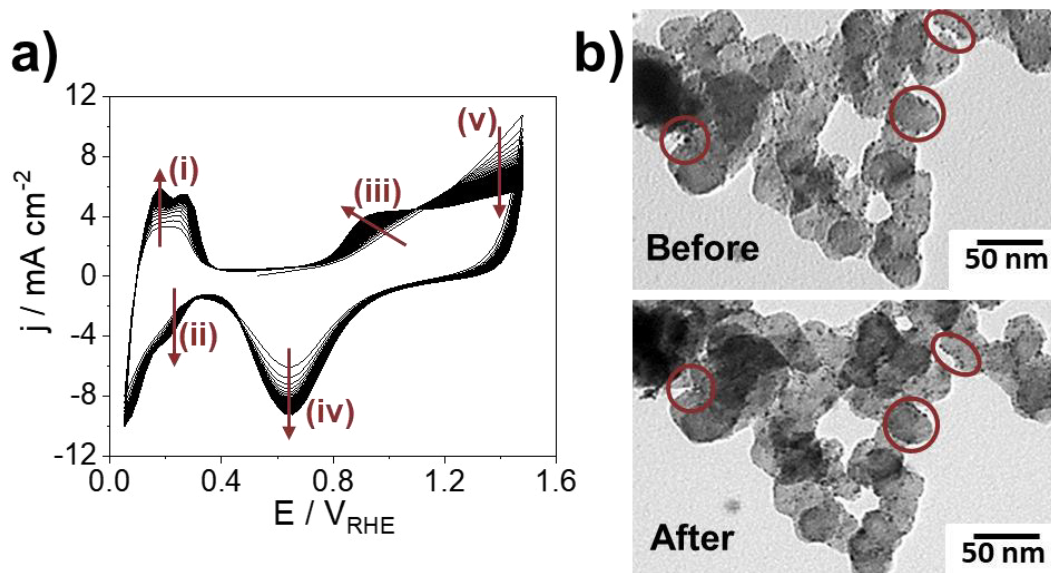


**Figure 64** Activation of Pt/C. Cyclic voltammetry with 100 cycles between 0.05–1.47  $V_{\text{RHE}}$  at  $500 \text{ mV s}^{-1}$  in  $\text{N}_2$ -sat.  $0.1 \text{ mol L}^{-1} \text{ HClO}_4$ ; increasing Pt signals in the hydrogen range (i, ii) and in the oxygen range (iii, iv); at high potentials above  $1.0 V_{\text{RHE}}$  (v) shrinking oxidative currents (a). IL-TEM images before and after CV (b).

# Abbreviations

4-point	Four-point probe method for electrical conductivity measurements
AEMFC	Anion exchange membrane fuel cell
AST	Accelerated stress testing
ATO	Sb-doped tin (IV) oxide
BET	N <sub>2</sub> adsorption with Brunauer-Emmett-Teller evaluation
C	Carbon black (Vulcan <sup>®</sup> XC72R)
CHP	Combined heat and power systems
CV	Cyclic voltammetry
CVD	Chemical vapor deposition
DFT	Density functional theory
DOE	U.S. Department of Energy
ECSA	Electrochemical surface area
EDS	Energy-dispersive X-ray spectroscopy
FC	Fuel cell
FCHJU	Fuel Cells and Hydrogen Joint Undertaking
FTO	Fluorine-doped tin (IV) oxide
GDE	Gas diffusion electrode
GDL	Gas diffusion layer
GO	Graphite Oxide
Gr	Graphite
HOR	Hydrogen oxidation reaction
HQ/Q	Hydroquinone/quinone
HR-TEM	High resolution transmission electron microscopy
HTC	Hydrothermal carbonization
HTC-C	Carbon derived from HTC of coconut shells; activated by pyrolysis
HT-PEMFC	High temperature proton exchange membrane fuel cell
ICP-MS	Mass spectrometry with inductive coupled plasma
ICSD	Inorganic crystal structure database
IL-TEM	Identical location transmission electron microscopy
IR	Infrared spectroscopy
ITO	Tin-doped indium (III) oxide
K-L	Koutecky-Levich
LT-PEMFC	Low temperature proton exchange membrane fuel cell

MCFC	Molten carbonate fuel cell
MEA	Membrane electrode assembly
MPL	Microporous layer
MWCNTs	Multi-walled carbon nanotubes
OCV	Open circuit voltage
ORR	Oxygen reduction reaction
ORR	Oxygen reduction reaction
PBI	Polybenzimidazole
PEMFC	Proton exchange membrane fuel cell
Raman	Raman spectroscopy
RDE	Rotating disk electrode
rGO	Reduced graphene oxide
RHE	Reversible hydrogen electrode
SCE	Standard calomel electrode
SEM	Scanning electron microscopy
SHE	Standard hydrogen electrode
SOFC	Solid oxide fuel cell
SWCNTs	Single-walled carbon nanotubes
TCO	Transparent conductive oxides
TEM	Transmission electron microscopy
TGA	Thermogravimetric analysis
XPS	X-ray photoelectron spectroscopy
XRD	X-ray diffraction

# Symbols

$\eta$	Overpotential
$\theta$	Angle of reflection in X-ray diffraction
$\nu$	Scan rate
$\varrho$	Kinematic viscosity
$\omega$	Rotation speed
$BE$	Binding energy
$BE_{\text{Oxygen}}$	Oxygen binding energy
$c_{\text{O}_2}^*$	Concentration of oxygen in solution
$C_{\text{DL}}$	Double layer capacitance
$c_i$	Concentration
$d$	Interplanar atomic distance
$D_{\text{O}_2}$	Diffusion coefficient of oxygen
$E$	Potential
$E^\circ$	Standard potential
$E_a$	Activation energy
$E_{\text{incident}}$	Incident energy
$E_{\text{emitted}}$	Emitted energy
$E_{\text{kin}}$	Kinetic energy
$\varepsilon$	Energy state
$\varepsilon_{\text{F}}$	Fermi energy
$ECSA_{\text{CO}}$	Electrochemical surface area via CO stripping voltammetry
$ECSA_{\text{HUPD}}$	Electrochemical surface area via hydrogen underpotential deposition
$E_{\text{onset}}$	Onset potential
$F$	Faraday constant
$FWHM$	Fully peak width at half maximum
$h$	Planck constant
$I$	Current
$I_a$	Anodic current
$I_c$	Cathodic current
$I_{\text{D}}/I_{\text{G}}$	Ratio of D band intensity to G band intensity during Raman spectroscopy
$j$	Current density
$j_0$	Exchange current density
$j_{\text{kin}}$	Kinetic current density

$j_{\text{lim}}$	Diffusion-limited current density
$K$	Form factor for Scherrer Equation
$k_0$	Standard rate constant
$k_i$	Rate constant of forward or backward reaction
$L$	Crystallite size
$m_{\text{Pt}}$	Pt loading
$MA$	Mass activity of oxygen reduction reaction
$m_{\text{I}}$	Tafel slope in region I
$m_{\text{II}}$	Tafel slope in region II
$n$	Number of transferred electrons during reaction
$p/p_0$	Relative pressure
$p_i$	Partial pressure
$Q_{\text{HQ}}$	Charge amount of hydroquinone oxidation
$Q_i$	Charge amount
$R$	Gas constant
$r$	Reaction rate
$SA$	Specific activity of oxygen reduction reaction
$T$	Temperature
$t$	Time
$\nu$	Frequency
$V_{\text{ads}}$	Volume of adsorbed species
$V_i$	Volume
$W$	Spectrometer work function
$z$	Positive integer of a radiation wavelength
$\alpha$	Transfer coefficient
$\lambda$	Radiation wavelength
$\rho$	Charge density
$\Delta G$	Gibbs free energy
$\Delta G^\circ$	Standard Gibbs free energy
$\Delta H$	Reaction enthalpy

# Figures

Figure 1 Global air temperature against the year, adapted from <sup>[5]</sup> (a) and global emission of carbon dioxide against the year, adapted from <sup>[6]</sup> (b).....	1
Figure 2 Schematic depiction of a PEM fuel cell with microscopic image of a membrane electrode assembly (left) and schematic enlarged view into the catalyst layer with microscopic image of Pt on carbon black (right), adapted from <sup>[52]</sup> .....	7
Figure 3 Schematic PEMFC polarization curve; indication of $\Delta G$ and subscription of voltage $U$ losses as a function of the current $I$ , adapted from <sup>[57]</sup> .....	11
Figure 4 Volcano plot showing ORR activity in the form of kinetic current density $j_{kin}$ plotted against oxygen binding energy $BE_{Oxygen}$ , adapted from <sup>[58]</sup> .....	12
Figure 5 Change in electronic structure by O atom adsorption on Pt (111) surface with energy states $\epsilon$ and the Fermi energy $\epsilon_F$ and the formation of covalent bonding and antibonding states, adapted from <sup>[66]</sup> .....	14
Figure 6 Schematically presented paths of Pt degradation occurring in a PEM fuel cell, adapted from <sup>[15, 17, 71]</sup> .....	16
Figure 7 $Pt^{2+}$ concentration in dependence of electrode potential and temperature. Theoretical data from Pourbaix <sup>[76]</sup> in grey lines (solid 25 °C, dashed 80 °C and dotted 196 °C) and experimental data in black lines (filled dots Honji <sup>[77]</sup> , squares Bindra <sup>[78]</sup> , unfilled dots Ferreira <sup>[79]</sup> and stars Wang <sup>[74]</sup> ), adapted from <sup>[15]</sup> .....	17
Figure 8 Illustration of the carbon impact on stability and activity for ORR, summarized from Sections 3.2.2 and 3.2.3. Arrows up means higher and arrows down means lower number of appropriate carbon property required. <sup>[137]</sup> .....	23
Figure 9 Scheme of layer arrangement in graphitic carbons with exemplary part of the chemical structure: Hexagonal coordinated graphite (a), graphite oxide (b), reduced graphene oxide (c), carbon black particle (d) and single-walled carbon nanotube (e). <sup>[133, 162, 166]</sup> .....	27
Figure 10 Potential–pH diagram of tin (cobalt as example to show the opposite). <sup>[186]</sup> .....	29
Figure 11 TEM images (a) and HAADF–STEM images with Pt depicted in blue, In in green and Sn in red (b) before and after stressing Pt/ITO by potential cycling between 0.60–0.95 $V_{RHE}$ . <sup>[210]</sup> .....	32
Figure 12 Schematic view on a carbon section (grey) with a fixed metal oxide particle (green) and a Pt nanoparticle anchored at the carbon–metal oxide interface (red), adapted from <sup>[47]</sup> .....	33
Figure 13 LaMer model, adapted from <sup>[223]</sup> .....	37
Figure 14 Functional principle of the four–point probe method. ....	46
Figure 15 Setup consisting of rotator with rotating disk electrode (RDE) as working electrode (1), reference electrode with salt bridge and Luggin capillary (2), counter electrode (3), glass cell filled with electrolyte (4) and gas inlet (5).....	48
Figure 16 Exemplary CV curve (a) and CO stripping curve (b) of commercial Pt/C in 0.1 mol L <sup>-1</sup> HClO <sub>4</sub> . Illustration of typical electrochemical Pt signals with	

crosshatched signals for ECSA determination via HUPD and CO (green marks). Illustration of support characteristics (red marks).....	51
Figure 17 Exemplary CV curve with suppressed faradaic currents (a) and CV curve with enlarged HQ/Q region (b) of commercial Pt/C in 0.1 mol L <sup>-1</sup> HClO <sub>4</sub> .....	52
Figure 18 Exemplary ORR curve of commercial Pt/C in 0.1 mol L <sup>-1</sup> HClO <sub>4</sub> at 1,600 rpm (a) and the associated Tafel Plot (b).....	54
Figure 19 Accelerated stress test in oxygen-saturated 0.1 mol L <sup>-1</sup> HClO <sub>4</sub> . Potential against the time for the whole AST (a) and for a part of AST with one labeled cycle (b). ....	55
Figure 20 SEM images of Gr (a) in contrast to rGO (b) with images of rGO in higher magnification (c, d).....	58
Figure 21 TEM images of graphite (a), graphite oxide (b) and reduced graphene oxide (c).....	59
Figure 22 XRD of graphite, graphite oxide and reduced graphene oxide (a) with zoomed XRD of GO (b) and of rGO sample (c). ....	60
Figure 23 Raman spectra of graphite, graphite oxide and reduced graphene oxide (a) with zoomed and lapped range of D- and G-band (b). ....	62
Figure 24 TGA of GO and rGO from 30–900 °C using N <sub>2</sub> atmosphere and 10 min holding at 100 °C (a) and IR spectra of GO and rGO (b). ....	63
Figure 25 TEM images of rGO (a), carbon black (b) MWCNTs (c) and HTC-C (d). ....	65
Figure 26 BET isotherms of rGO, carbon black, MWCNTs and HTC-C. ....	67
Figure 27 XRD (a) and Raman (b) of rGO, C, MWCNTs and HTC-C. ....	68
Figure 28 TGA of rGO, C, MWCNTs and HTC-C from 30–900 °C using N <sub>2</sub> atmosphere and 10 min holding at 100 °C. ....	71
Figure 29 XP survey spectra of rGO, C, MWCNTs and HTC-C. ....	72
Figure 30 XP spectra of rGO, C, MWCNTs and HTC-C. C1s high resolution spectra (a) and O1s high resolution spectra (b). ....	74
Figure 31 Scheme of the proposed carbon structures: Reduced graphene oxide (a), carbon black (b), MWCNT (c) and HTC-C (d). ....	75
Figure 32 Electron microscopy of ITO–rGO: SEM image (a), TEM and HR-TEM of larger ITO crystals at rGO edges (b), TEM images of distributed ITO nanoparticles on rGO (c, d), ITO nanoparticle size distribution (e) and atomic lattice distances of ITO at rGO surface (f). ....	77
Figure 33 Electron microscopy of FTO–rGO: SEM image (a), TEM images of distributed FTO nanoparticles on rGO (b, c), FTO nanoparticle size distribution (d) and atomic lattice distances of FTO (e). ....	78
Figure 34 XRD of ITO–rGO with ICSD reference pattern 00-001-0929 (a) and FTO–rGO with ICSD reference pattern 98-000-9163 (b). <sup>[230, 231]</sup> .....	80
Figure 35 XPS of ITO–rGO and FTO–rGO nanocomposites. Survey scan (a), In3d (b) and Sn3d (c) scans of ITO–rGO; Survey scan (d), Sn3d (e) and F1s (f) scans of FTO–rGO; C1s (g) and O1s (h) spectra of both nanocomposites (solid lines) and of pristine rGO (dashed lines). <sup>[231]</sup> .....	82
Figure 36 TEM images with Pt particle size distribution of Pt/rGO (a), Pt/C (b), Pt/MWCNT (c), Pt/HTC-C (d) and Pt/C-commercial (e). ....	86

Figure 37 TEM images with Pt particle size distribution of platinum on ITO-rGO (a) and FTO-rGO supports (b).	87
Figure 38 XRD of Pt catalysts in comparison with ICSD reference patterns: 00-001-1194 for Pt, 00-001-0929 for In <sub>2</sub> O <sub>3</sub> and 98-000-9163 for SnO <sub>2</sub> . <sup>[230, 231]</sup>	88
Figure 39 HR-TEM images of Pt/ITO-rGO with visualized atomic lattice distances of ITO and Pt.	90
Figure 40 HR-TEM images of Pt/FTO-rGO with visualized atomic lattice distances of FTO and Pt. <sup>[231]</sup>	90
Figure 41 EDS mapping of Pt/ITO-rGO with elemental distribution of Sn, In and Pt (a) and of Pt/FTO-rGO with elemental distribution of Sn, F and Pt (b). <sup>[231]</sup>	92
Figure 42 Cyclic voltammetry (a) and CO stripping voltammetry (b) of carbon-based Pt catalysts in comparison.	95
Figure 43 Cyclic voltammetry of carbon-based Pt catalysts after CO sorption.	96
Figure 44 ORR data of carbon-based Pt catalysts. Cathodic scans at different rotation speeds with K-L and Tafel plots for Pt/rGO (a), Pt/C (b), Pt/MWCNT (c) and Pt/C-commercial (d).	98
Figure 45 Selected potential cycles during AST with inset of ECSA change for Pt/rGO (a), Pt/C (b), Pt/MWCNT (c) and Pt/C-commercial (d).	101
Figure 46 Comparison of cyclic and CO stripping voltammetry curves before and after AST with insets of HQ/Q redox activities. Pt/rGO (a), Pt/C (b), Pt/MWCNT (c) and Pt/C-commercial (d).	103
Figure 47 Comparison of CV curves after CO sorption before and after AST. Pt/rGO (a), Pt/C (b), Pt/MWCNT (c) and Pt/C-commercial (d).	105
Figure 48 Comparison of cathodic ORR scans at 1,600 rpm before and after AST with insets of Tafel plots. Pt/rGO (a), Pt/C (b), Pt/MWCNT (c) and Pt/C-commercial (d).	106
Figure 49 Cyclic and CO stripping voltammetry of Pt/HTC-C catalyst and HTC-C support in comparison (a). CV of Pt/HTC-C catalyst and HTC-C support after CO sorption (b).	110
Figure 50 ORR data of Pt/HTC-C catalyst and HTC-C support. Cathodic scans at different rotation speeds with K-L and Tafel plots for Pt/HTC-C and at 1,600 rpm for HTC-C.	111
Figure 51 Selected potential cycles during AST with inset of ECSA change for Pt/HTC-C catalyst (a) and HTC-C support (b).	112
Figure 52 Cyclic voltammetry of Pt/HTC-C catalyst and HTC-C support after CO sorption. Comparison of curves before and after AST.	113
Figure 53 Comparison of cyclic and CO stripping voltammetry curves before and after AST with insets of HQ/Q redox activities for Pt/HTC-C (a) and comparison of cathodic ORR scans at 1,600 rpm before and after AST with insets of Tafel plots for Pt/HTC-C (b).	114
Figure 54 Cyclic voltammetry and CO stripping voltammetry for Pt/ITO-rGO catalyst and ITO-rGO support (a) and for Pt/FTO-rGO catalyst and FTO-rGO support (b) in comparison.	117

Figure 55 Cyclic voltammetry of Pt/ITO-rGO catalyst and ITO-rGO support as well as Pt/FTO-rGO catalyst and FTO-rGO support after CO sorption. ....	118
Figure 56 ORR data of Pt catalysts based on nanocomposites. Cathodic scans at different rotation speeds with K-L and Tafel plots for Pt/ITO-rGO and at 1,600 rpm for ITO-rGO (a) and scans for Pt/FTO-rGO and FTO-rGO (b). ....	119
Figure 57 Selected potential cycles during AST with inset of ECSA change for Pt/ITO-rGO (a) and ITO-rGO (b) and for Pt/FTO-rGO (c) and FTO-rGO (d). ....	122
Figure 58 Comparison of cyclic and CO stripping voltammetry curves with insets of HQ/Q redox activities before and after AST. Pt/ITO-rGO (a) and Pt/FTO-rGO (b). ....	123
Figure 59 Comparison of CV curves after CO sorption before and after AST. Pt/ITO-rGO (a) and Pt/FTO-rGO (b). ....	126
Figure 60 Comparison of cathodic ORR scans at 1,600 rpm with insets of Tafel plots before and after AST. Pt/ITO-rGO (a) and Pt/FTO-rGO (b). ....	127
Figure 61 IL-TEM images of Pt/rGO (a), Pt/FTO-rGO (b) and Pt/ ITO-rGO (c) before and after AST. Pt agglomeration marked with 1, Pt dissolution/ detachment/ migration marked with 2 and metal oxide particles marked with 3. ....	129
Figure 62 Scheme of proposed degradation mechanisms for Pt/ITO-rGO (a) and Pt/FTO-rGO (b). ....	134
Figure 63 BET isotherms of reduced graphene oxide in comparison to the precursor material graphite. ....	148
Figure 64 Activation of Pt/C. Cyclic voltammetry with 100 cycles between 0.05–1.47 V <sub>RHE</sub> at 500 mV s <sup>-1</sup> in N <sub>2</sub> -sat. 0.1 mol L <sup>-1</sup> HClO <sub>4</sub> ; increasing Pt signals in the hydrogen range (i, ii) and in the oxygen range (iii, iv); at high potentials above 1.0 V <sub>RHE</sub> (v) shrinking oxidative currents (a). IL-TEM images before and after CV (b). ....	148

# Tables

Table 1 Comparison of PEMFC types. <sup>[53]</sup> .....	9
Table 2 Requirements on Pt supports in PEMFCs. <sup>[24, 46, 132, 133]</sup> .....	22
Table 3 Applied methods to physically analyze Pt nanoparticle and support properties. ....	40
Table 4 RDE preparation in dependence on the catalyst being used. ....	49
Table 5 Summary of technical parameters for electrochemical investigation. ....	56
Table 6 Parameters from XRD and Raman analyses for graphite, GO and rGO. <sup>[230]</sup> .....	60
Table 7 Summarized physical parameters for rGO, C, MWCNTs and HTC-C. <sup>[230]</sup> .....	69
Table 8 Summarized physical parameters for ITO-rGO and FTO-rGO. <sup>[230, 231]</sup> .....	80
Table 9 Overview of Pt particle diameters from TEM and Pt contents on the supports materials from ICP-MS. <sup>[230, 231]</sup> .....	89
Table 10 Electrochemical parameters of carbon-based Pt catalysts. <sup>[230, 231]</sup> .....	100
Table 11 Change of electrochemical parameters during stress testing on carbon-based Pt catalysts. <sup>[230, 231]</sup> .....	107
Table 12 Electrochemical parameters of Pt catalysts based on nanocomposites. <sup>[230, 231]</sup> .....	120
Table 13 Change of electrochemical parameters due to stress testing on Pt catalysts based on nanocomposites. <sup>[230, 231]</sup> .....	125

# Publication List

## Journal Publications

- I. D. Schonvogel, H. Multhaupt, M. Nowotny, T. Worriescheck, P. Wagner, A. Dyck, C. Agert, M. Wark, *ChemSusChem* **2018**, in preparation.
- II. D. Schonvogel, J. Hülstede, P. Wagner, A. Dyck, C. Agert, M. Wark, *J. Electrochem. Soc.* **2018**, *165*, F3373–F3382.
- III. D. Schonvogel, J. Hülstede, P. Wagner, A. Dyck, C. Agert, M. Wark, *ECS Trans.* **2017**, *80*, 879–895.
- IV. D. Schonvogel, J. Hülstede, P. Wagner, I. Kruusenberg, K. Tammeveski, A. Dyck, C. Agert, M. Wark, *J. Electrochem. Soc.* **2017**, *164*, F995–F1004.

## Conference Contributions

- V. D. Schonvogel, P. Wagner, A. Dyck, C. Agert, M. Wark, EMN Meeting – Energy Materials and Nanotechnology, Berlin, Germany **2018**, *Graphene-Based Platinum Catalysts for PEM Fuel Cell Application*, Oral Presentation (Invited).
- VI. D. Schonvogel, J. Hülstede, P. Wagner, A. Dyck, C. Agert, M. Wark, 232<sup>nd</sup> ECS Meeting, National Harbor, USA **2017**, *Investigation of Reduced Graphene Oxide with F-Doped SnO<sub>2</sub> as Catalyst Support in Fuel Cells*, Oral Presentation.
- VII. D. Schonvogel, J. Hülstede, M. Wark, P. Wagner, A. Dyck, C. Agert, 50. Jahrestreffen Deutscher Katalytiker, Weimar, Germany **2017**, *A Comparison Study to Pt Nanoparticles on Carbon Supports as Electrocatalyst in Fuel Cells*, Poster.
- VIII. D. Schonvogel, P. Wagner, A. Dyck, C. Agert, M. Wark, TNT – Trends in Nanotechnology, Fribourg, Switzerland **2016**, *Hybrids of Reduced Graphene Oxide and Metal Oxides as Catalyst Support in Fuel Cells*, Oral Presentation.
- IX. D. Schonvogel, P. Wagner, A. Dyck, C. Agert, M. Wark, Graphene 2016, Genova, Italy **2016**, *Graphene-Based Nanocomposites as Catalyst Support in High Temperature PEM Fuel Cells*, Poster.

## Publications and Contributions beyond PhD Work

- X. M. Rastedt, V. Tullius, J. Büsselmann, D. Schonvogel, P. Wagner, A. Dyck, *ECS Trans.* **2017**, *80*, 3–17.
- XI. M. Rastedt, V. Tullius, J. Büsselmann, D. Schonvogel, P. Wagner, A. Dyck, 232<sup>nd</sup> ECS Meeting, National Harbor, USA **2017**, *Evaluation of HT-PEM Fuel Cells via Load Cycling at High Current Densities*, Oral Presentation.
- XII. M. Rastedt, V. Tullius, J. Büsselmann, D. Schonvogel, P. Wagner, A. Dyck, 232<sup>nd</sup> ECS Meeting, National Harbor, USA **2017**, *Evaluation of HT-PEM Fuel Cells via Start-Stop Cycling*, Oral Presentation.
- XIII. D. Schonvogel, M. Rastedt, P. Wagner, M. Wark, A. Dyck, *Fuel Cells* **2016**, *16*, 480–489.
- XIV. D. Schonvogel, M. Rastedt, P. Wagner, M. Wark, A. Dyck, 5<sup>th</sup> European PEFC & H<sub>2</sub> Forum, Lucerne, Switzerland **2015**, *Impact of Accelerated Stress Tests on High Temperature PEMFC Degradation*, Oral Presentation.
- XV. M. Rastedt, D. Schonvogel, P. Wagner, *ECS Trans.* **2014**, *64*, 741–753.
- XVI. C. Harms, D. Schonvogel, W. Germer, 6<sup>th</sup> Int. Conference on Polymer Batteries and Fuel Cells, Ulm, Germany **2013**, *Trace Analysis of Metals in Process Waters of Fuel Cells by ICP-MS*, Poster.

# Danksagung

Im Nachfolgenden möchte ich all denjenigen danken, die zu dieser Dissertation durch Mitwirkung und Unterstützung beigetragen haben. Zu allererst danke ich Prof. Dr. Michael Wark, der neben dem Erstellen des Erstgutachtens die wissenschaftliche Betreuung der Arbeit übernahm. Für regelmäßige, fachliche Diskussionen nahm er sich stets Zeit und hat diese Arbeit auch bei organisatorischen Fragen immer auf unkomplizierte Art betreut. Ich danke auch Prof. Dr. Carsten Agert, der ebenfalls betreuend an dieser Arbeit mitwirkte und immer Interesse an fachlicher Diskussion zeigte. Herrn Prof. Dr. Andreas Friedrich danke ich für die Übernahme der Zweitbegutachtung.

Mein besonderer Dank gilt Peter Wagner für die Begleitung dieser Arbeit in Form des stetigen, fachlichen Austauschs sowie Julia Hülstede für ihre großartige Unterstützung im Labor. Auch möchte ich allen Kollegen beim DLR-Institut für Vernetzte Energiesysteme (ehemals NEXT ENERGY) für die hilfsbereite und freundschaftliche Zusammenarbeit danken. Für die Unterstützung auf verschiedenste Art und Weise möchte ich mich insbesondere bei Dr. Fang Liu, Khrystyna Yezerska, Dr. Maren Rastedt, Dr. Lidiya Komsyyska und Dr. Dereje Taffa bedanken.

Weiterhin danke ich der Arbeitsgruppe Tammeveski von der Universität Tartu für die sehr gute Kooperation im Rahmen meines Forschungsaufenthalts in Estland. Für die Möglichkeit der Gerätenutzungen möchte ich den Arbeitsgruppen Wark, Özaslan, Wittstock und Al-Shamery danken. Außerdem danke ich dem Bundesministerium für Wirtschaft und Energie sowie dem Bundesministerium für Bildung und Forschung für die Förderung dieser Arbeit innerhalb der Projekte QUALIFIX (03ET6046A) und NETonia (01DS16011A).

Abschließend gilt das allergrößte Dankeschön meinem Mann Christian für den bedingungslosen Rückhalt während der gesamten Zeit sowie meiner Familie und meinen Freunden für ihre Unterstützung in jeglicher Art.

# Erklärung

Hiermit erkläre ich, Dana Schonvogel, geb. 13.05.1987 in Varel, dass ich die Dissertation selbständig verfasst und nur die angegebenen Hilfsmittel benutzt habe. Die vorliegende Arbeit wurde in Teilen bereits veröffentlicht. Eine Publikationsliste ist der Dissertation beigelegt. Ich erkläre, dass die Dissertation weder in ihrer Gesamtheit noch in Teilen einer anderen wissenschaftlichen Hochschule zur Begutachtung in einem Promotionsverfahren vorliegt bzw. vorlag. Hiermit erkläre ich, dass mir die Leitlinien guter wissenschaftlicher Praxis der Carl von Ossietzky Universität Oldenburg bekannt sind und von mir befolgt wurden. Weiterhin erkläre ich, dass im Zusammenhang mit dem Promotionsvorhaben keine kommerzielle Vermittlungs- oder Beratungsdienste (Promotionsberatung) in Anspruch genommen worden sind.

Oldenburg, den \_\_\_\_\_

(Dana Schonvogel)